PARTICLE MICROSTRUCTURE AND POLYMER DYNAMICS IN CONCENTRATED POLYMER SOLUTIONS

BY

SO YOUN KIM

DISSERTATION

Submitted in partial fulfillment of the requirements
for the degree of Doctor of Philosophy in Chemical Engineering
in the Graduate College of the
University of Illinois at Urbana-Champaign, 2011

Urbana, Illinois

Doctoral Committee:

Professor Charles F. Zukoski, Chair
Professor Kenneth S. Schweizer
Professor Paul J. A. Kenis
Assistant Professor Charles M. Schroeder

Abstract

The states of nanoparticle dispersions in concentrated polymer solutions are studied with extensive small angle scattering and NMR experiments. Silica nanoparticles are suspended in polymer-solvent mixtures. The effects of polymer induced interactions on the particle microstructure are examined with varying (i) polymer concentration, (ii) solvent type, (iii) temperature, (iv) particle volume fraction and (v) polymer chemistry while polymer-to-solvent volume ratio is held between 0.45 and 1. The local order and long wave length concentration fluctuations of nanoparticles are obtained from the analysis of scattering structure factors and compared with the Polymer Reference Site Interaction Model (PRISM) theory. Exploiting contrast matching small-angle neutron scattering all partial collective structure factors of particles, polymers and their interface are characterized establishing the existence and size of adsorbed polymer layers. Comparisons of experimental structure factors to PRISM predictions yield a key parameter, the polymer segment-nanoparticle attractive contact interaction energy. This cohesive energy controls the state of particle and polymer dispersions. The thermodynamic information obtained in these experiments is linked to the polymer dynamics using free induction decay of NMR experiments, which directly quantify the amount of polymer adsorption while multi-quantum NMR experiments probe the existence of physical crosslinks and entanglements. Taken together this thesis provides detailed information of nanoparticle dispersions in dense polymer solutions and polymer nanocomposites and insight into how to manipulate particles and polymer to control particle aggregation.

Acknowledgement

Most of all I would like to thank my advisor, Charles F. Zukoski. During my PhD, it has been a great honor and pleasure to work with him. His enthusiastic, passionate and keen guidance towards science led me to identify and address problems, enjoy the experiments and realize what research is. His support and help not only as an academic advisor, but as a mentor continuously inspired me to finish my PhD and set my future careers.

I also would like to thank Dr. Kenneth Schweizer and Dr. Lisa Hall for collaboration, helpful discussions and kindly provided codes for the theoretical comparisons reported in this thesis. I appreciate Dr. Kay Saalwächter for the help on the NMR experiments. I also appreciate previous and current Zukoski group members for their help and kind friendship.

I acknowledge the XOR 32ID and DND-CAT 5ID beamlines where ultra-small angle x-ray scattering and small angle x-ray scattering experiments were conducted. DND-CAT is supported by E.I. DuPont de Nemours & Co., The Dow Chemical Company and Northwestern University. Use of the Advanced Photon Source, an Office of Science User Facility operated for the U.S. Department of Energy (DOE) Office of Science by Argonne National Laboratory, was supported by the U.S. DOE under Contract No. DE-AC02-06CH11357. I also acknowledge support of the National Institute of Standards and Technology, U.S. Department of Commerce, in providing access to the neutron research facilities used in this work. The work utilized facilities supported in part by the National Science Foundation under Agreement No. DMR-0944772.

The research reported in this thesis was supported by the Nanoscale Science and Engineering Initiative of the National Science Foundation under NSF Award DMR-0642573.

Lastly, I thank my parents, sister and parents-in-law for their devoted help and their endless support to help me to finish my PhD. I especially thank my husband, Chaenyung, who always patiently waited, helped and encouraged me to continue and finish my research.

Table of Contents

CHAPTER 1 INTRODUCTION 1

1.1 Overview 1

1.2 References 4

CHAPTER 2 LONG WAVELENGTH CONCENTRATION FLUCTUATIONS AND CAGE SCALE ORDERING OF NANOPARTICLES IN CONCENTRATED POLYMER SOLUTIONS: EFFECT OF POLYMER TO SOLVENT RATIO 5

2.1 Introduction 5

2.2 Experiments 7

2.2.1 Sample Preparation 7

2.2.2 Side-Bounce Ultra Small X-ray Scattering (SBUSAXS) 9

2.2.3 Experimental Structure Factor 11

2.3 Theory and Model 14

2.3.1 Background 14

2.3.2 Effect of Solvent Dilution 17

2.3.3 Sample Theoretical Results 20

2.4 Comparison of Experiment and Theory 21

2.5 Summary 26

2.6 Table and Figures 28

2.7 References 36

CHAPTER 3 LONG WAVELENGTH CONCENTRATION FLUCTUATIONS AND CAGE SCALE ORDERING OF NANOPARTICLES IN CONCENTRATED POLYMER SOLUTIONS: EFFECT OF SOLVENT CHANGE AND TEMPERATURE 38

3.1 Introduction 38

3.2 Experiment 40

3.2.1 Sample Preparation 40

3.2.2 Side-Bounce Ultra Small X-ray Scattering (SBUSAXS) 42

3.2.3 Small Angle Neutron Scattering (SANS) 42

3.2.4 Experimental Structure Factor 43
3.2.5 Polymer Characterization 45
3.3 Theory 47
3.3.1 Background 47
3.3.2 Effect of Solvent Dilution 47
3.4 Results 49
3.4.1 Effects of Changing Solvent 50
3.4.2 Effect of Polymer-to-Solvent Ratios 51
3.4.3 Effect of Temperature 52
3.5 Summary 55
3.6 Table and Figures 57
3.7 References 67

CHAPTER 4 PARTICLE MICROSTRUCTURES AND FLOW PROPERTIES : EFFECT OF POLYMER TYPES 69
4.1 Introduction 69
4.2 Experiments and Theory Background 73
4.2.1 Sample Preparation 73
4.2.2 Polymer Concentration, R_p 74
4.2.3 Rheological Measurement 74
4.2.4 Small Angle X-ray Scattering 75
4.2.5 PRISM Theory 76
4.3 Intrinsic Viscosity 78
4.3.1 Continuum Model for Intrinsic Viscosity 80
4.4 Polymer Segment-Particle Surface Interaction 81
4.4.1 Experimental Structure Factors 82
4.4.2 Effects of Polymer Dilution 83
4.4.3 Influence of Changing Polymer Chemistry 84
4.4.4 Microstructure of Particles Suspended in PEGDME at R_p = 0.45 87
4.5 Linking Intrinsic Viscosities to Polymer Chemistry 88

4.6 Summary 90
4.7 Tables and Figures 92
4.8 References 103

CHAPTER 5 A UNIFIED APPROACH TO UNDERSTANDING MULTISCALE STRUCTURE, INTERFACIAL COHESION, ADSORBED LAYERS AND THERMODYNAMICS IN DENSE POLYMER-NANOPARTICLE MIXTURES 105
5.1 Introduction 105
5.2 Experiments 107
5.2.1 Sample Preparation 107
5.3 Small Angle Neutron Scattering 108
5.3.1 Scattering Length Density Calculations 109
5.3.2 Particle Form Factor 109
5.3.3 Determination of Partial Structure Factors: Methods and Example 110
5.3.4 Sphere and Core-shell Model Form Factors 112
5.4 PRISM Theory 113
5.5 Results and Discussion 114
5.6 Summary 122
5.7 Figures 123
5.8 References 132

CHAPTER 6 POLYMER DYNAMICS IN POLYMER NANOCOMPOSITES: EFFECTS OF POLYMER MOLECULAR WEIGHT, TEMPERATURE AND SOLVENT DILUTION 134
6.1 Introduction 134
6.2 Experiments 137
6.2.1 Sample Preparation 137
6.2.2 Low-Field NMR 138
6.2.3 Magic-Sandwich Echo Experiments 138
6.2.4 Multiple-Quantum (MQ) NMR 140
6.2.5 Small-Angle Neutron Scattering (SANS) 142
6.3 FID Measurement 142

6.3.1 Particle Concentration and Molecular Weight Effects 144
6.3.2 Effect of Temperature 146
6.3.3 Effect of Dilution 147
6.3.4 Hydroxyl Groups from Silica Surface 149
6.4 MQ Experiments 150
6.4.1 Particle Concentration and Molecular Weight Effect 151
6.4.2 Dilution Effect 155
6.5 Connections to the Particle Dispersions and Physical Properties 156
6.6 Summary 158
6.7 Table and Figures 160
6.8 References 170

CHAPTER 7 MOLECULAR WEIGHT EFFECTS ON PARTICLE AND POLYMER MICROSTRUCTURE IN CONCENTRATED POLYMER SOLUTIONS 172
7.1 Introduction 172
7.2 Experiment and Theory 174
7.2.1 Sample Preparation 174
7.2.2 Small Angle X-ray Scattering 174
7.2.3 PRISM theory 175
7.2.4 MSE-FID 175
7.2.5 Small Angle Neutron Scattering (SANS) 175
7.3 Results 178
7.3.1 Small Angle X-ray Scattering 178
7.3.2 PRISM 179
7.3.3 Polymer Mobility 185
7.3.4 Polymer-Polymer Density Fluctuations 188
7.4 Summary 190
7.5 Table and Figures 192
7.6 References 208

CHAPTER 8 A DEFINITE APPROACH TO UNDERSTAND THE EFFECTS OF SOLVENT QUALITY ON THE PARTICLE AND POLYMER STABILITY 209
8.1 Introduction 209
8.2 Experiments 211
8.2.1 Sample Preparation 211
8.2.2 MSE-FID 212
8.2.3 Small Angle Neutron Scattering 212
8.3 Results and Discussion 213
8.3.1 Polymer Dynamics 213
8.3.2 Local Structures and Compressibility of Particle and Polymer Interactions 215
8.4 Summary 221
8.5 Table and Figures 222
8.6 References 228

CHAPTER 9 CONCLUSION 229

CHAPTER 1 INTRODUCTION

1.1 Overview

Polymers are ubiquitous in applications to control aggregation and properties of colloidal suspensions. Particles are widely employed as additives to polymer solutions and melts to realize new properties. As a result, colloid-polymer mixtures are routinely employed in a variety of applications from personal care products to coatings and composites. Recently with the emergence of nanotechnology, their application has expanded to electronics, circuit fabrications, microelectromechnical devices and advanced polymeric composites.[1-4]

Both in concentrated colloids-particle mixtures and in nanocomposites, particle aggregation profoundly alters the system's mechanical, optical and electrical properties.[1,3-13] Increasingly it is clear that the interaction between nanoparticle surface and polymer segments is an important parameter to determine the state of particle dispersions and further to tune the physical property of the composites.[14-17] As an example, in recent years, great strides have been made is reducing rolling resistance in truck tires by fully dispersing carbon black in the rubber matrix. With 40% of the energy required to drive the truck forward being dissipated in rolling resistance at 88 km/hr, substantial improvements on the fuel consumption of the long haul trucking fleet are gained by these improvements to particle dispersion.[11] As another example, due to their high current carrying capacity, superconductivity, and high tensile and compressive strengths, carbon nanotubes are used as nanofibers to reinforce polymer matrices where good dispersions can enhance the optical and dielectric properties of the composites.[1,18,19] Despite

these advances in know-how, understanding factors controlling the degree of nanoparticle dispersion in concentrated polymer solutions and polymer melts has proven difficult.

Previously, many studies focused on phase behavior and the degree of particle aggregation when particles are suspended in dilute and semi-dilute polymer solutions, especially under non-adsorbing conditions where polymers mediate depletion attractions between the colloidal particles.[20-25] Less well explored are properties of particles suspended in concentrated polymer solutions and polymer nanocomposites. As a result understanding of mechanisms that control the state of particle aggregation in these complex mixtures remain elusive and poorly understood. In this thesis, the state of particle dispersions and polymer dynamics are experimentally studied in concentrated particle-polymer mixtures and polymer nanocomposites. We compare our results with the recently developed statistical mechanical theory of Schweizer and co-workers.[16,17,26] In Chapter 2 the effects of polymer-to-solvent ratios on changes of particle microstructures are analyzed and compared with microscopic Polymer Reference Interaction Site Model (PRISM) theory. PRISM theory is extensively employed to compare with the details of particle and polymer structures in Chapter 3, 4, 5 and 7 as well. In Chapter 3, changes in solvent quality with variation of solvent type and temperature are shown to alter the particle microstructures. This is understood as resulting in variations in the strength of segment-particle surface cohesion. Chapter 4 explores how variations in particle microstructure and flow properties are altered with slight changes in the backbone and end group chemistry of the polymer. This work demonstrates a dramatic link between the strength of polymer-particle cohesion and the intrinsic viscosity of the suspended particles. In Chapter 5, a complete set of collective structure factors for a ternary mix or polymer/particles and low molecular weight solvent are provided. This work demonstrates the existence of thin adsorbed polymer layers in

concentrated polymer particle mixtures. In Chapter 6, particle density fluctuations are linked to the polymer dynamics showing their close relationships in controlling the state of particle dispersion. Chapter 7 explores the effects of molecular weight on the state of particle/polymer dispersions and polymer dynamics. Evidence is provided that dispersion stability systematically decreases as polyethylene glycol molecular weight and temperature increase. This observation cannot be predicted by PRISM and we conclude that while enormously successful for low molecular weight polymer-colloid mixtures, physically unrealistic changes must be made to PRISM to capture the observed changes with polymer degree of polymerization. In Chapter 8 the effects of temperature changes on particle dispersion are linked to the local structure of polymer dispersions. Conclusions are drawn in Chapter 9.

1.2 References

1. Ajayan, P. M.; Schadler, L. S.; Braun, P. V. *Nanocomposite Science and Technology* Wiley-VCH: Weinheim, 2003.
2. Rahman, A.; Ali, I.; Al Zahrani, S. M.; Eleithy, R. H. *Nano* **2011**, *6*, 185.
3. Ebbesen, T. W.; Lezec, H. J.; Hiura, H.; Bennett, J. W.; Ghaemi, H. F.; Thio, T. *Nature* **1996**, *382*, 54.
4. Zhang, W.; Dehghani-Sanij, A. A.; Blackburn, R. S. *J. Mater. Sci.* **2007**, *42*, 3408.
5. Bansal, A.; Yang, H.; Li, C.; Cho, K.; Benicewicz, B. C.; Kumar, S. K.; Schadler, L. S. *Nat. Mater.* **2005**, *4*, 693.
6. Mackay, M. E.; Dao, T. T.; Tuteja, A.; Ho, D. L.; Van Horn, B.; Kim, H. C.; Hawker, C. J. *Nat. Mater.* **2003**, *2*, 762.
7. Oberdisse, J. *Soft Matter* **2006**, *2*, 29.
8. Oberdisse, J.; Hine, P.; Pyckhout-Hintzen, W. *Soft Matter* **2007**, *3*, 476.
9. Oh, H.; Green, P. F. *Nat. Mater.* **2009**, *8*, 139.
10. Rittigstein, P.; Priestley, R. D.; Broadbelt, L. J.; Torkelson, J. M. *Nat. Mater.* **2007**, *6*, 278.
11. Wang, M. J. *Rubber Chem. Technol.* **1998**, *71*, 520.
12. Giannelis, E. P. *Adv.Mater.* **1996**, *8*, 29.
13. Gangopadhyay, R.; De, A. *Chem. Mater.* **2000**, *12*, 608.
14. Ganesan, V.; Ellison, C. J.; Pryamitsyn, V. *Soft Matter* **2011**, *6*, 4010.
15. Hall, L. M.; Jayaraman, A.; Schweizer, K. S. *Curr. Opin. Solid St. M.* **2010**, *14*, 38.
16. Hall, L. M.; Schweizer, K. S. *J. Chem. Phys.* **2008**, *128*.
17. Hooper, J. B.; Schweizer, K. S. *Macromolecules* **2005**, *38*, 8858.
18. Ajayan, P. M.; Stephan, O.; Colliex, C.; Trauth, D. *Science* **1994**, *265*, 1212.
19. Moniruzzaman, M.; Winey, K. I. *Macromolecules* **2006**, *39*, 5194.
20. Poon, W. C. K. *J. Phys. Condens. Mat.* **2002**, *14*.
21. Russel, W. B.; Saville, D. A.; Schowalter, W. R. *Colloidal Dispersions*; Cambridge University Press: Cambridge, UK, 1989.
22. Tuinier, R.; Rieger, J.; De Kruif, C. G. *Adv. Colloid Interfac.* **2003**, *103*, 1.
23. Pusey, P. N.; Poon, W. C. K.; Ilett, S. M.; Bartlett, P. *J. Phys. Condens. Mat.* **1994**, *6*, A29.
24. Ramakrishnan, S.; Fuchs, M.; Schweizer, K. S.; Zukoski, C. F. *J. Chem. Phys.* **2002**, *116*, 2201.
25. Stiakakis, E.; Petekidis, G.; Vlassopoulos, D.; Likos, C. N.; Iatrou, H.; Hadjichristidis, N.; Roovers, J. *Europhys. Lett.* **2005**, *72*, 664.
26. Schweizer, K. S.; Curro, J. G. *Adv. Chem. Phys.* **1997**, *98*, 1.

CHAPTER 2 LONG WAVELENGTH CONCENTRATION FLUCTUATIONS AND CAGE SCALE ORDERING OF NANOPARTICLES IN CONCENTRATED POLYMER SOLUTIONS: EFFECT OF POLYMER TO SOLVENT RATIO[1]

2.1 Introduction

Polymer-colloid mixtures find application in a wide range of products, from coatings and structural composites, to car tires. These applications rely on different degrees of particle dispersion to deliver the desired chemical, mechanical and optical properties. A great deal is understood about suspension phase behavior and degree of particle aggregation when particles are suspended in dilute and semi-dilute polymer solutions, especially under non-adsorbing conditions where polymers mediate depletion attractions between the colloids.[1, 2] The depletion attraction increases in strength with polymer concentration and can induce the formation of discrete particle aggregates, a space-spanning gel, or liquid-liquid phase separation, depending on particle size and volume fraction, and polymer concentration and molecular weight.[1, 3-7] Less is understood for adsorbing polymers in suspension, which can drive bridging flocculation or steric stabilization corresponding to polymer-mediated attractive and repulsive forces, respectively[8] or in the case of block copolymers with different strengths of adsorption which can result in ordered and bicontinuous phases.[9] Even less is known about the microstructure and effective interactions of nanoparticles in concentrated polymer solutions or dense melts. Of great interest in the manufacture of polymer nanocomposites are methods to control the degree of dispersion under concentrated polymer solution conditions.[3, 4, 6, 7] Here we investigate nanoparticle structure and osmotic compressibility at polymer concentrations from semi-dilute

[1] Reproduced with permission from *Macromolecules* DOI 10.1021/ma1021677. Copyright © 2010 American Chemical Society

up to homopolymer melt densities with particular attention paid to the role of polymer segment-particle surface interactions in controlling how nanoparticles are spatially organized.

Recent theoretical and experimental advances in understanding melt polymer nanocomposites have established that the quantitative strength and spatial range of the polymer segment-particle surface interactions control the qualitative nature of nanoparticle dispersion[5, 10-14]. One key prediction is that the degree of aggregation is a nonmonotonic function of the strength of polymer segment-particle contact attraction strength, ε_{pc}. For very small ε_{pc} compared to thermal energy ("dewetting" interface), depletion attractions dominate and nanoparticles aggregate into large compact clusters at nearly all particle volume fractions. For large ε_{pc}, polymers form tight bridges between the nanoparticles resulting in phase separation or perhaps non-equilibrium polymer-particle network formation. But at intermediate ε_{pc}, adsorbed polymer layers form that remain discrete, nonoverlapping, and *thermodynamically stable*, resulting in a net repulsive interparticle potential-of-mean-force (PMF) between the nanoparticles and mixture stability[5, 10-14]. Scattering structure factor and second virial coefficient measurements for melts of silica nanoparticles in PEG and PTHF have confirmed the basic features of the theoretical predictions.[5, 15]

We investigate the effect of solvent (ethanol) dilution on the same 44nm silica plus PEG (400 MW) mixtures studied previously which is fully dispersed under melt conditions. If the polymer is diluted by ethanol, the nanoparticles strongly aggregate. Hence, this system shows a re-entrant type of behavior, unstable at lower polymer concentration, but stable at high polymer concentration, a phenomenon often called depletion restabilization that is observed in a variety of experimental systems.[3, 6, 16] Models for the origin of depletion restabilization remain tentative, and rely on changes in the range of the depletion attraction as polymer concentration increases

above their overlap concentration and polymer adsorption is claimed to induce *kinetic* barriers to aggregation[2, 4]. Here we extend the successful microscopic Polymer Reference Interaction Site Model (PRISM) theory of melt polymer nanocomposites[10-12] to account for solvent addition and address this question of depletion restabilization in the context of *equilibrium* statistical mechanics. We experimentally and theoretically find that as modest amounts of *good* solvent are added to the nanocomposite, polymer segments are driven away from the particle surface resulting in decreased stabilization.

In Section 2.2, the experimental methods used to prepare and characterize the polymer-particle solutions are described. Section 2.2 also presents and discusses experimental structure factors. Microstructural studies are carried out using ultra small angle x-ray scattering on suspensions where particle volume fraction is varied at constant volume ratio of polymer-to-ethanol. This protocol is adopted in order to mimic, to a first approximation, holding the polymer chemical potential constant as particle volume fraction is raised. Such an approach facilitates consideration of the particles as a pseudo-one component system[17] where the effective particle pair interaction potential is independent of particle volume fraction. In Section 2.3 we briefly discuss PRISM theory and its extension to the three-component system of present interest focusing mainly on the changes necessary to account for the presence of solvent. Section 2.4 compares theory and experiment for the collective nanoparticle structure factors. Conclusions are drawn in Section 2.5.

2.2 Experiments

2.2.1 Sample Preparation

Silica nanoparticles were synthesized based on the method of Stöber *et al.*[18] using the base-catalyzed hydrolysis and condensation of tetraethylorthosilicate (TEOS). The reaction

temperature was 55°C. 3610 ml of pure ethanol was mixed with 96ml of deionized water, and 156ml of ammonium hydroxide was then added as a catalyst. The reaction was allowed to run for 4 hours. After mixing, 156ml of TEOS was added. This procedure produces nanoparticles of diameter D = 44±4nm suspended in ethyl alcohol. Particle diameters were determined based on SEM performed on 100 particles yielding a diameter of 43±5nm; alternatively, fitting of the single particle form factor determined by the angle dependence of x-ray scattering from a dilute suspension of particles yielded a diameter of 43±1nm.

PEG 400 was purchased from Sigma-Aldrich, and ethyl alcohol was supplied from Decon Lab. Inc. As discussed previously[5], the effective diameter of a PEG monomer is $d \sim 0.6$ nm. The nanoparticle size was chosen to minimize the size asymmetry ratio, D/d, but have a large enough particle such that small angle x-ray scattering can be used to probe both long wavelength and cage scale collective concentration fluctuations.

After particle synthesis, the alcosol was concentrated approximately 10 times by heating in a ventilation hood. During this process, the excess of ammonium hydroxide was removed. For the preparation of polymer suspensions, the exact mass of each component (silica, PEG 400, ethanol) was determined in order to create the desired particle and polymer concentrations. In this process, the initial volume fraction of particles is required. Particle volume fractions were calculated using the masses of each component and their densities. The silica particle density is 1.6g/cm^3.[15] The defined mass of alcosol is then mixed with the defined mass of PEG 400. Samples were heated in a vacuum oven to drive off ethanol. The vacuum oven was purged several times with nitrogen followed by evacuation of the chamber to remove oxygen which degrades PEG at high temperature.[19] Once the ethanol was evaporated, the necessary amount of

ethanol was added to the sample and fully mixed on the vortex mixer to produce the desired concentrations of particles and PEG.

PEG 400 is a liquid at room temperature and is completely miscible with ethanol ($T_{m,PEO400} = 8\,°C$). In the absence of PEG, the alcosol appears transparent blue. As the silica and PEG have nearly identical refractive indices (n_{silica} =1.4555, n_{PEG}=1.4539), the polymer/particle mixture becomes increasingly transparent as polymer concentration is increased. In the absence of ethanol, the polymer nanocomposite melt is fully transparent and this index matching greatly reduces (nearly eliminates) van der Waals attractions between silica particles thereby rendering them model hard spheres.[15] In the absence of polymer, particle surface charge is implicated as a source of stability through large positive second virial coefficients that drop rapidly upon addition of soluble electrolyte. Increasing polymer concentration rapidly decreases the particle charge such that at the polymer concentrations studied here, there is no evidence of particle charge in particle second virial coefficients or particle microstructure at elevated volume fractions. [20]

Polymer concentration will be described in terms of the parameter R_{PEG}, defined as the ratio of the polymer volume to the polymer plus solvent volume. For $0.05<R_{PEG}<0.45$, we find the nanoparticles slowly aggregate. For $R_{PEG}<0.05$ or $R_{PEG}>0.45$, the suspensions are observed to be stable and well dispersed. Table 2.1 lists the experimental values of R_{PEG} explored in this study.[20]

2.2.2 Side-Bounce Ultra Small X-ray Scattering (SBUSAXS)

SBUSAXS experiments were conducted at the x-ray operations and Research beamline on the 32ID-B at the Advanced Photon Source (APS), Argonne National laboratory. The instrument employs a Bonse-Hart camera and Si(111) optics, which extends the q-range to

scattering vectors as small as 2×10^{-3} Å^{-1}. Additional side-reflection Si(111) stages enables effective pin-hole collimation which reduces slit smearing to a minimum. An absolute calibration converts the scattering intensity from counts per second to absolute units of cm^{-1} based knowledge of the sample thickness along the beam path. Samples were loaded in multi-position holders supplied by the beam line scientist. The sides of each cell chamber in the holders were sealed with two Kapton polyimide slides. All measurements were performed at room temperature. Measurements on each sample took about 30 minutes including loading and experiments. The background intensity, measured every fifth sample, was subtracted from the total scattering intensity. The background scattering intensity at each polymer concentration was negligible compared to the scattering by the particles (the background intensity from ethanol differs from 90wt% PEG solution only by a factor of 10^{-13} cm^{-1}, while the scattering intensity of the sample with silica particles is of order 10^{-3} cm^{-1})

The measured scattering, after subtraction of the scattering of the corresponding polymer solution in absence of the particles, was considered to arise only from the silica nanoparticles thereby enabling use of the effective one-component model.[15] The x-ray scattering intensity from a single component material can be written as

$$I(q,\phi_c) = \phi_c V_c \Delta\rho_e^2 P(q) S(q,\phi_c) + B \qquad (2.1)$$

where ϕ_c is the nanoparticle volume fraction, $\Delta\rho_e$ is the excess electron scattering length density of the particles relative to the PEG solution phase, V_c is the particle volume, $P(q)$ is the single particle form factor, $S(q,\phi_c)$ is the collective nanoparticle structure factor (normalized to unity at large q), and B is the background scattering amplitude. For spheres of diameter D, the form factor is:

$$P(q) = (3\frac{\sin(qD/2) - (qD/2)\cos(qD/2)}{(qD/2)^3})^2 \qquad (2.2)$$

Moderate nanoparticle polydispersity is taken into account using a Gaussian diameter distribution to calculate an average form factor given by

$$\overline{P}(q) = \frac{\int \frac{1}{\sqrt{2\pi\nu}} e^{(-D_c - \overline{D}_c)^2/2\nu^2)} D_c^{\,6} P(q) dD_c}{\int \frac{1}{\sqrt{2\pi\nu}} e^{(-D_c - \overline{D}_c)^2/2\nu^2)} D_c^{\,6} dD_c} \qquad (2.3)$$

Fitting the experimental form factor to the experimental data yields a standard deviation in size of $0.07\,\overline{D_c}$.

2.2.3 Experimental Structure Factor

Figure 2.1 shows the change in scattering intensity with increasing particle volume fraction at a fixed R_{PEG} ratio of 0.9. The intensity plots result from a convolution of scattering from single particles and correlations of particle centers-of-mass. We note that in the polymer concentration range studied, the solutions are clear and transparent indicating almost perfect index of refraction matching. Thus, we expect van der Waals attractions between the nanoparticles are effectively suppressed. As the nanoparticle volume fraction grows, the low q intensity generally decreases due to reduced osmotic compressibility of the particle subsystem, while a peak of increasing intensity emerges on the cage ($qD \sim 2\pi$) scale associated with local nanoparticle spatial order.

Collective nanoparticle structure factors were obtained by dividing the scattering intensity from the concentrated particle suspension by its dilute limit analog (ds) at the same polymer concentration.

$$S(q,\phi_c) = \frac{I(q,\phi_c)}{I_{ds}(q,\phi_c)} \frac{\phi_{c,ds}}{\phi_c} \tag{2.4}$$

In the dilute particle limit, $S(q)$=1. Structure factors are extracted under high polymer concentration conditions where the nanoparticles are stable (miscible homogenous phase). Particle volume fractions from 0.05 to 0.4 have been studied at a fixed R_{PEG} (see Table 2.1). For example, when R_{PEG}=0.6 with ϕ_c =0.10, 10% of the total sample volume is occupied by the silica particles and the remaining 90% is polymer and ethanol. Since the ratio of PEG to ethanol volumes is fixed at 3:2, the volume fraction of polymer in the mixture is 0.54, while the volume fraction of ethanol is 0.36. As ϕ_c is increased at R_{PEG}= 0.6, the polymer concentration based on total suspension mass decreases such that as ϕ_c changes from 0.1 to 0.4, and the polymer concentration drops from 61 to 41 wt%.

All experimental structure factors are liquid-like in the sense of showing a plateau value at low qD with a wide angle, amorphous fluid-like peak that grows in magnitude and moves to larger qD as volume fraction is raised. For the studied experimental conditions, the silica particles show no signs of aggregation as would be indicated by upturns in $S(q)$ as $q \rightarrow 0$.

The structure factors corresponding to the scattering intensities in Fig. 2.1 are shown in Fig. 2.2 based on $\phi_{c,ds}$ = 0.05. For this low solvent concentration sample, three monotonic trends with particle volume fraction emerge that are typical of all our data. (1) The low wave vector amplitude strongly decreases corresponding to the nanoparticle subsystem becoming less compressible. (2) The wide angle peak at $q=q^*$ shifts from $q^*D \sim 4$ to $q^*D \sim 6$ corresponding to

a shorter length scale of local cage order. This trend follows since $2\pi/q^{*}D$ is a measure of the mean distance between a central particle and its first nearest neighbor shell. (3) The cage peak intensity, $S(q^{*})$, initially increases very weakly, and then strongly grows for the more concentrated particle mixtures implying greater coherence of the cage scale packing. The behavior shown in Fig. 2.2 is typical of all R_{PEG} values studied. Our quantitative analysis, including comparison with theory, in Section 2.4 will focus on how these three features systematically evolve as a function of polymer-to-solvent ratio and particle volume fraction.

Figure 2.3 shows an example of how the nanoparticle collective structure factor changes with polymer-solvent ratio at a fixed, high particle volume fraction of 0.3. As solvent replaces polymer (decreasing R_{PEG}) in the concentrated solution regime, the inverse dimensionless osmotic compressibility, $1/S(0)$, decreases significantly, the peak position shifts slightly to higher wave vectors, and the peak intensity strongly decreases. Physically, these three trends are largely a consequence of solvent reducing the degree of nanoparticle ordering, on both local and global length scales, or equivalently that the nanoparticles experience stronger effective repulsions as R_{PEG} increases. Although the particle volume fraction is fixed, the consequences of solvent dilution on the intensity at $q\sim0$, and on the cage scale, "look like" how the structure of a one-component particle fluid changes if its volume fraction is reduced. However, such a picture would imply the location of the cage peak would decrease with solvent dilution. This is not the case experimentally, which is one indication of the more complex structural rearrangements that occur in a ternary mixture, and is qualitatively consistent with the theoretically-motivated idea that as more good solvent is added the amount of adsorbed polymer, and the corresponding effective steric layer thickness, decreases.

2.3 Theory and Model

2.3.1 Background

PRISM theory has been extensively applied to dense polymer nanocomposites.[10-14] Recently it was extended to account for the expected increase in total system packing fraction with the addition of hard nanoparticles to a polymer melt composed of small monomers which can approximately fill the interstitial space between nanoparticles at the pure polymer melt density.[5] Here we further extend this model to the case of variable bulk polymer packing fraction when the suspending medium is a polymer solution. The solvent will be treated implicitly by reducing the polymer packing fraction and adjusting the polymer adsorption strength, roughly in the spirit of an effective mean field chi-parameter and effective (but compressible) 2-component mixture model.[21]

PRISM theory[22] as implemented here consists of 3 coupled nonlinear integral equations[5, 11-14] for the site-site intermolecular pair correlation functions, $g_{ij}(r)$, where i and j refer to polymer monomer (p) or nanoparticle (c).[10-14] The nanoparticles are hard spheres of diameter D, and the polymer is a freely jointed chain (FJC) composed of N identical spherical interaction sites. The single chain structure factor in Fourier space is: [22]

$$\omega_p(k) = [1 - f^2 - 2N^{-1}f + 2N^{-1}f^{N+1}]/(1-f)^2 \qquad (2.5)$$

where $f=\sin(kl)/(kl)$, and the persistence length $l=4/3\ d$ (typical of flexible polymers).[3, 17] The generalized Ornstein-Zernike, or Chandler-Andersen[22], matrix integral equations relate g=1+h to C in Fourier space as[22]

$$\mathbf{H}(k) = \mathbf{\Omega}(k)\mathbf{C}(k)[\mathbf{\Omega}(k) + \mathbf{H}(k)] \qquad (2.6)$$

where the diagonal matrix $\mathbf{\Omega}(k)$ contains the elements $\rho_i\omega_i(k)\delta_{ij}$, $\mathbf{C}(k)$ consists of the elements $C_{ij}(k)$, and $\mathbf{H}(k)$ is composed of the elements $\rho_i\rho_j h_{ij}(k)$, where $h_{ij}(r) = g_{ij}(r)-1$. The number densities are $\rho_p = \phi_p/(d^3\pi/6)$ and $\rho_c = \phi_c/(D^3\pi/6)$, where ϕ_p and ϕ_c are the polymer and particle packing fractions, respectively, as discussed in more detail below.

The site-site Percus-Yevick closure approximation is used for polymer-polymer (p-p) and polymer-nanoparticle (p-c) correlation functions, while the hypernetted chain (HNC) closure is used for the nanoparticle-nanoparticle correlation function[11]:

$$C_{ij}(r) = \left(e^{-U_{ij}(r)} - 1\right)\left(1 + h_{ij}(r) - C_{ij}(r)\right) \tag{2.7}$$

$$C_{cc}(r) = -U_{cc}(r) + h_{cc}(r) - \ln g_{cc}(r) \tag{2.8}$$

This specific model and version of PRISM theory has been previously developed, and compared with experiment, only for dense melt polymer-particle mixtures. Possible swelling of polymer chains in a good solvent is not taken into account. However, in our present applications, the polymers are short and hence intrachain excluded volume effects are expected to be very weak.[24] Moreover, we focus on the concentrated polymer solution regime which further minimizes conformational nonideality effects.

In Eqs. (2.7) and (2.8), U_{ij} are the pair decomposable site-site potentials, where U_{cc} and U_{pp} are taken to be purely hard core. The chemical nature of the mixture enters solely via the two parameters of an attractive monomer-particle interfacial attraction: the strength at contact ε_{pc} (in units of thermal energy) and spatial range α (in units of the monomer diameter). Beyond the hard core distance of closest approach, the exponential interfacial potential is given by:

$$U_{pc}(r) = -\varepsilon_{pc} \exp\left(\frac{-(r-(D+d)/2)}{\alpha d}\right) \tag{2.9}$$

Henceforth, all lengths (energies) are expressed in units of the monomer diameter (thermal energy). The key parameter ε_{pc} describes the effective energetics of transferring a polymer segment from a particle-free solution to being adsorbed on the nanoparticle surface. As such, it implicitly depends on the material-specific cohesive interactions among the polymer, solvent, and nanoparticle. In all calculations reported below, the degree of polymerization is taken to be N=100, the size asymmetry ratio D/d=10, and the spatial range of attraction is α=0.5. These are typical values as motivated in prior work, [5, 11-14] and have been shown to result in PRISM theory predictions for nanoparticle structure factors in good agreement with experiment for the silica-PEG melt mixture.[5]

An inexact Newton's method is employed to numerically solve the coupled nonlinear PRISM integral equations, which yield the real space pair correlation functions, $g_{ij}(r)$. The polymer and nanoparticle collective partial structure factors then follow as

$$\mathbf{S}'(k)= \mathbf{\Omega}(k)+\mathbf{H}(k) =(\mathbf{I}- \mathbf{\Omega}(k)\mathbf{C}(k))^{-1}\mathbf{\Omega}(k) \qquad (2.10)$$

where $\mathbf{I}$ is the identity matrix and $\mathbf{S}'$ is the dimensionalized version of $\mathbf{S}$, $S'_{ii}= \rho_i S_{ii}$.

As nanoparticles are added to the mixture, the total packing fraction is increased such that the theoretical polymer packing fraction outside the volume excluded by nanoparticles remains constant[25] at ϕ_{p0}:

$$\phi_t = \phi_c + \phi_{p0}\left(1-\phi_c\left(1+\left(d/D\right)\right)^3\right) \qquad (2.11)$$

In Eq. (2.11), the suspension is considered of fixed total volume. When a fixed volume of particles is added, a volume of polymer solution at concentration ϕ_{p0} must be removed. The term in brackets in Eq. (2.11) accounts for the reduction in number of polymer segment number when that volume is removed. Calculations based on it for polymer-particle melts have been shown to

agree well with experimental scattering profiles over a wide range of particle packing fractions, and under both weak and intermediate strength interfacial cohesion conditions.[5]

To summarize, the above set of equations can be numerically solved to determine the microstructure of a nanoparticle-polymer mixture as described in detail in Ref. 5. Originally developed for particles in a polymer melt, we have here extended the theoretical approach to account for variable polymer density due to solvent. Of particular interest in the present work is the effect of reducing ϕ_{p0}.

2.3.2 Effect of Solvent Dilution

Previously we have investigated the effects of varying ε_{pc} through changes in polymer chemistry at ϕ_{p0} fixed at the melt polymer density.[5] For example, polytetrahydrofuran (PTHF) which is known to weakly adsorb on silica was shown to have a lower interfacial strength (ε_{pc} = 0.35) than PEG (ε_{pc} = 0.55). In this work we explore the effects of changing ϕ_{p0} on mixture microstructure and particle stability. One of our key findings is that adding solvent may allow a simple means to adjust the effective ε_{pc}, and thus provide a new method to process nanocomposites and cast films In principle, dilute polymers in a good solvent will adsorb less strongly (or not at all) to nanoparticle surfaces compared with those in the dense melt since there is an additional free energy penalty for a segment to leave the good solvent environment and contact the particle surface. The solvent used here, ethanol, is chemically similar to the polymer monomers, as each are composed of two saturated carbons and an oxygen. Ignoring the chemical differences between the hydroxyl group of ethanol and the ether group of PEG as a first approximation, the major difference between the monomer and solvent is size. A segment of the FJC model is a sphere of diameter d which represents several (~3) PEG monomers,[5] each

approximately the size of ethanol. Due to its smaller size, and for simplicity, ethanol is represented only implicitly (continuum solvent model). Therefore, the polymer packing fraction is lowered as solvent is added. Specifically, the initial polymer concentration, ϕ_{p0}, that enters Eq. (2.11) is calculated from the volume fraction of polymer in the polymer/solvent mixture, R_{PEG}, which remains constant as particles are added, and the polymer melt packing fraction $\phi_{p0,m}$, as:

$$\phi_{p0} = R_{PEG}\phi_{p0,m} \tag{2.12}$$

In the experiment, mixtures are created with fixed R_{PEG} and fixed ϕ_{p0}, but increasing ϕ_c as shown in Table 2.1. The theoretical melt packing fraction $\phi_{p0,m} = 0.40$ as used in previous studies[5] which yields a realistic dimensionless isothermal compressibility of a pure polymer melt of $S_{pp}(q=0) \sim 0.2$.

The key material parameter is the polymer segment-nanoparticle attractive contact strength, ε_{pc}, the absolute value of which controls the aggregation state[5, 10-14]. For intermediate ε_{pc} values, thermodynamically stable "bound polymer layers" form around nanoparticles, resulting in a miscibility window in the phase diagram such that in melts the nanoparticles are stable and fully dispersed at all particle volume fractions. Because the monomers are represented as hard spheres and the solvent is implicit, the interfacial attraction strength ε_{pc} actually represents the overall enthalpic gain of transferring a monomer from the continuous suspending phase to the particle surface. Ref.5 found $\varepsilon_{pc}=0.55$ for the PEG melt and silica based on quantitative comparisons of theory and experiment for the nanoparticle collective structure factor. If the adsorbed monomer originates from a polymer-solvent mixture, the relevant enthalpic considerations upon its placement near the particle surface are: loss of polymer-solvent interactions (strength ε_{ps}), loss of nanoparticle-solvent interactions (strength ε_{cs}), and gain of

solvent-solvent interactions (strength ε_{ss}). The former two occur with frequency proportional to the fraction of solvent ($1-R_{PEG}$), while the latter is proportional to $(1-R_{PEG})^2$. Hence, we propose a simple mean-field-like estimate of the effective interfacial attraction strength as:

$$\varepsilon_{pc,effective} = \varepsilon_{pc,melt} - (1-R_{PEG})\varepsilon_{ps} - (1-R_{PEG})\varepsilon_{cs} + (1-R_{PEG})^2 \varepsilon_{ss} \qquad (2.13)$$

Eq. (2.13) is reminiscent of the dilution approximation for the chi-parameter of a ternary solvent plus a AB polymer blend[21] , allowing for the possibility of solvent selectivity.

For our system, the solvent is chemically similar to the monomer. Hence, interactions with itself and with the monomer are modeled per an athermal good solvent (ε_{ps}=ε_{ss}=0), and interaction with the nanoparticle is the same as that of the monomer ($\varepsilon_{cs} = \varepsilon_{pc,melt}$). Under these specific conditions, Eq. (2.13) becomes :

$$\varepsilon_{pc,effective} = R_{PEG}\varepsilon_{pc,melt} = 0.55R_{PEG} \qquad (2.14)$$

This simple zeroth order model has no adjustable parameters. The polymer-nanoparticle effective interfacial attraction strength decreases linearly to zero with polymer: solvent ratio (R_{PEG}). The physical picture is that the addition of good solvent reduces the tendency for polymer adsorption, which ultimately results in such a small effective ε_{pc} that depletion attraction and/or unshielding of the van der Waals attraction due to dielectric constant changes results in nanoparticle aggregation. The calculated ε_{pc} for each polymer-to-solvent ratio are given in Table 2.1.

As further motivation for the applicability of this model to our experimental system, we note that it is known there is a favorable adsorption energy for ethanol on silica surfaces.[26-28] Experiment indicates that PEG400 adsorbs to the silica surfaces out of ethanol with an affinity that is an order of magnitude smaller than adsorption out of water.[20] This implies that the polymer-particle attraction strength in dilute solution is much smaller than in the melt. By

assuming a simple linear relationship between $\varepsilon_{pc,effective}$ and solvent concentration, and that the $\varepsilon_{pc,effective}$ is negligible in the dilute limit, we again obtain Eq.(2.14).

2.3.3 Sample Theoretical Results

In the theoretical model, solvent dilution is accounted for by reducing both the polymer volume fraction and changing the effective interfacial adsorption strength using Eqs. (2.12) and (2.14). To investigate the relative and absolute importance of these two effects of solvent dilution, we first implement them separately.

Previously we showed that in a polymer melt, stable (dispersed) nanoparticle microstructures were well captured by the theory. Specifically, the three distinguishing features of the predicted and measured collective nanoparticle structure factors were quantitatively compared: the height, $S(q^*)$ and location, q^*, of the wide angle cage peak, and the nanoparticle osmotic compressibility $S(0)$. With decreasing ε_{pc}, $S(0)$ increases, and the particle cage scale peak decreases in intensity and shifts to higher wavevector.[5] As a result, measuring $S(q)$ over a range of wave vectors and particle volume fractions provided a set of internally consistent checks for the determination of the crucial material parameter ε_{pc}. This comparison showed that all three measures of the microstructure are well described by an ε_{pc} that is independent of particle volume fraction. In addition, ε_{pc} was found to vary with polymer chemistry.[5] For example, at fixed particle volume fraction, ε_{pc} decreases when the silica nanoparticle is transferred from the more strongly adsorbing PEG melt to the more hydrophobic polytetrahydrofuran (PTHF) melt. As ε_{pc} decreases, the PTHF system is predicted to move closer to depletion phase separation. Indeed while PEG nanocomposite melts were stable at all volume fractions, above a critical

volume fraction the PTHF nanocomposite melts are observed to exhibit strong aggregation and ultimately gelation.

In the present work we extend these studies to explore the effects of decreasing polymer concentration via solvent dilution. Theoretically we do this in two steps. First we assume ε_{pc} is independent of ϕ_{p0}. Second, we explore changes in microstructure when ε_{pc} is varied with ϕ_{p0} as in Eq. (2.14).

Figure 2.4 shows representative theoretical calculations of the inverse of the nanoparticle osmotic compressibility as a function of nanoparticle volume fraction as R_{PEG} is decreased from 0.9 to 0.5 for : (a) a fixed ε_{pc}=0.55, and (b) a diluted ε_{pc} given in Eq.(2.14). At constant $\varepsilon_{pc} = 0.55$, decreasing R_{PEG} only slightly increases *S(0)*. However, if both R_{PEG} and ε_{pc} decrease then *S(0)* increases far more, although the increase is still less than that due to lowering ε_{pc} at constant R_{PEG}=1 (not shown, but reported in Ref. 5). Reduction of the local polymer density close to nanoparticles drives depletion attraction, so it is physically reasonable that decreasing the amount of polymer has little effect in the miscible regime but a much greater effect at low ε_{pc}, and serves to push the system further from strong depletion behavior resulting in an upturn of *S(0)* at low wave vectors. The experimental trends for S(0) in Fig. 2.3 suggest the particles experience enhanced repulsion as R_{PEG} increases, qualitatively as predicted in Fig. 2.4b if ε_{pc} increases with R_{PEG}.

2.4 Comparison of Experiment and Theory

We now analyze experimentally and theoretically the three characteristic features of *S(q)* discussed in Section 2.3 over a wide range of R_{PEG} and ϕ_c. The volume fraction dependencies of

1/S(0), $S(q^*D)$ and q^*D are shown in Fig. 2.5, 2.6, and 2.7, respectively, for R_{PEG}=0.5, 0.6, 0.7, 0.8, 0.9. The results confirm the observations in Fig. 2.3 namely that, for all volume fractions, as the polymer concentration is increased at *fixed* ϕ_c three observations are made: (i) long wavelength density fluctuations are suppressed (*S(0)* decreases), (ii) coherency of the cage scale order increases ($S(q^*)$ increases), and (iii) the position of the cage peak is a weak function of R_{PEG}, with no obvious trend.

At fixed R_{PEG}, Fig. 2.5 and 2.6 show that the growth of *1/S(0)* and *S(q*)*, respectively, with volume fraction becomes weaker as the amount of solvent present grows, with subtle exceptions at lower R_{PEG} values. Also shown in Fig. 2.5 and 2.6 are predictions assuming the particles are hard spheres in a vacuum at the same packing fractions as the nanoparticles in the polymer solution. Comparing the reference hard sphere and experimental results, one sees that while the presence of polymer increases *1/S(0)* for all R_{PEG} at low volume fractions suggesting enhanced repulsions due to the presence of polymer, at high volume fractions and at low R_{PEG} values the experimental values fall below the analogous hard sphere behavior indicating enhanced long wavelength concentration fluctuations over those of the analogous hard sphere fluid. Nanoparticle cage coherency, as quantified by the magnitude of $S(q^*)$, shows similar trends: at large values of R_{PEG} the particle cages are better defined (more order) that expected from the analogous hard sphere fluid, while at low R_{PEG} the cages are less well defined than expected for hard spheres suggesting diminished repulsions relative to the hard sphere reference. Hence, to summarize, at high R_{PEG} the strongly adsorbed polymer layer results in a significantly lower nanoparticle compressibility and increased cage scale ordering compared to the hard sphere fluid analog, but at lower R_{PEG} polymer adsorption is reduced resulting in depletion attraction and hence (at R_{PEG}=0.5) both *1/S(0)* and *S(q*)* fall below that of the reference hard

sphere fluid. These differences in behavior of the hard sphere fluid reference system and nanocomposite clearly demonstrate the important role of polymer and solvent on the nanoparticle scattering features. Figure 2.7 reinforces this conclusion since in all cases the experimental q^* data fall below the reference hard sphere fluid curve indicating that the silica nanoparticles order on a larger length scale than bare hard spheres in a vacuum at the same volume fraction, consistent with steric repulsion between adsorbed polymers on the particle surfaces.

A detailed comparison of the experimental data with theory is also shown in Fig. 2.5-2.7 based on the linear variation of ε_{pc} with R_{PEG} model of Eq. (2.14). Recall there are no adjustable parameters in the theoretical calculations. Overall, the measured and theoretically predicted trends agree qualitatively, if not quantitatively. Figure 2.5 shows PRISM theory predicts that with increasing solvent dilution $S(0)$ increases by an amount that is in good agreement with experiment for all values of ϕ_c studied. Recall that the analogous constant ε_{pc} model PRISM results in Fig. 2.4a are very different and disagree with experiment. This strongly suggests that the decrease in effective ε_{pc} (as opposed to entropic depletion effects of dilution) is the main driver of the nanoparticle structural changes upon solvent addition.

The theory also compares well to experimental results for cage peak height $S(q^*)$, as seen in Fig. 2.6. At low ϕ_c the peak height is small, and the experimental trend versus R_{PEG} is unclear, while the theory predicts a slight decrease in peak height with solvent addition. At intermediate and high nanoparticle volume fractions, both experiment and theory show decreasing local order as R_{PEG} decreases from 0.9 to 0.6. At the lowest R_{PEG} = 0.5, this trend reverses experimentally with a slightly higher $S(q^*)$ than observed for R_{PEG} = 0.6. Interestingly, at high ϕ_c the analogous PRISM theory results also shows this small increase in $S(q^*)$. Again, the agreement of parameter

free comparisons of PRISM and the experimental data is qualitatively excellent and nearly quantitatively accurate over a wide range of R_{PEG} and particle volume fraction.

Figure 2.7 compares theoretical and experimental values of the dimensionless wave vector of the primary cage peak. As seen in the experimental data, the theoretical results for R_{PEG} >0.6 also show q^* is smaller than that of the reference hard sphere fluid. Moreover, q^* varies approximately linearly with ϕ_c, as observed experimentally. At the lowest polymer concentrations, as ϕ_c increases the theoretical q^* increases above that of pure hard spheres. This is perhaps due to the decreasing amount of adsorbed polymer as ε_{pc} becomes small, and the resulting tendency of particles to aggregate. For the experimental data, q^* remains nearly constant regardless of R_{PEG}, and is smaller than the theoretical result suggesting that the extent of adsorbed layer polymer-mediated repulsions are a bit larger than captured in the model. Note all values of q^* in the presence of ethanol are larger than observed in melts at all measured volume fractions (as reported in Fig. 2.5 of Ref. 5), again indicating the greater polymer-mediated repulsive interactions at higher polymer concentrations, an effect that is captured by the theory.

Figure 2.7 compares theoretical and experimental values of the dimensionless wave vector of the primary cage peak. As seen in the experimental data, the theoretical results for R_{PEG} >0.6 also show q^* is smaller than that of the reference hard sphere fluid. Moreover, q^* varies approximately linearly with ϕ_c, as observed experimentally. At the lowest polymer concentrations, as ϕ_c increases the theoretical q^* increases above that of pure hard spheres. This is perhaps due to the decreasing amount of adsorbed polymer as ε_{pc} becomes small, and the resulting tendency of particles to aggregate. For the experimental data, q^* remains nearly constant regardless of R_{PEG}, and is smaller than the theoretical result suggesting that the extent of adsorbed layer polymer-mediated repulsions are a bit larger than captured in the model. Note all

values of q^* in the presence of ethanol are larger than observed in melts at all measured volume fractions (as reported in Fig. 2.5 of Ref.5), again indicating the greater polymer-mediated repulsive interactions at higher polymer concentrations, an effect that is captured by the theory.

Collectively, the results in Fig. 2.5-2.7 demonstrate that the no adjustable parameter predictions of PRISM theory for the structural consequences of solvent dilution are quite accurate, essentially as good as found previously for the melt nanocomposite.[5] Moreover, the combined experimental and theoretical results demonstrate that with increasing polymer concentration the nanoparticles are stabilized via the formation of adsorbed polymer layers. This physical picture is at odds with the naïve application of depletion potential concepts where increased polymer solution concentration will produce increased strengths of attraction between the particles.[1, 30-32] Hence, we suggest a new mechanism for polymer-induced restabilization based on the formation of thermodynamically stable and discrete adsorbed polymer layers when the effective monomer-particle attraction strength is modest (of order kT). At a more detailed level, PRISM theory suggests the increased stability arises from two factors. First, the van der Waals attraction between nanoparticles are essentially eliminated due to index matching at polymer concentrations greater than R_{PEG}=0.5. [20] As a result, in the pseudo 2-component mixture of particles and polymer, the direct particle interactions are primarily volume exclusion. Second, with increased polymer concentration there is an increased effective enthalpic attraction between the polymer and nanoparticle which drives more segmental adsorption thereby creating larger repulsive steric interactions and increased particle stability.

The experiments described here have been designed to approximately hold the polymer chemical potential constant as particle concentration is increased. Such an approximate pseudo-one-component model is often invoked to treat a suspension as composed of particles interacting

with a volume fraction independent PMF[17]. In applying the effective 2-component PRISM theory, we relax this view by explicitly accounting for the polymeric species. Our results suggest that at fixed polymer chemical potential ε_{pc} is independent of particle volume fraction, thereby restoring its microscopic nature.

2.5 Summary

In a recent combined experiment-theory study Anderson and three of us performed a quantitative analysis of the effects of changing polymer chemistry and adsorption strength on the collective nanoparticle structure factor under dense melt conditions[6]. It was shown that PRISM theory accurately describes the microstructural features based solely on the chemically-specific value of the interfacial attraction strength ε_{pc}. In the present study we have explored the effect of adding a good solvent, ethanol, to the PEG-silica mixture, as a function of nanoparticle volume fraction and the polymer-to-solvent volume ratio in the concentrated polymer solution regime. The experimental scattering results compare well with the no adjustable parameter PRISM theory calculations based on the simple idea that solvent dilution simultaneously modifies the polymer packing fraction and effective interfacial attraction strength. More broadly, our results demonstrate that measurement of nanoparticle concentration fluctuations in dense polymer solutions and melts, in conjunction with microscopic theory, can be used as an in situ tool for extracting the strength of particle-polymer segment attraction.

The key new finding discussed in this paper is the strong nanoparticle microstructural changes that occur upon variation of monomer-nanoparticle attraction strength, ε_{pc}, via solvent dilution of the melt mixture. We emphasize the discovered structural changes are not universal since ε_{pc} depends on the chemistry of the polymer and particle as well as the solvent-solvent and

solvent-nanoparticle interactions. However, our results do suggest a practical method for manipulating ε_{pc}. As a result, one can imagine processing conditions where nanoparticles are stabilized during processing by driving polymer to the particle surface through the addition of an anti-solvent which is later removed resulting in nanoparticles trapped in a dispersed state. Poor solvent conditions may also be interesting in creating conditions where ε_{pc} increases to a point of triggering the formation of polymer-nanoparticle bridging complexes as predicted theoretically[10-12]. Finally, the generalization of the PRISM approach to explicitly treat solvent molecules is a worthy future goal.

2.6 Table and Figures

PEG to ethanol vol. ratio (PEG:EtOH)	R_{PEG}	ϕ_{p0}	ε_{pc}(kT)	Particle volume fractions (ϕ_c) (Polymer concentration in a unit of weight % of total mixture)						
0.5 : 0.5	0.5	0.20	0.275	0.05 (54wt%)	0.10 (51wt%)		0.20 (45wt%)	0.30 (40wt%)	0.35 (37wt%)	
0.6 : 0.4	0.6	0.24	0.33		0.10[a] (61wt%)	0.15 (58wt%)	0.20 (54wt)	0.30 (48wt%)		0.40 (41wt%)
0.7 : 0.3	0.7	0.28	0.385	0.05 (75wt%)	0.10 (71wt%)	0.15 (67wt%)	0.20 (63wt%)	0.30 (55wt%)	0.35 (51wt%)	
0.8 : 0.2	0.8	0.32	0.44		0.10 (81wt%)	0.15 (76wt%)	0.20 (71wt%)	0.30 (63wt%)		
0.9 : 0.1	0.9	0.36	0.495	0.05 (96wt%)	0.10 (91wt%)	0.15 (86wt%)	0.20 (81wt%)	0.30 (71wt%)		

Table 2.1 Polymer-to-ethanol volume ratios and nanoparticle volume fractions studied in this work. The quantity ϕ_{p0} denotes the packing fraction of polymer in the region of space not occupied by nanoparticles; to a first approximation it is the polymer concentration that would exist in a reservoir in equilibrium with the suspension across a membrane that will pass solvent and polymer but not particles.

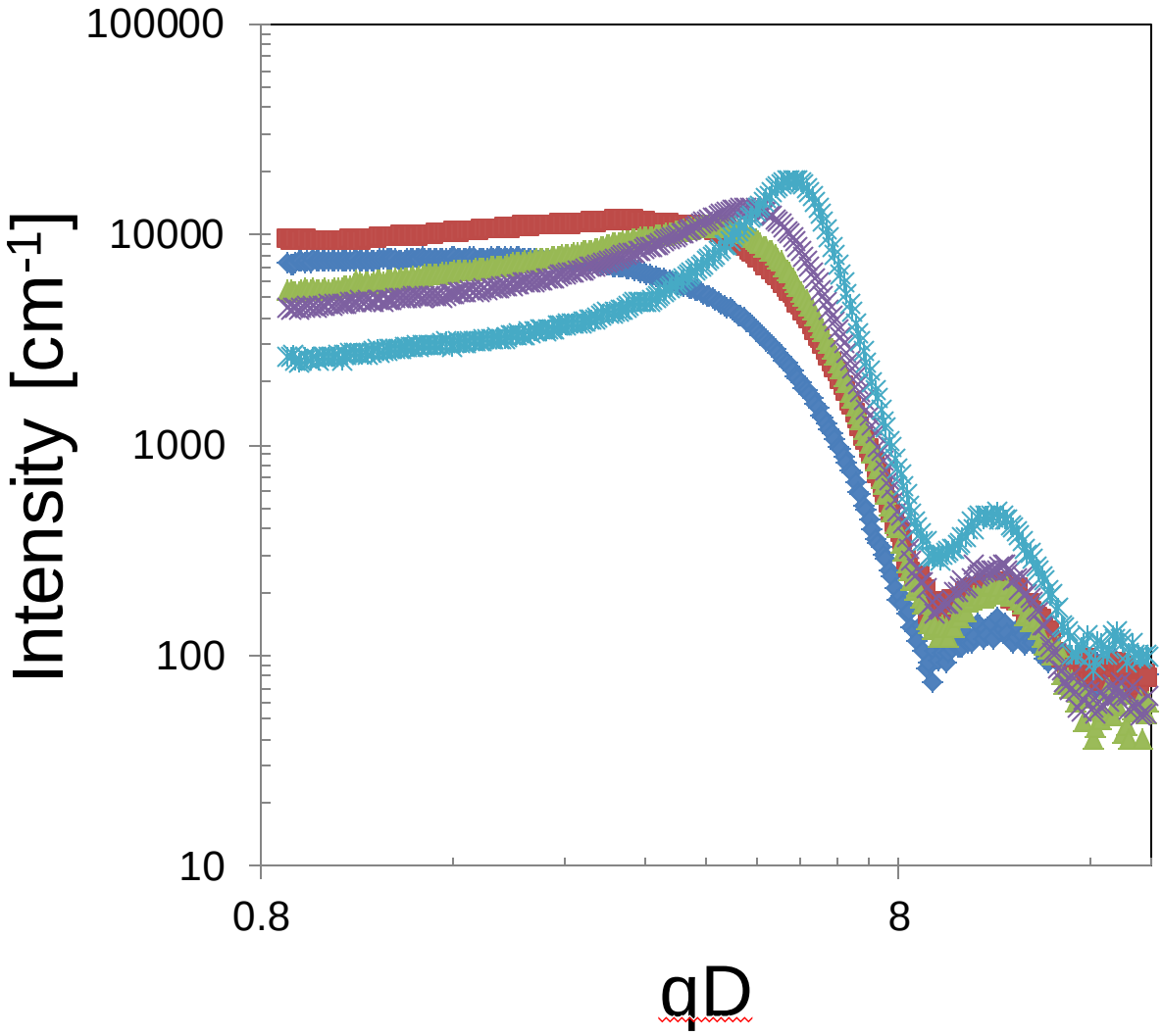

Figure 2.1 Experimental scattered intensity versus dimensionless wave vector at fixed polymer: ethanol volume ratio R_{PEG}=0.9 and ϕ_c = 0.05(◆), 0.10(■), 0.15(▲), 0.20 (×) and 0.30(✳).

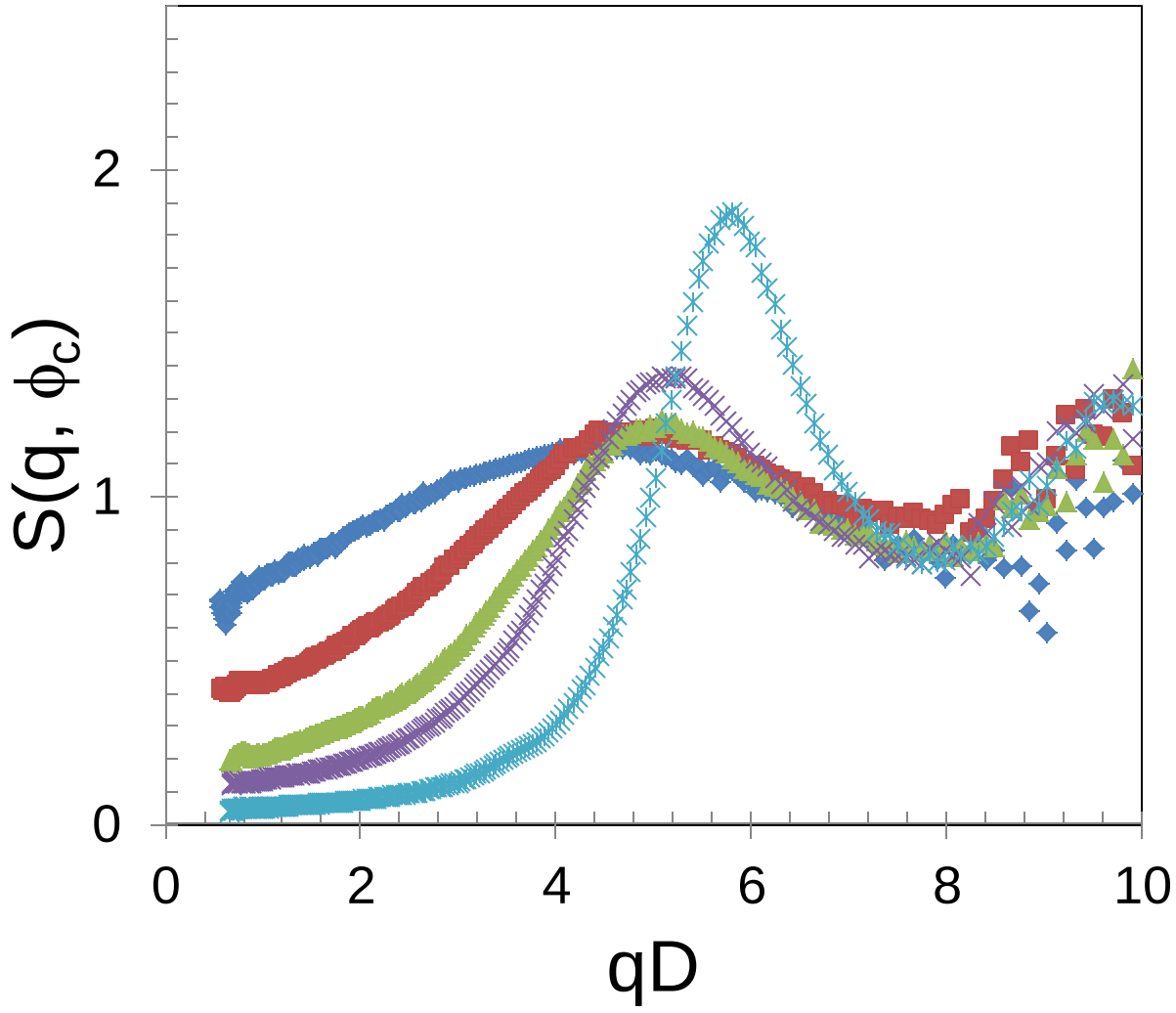

Figure 2.2 Experimental particle structure factor versus wave vector at R_{PEG}=0.9 and ϕ_c of 0.05(◆), 0.10(■), 0.15(▲), 0.20 (×) and 0.30(✳).

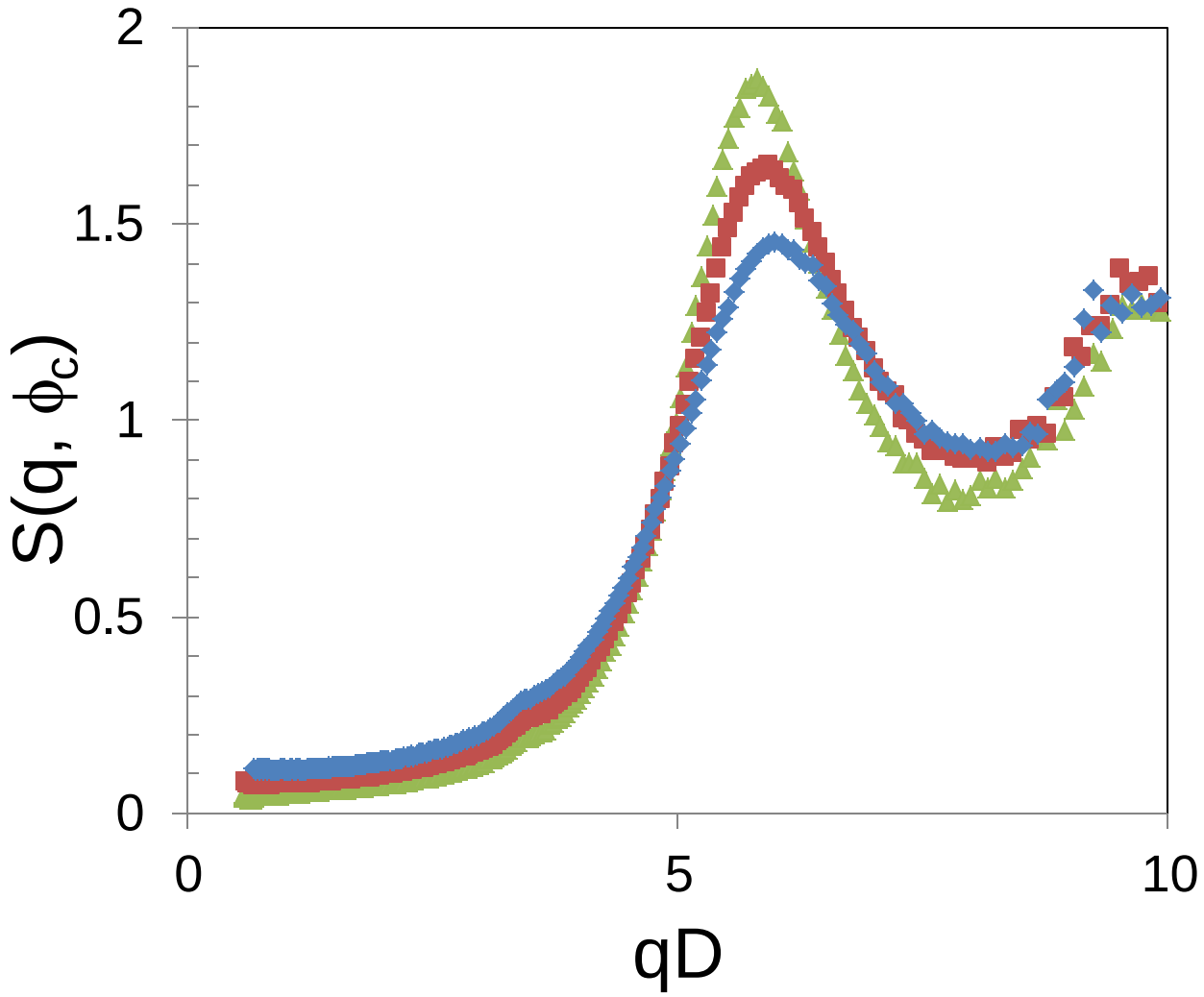

Figure 2.3 Experimental particle structure factors versus wave vector at a particle volume fraction of 0.30 and varying polymer: ethanol volume ratio R_{PEG} = 0.9(▲), 0.7(■), and 0.5(◆).

(a)

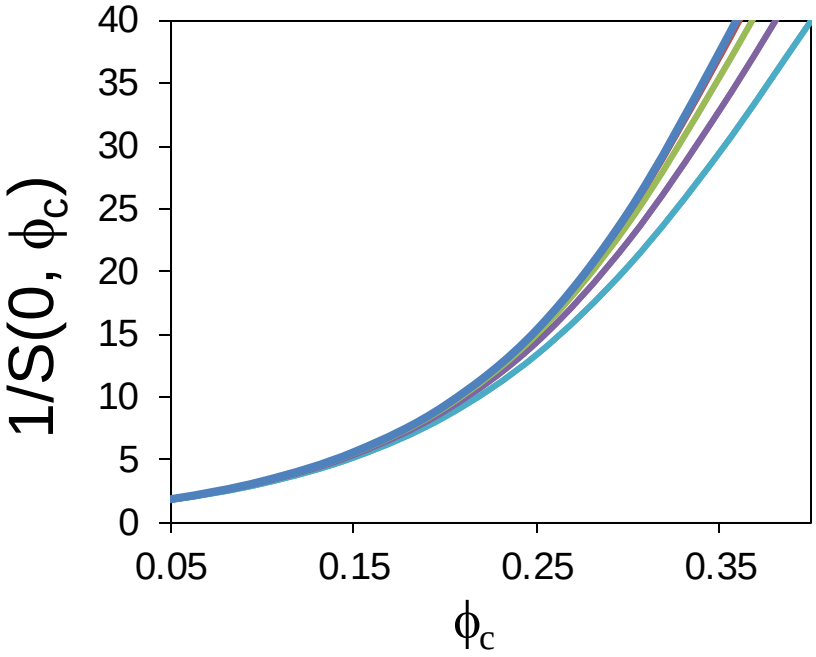

(b)

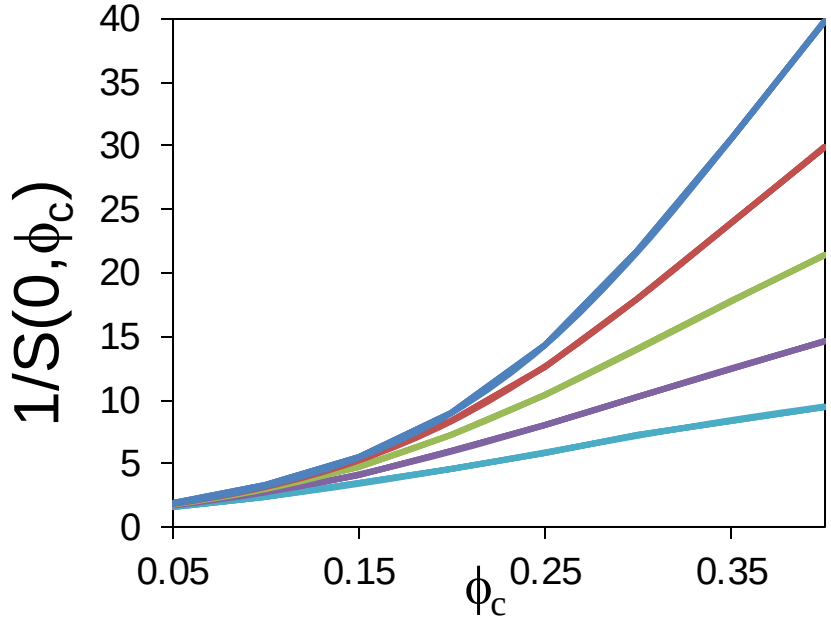

Figure 2.4 PRISM predictions for the inverse osmotic compressibility as a function of particle volume fraction (ϕ_c) with varying R_{PEG} at (a) fixed ε_{pc}=0.55 and (b) adjusted ε_{pc} as shown in Table 2.1. For both (a) and (b), R_{PEG} are 0.9, 0.8, 0.7, 0.6 and 0.5 from top to bottom.

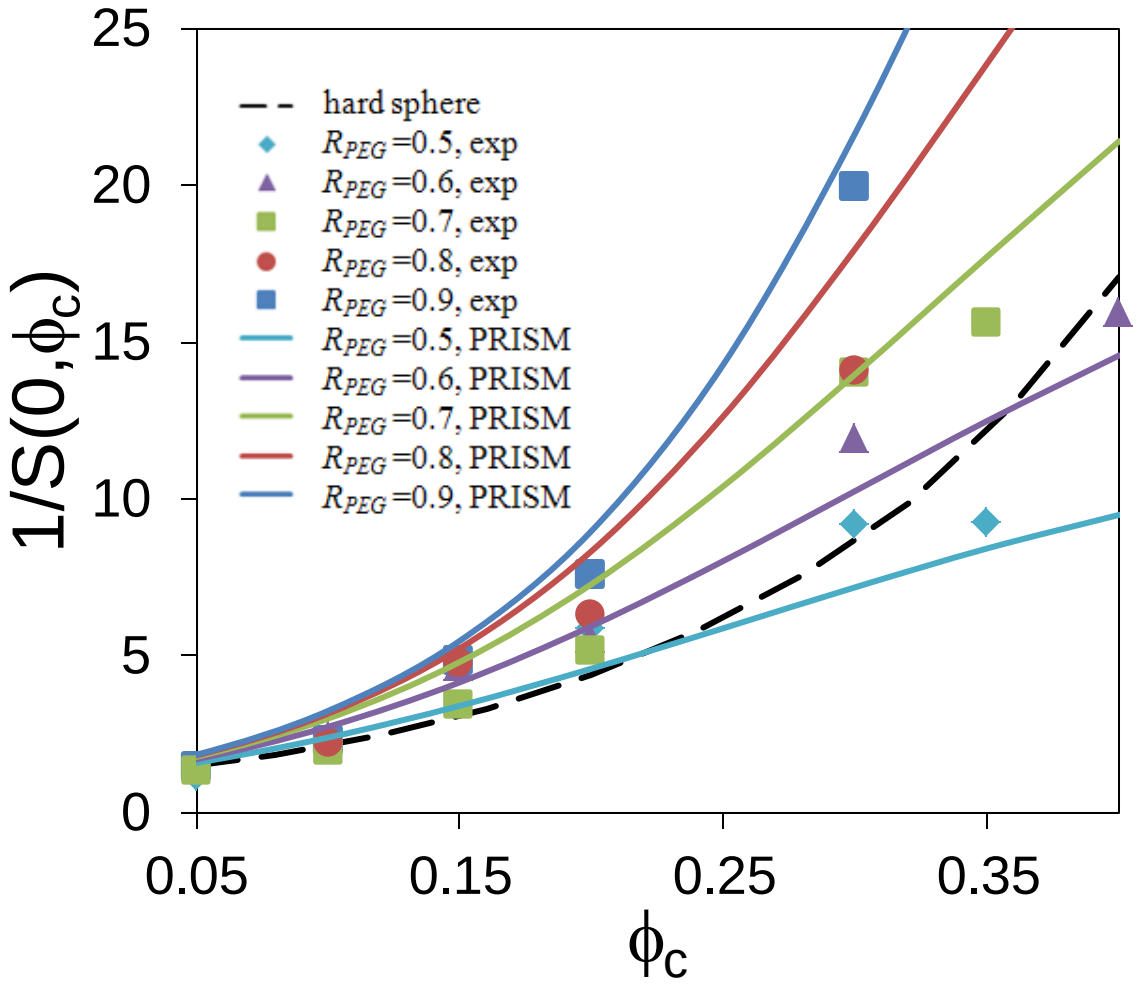

Figure 2.5 Experimental inverse osmotic compressibilities ($1/S(0,\phi_c)$) as a function of particle volume fraction (ϕ_c) at various R_{PEG}. The corresponding PRISM predictions are plotted as solid curves. The reference hard sphere fluid result is also shown (dashed curved).

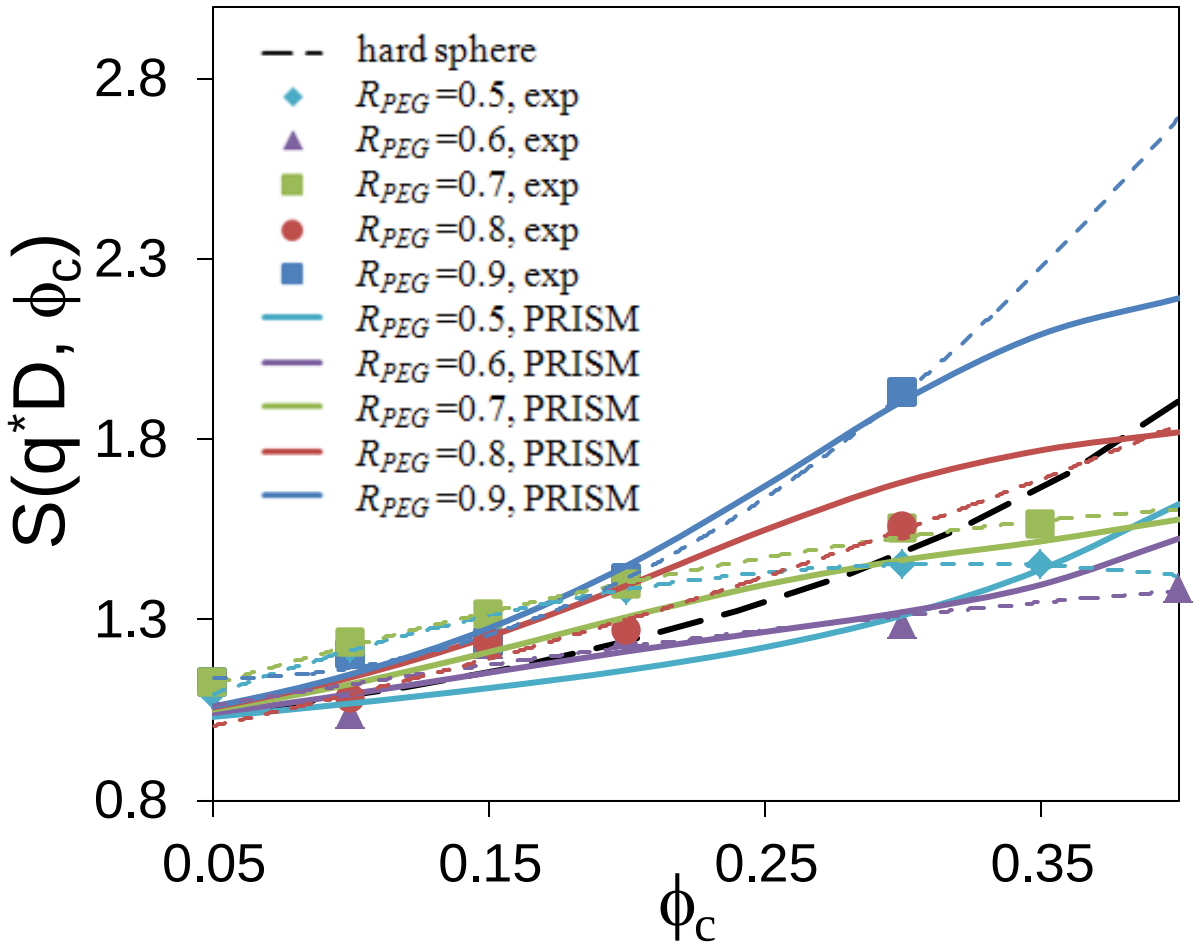

Figure 2.6 Experimental height of the cage peak of the particle structure factor ($S(q^*D, \phi_c)$) as a function of particle volume fraction (ϕ_c) at various R_{PEG}. The corresponding PRISM predictions are plotted as solid curves. The reference hard sphere fluid result is also shown (long dashed).

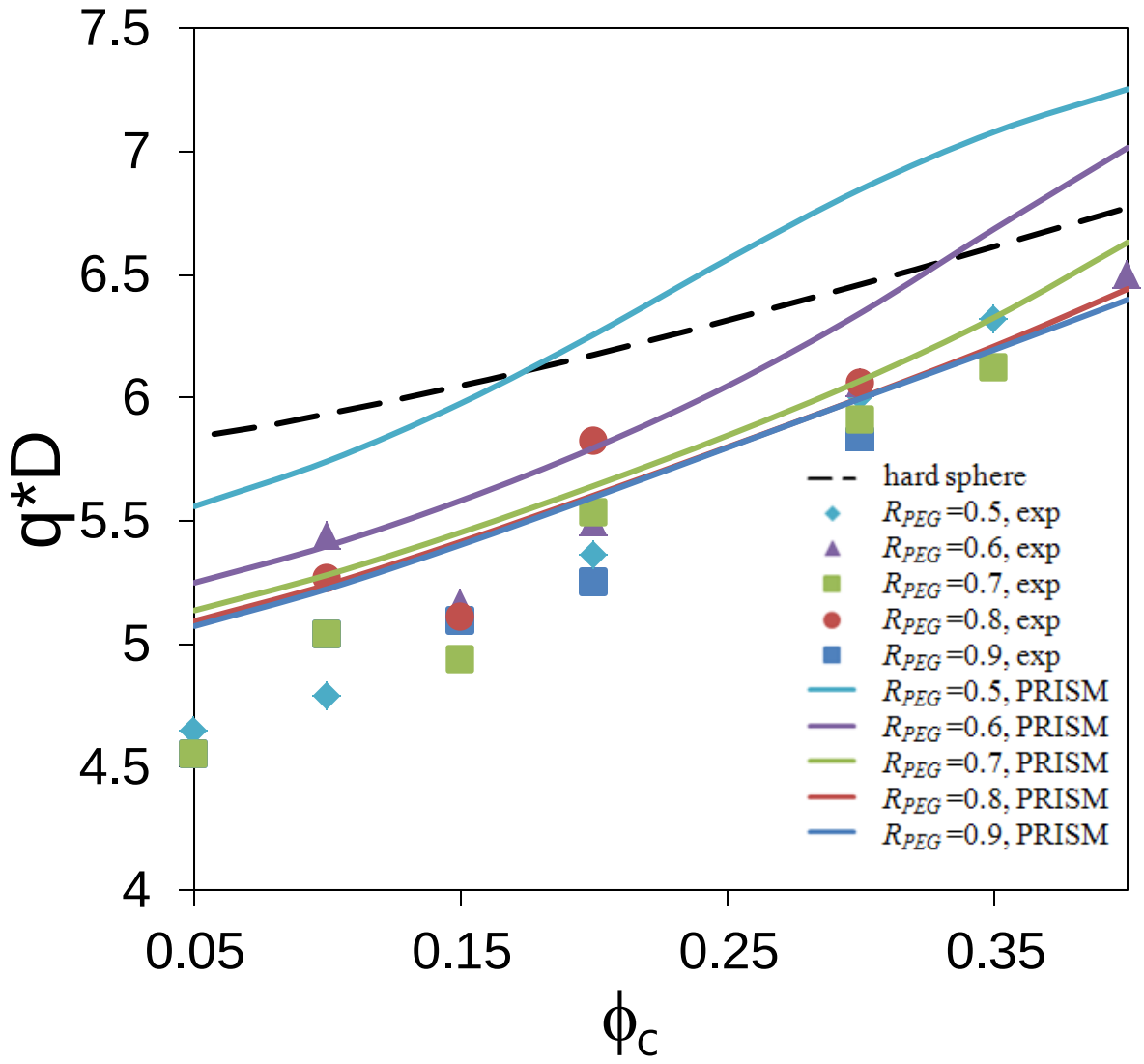

Figure 2.7 Experimental normalized wavevector at the cage peak of the particle structure factor, q^*D, as a function of particle volume fraction (ϕ_c). The corresponding PRISM predictions are plotted as solid curves. The reference hard sphere fluid result is also shown (dashed curved).

2.7 References

1. Poon, W. C. K., *J. Phys. Condens.Matter* **2002,** *14*.
2. Russel, W. B.; Saville, D. A.; Schowalter, W. R., *Colloidal Dispersions*. Cambridge University Press: Cambridge, UK, 1989.
3. Dutta, N.; Green, D., *Langmuir* **2008,** *24*, 5260-5269.
4. Feigin, R. I.; Napper, D. H., *J. Colloid Interface Sci.* **1980,** *75*, 525-541.
5. Hall, L. M.; Anderson, B. J.; Zukoski, C. F.; Schweizer, K. S., *Macromolecules* **2009,** *42*, 8435-8442.
6. Huang, H.; Ruckenstein, E., *Langmuir* **2006,** *22*, 4541-4546.
7. Semenov, A. N., *Macromolecules* **2008,** *41*, 2243-2249.
8. Surve, M.; Pryamitsyn, V.; Ganesan, V., *J. Chem. Phys.* **2006,** *125*.
9. Anderson, J. A.; Sknepnek, R.; Travesset, A., *Phys. Rev. E* **2010** 82 (2) 021803.
10. Hall, L. M.; Jayaraman, A.; Schweizer, K. S., *Curr. Opin. Solid State Mater. Sci.* **2010,** *14*, 38-48.
11. Hall, L. M.; Schweizer, K. S., *J. Chem. Phys.* **2008,** *128*.
12. Hooper, J. B.; Schweizer, K. S., *Macromolecules* **2005,** *38*, 8858-8869.
13. Hooper, J. B.; Schweizer, K. S., *Macromolecules* **2006,** *39*, 5133-5142.
14. Hooper, J. B.; Schweizer, K. S., *Macromolecules* **2007,** *40*, 6998-7008.
15. Anderson, B. J.; Zukoski, C. F., *Macromolecules* **2007,** *40*, 5133-5140.
16. Sharma, A.; Tan, S. N.; Walz, J. Y., *J. Colloid Interface Sci.* **1997,** *190*, 392-407.
17. Lekkerkerker, H. N. W.; Poon, W. C. K.; Pusey, P. N.; Stroobants, A.; Warren, P. B., *Europhys. Lett*. **1992,** *20*, 559-564.
18. Stober, W.; Fink, A.; Bohn, E., *J. Colloid Interface Sci.* **1968,** *26*, 62.
19. Mkhatresh, O. A.; Heatley, F., *Polym.Int*.**2004,** *53*, 1336-1342.
20. Kim, S. Y. M. S. thesis, University of Illinois at urbana-Champaign, Urbana, 2009.
21. Fredrickson, G. H., *The Equilibrium Theory of Inhomogeneous Polymers*. Oxford University Press 2005.
22. Schweizer, K. S.; Curro, J. G., Integral equation theories of the structure, thermodynamics, and phase transitions of polymer fluids. In *Advances in Chemical Physics*, 1997; Vol. 98, p 1-142.
23. Chandler, D.; Anderson, H. C., *J. Chem. Phys.* **1972,** *57*, 1930.
24. Rubinstein, M.; Colby, R. H., *Polymer Physics*. Oxford: New York, 2003.
25. Biben, T.; Hansen, J. P., *Phys. Rev. Lett*. **1991,** *66*, 2215-2218.
26. Evans, D. F.; Wennerström, H., *The Colloidal Domain: Where Physics, Chemistry, Biology, and Technology Meet*. VCH: Cambridge, 1994.
27. Kawaguchi, M.; Hada, T.; Takahashi, A., *Macromolecules* **1989,** *22*, 4045-4047.
28. Kawaguchi, M.; Sakakida, K., *Macromolecules* **1990,** *23*, 4477-4479.
29. Ramakrishnan, S.; Fuchs, M.; Schweizer, K. S.; Zukoski, C. F., *J. Chem. Phys* **2002,** *116*, 2201-2212.

30. Ramakrishnan, S.; Fuchs, M.; Schweizer, K. S.; Zukoski, C. F., *Langmuir* **2002,** *18*, 1082-1090.
31. Shah, S. A.; Chen, Y. L.; Ramakrishnan, S.; Schweizer, K. S.; Zukoski, C. F., *J. of Phys. Condens. Matter* **2003,** *15*, 4751-4778.
32. Shah, S. A.; Chen, Y. L.; Schweizer, K. S.; Zukoski, C. F., *J. Chem. Phys* **2003,** *118*, 3350-3361.

CHAPTER 3 LONG WAVELENGTH CONCENTRATION FLUCTUATIONS AND CAGE SCALE ORDERING OF NANOPARTICLES IN CONCENTRATED POLYMER SOLUTIONS: EFFECT OF SOLVENT CHANGE AND TEMPERATURE[2]

3.1 Introduction

Products containing polymer-colloid mixtures range from coatings to structural composites. In these products, achieving desired properties requires controlling the degree of particle dispersion. As a result, the state of aggregation of polymer-colloid mixtures has been extensively studied with the preponderance of work occurring in dilute and semi-dilute polymer solutions and under conditions when the polymer is nonadsorbing.[1, 2] Key challenges remain in developing dispersions in concentrated polymer solutions and melt where polymer adsorption is essential to reduce particle aggregation.

Recent theoretical and experimental advances in understanding polymer nanocomposites have established that the strength and spatial range of the polymer segment-particle surface interactions control microstructure of nanoparticle dispersions[3-8]. One key prediction is that the degree of aggregation is a nonmonotonic function of the strength of attraction of polymer segment-particle contact, ε_{pc}. For very small ε_{pc} compared to the average thermal energy of the system, kT, (a "dewetting" interface), depletion attractions make nanoparticles aggregate into compact clusters at nearly all particle volume fractions. For large ε_{pc}, polymers form tight bridges between the nanoparticles resulting in phase separation or perhaps formation of non-equilibrium polymer-particle networks. However at intermediate ε_{pc}, adsorbed polymer segments

[2] Reproduced with permission from *Langmuir* DOI 10.1021/la201704u. Copyright © 2011 American Chemical Society

form discrete, nonoverlapping, and *thermodynamically stable* layers, resulting in a net repulsive interparticle potential-of-mean-force (PMF) between the nanoparticles.[3-8]

In previous studies changes of particle microstructures in nanocomposite melts consisting of silica particles in polyethylene glycol (PEG) and polytetrahydrofuran (PTHF) were measured and interpreted using Polymer Reference Interaction Site Model (PRISM).[3, 9] In these polymers, the intrinsic particle interaction potential is that of hard spheres and changes in microstructures were well described by a particle volume fraction independent ε_{pc} which is varied with polymer type. For PTHF melt, $\varepsilon_{pc,m}$, the polymer segment-particle surface contact potential value in a polymer melt, was determined as $0.35kT$. This modest strength of binding was confirmed by polymer slip at the particle surface and the onset of aggregation at low volume fraction. For PEG melts, on the other hand, $\varepsilon_{pc,m}$ was determined as $0.55kT$, particles were stable and responded hydrodynamically as if they were hard spheres suspended in a Newtonian solvent where the particles have a diameter larger than that of the silica core. [3, 9, 10] More recently we explored changes to particle stability as PEG nanocomposite melts were diluted with *ethanol*[11] where we found that ε_{pc} decreased as *ethanol* concentration increased (PEG concentration decreased). Indeed our experiments show that particles are unstable to aggregation when particles are suspended in less than 45 wt% PEG 400 suggesting ethanol displaces polymer from the particle surface reducing the ability of PEG to form stabilizing bound layers. [11]

Here we extend these studies to investigate the generality of these observations by changing solvent and altering sample temperature. Our results suggest that a complex interplay of solvent/solvent, solvent/polymer, solvent/particle and polymer/particle interactions control the degree of stability but these changes can be monitored through changes in particle microstructure. In particular we report the effects of: i) diluting PEG 400 –silica nanocomposite melts with *water*

instead of *ethanol*; ii) changing polymer to *water* ratio in the mixture; and iii) changing temperature of the samples that have been diluted with *water* and *ethanol*. Our results are interpreted with PRISM where the point of interest is the effect of solvent type and temperature on ε_{pc}.

Below in Section 3.2 we describe our experimental system and measurement methods. Section 3.3 contains a discussion of experimental results where we compare changes in particle structure factors at varying polymer to solvent ratios, different solvent and increased temperature while Section 3.4 compares experimental results with theoretical predictions. We find that ε_{pc} for the silica/PEG/water system is weakly dependent on polymer concentration while changing temperature appears to reduce ε_{pc} in *water* but have limited effect in *ethanol*. In Section 3.5 we draw conclusions.

3.2 Experiment

3.2.1 Sample Preparation

Silica nanoparticles were synthesized based on the method of Stöber *et al.*[12], using the base-catalyzed hydrolysis and condensation of tetraethylorthosilicate (TEOS). The reaction temperature was 55°C. 3610 ml of ethanol was mixed with 96ml of deionized water, and 156ml of ammonium hydroxide was then added as a catalyst. The reaction was allowed to run for 4 hours. After mixing, 156ml of TEOS was added. Particle diameters were determined based on SEM performed on 100 particles yielding a diameter of 40±5nm; alternatively, fitting of the single particle form factor determined by the angle dependence of x-ray scattering from a dilute suspension of particles yielded a diameter of 40±4nm.

PEG 400 was purchased from Sigma-Aldrich, and pure ethanol was supplied from Decon Lab. Inc. As discussed previously[3, 11], the effective diameter of a PEG monomer (d) is ~ 0.6 nm. The nanoparticle size was chosen to minimize the size asymmetry ratio, *D/d*, but have a large enough particle such that small angle x-ray and neutron scattering can be used to probe both long wavelength and cage scale collective concentration fluctuations.

After particle synthesis, the alcosol was concentrated approximately 10 times by heating in a ventilation hood. During this process, the excess of ammonium hydroxide was removed. For the preparation of polymer suspensions, the exact mass of each component (silica, PEG 400, water) was determined in order to create the desired particle and polymer concentrations.

Particle volume fractions were calculated using the masses of each component and their densities. The silica particle density is 1.6g/cm^3.[9] In making the nanocomposite melts, a defined mass of alcosol is mixed with a defined mass of PEG 400. Samples were heated in a vacuum oven to drive off ethanol. The vacuum oven was purged several times with nitrogen followed by evacuation of the chamber to remove oxygen which degrades PEG at high temperature.[13] Once the ethanol was evaporated, the necessary amount of water or ethanol was added to the sample and fully mixed on the vortex mixer to produce the desired concentrations of particles and PEG.

PEG 400 is a liquid at room temperature and is completely soluble in water. In the absence of PEG, the alcosol appears transparent blue. As the silica and PEG have nearly identical refractive indices (n_{silica} =1.4555, n_{PEG}=1.4539), the polymer/particle mixture becomes increasingly transparent as polymer concentration is increased. In the absence of water, the polymer nanocomposite melt is fully transparent and this index matching greatly reduces (nearly eliminates) van der Waals attractions between silica particles thereby rendering them model hard

spheres.[9] In the absence of polymer, silica particles remained stable due to the dissociation of silanol group confirmed by positive second virial coefficient in dilute limit.[14]

Polymer concentration will be described in terms of the parameter 'R_{PEG}', defined as the ratio of the polymer volume to the volume of polymer plus volume of solvent. In the range of R_{PEG} where this study performed no evidence of particle aggregation observed. For $0.5<R_{PEG}<1$, we find the suspensions are stable and well dispersed. To confirm the experimental consistency we strengthened the results by adding newly obtained small angle neutron scattering (SANS) data to Ref. (11) at R_{PEG}=0.5 in *ethanol* to compare with R_{PEG}=0.5 in *water*.

Table 3.1 lists the experimental values of R_{PEG} explored in this study.

3.2.2 Side-Bounce Ultra Small X-ray Scattering (SBUSAXS)

The details for SBUSAXS and procedures to obtain scattering structure factors are already described in Section 2.2.2.

3.2.3 Small Angle Neutron Scattering (SANS)

SANS experiment was performed on the NG7 30 m SANS instrument in NIST Center for Neutron Research, National Institute of Standards and Technology (NIST). Samples used in SANS experiments are listed in Table 3.1. Samples were loaded into 1mm path length demountable titanium cells. The cell temperature was maintained to 20±0.1 ˚C and 60±0.1 ˚C using the 10CB sample holder with a NESLAB circulating bath. A large range in scattering wave vector, q ($0.001A^{-1}$ ~ $0.1A^{-1}$) , was obtained by combining the sector averaged scattering

intensity from two different instrument configurations at 4, and 15.3 m detector distances (with focusing lenses at15.3 m only). SANS data reduction and analysis of the scattering intensity, I, versus Q was performed using the SANS reduction and analysis program with IGOR Pro available from NIST. [15] For the scattering measurement at the temperature of 60°C noted in Table 3.1, samples used at 20°C were kept in a 60°C oven for 6 hours and held 30 minutes more in a sample holder at 60˚C before the measurement.

3.2.4 Experimental Structure Factor

Nanoparticle structure factors were measured under the conditions summarized in Table 3.1 with two different scattering techniques. In this section we present representative data, and discuss the key trends. Detailed discussion of methods to extract structure factors from scattering measurements are given in Section 2.2.3.

Collective nanoparticle structure factors were obtained by dividing the scattering intensity from the concentrated particle suspension by its dilute limit analog (*ds*) at the same polymer concentration as seen in Eq. (2.4).

In the dilute particle limit, $S(q)$=1. Structure factors are extracted under high polymer concentration conditions where the nanoparticles are stable (miscible homogenous phase). Particle volume fractions from 0.027 to 0.375 have been studied at a fixed R_{PEG} (see Table 3.1). As an example of how to interpret Table 3.1, consider the case of R_{PEG}=0.6 with ϕ_c =0.10. For this condition, 10% of the total sample volume is occupied by the silica particles and the

remaining 90% is polymer and water. Since the ratio of PEG to water volumes is fixed at 3:2, the total volume fraction of polymer in the mixture is 0.54, while the ethanol volume fraction is 0.36.

All experimental structure factors are liquid-like in the sense of showing a plateau value at low qD with a wide angle, amorphous fluid-like peak that grows in magnitude and moves to larger qD as volume fraction is raised. For all systems reported here, the silica particles show no signs of aggregation as would be indicated by upturns in $S(q)$ as $q \rightarrow 0$.

The structure factors at R_{PEG}=0.5 at 20˚C for various particle volume fractions are shown in Figure 3.1 based on $\phi_{c,ds}$ = 0.02. Three monotonic trends with particle volume fraction emerge that are typical of all our data: i) The low wave vector amplitude strongly decreases with increasing ϕ_c corresponding to the nanoparticle subsystem becoming less compressible as particle volume fraction is raised. ii) The cage peak intensity, $S(q^*)$, initially increases very weakly, and then grows rapidly as ϕ_c increases. This behavior is expected for stable dispersions as $S(q^*)$ is a measure of the coherence of the nearest neighbor cage which increases as particles become more crowded. iii) The wide angle peak at $q=q^*$ shifts from $q^*D \sim 4$ to $q^*D \sim 6$ corresponding to a shorter range local cage order. This trend follows since $2\pi/q^*D$ is a measure of the mean distance between a central particle and its first nearest neighbor shell.

The behavior shown in Figure 3.1 is typical of all R_{PEG} values studied. Analysis of the effects of diluting with *water* and changing temperature will focus on how these three features evolve as particle volume fraction increases.

3.2.5 Polymer Characterization

Below we characterize particle microstructure as functions of particle volume fraction, polymer concentration and composite temperature when the polymer nanocomposite melt is diluted with *water* and *ethanol*. Key results include the strength of cohesion between polymer segments and the particle surface. This parameter, ε_{pc}, varies with solvent type, solvent concentration and temperature. Understanding these changes is a complicated task. As part of our effort, we have investigated that theta state of PEG in *ethanol* and *water* at different temperatures by measuring the polymer solution second virial coefficient.

For this work we measured the second virial coefficient in dilute polymer solutions with light scattering. We were unable to obtain sufficient signal for PEG 400 and small radius of gyration of PEG 400 (less than 1 nm) and instead chose to work with PEG 10000. As a result, the observed trends will be used qualitatively in analysis of suspension microstructures.

Static light scattering (DLS- Brookhaven instruments BI-200 SM goniometer, Lexel Argon-Ion Model 95 laser, λ=514 nm) was carried out to obtain second virial coefficients of PEG-water and PEG-ethanol mixtures. The instrument was calibrated with the scattering of toluene at 90° to convert scattering intensity from counts per second to cm^{-1}. Samples were measured from 20 to 65 °C. Samples were stabilized to reach its equilibrium state for 6 hours at each temperature. To develop the Zimm plot[16], 5 dilute polymer concentrations were prepared and measurements were taken from θ=40°-130°.

Shown in Fig. 3.2 are values of polymer solution second virial coefficient (A_2) as a function of temperature. Solvent quality is often described with intermolecular interactions between polymer segments and solvent molecules. For a good solvent, interactions between

polymer segments and solvent molecules are energetically favorable resulting in positive A_2, while for a poor solvent, polymer-polymer self-interactions are preferred resulting in negative A_2. *Water* is a good solvent for PEG 10000 at low temperature with large positive A_2 but A_2 decreases towards zero at 60°C. When suspended in *ethanol*, A_2 is large and positive at 60°C and decreases as the temperature is lowered. At 20°C, A_2 cannot be measured since PEG 10000 is not soluble in *ethanol* suggesting A_2 is large and negative. However, smaller A_2 for *ethanol* is expected than in *water* based on the given trend suggesting *water* is a better solvent than *ethanol*. These results are in agreement with previous studies of the effect of temperature on solvent quality for PEG in ethanol/water mixtures showing that the solvent quality in *water* and *ethanol* are approximately equal at 40°C and solvent quality in water decreases as *ethanol* is added.[17-19] Thus, we conclude that at 20°C PEG 400 in *ethanol* is in a near theta state while it *water* is a good solvent. However at 60°C, *ethanol* is a good solvent for PEG400 while *water* is close to a theta state.

In the Flory-Huggins treatment[20], the second virial coefficient will be written $A_2 \sim (1-2\chi)$ where χ is the chi parameter with $\chi = (\varepsilon_{ss}+\varepsilon_{pp}-2\varepsilon_{ps})/kT$. Here ε_{ss}, ε_{pp}, ε_{ps} represent the strengths of cohesion between pairs of solvent molecules, pairs of polymer segments and solvent molecules and polymer segments respectively. The theta state is defined as $\chi=1/2$. For $\chi>1/2$ ($A_2>0$), the polymer segments find themselves in a good solvent often referred to as athermal where to a good first approximation $\varepsilon_{ss} \sim \varepsilon_{pp}$. From the data in Fig. 3.2, we conclude that for PEG 400 suspended in *water* or *ethanol*, the polymer segments always find themselves in a good solvent and *water* is better solvent than *ethanol* for PEG at low temperature. When suspended in *water*, $\varepsilon_{ps}/\varepsilon_{ss}$ decreases as temperature is raised while when suspended in *ethanol*, $\varepsilon_{ps}/\varepsilon_{ss}$ increases with temperature.

3.3 Theory

3.3.1 Background

PRISM theory has been extensively applied to polymer nanocomposite melts and concentrated polymer solutions.[4-8] Recently PRISM was extended to account for the expected increase in total system packing fraction with the addition of hard nanoparticles to a polymer melt composed of monomers which can fill the interstitial space between the nanoparticles. The model accounts for an excluded volume around each particle corresponding to a polymer segment radius while at larger segment-surface separations the polymer takes on its pure melt density.[3] In our recent studies, we extended this model to a three phase system where the polymer density outside the excluded volume is variable. Experimentally the polymer density is decreased from that of the melt by the addition of solvent- *water* or *ethanol*. In the model, the solvent is treated implicitly by reducing the polymer packing fraction and adjusting the polymer adsorption strength, roughly in the spirit of an effective mean field χ-parameter and effective (but compressible) 2-component mixture model. [21]

The mixture model and PRISM theory[21, 22] employed here are identical to these prior studies [3, 5-8, 11] and given in Section 2.3.

3.3.2 Effect of Solvent Dilution

Previous studies have explored the ability of PRISM to capture the microstructure of nanoparticle composites through changes in polymer chemistry at the melt[3] showing that $S(q,\phi_c)$ are well described with ε_{pc} that is independent to particle volume fraction. As discussed in the introduction, microstructures were shown to be sensitive to polymer backbone chemistry. In a

more recent study of PEG-*ethanol* mixtures we report that at fixed particle volume fraction as R_{PEG} is decreased, the particles experience weaker repulsions. The reduction in repulsions was apparent in increasing long wave length density fluctuations and weaker correlations associated with first nearest neighbor distances where $S(q^*,\phi)$ and q^* decrease with increasing R_{PEG}. PRISM associates these changes with:

1) Dilution of polymer segments where upon addition of solvent, ϕ_{p0} was written in Section 2.3.2 as:

$$\phi_{p0} = R_{PEG}\phi_{p0,m} \tag{2.12}$$

where $\phi_{p0,m} = 0.40$ is the polymer volume fraction in the melt.[3]

2) Reduction in repulsive interactions between the particles. The key material parameter controlling the interaction is the polymer segment-nanoparticle attractive contact strength, ε_{pc}. [3, 5-8]. Reductions in ε_{pc} result in weaker correlations of polymer segments with particle surfaces reducing repulsions in particle potential of mean force and allowing larger long wave length density fluctuations. If ε_{pc} is small enough, strong depletion attractions are predicted to result in phase separation that would be observed as particle aggregation.

In the case of a mixture of polymer and solvent, PRISM treats the solvent as implicit. See the Section 2.3.2. Hence, we proposed a simple mean-field-like estimate of the effective interfacial attraction strength as: [11]

$$\varepsilon_{pc} = \varepsilon_{pc,m} - (1-R_{PEG})\varepsilon_{ps} - (1-R_{PEG})\varepsilon_{cs} + (1-R_{PEG})^2\varepsilon_{ss} \tag{2.13}$$

Experimentally we reported in Chapter 2 that when diluting the melt with *ethanol* at 20°C resulted in a reduction in ε_{pc} suggesting that with increasing ethanol concentration, the solvent displaces the polymer segments from the particle surface. Assuming the polymer is in a good solvent, we expect $\varepsilon_{ps} \sim \varepsilon_{ss}$ in *ethanol* at 20°C. Assuming that ε_{ps} and $(1-R_{PEG})^2\varepsilon_{ss}$ values are small (not incompatible with PEG 400 being in a near theta state at 20°C when suspended in *ethanol*) and that $\varepsilon_{cs} = \varepsilon_{pc,m}$ allowed us to rationalize from Eq. (2.13) and this relation was proved to be an good approximation in the previous study: [11]

$$\varepsilon_{pc} = R_{PEG}\varepsilon_{pc,m} = 0.55R_{PEG} \qquad in\ ethanol\ at\ 20°C \tag{2.14}$$

Below we explore these initial ideas by systematically varying the theta state of the polymer through chances in temperature and solvent. What emerges is a complex picture of how ε_{pc} changes with these variables indicating that theta state of the polymer is a poor indication of the ability of the polymer to drive miscibility in polymer/particle/solvent mixtures.

3.4 Results

In Fig. 3.3 we show particle structure factors for silica particles in water at R_{PEG}=0.9 for two volume fractions. We see that the particles are well dispersed, that the compressibility decreases while the coherency of the cage of nearest neighbors increases with increasing volume fraction.

Drawn in Fig 3.3 are predictions of PRISM for ε_{pc}=0.45 showing the sort of quantitative agreement that we can achieve with this theory. Below we discuss our results by comparing predictions of PRISM with experimental data as we change solvent and temperature with specific attention of S(0), q^*D and $S(q^*D)$.

3.4.1 Effects of Changing Solvent

The inverse of osmotic compressibility *(1/S(0))* is given as a function of particle volume fraction (ϕ_c) when nanoparticles are suspended in PEG-*ethanol* and in PEG-*water* mixtures in Fig. 3.4a. For fixed R_{PEG}, inverse osmotic compressibilities in *water* are larger than in *ethanol* for all particle volume fractions. This indicates that in comparison with ethanol, long wave length density fluctuations are suppressed for particles in PEG-*water* systems. This suggests the particles experience larger repulsive potentials of mean force than exist in the PEG-*ethanol* system. This pattern is repeated for $S(q^*)$ where the first cage peak height is larger in water than in ethanol at the same R_{PEG} and ϕ_c. (Fig. 3.4b). Again these results are consistent with an interpretation where greater cage coherency results from larger interparticle repulsions in *water* over those seen when the solvent is *ethanol*.

To compare experimental results with PRISM predictions, we first adjust the polymer melt packing fractions based on Eq. (2.12) to the case of R_{PEG}=0.5. Predictions are then made for ε_{pc} =0.02 through ε_{pc} =0.5 where ε_{pc} is held constant as ϕ_c increases. (Fig. 3.4a) Particle scattering features are in good agreement with the PRISM predictions when ε_{pc}=0.42. At R_{PEG}=0.5, in keeping with previous studies when the PEG melt is diluted with *ethanol*, we find that volume fraction dependencies of *1/S(0)* and $S(q^*)$ are well captured with ε_{pc} =0.275. (Fig. 3.4a and b)

Fig. 3.4c compares theoretical and experimental values of dimensionless wave vector of the primary cage peak in *ethanol* and in *water*. Theoretical values of q^* vary approximately linearly with ϕ_c, as observed experimentally. The position of cage peak is weakly dependent on solvent type.

These results indicate that ε_{pc} is a weak function of particle volume fraction but does depend on the chemical nature of the solvent used to dilute the polymer. Below we gain insights on the relative roles of ε_{ss}, ε_{ps} and ε_{ss} in determining ε_{pc} by varying R_{PEG}.

3.4.2 Effect of Polymer-to-Solvent Ratios

At a fixed particle volume fraction, long wavelength density fluctuations and the coherency of the first nearest neighbor cage shown in Fig. 3.5 are weak functions of R_{PEG} when the melt is diluted with *water*. These results indicate that the potential of mean force felt by the particles is weakly sensitive to exchanging a polymer segment with *water* molecules in the bulk and are qualitatively different than those observed when the polymer is diluted with *ethanol* where with long wave length fluctuations grow while the coherency of the first nearest neighbors cage decreases with increasing polymer dilution.

In applying PRISM to the data set in Fig. 3.5, the data are well described when ε_{pc} is independent of volume fraction and takes on values of 0.42, 0.43, 0.44, 0.45 and 0.45 for R_{PEG} =0.5, 0.6, 0.7, 0.8 and 0.9, respectively. The PRISM predictions for $1/S(0)$ and $S(q^*)$ using these values of ε_{pc} are shown in Fig. 3.5 a and b. When the polymer melt is diluted from R_{PEG} =0.9 to 0.5 with *ethanol*, ε_{pc} decreases from 0.495 to 0.275, a difference of $0.2kT$. Dilution with *water* results in a decrease of 0.02kT.

To understand small changes of ε_{pc} for nanoparticles suspended in PEG-*water* mixtures we refer to Eq. (2.13). In PEG-*ethanol* mixtures, the linear increase of ε_{pc} with R_{PEG} could be reproduced with $\varepsilon_{cs}=\varepsilon_{pc,m}$ and $\varepsilon_{ps}/\varepsilon_{cs}$ and $(1-R_{PEG})^2\varepsilon_{ss}/\varepsilon_{cs}$ are small. These assignments are reasonable based on chemical similarities of PEG backbone and *ethanol*, and the athermal

solvent properties for *ethanol* and PEG. In the dilute polymer solutions, based on adsorption isotherm of PEG to silica in these two solvents, we expect ε_{pc} in *water* to exceed that in *ethanol* [14, 25, 26] Thus *water* is more easily displaced from the particle surface by polymer segments than *ethanol,* suggesting we can no longer assume $\varepsilon_{cs} = \varepsilon_{pc,m}$. Because of this ease of displacement we expect ε_{cs} to be smaller than $\varepsilon_{pc,m}$.

Due to the lack of information of ε_{cs}, ε_{ps} and ε_{ss}, choices of their values are arbitrary. However, to demonstrate that Eq. (2.13) can predict a weak dependence of ε_{pc} on R_{PEG} we here choose plausible parameters. Recognizing much stronger polymer adsorption PEG in water, we set ε_{cs}=0.25 and ε_{ps}= ε_{ss}=0.125 and $\varepsilon_{pc,m}$=0.55. Then, for polymer diluted with water we obtain:

$$\varepsilon_{pc} = 0.3 + 0.125R_{PEG} + 0.125R_{PEG}^2 \qquad (3.1)$$

These approximations for ε_{ps} for silica nanoparticles in PEG400 diluted with *ethanol* and *water* from Eq. (2.14) and (3.1) are plotted along with values derived from applying PRISM to the experimental data in Fig. 3.6. We emphasize the arbitrary choices of values of ε_{cs}, ε_{ps} and ε_{ss} used in drawing the lines in Fig. 3.6 but present the lines to demonstrate the sensitivity of ε_{pc} to particle-solvent, segment-solvent and solvent-solvent interactions.

3.4.3 Effect of Temperature

A set of samples labeled with subscript ‘a’ in Table 3.1 was prepared to measure scattering intensity at both 20°C and at 60°C.

Figure 3.7 a shows selected scattering factors at a fixed R_{PEG} =0.5 for two volume fractions at 20 °C and 60°C for polymer diluted with *water*. At low volume fraction (ϕ_c =0.056), there are negligible changes in structure factor. However, at higher particle volume fraction (ϕ_c=0.183) as temperature increases from 20°C to 60°C we observe: i) the system becomes more compressible as evidenced by increased *S(0)*; ii) $S(q^*)$ decreases indicating reduced cage coherency; and iii) q^* shifts slightly to higher q^*D. These changes to $S(q, \phi_c)$ indicate that the particles experience reduced repulsions at elevated temperature suggesting decreased particle stability. For all particle volume fractions, when suspended in PEG-*water* mixtures, *1/S(0)* and $S(q^*)$ decrease when temperature increases from 20°C to 60°C . (Fig. 3.7b and c)

The phase behavior of PEG in aqueous systems has been widely investigated[27-30] where higher molecular weights of PEG display a lower critical solution temperature (LCST)[31] and a closed loop high-temperature two phased region. These results indicate that free energies of PEG-*water* solution are lowered by creating water rich and water poor regions when temperature is elevated. The decrease in the particle's repulsive potential of mean force with increasing temperature is consistent with reports that PEG400 adsorption onto silica is negligible at 45°C. [32] This suggests that the fluctuations arising from PEG approaching poor solvent conditions are sufficient to drive water to the surface and PEG segments to the bulk.

In contrast, when the polymer melt is diluted with *ethanol*, at all particle volume fractions, *1/S(0)* and $S(q^*)$ are insensitive to temperature. The lack of change in microstructure with temperature for PEG in *ethanol* solutions supports the concept that the polymer is in a good solvent.

The changes to particle microstructure are quantified by using PRISM to estimate ε_{pc} as a function of temperature. As expected there are no changes in ε_{pc} for the PEG-*ethanol* system but ε_{pc} decreases by ~0.1kT in the PEG-*water* system as temperature is raised from 20°C to 60°C.

Depletion attractions produced by non-adsorbing thermal polymers in a protein or small particle limit show great sensitivity to spinodal phase separation in polymer solution. [33, 34 35, 36] The critical points for lower solution phase separations occur in the region of R_{PEG} =0.01~0.2 depending on the PEG molecular weight[31] indicating that at R_{PEG} =0.5 our system is well away from the critical point. As a result, we would expect the PEG -*water* system is approaching athermal behavior. Nevertheless, large enhancements of depletion attractions were measured 50°C from the spinodal temperature. Therefore, changes in remnant polymer density fluctuations associated with the lower critical solution temperature may be the origin of the small but measurable decreased repulsions observed at R_{PEG}=0.5 in the PEG-*water* system as temperature is raised.

Finally we note that in the current formulation of PRISM, the polymer is assumed to exist in an athermal state. Here we stretch its application to conditions where there is incipient polymer solution phase separation. Nevertheless, we observe that by allowing ε_{pc} to vary with solvent type and temperature, microstructures are well described with a volume fraction independent ε_{pc}.

A key conclusion that we draw is that the miscibility of particles in concentrated polymer solutions is a complex function of the theta state of the polymer as well as solvent-surface and polymer segment-surface interactions. At low temperature, PEG adsorbs to silica surfaces from aqueous solutions with a much greater affinity and larger monolayer coverage than is observed

when the solvent is *ethanol*. These observations are supported by a larger value of ε_{pc} in *water* than in *ethanol* as measured in concentrated polymer solutions. On the other hand, as the polymer is driven from a near theta state to a being in a good solvent by raising temperature, there is no change in the repulsive potential of mean force when the nanocomposite is diluted with *ethanol*. However, in the case of dilution with *water*, there are substantial changes to the repulsive potential of mean force as solvent quality shifts from good to poor solvent state. In the case of *ethanol*, this can be rationalized by arguing that $\varepsilon_{pc,m}$ is large and weakly dependent on temperature such that ε_{pc} is independent of the polymer theta state. On the other hand, in *water*, the water-surface interactions must grow with temperature such that as the polymer approaches a theta state in the bulk, solvent is driven preferentially to the particle surface displacing polymer and lowering ε_{pc}. Independent of the detailed causes, we are able to conclude that when the polymer segments do not adsorb, the particles are less stable.

3.5 Summary

The aim of this study was to understand how particle miscibility in concentrated particle/polymer/solvent mixtures is influenced by changing i) solvent, ii) polymer-to-solvent ratio, and iii) temperature. We show that all those parameters influence the particle stability. Microstructures measured with SANS and USAXS compare well with PRISM predictions where we use a single a volume fraction independent fitting parameter; the strength of attraction between polymer segments and particle, ε_{pc}. Reinforcing previous studies showing polymer chemistry can control ε_{pc}, here we demonstrate that miscibility is not directly tied to solvent quality. Instead we find that while increasing solvent quality (as measured by an increasing value

of the polymer solution second virial coefficient) tends to stabilize the particles, we also can find cases where stability is weakly coupled to polymer's theta state.

3.6 Table and Figures

PEG to solvent vol. ratio (PEG: solvent)	R_{PEG}	solvent	Technique	Particle volume fractions (ϕ_c)					
0.5 : 0.5	0.5	Ethanol	USAXS	0.1	0.25	0.3	0.325		
			SANS	0.027[a]	0.056[a]	0.12[a]	0.18[a]		
		H_2O	USAXS	0.05	0.3	0.35			
			SANS	0.027[a]	0.056[a]	0.12[a]	0.18[a]		
0.6 : 0.4	0.6	H_2O	USAXS	0.1[b]	0.2	0.25	0.3	0.35	
0.7 : 0.3	0.7	ethanol	USAXS	0.1	0.2	0.25	0.35		
			SANS	0.05[a]	0.1[a]	0.2[a]	0.3[a]		
		H_2O	USAXS	0.1	0.2	0.25	0.35		
			SANS	0.05[a]	0.1[a]	0.2[a]	0.3[a]		
0.8 : 0.2	0.8	H_2O	USAXS	0.1	0.2	0.25	0.3	0.35	0.375
0.9 : 0.1	0.9	H_2O	USAXS	0.1	0.2	0.25	0.35	0.375	

a : also performed at 60˚C, b: exampled in Section 3.2.4

Table 3.1 Sample descriptions used in the study. All data was collected at 20°C

.

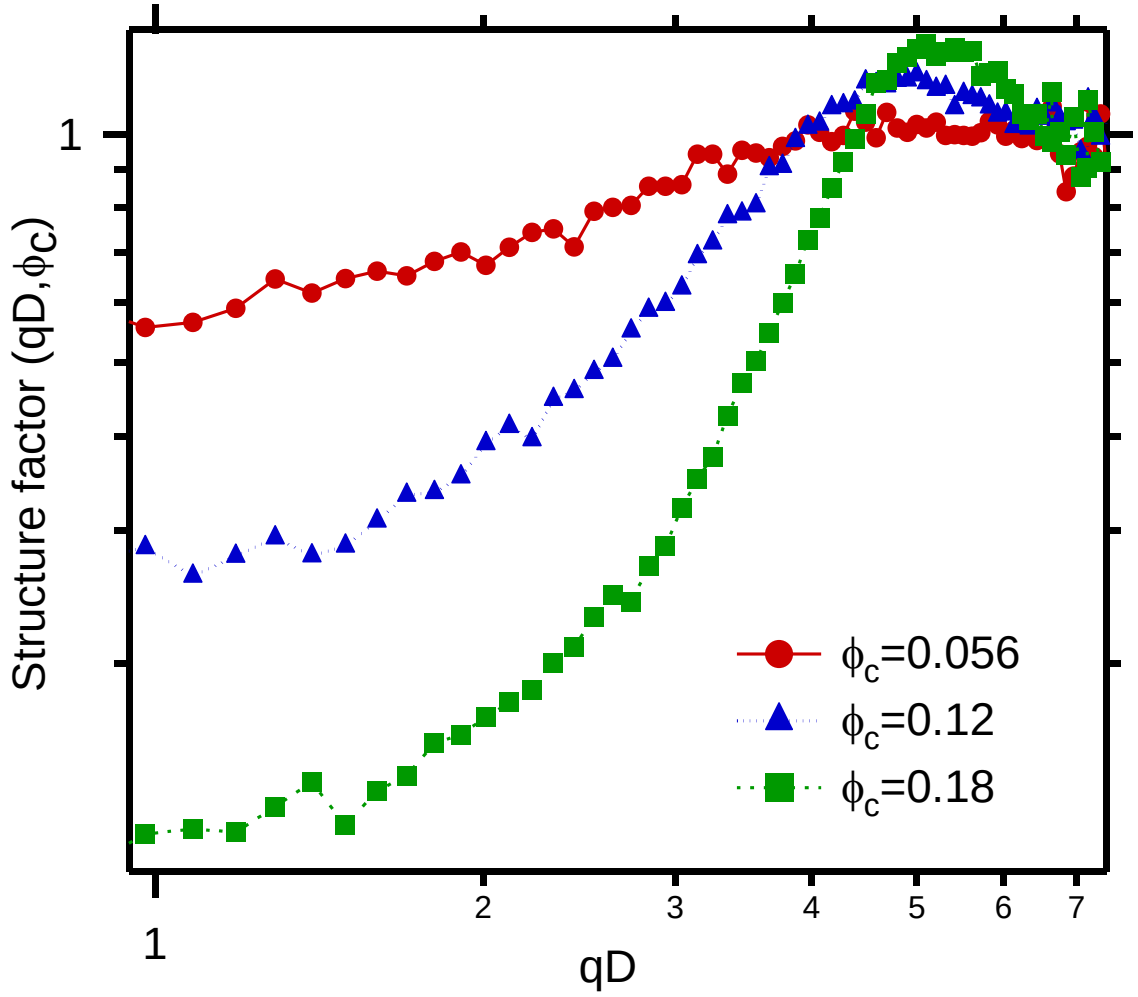

Figure 3.1 Experimental particle structure factor as a function of dimensionless wave vector at R_{PEG}=0.5 in water at 20°C and ϕ_c of 0.056, 0.12 and 0.18 as shown in the legend.

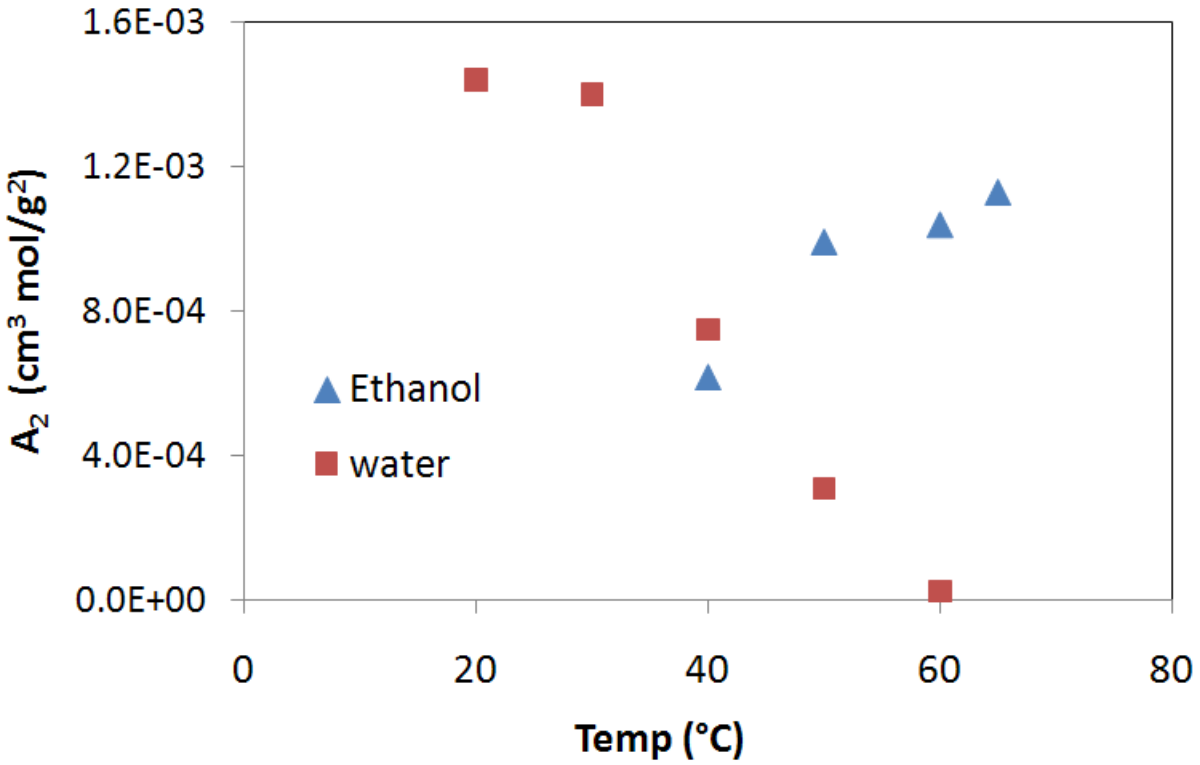

Figure 3.2 Measured second virial coefficients of PEG in water and ethanol at various temperature from 20 °C to 65 °C.

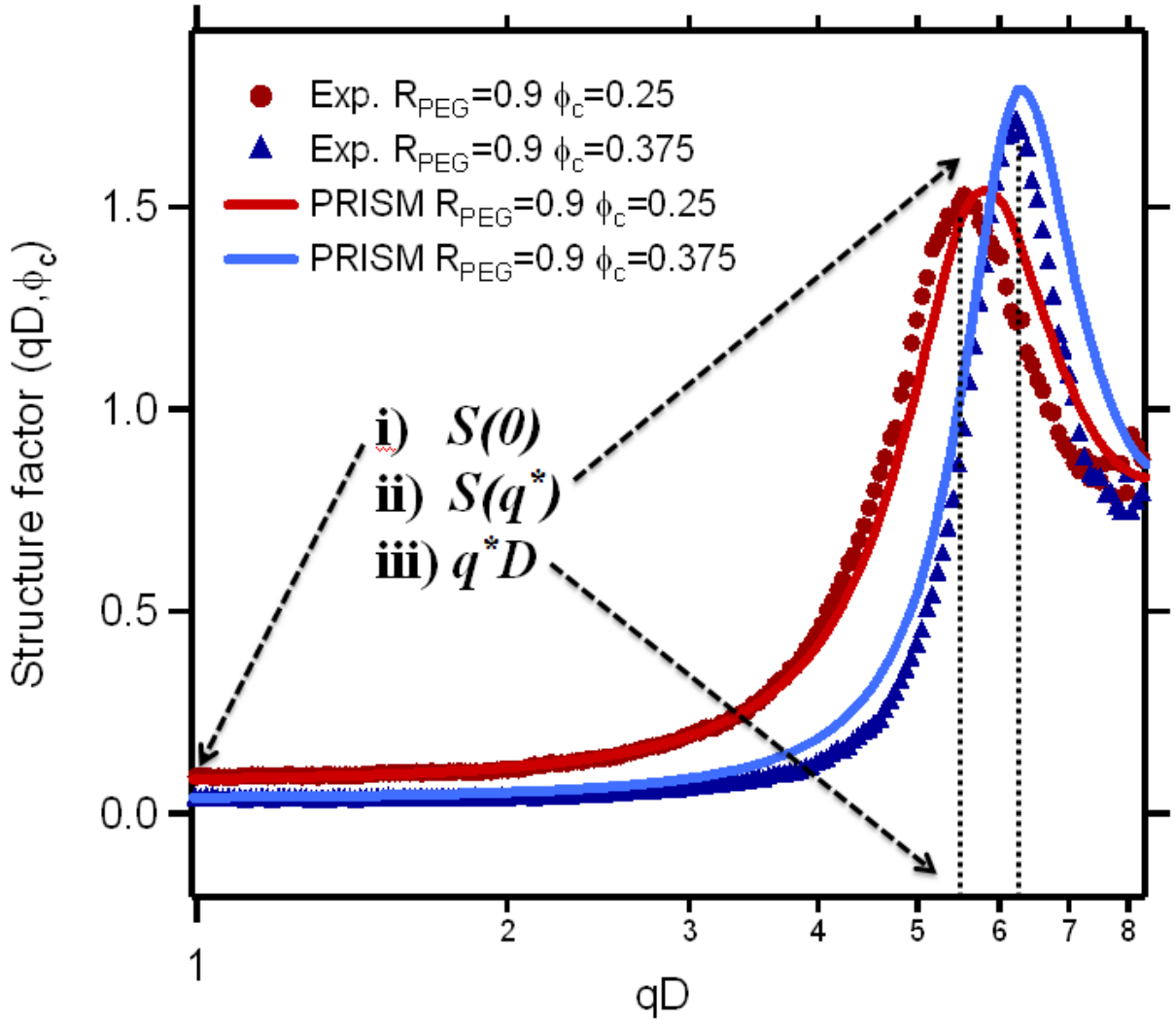

Figure 3.3 Experimental particle structure factor as a function of dimensionless wave vector at R_{PEG}=0.9 in water at 20°C and ϕ_c of 0.25 and 0.375 shown in the legend. The corresponding PRISM predictions with ε_{pc} =0.45 at a given R_{PEG}=0.9 are plotted with solid curves

(a)

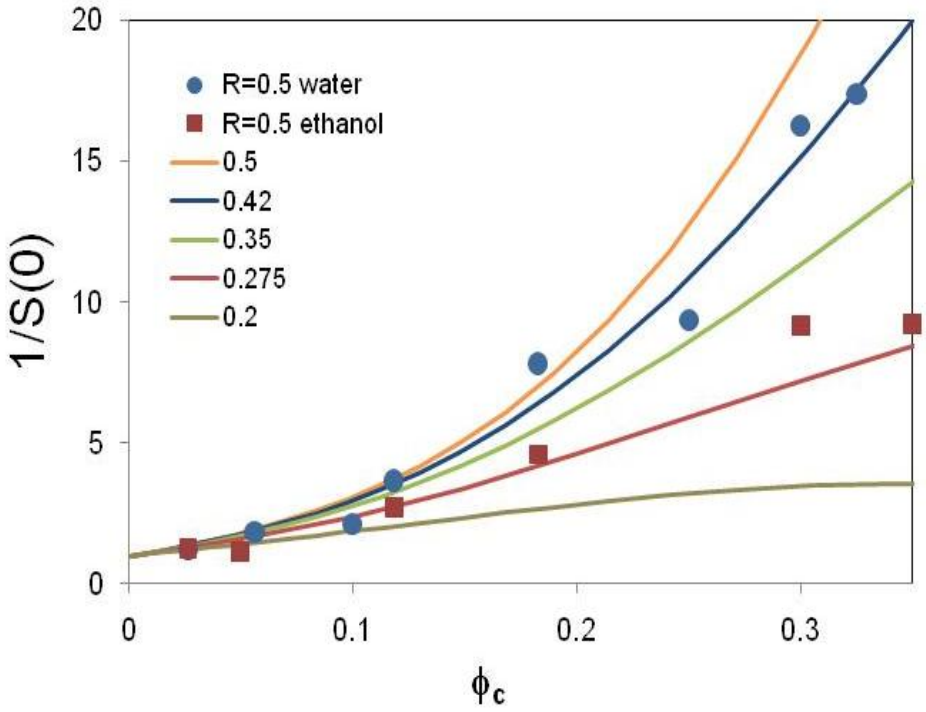

(b)

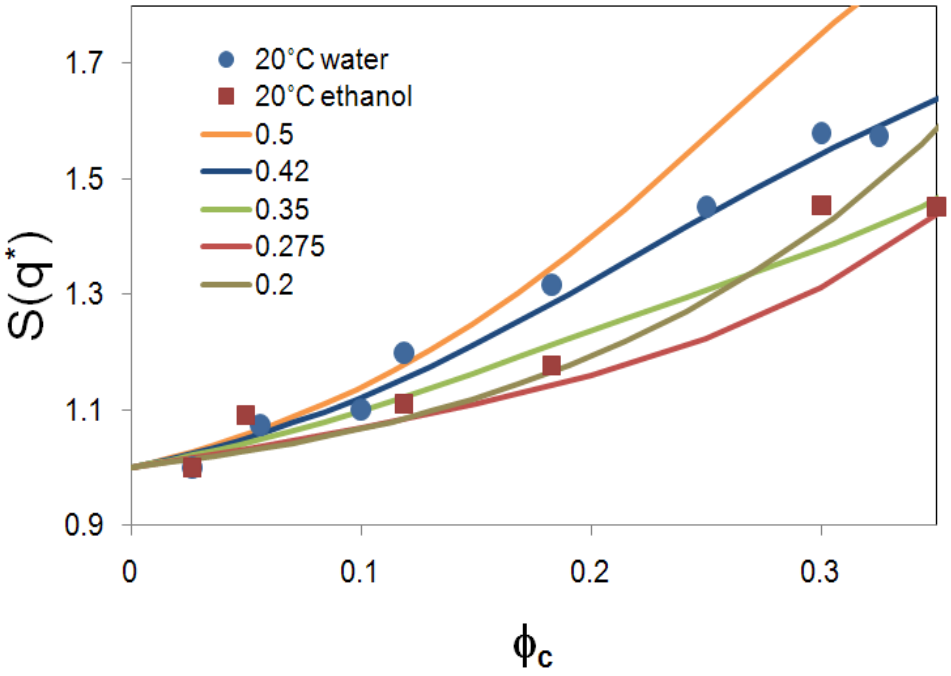

Figure 3.4 (cont. on next page)

(c)

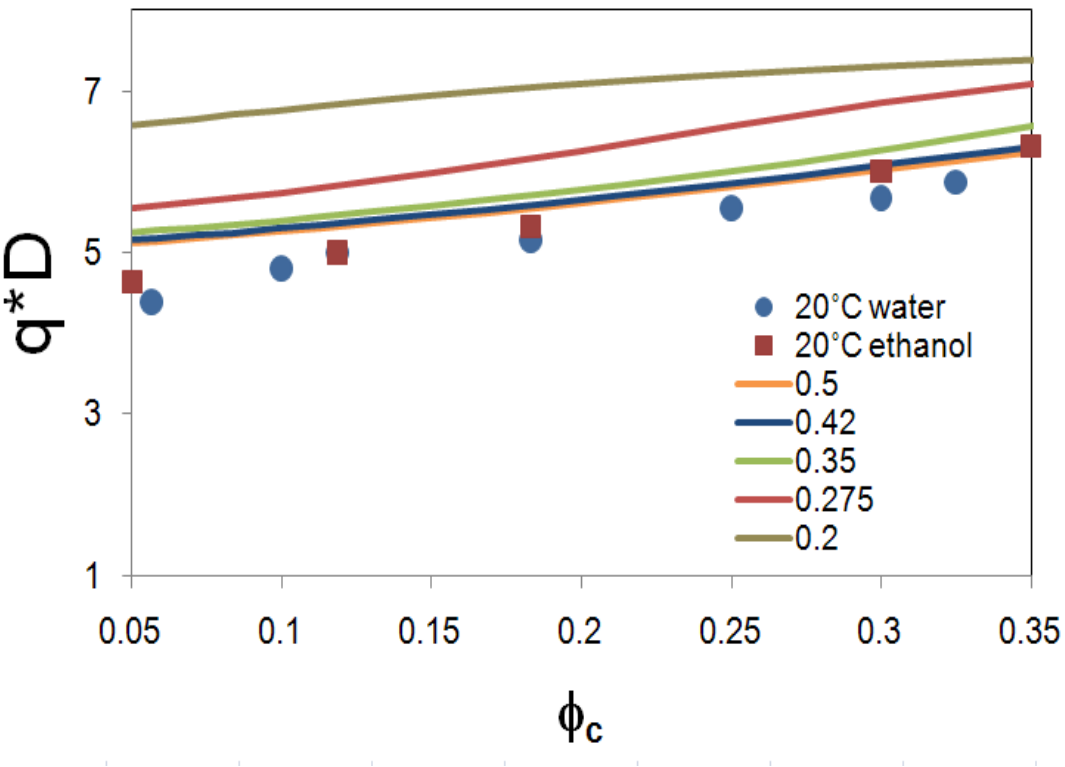

Figure 3.4 (a) Experimental inverse osmotic compressibilities ($1/S(0,\phi_c)$) as a function of particle volume fraction (ϕ_c) at a fixed R_{PEG}=0.5 in ethanol and water. (b) Experimental height of the cage peak of the particle structure factor ($S(q^*D,\phi_c)$) and (c) Experimental normalized wave vector at the cage peak of the particle structure factor. The corresponding PRISM predictions with varying ε_{pc} at a given R_{PEG}=0.5 are plotted with solid curves in (a) (b) and (c)

(a)

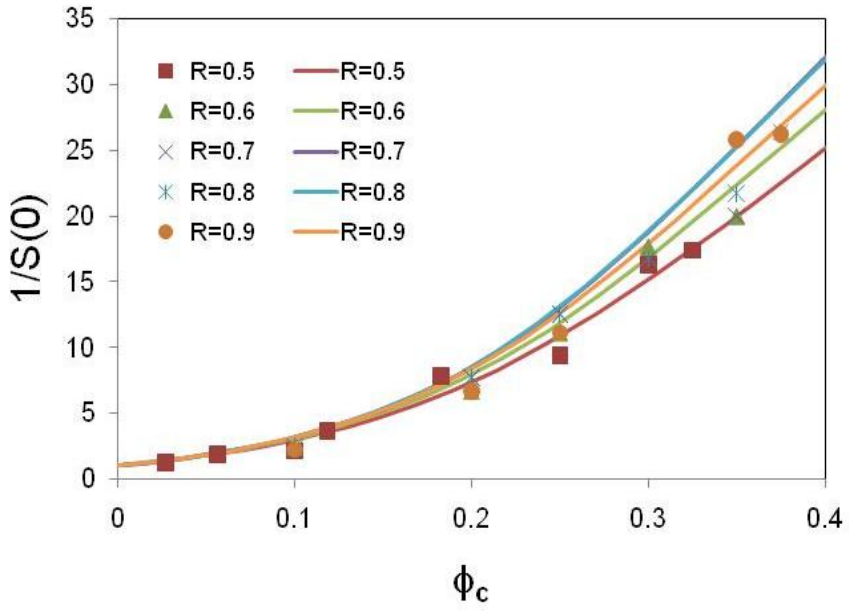

(b)

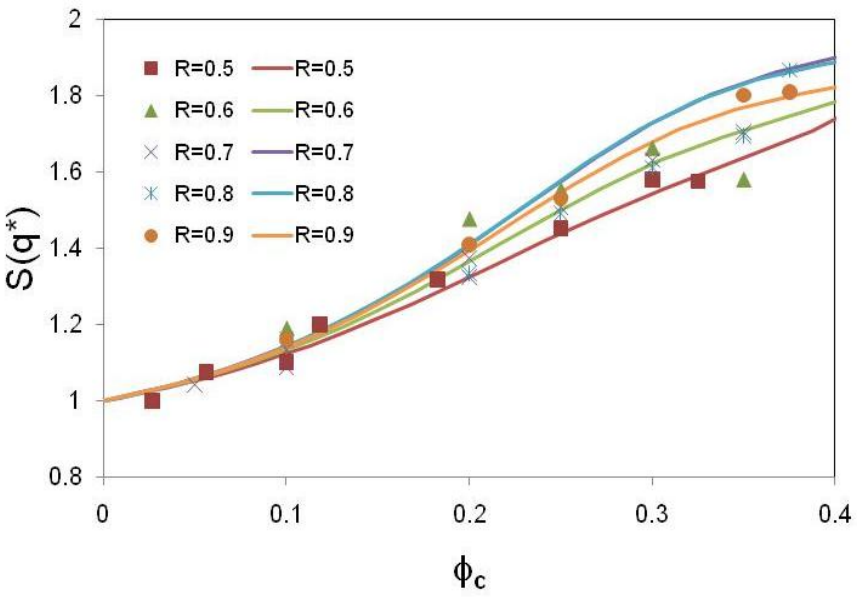

Figure 3.5 (a) Experimental inverse osmotic compressibilities ($1/S(0, \phi_c)$) as a function of particle volume fraction (ϕ_c) at various R_{PEG}. (b) Experimental height of the cage peak of the particle structure factor ($S(q^*D, \phi_c)$) as a function of particle volume fraction (ϕ_c) at various R_{PEG}. The corresponding PRISM predictions are plotted as solid curves in (a) and (b)

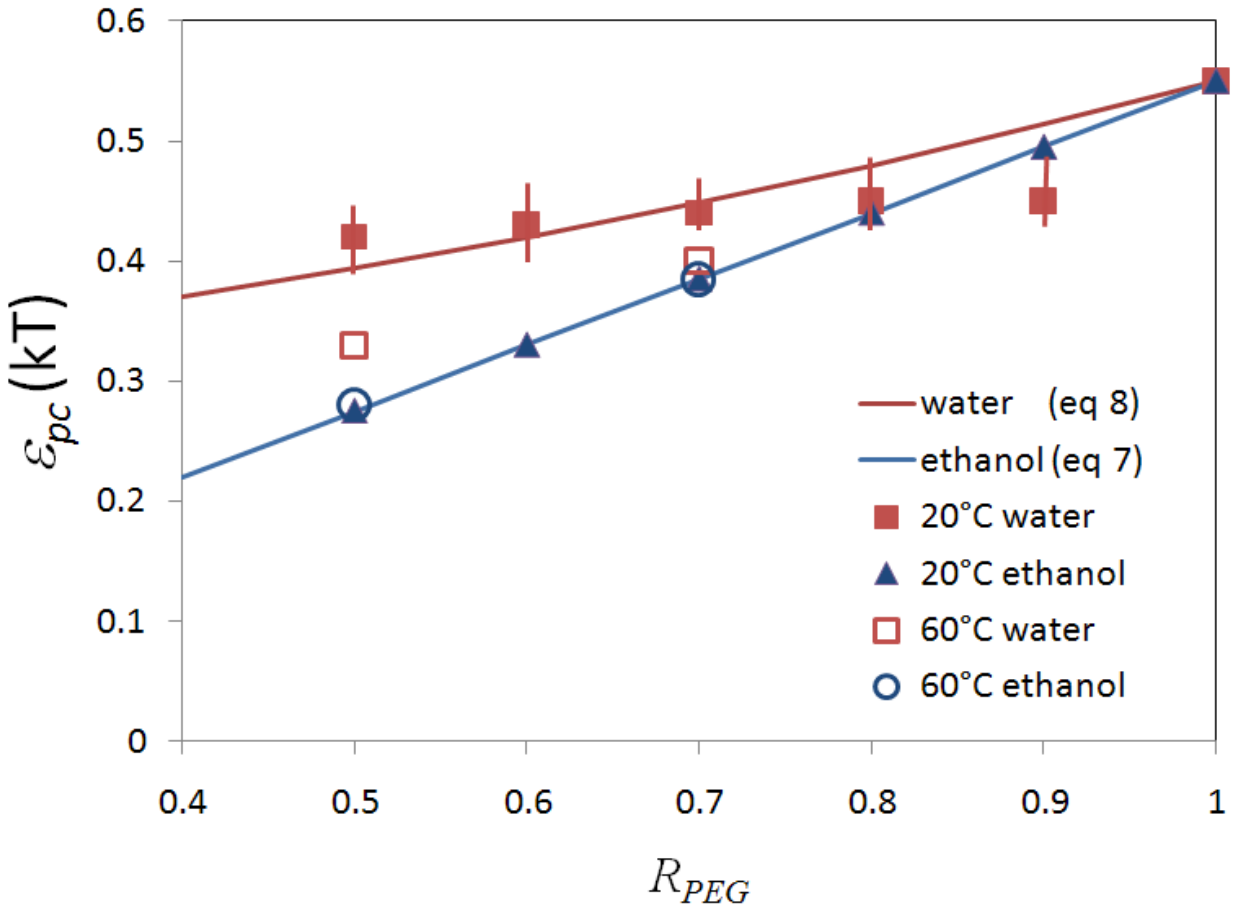

Figure 3.6 The strength of attraction between polymer segment and particle ε_{pc} as a function of polymer to solvent ratio (R_{PEG}) Experimental data from ethanol is double-confirmed from the present study and Ref. [11]. Experimental data at R_{PEG}=1 is provided from Ref. (3).

(a)

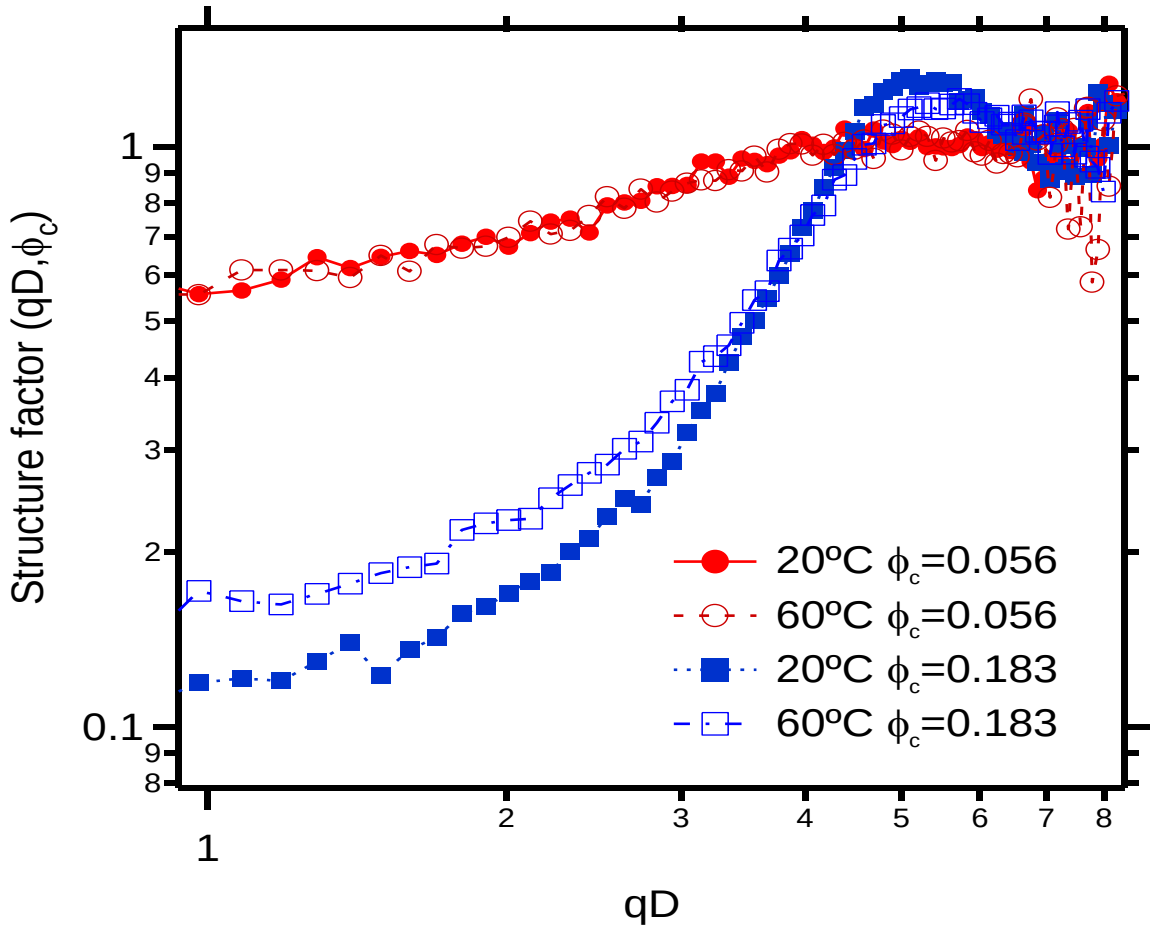

Figure 3.7 (cont. on next page)

(b)

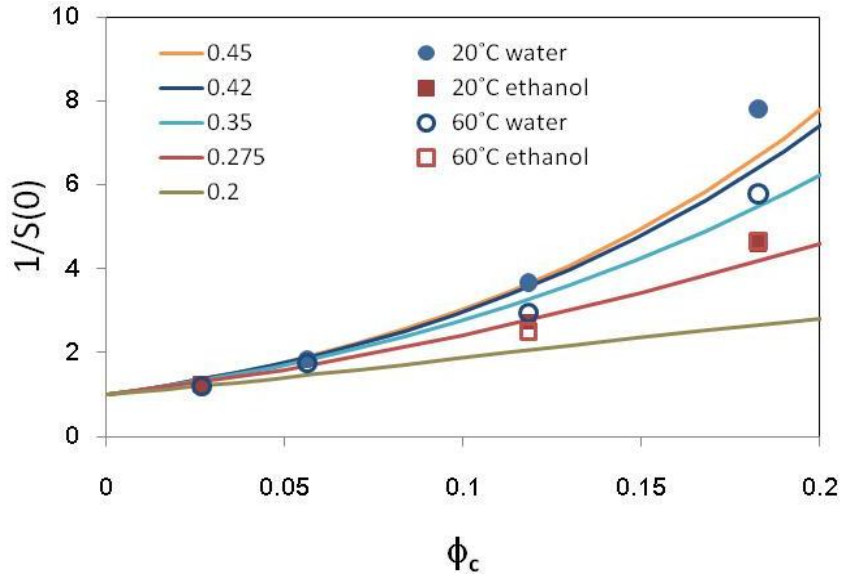

(c)

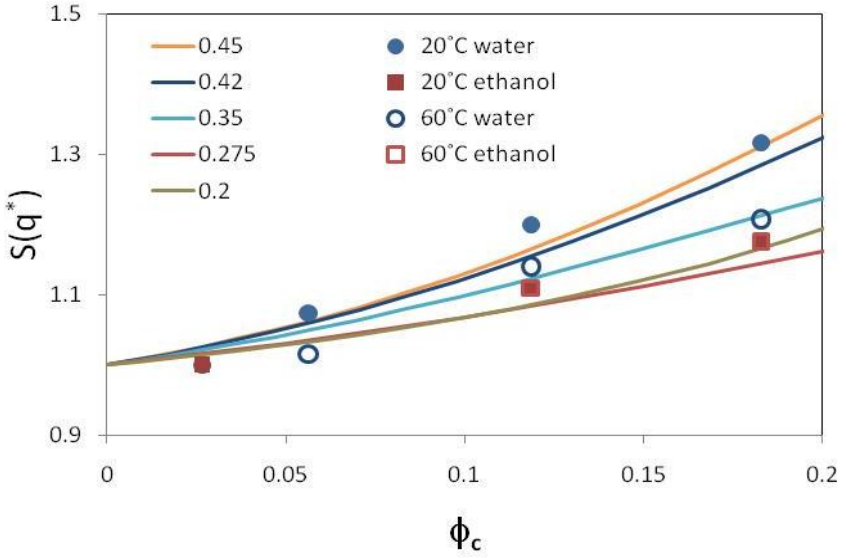

Figure 3.7 (a) Experimental particle structure factor versus wave vector at a fixed R_{PEG}=0.5 and ϕ_c=0.056 and ϕ_c=0.183 at different temperature (20°C and 60°C) in PEG-water mixtures (b) Experimental inverse osmotic compressibilities ($1/S(0,\phi_c)$) as a function of particle volume fraction (ϕ_c) at a fixed R_{PEG} at 20°C and 60°C (c) Experimental height of the cage peak of the particle structure factor ($S(q^*,\phi_c)$) as a function of particle volume fraction (ϕ_c) at a fixed R_{PEG} =0.5 at 20°C and 60° C.

3.7 References

1. Poon, W. C. K., *J. Phys-Condens. Mat*. **2002,** *14* (33).
2. Russel, W. B.; Saville, D. A.; Schowalter, W. R., *Colloidal Dispersions*. Cambridge University Press: Cambridge, UK, 1989.
3. Hall, L. M.; Anderson, B. J.; Zukoski, C. F.; Schweizer, K. S., *Macromolecules* **2009,** *42* (21), 8435-8442.
4. Hall, L. M.;Jayaraman, A.; Schweizer, K. S., *Curr. Opin. Solid St.M.* **2010,** *14* (2), 38-48.
5. Hall, L. M.; Schweizer, K. S., *J. Chem. Phys.* **2008,** *128* (23).
6. Hooper, J. B.; Schweizer, K. S., *Macromolecules* **2005,** *38* (21), 8858-8869.
7. Hooper, J. B.; Schweizer, K. S., *Macromolecules* **2006,** *39* (15), 5133-5142.
8. Hooper, J. B.; Schweizer, K. S., *Macromolecules* **2007,** *40* (19), 6998-7008.
9. Anderson, B. J.; Zukoski, C. F., *Macromolecules* **2007,** *40* (14), 5133-5140.
10. Anderson, B. J.; Zukoski, C. F., *Langmuir* **2010** *26* (11), 8709-8720.
11. Kim, S. Y.; Hall, L. M.; Schweizer, K. S.; Zukoski, C. F., *Macromolecules* **2010,** *43* (23), 10123-10131.
12. Stober, W.; Fink, A.; Bohn, E., *J. Colloid Interf. Sci.* **1968,** *26*, 62.
13. Mkhatresh, O. A.; Heatley, F., *Polymer International* **2004,** *53* (9), 1336-1342.
14. Kim, S. Y.; Zukoski, C. F., *Langmuir* **2011**, 27 (9) 5211-5221
15. Kline, S. R., *J. Appl. Cryst*. **2006,** *39* (6), 895.
16. Zimm, B. H., *J. Chem. Phys.* **1948,** (16), 62-69.
17. Mehrdad, A.; Akbarzadeh, R., *J. Chem. Eng. Data 55* (7), 2537-2541.
18. Briscoe, B.; Luckham, P.; Zhu, S., *J. Appl. Polym. Sci.* **1998,** *70* (3), 419-429.
19. Hammouda, B.; Ho, D. L., *J. Polym. Sci. Pol. Phys.* **2007,** *45* (16), 2196-2200.
20. Flory, P. J., *Statistical mechanics of Chain Molecules*. Interscience: New York, 1969.
21. Fredrickson, G. H., *The Equilibrium Theory of Inhomogeneous Polymer*. Oxford University press: New York, 2005.
22. Schweizer, K. S.; Curro, J. G., *Adv. Chem. Phys.* **1997,** *98*, 1-142.
23. Hooper, J. B.; Schweizer, K. S.; Desai, T. G.; Koshy, R.; Keblinski, P., *J. Chem. Phys.* **2004,** *121* (14), 6986-6997.
24. Biben, T.; Hansen, J. P., *Phys. Rev. Lett*. **1991,** *66* (17), 2215-2218.
25. Eskilsson, K.; Ninham, B. W.; Tiberg, F.; Yaminsky, V. V., *Langmuir* **1998,** *14* (25), 7287-7291.
26. Flood, C.; Cosgrove, T.; Espidel, Y.; Welfare, E.; Howell, I.; Revell, P., *Langmuir* **2008,** *24* (15), 7875-7880.
27. Cox, H. L.; Cretcher, L. H., *J. Am. Chem. Soc* **1926,** *48*, 451.
28. Malcolm, G. N.; Rowlinson, J. S., *Trans. Faraday Soc.* **1957,** *53*.
29. Saeki, S.; Kuwahara, N.; Nakata, M.; Kaneko, M., *Polymer* **1976,** *17* (8), 685-689.
30. Polik, W. F.; Burchard, W., *Macromolecules* **1983,** *16* (6), 978-982.

31. Kjellander, R.; Florin, E., *J. Chem. Soc. Farad. T. 1: Physical Chemistry in Condensed Phases* **1981,** *77* (9), 2053-2077.
32. Derkaoui, N.; Said, S.; Grohens, Y.; Olier, R.; Privat, M., *Langmuir* **2007,** *23* (12), 6631-6637.
33. Chatterjee, A. P.; Schweizer, K. S., *Macromolecules* **1999,** *32*, 923-934.
34. Tuinier, R.; Fleer, G. J., *Macromolecules* **2004,** *37* (23), 8764-8772.
35. Kulkarni, A. M.; Chatterjee, A. P.; Schweizer, K. S.; Zukoski, C. F., *Phys. Rev. Lett.* **1999,** *83* (22), 4554-4557.
36. Kulkarni, A. M.; Chatterjee, A. P.; Schweizer, K. S.; Zukoski, C. F., *J. Chem. Phys.* **2000,** *113* (21), 9863-9873.

CHAPTER 4 PARTICLE MICROSTRUCTURES AND FLOW PROPERTIES : EFFECT OF POLYMER TYPES[3]

4.1 Introduction

Polymer-colloid mixtures are used in a wide diversity of products including coatings and structural composites.[1, 2] As the particle size drops into the sub-100 nm size region, new features develop which are not explained by sum rules expected for simple composites. It is these optical, mechanical and electrical properties that drive interest in nanocomposites.[1, 3] Of particular interest here is how the strength of interaction of polymer segments with the particle surface (ε_{pc}) alters two features of nanocomposites: particle miscibility and energy dissipated per particle in shear flow.

When suspended in a fluid of viscosity (η_0) in the limit of low particle volume fraction (ϕ_c) the suspension viscosity (η) can be written:

$$\eta / \eta_0 = 1 + [\eta]\phi_c + h\phi_c^2. \qquad (4.1)$$

Standard models would suggest that when the strength of polymer segment-particle surface attraction, ε_{pc}, is large, the particle will acquire an adsorbed polymer layer, be stable from aggregation and have a hydrodynamic size larger than the core particle diameter (D). The increase in the particle's hydrodynamic size increases the suspension's intrinsic viscosity ($[\eta]$) and the Huggins coefficient (h) which characterizes the strength of pair interactions. On the other hand, we expect that if polymer segments adsorb weakly or not at all such that ε_{pc} is small,

[3] This work is reproduced from *Soft Matter* submitted. Unpublished work copyright © 2011 Royal Society of Chemistry.

depletion of polymer segments at the particle surfaces will lead to an attractive potential of mean force, again raising h but reducing $[\eta]$.[4-6]

The intrinsic viscosity of stable spherical particles in concentrated polymer solutions and polymer melts has been reported to vary from being large and positive to being large and negative. Following the standard models, large positive intrinsic viscosities are associated with layers of adsorbed polymer at the particle surface. Negative values are less well understood and are associated with i) particles whose diameter (D) is on the order of the size of the polymer radius of gyration (R_g),[7] ii) the polymer being above the entanglement molecular weight,[8] and iii) particle spacing being on the order of the polymer radius of gyration.[9-12] While negative values of $[\eta]$ are certainly eye catching and technologically important, surprisingly little work has been done investigating how intrinsic viscosities vary with chemical nature of polymers. The significance of such a study lies in the importance of processing the majority of nanocomposites where negative values of $[\eta]$ are not observed.

Considerable interest has developed recently in slip of fluids at solid interfaces.[13-19] Slip is considered to be a real or apparent violation of the commonly assumed condition that, at contact, the fluid and the solid have the same velocity. The degree of slip is quantified through a slip length, b, where the velocity of the fluid at contact can be written, $v_w = b dv_f/dr$ where v_w is the slip velocity at the surface, and dv_f/dr is the variation of the fluid velocity with distance normal to the wall evaluated at the wall. For b=0, there is no slip while b approaching infinity indicates perfect slip. Slip has been demonstrated for both low and high molecular liquids[8, 20] with values of b ranging from 0 to a hundred nanometers.[20] Simulation and experimental studies suggest that b increases with decreasing strength of association between the liquid and surface molecules.[18, 21, 22] Often the strength of association between the solvent and the surface is characterized in terms

of a contact angle at the gas-liquid-solid interface.[17, 20] The greater the contact angle, the greater the tendency of the liquid to slip. These studies tend to focus on flat surfaces.[22, 23]

In this study our interest lies in understanding the hydrodynamic boundary condition at the surface of nanoparticles suspended in dense polymer solutions and polymer melts to characterize the variations of intrinsic viscosity. For these systems we are unable to measure a contact angle and instead seek alternative methods for characterizing the strength of polymer segment- particle surface interaction, ε_{pc}.

First, we explore the conditions at the solid-fluid interface by measuring the intrinsic viscosity of particles suspended in dense polymer solutions and melts. Polymer chemistry is varied to investigate the effects of different strengths of cohesion. Then, small angle x-ray scattering (SAXS) is used to extract particle structure factors which are analyzed using the Polymer Reference Interaction Site Model (PRISM) of Schweizer and co-workers to characterize ε_{pc}.[4, 24-26]

The key parameter in PRISM theory controlling suspension microstructure and the state of particle dispersion is ε_{pc}. PRISM predicts that when ε_{pc} is small, the polymer is depleted near the particle surface resulting in a strongly attractive interparticle potential of mean force and immiscibility of the particles and polymer. For large ε_{pc}, PRISM predicts polymers adsorb strongly and bridge particles resulting in bridging aggregation. Only at intermediate ε_{pc} ($\sim 0.2 < \varepsilon_{pc}/kT < \sim 2$) are polymer layers formed that result in a homogeneous, thermodynamically stable phase. PRISM predictions have been extensively tested through comparisons with both polymer and particle structure factors measured with small angle scattering techniques.[25, 26] Connection is made between theory and experiment by choosing ε_{pc} to give the best agreement between predicted and measured particle structure factors. These studies demonstrate that ε_{pc} is weakly

dependent on volume fraction but is a function of polymer type, solvent type and, for some systems, polymer concentration.[24-26] We here exploit the sensitivity of suspension microstructure to polymer segment- particle surface interactions to determine ε_{pc}.

40 nm of silica particles are suspended in dense polymer-water mixtures choosing three different polymers with similar backbones but distinct chemical properties; hydroxyl terminated polyethylene glycol (PEG) with a molecular weight of 300 g/mol, methyl terminated polyethylene glycol dimethyl ether (PEGDME) with a molecular weight 250 g/mol and polytetrahydrofuran (PTHF) with a molecular weight of 250 g/mol. The intrinsic viscosities are measured at low particle volume fractions. Thus, the suspending phases are Newtonian and composed of small solvent molecules and oligomers with degrees of polymerization of 6 or less. As a result we characterize our systems using continuum models. Wang and Hill[27] recently developed a theory for intrinsic viscosities yielding super- and sub-Einstein intrinsic viscosities due to fluid layers at the particle surface that have different properties than the bulk. Thus, attention is paid to adsorbed layer thickness, its viscosity and if it slips at the particle surface.

Below in Section 4.2 we describe our experimental methods and theory while in Section 4.3 we describe the effect of polymer type on intrinsic viscosities. In Section 4.4 ε_{pc} is characterized through the comparisons of SAXS experiment to the PRISM theory. A direct link between intrinsic viscosities and ε_{pc} is made in Section 4.5. We summarize our results in Section 4.6.

4.2 Experiments and Theory Background

4.2.1 Sample Preparation

Silica nanoparticles were synthesized based on the method of Stöber *et al.*,[28] using the base-catalyzed hydrolysis and condensation of tetraethylorthosilicate (TEOS). The reaction temperature was 55°C. 3610 ml of ethanol was mixed with 96ml of deionized water, and 156ml of ammonium hydroxide was then added as a catalyst. The reaction was allowed to run for 4 hours. After mixing, 156ml of TEOS was added. Particle diameters (*D*) were determined based on SEM performed on 100 particles yielding a diameter of 40±5nm; alternatively, fitting of the single particle form factor determined by the angle dependence of x-ray scattering from a dilute suspension of particles yielded a diameter of 40±4nm.

PEG 300, PEGDME 250 and PTHF250 were purchased from Sigma-Aldrich. The effective diameter of a PEG segment (*d*) is ~ 0.6 nm. The nanoparticle size was chosen to minimize the size asymmetry ratio (*D/d*), but have a large enough particle such that small angle x-ray scattering can be used to probe both long wavelength and cage scale collective concentration fluctuations. These polymers have degrees of polymerization of 6, 5 and 4 respectively.

After particle synthesis, the alcosol (mixture of silica particles and ethanol) was concentrated approximately 10 times by heating in a ventilation hood. During this process, the excess of ammonium hydroxide was removed. For the preparation of polymer suspensions, the exact mass of each component (silica, polymer, water) was determined in order to create the desired particle and polymer concentrations. In this process, the initial volume fraction of particles is required. Particle volume fractions were calculated using the masses of each component and their densities. The silica particle density is 1.6g/cm^3.[29] The defined mass of

alcosol is then mixed with the defined mass of polymer. Samples were heated in a vacuum oven to drive off ethanol. The vacuum oven was purged several times with nitrogen followed by evacuation of the chamber to remove oxygen which degrades PEG at high temperature. Once the ethanol was evaporated, the necessary amount of water was added to the sample and fully mixed on the vortex mixer to produce the desired concentrations of particles and PEG 300, PEGDME 250 and PTHF250 are liquids at room temperature and miscible with water.

4.2.2 Polymer Concentration, R_p

Polymer concentration will be described in terms of the parameter 'R_p', defined as the ratio of the polymer volume to the volume of polymer plus volume of solvent. Nanoparticles in polymer melts were diluted with water. As an example of how to interpret Table 4.1, consider the case of superscript 'a' where R_p=0.5 with ϕ_c =0.301. For this condition, 30% of the total sample volume is occupied by the silica particles and the remaining 70% is polymer and water. Since the ratio of PEG to water volumes is fixed at 7:3, the volume fraction of polymer and solvent in the mixture is 0.49 (=0.7×0.7) and 0.21(=0.7×0.3), respectively. In the range of R_p where this study was performed no evidence of particle aggregation was observed.[26, 29]

4.2.3 Rheological Measurement

Rheological measurements were performed using a constant stress C-VOR Bohlin rheometer with cup and bob geometry. The bob is a made from roughened titanium with a diameter of 14mm, a gap size of 0.7 mm, and a sample volume of 3mL. Temperature was maintained at 20±1°C to be consistent with previous measurements on small angle x-ray

scatterings. Measurement time is less than 10 minutes from the lowest shear rate to the highest and evaporation during the measurement is minimized using the solvent trap. Data from the second measurement of viscosity confirms change of viscosity is negligible before and after the measurement.

4.2.4 Small Angle X-ray Scattering

Small-angle x-ray scattering (SAXS) experiments were conducted at the Sector 5 of the Advanced Photon Source (Argonne National Laboratory) to explore the microstructure of silica nanoparticles in polymer solutions, employing a sample-to-detector distance of 4.04 m and radiation wavelength $\lambda = 1.378$ Å. Scattered x-rays were recorded on a Mar CCD area detector. 2-D SAXS patterns were then azimuthally averaged and relative one dimensional scattering intensity was plotted as a function of scattering vector q, ($q=4\pi sin(\theta/2)/\lambda$) where θ is the scattering angle.

The measured scattering, after subtraction of the scattering of the corresponding polymer solution in absence of the particles, was considered to arise only from the silica nanoparticles thereby enabling use of the effective one-component model. The x-ray scattering intensity from a single component material was written as in Eq. (2.1).

Moderate nanoparticle polydispersity is taken into account using a Gaussian diameter distribution to calculate an average form factor.[29] Fitting the experimental form factor to the experimental data yields a standard deviation in size of $0.13\,\overline{D}$ where $\overline{D}$ is the average diameter.

As described in Section 2.2.3, collective nanoparticle structure factors were obtained by dividing the scattering intensity from the concentrated particle suspension by its dilute limit

analogue (*ds*) at the same polymer concentration in Eq. (2.4) Particle volume fractions from 0.087 to 0.446 have been studied at a fixed R_p (see Table 4.1).

4.2.5 PRISM Theory

PRISM theory has been extensively applied to polymer nanocomposite melts and concentrated polymer solutions.[4-6, 26] Recently PRISM was extended to account for the expected increase in total system packing fraction with the addition of hard nanoparticles to a polymer melt composed of monomers which can fill the interstitial space between the nanoparticles.[24] The model accounts for an excluded volume around each particle corresponding to a polymer segment radius while at larger segment-surface separations the polymer takes on its pure melt density.[24] Following our recent studies, we here explore extending this model to a three phase system. In the model, the solvent is treated implicitly by reducing the bulk polymer packing fraction and adjusting the polymer adsorption strength, roughly in the spirit of an effective mean field chi-parameter and effective (but compressible) 2-component mixture model.

The mixture model and PRISM theory employed here are identical to prior studies and well-summarized in Section 2.3.[4-6, 24, 25] The homopolymer is a freely jointed chain composed of N spherical sites (diameter *d*) with a bond length of *l/d*=4/3, nanoparticles are spheres of diameter *D*, and all species interact via pair decomposable hard core repulsions. The chemical nature of the polymer-particle mixtures enters via a two-parameter Yukawa interfacial attraction with contact attractive energy of ε_{pc} and decay length of the segment-colloid interaction of αd. In the context used here, PRISM theory consists of three coupled nonlinear integral equations for the site-site intermolecular pair correlation functions, $g_{ij}(r)$, where i and j refer to the polymer monomer (p) or nanoparticle (c). The dimensionless partial structure factors, $S_{ij}(q)$, describe

collective concentration fluctuations on a length scale $2\pi/q$. The theory uses the site-site Percus-Yevick closure for p-p and p-c correlations and the hypernetted chain approximation for c-c correlations.[5] Unless otherwise noted, N=100, D/d=10, and α=0.5, which are typical values for the current experimental studies. The interfacial cohesion strength, ε_{pc}, is varied to make contact with specific experimental systems explained below. Details of the theory are summarized in references.[4, 24, 25]

The final input to the theory is the monomer and particle packing (volume) fractions: $\phi_p \equiv \pi\rho_p d^3/6$ and $\phi_c \equiv \pi\rho_c D^3/6$, respectively, where ρ_j are the corresponding number densities. For simplicity, we treat the polymer solution as having a volume fraction of ϕ_{p0} set by R_p.[25] In the melt $\phi_{p0,m}$=0.4 as this yields a realistic dimensionless isothermal compressibility $S_{pp}(\phi_c=0, q=0) \sim 0.2$. In the presence of particles, total particle volume fraction (ϕ_t), (colloid plus polymer segments) is adjusted to account for the ability of polymer segments to pack in the interstices between particle segments.[24] Calculations based on this approach for particle-polymer mixtures have been shown to agree well with experimental scattering profiles over a wide range of particle volume fractions and under both weak and intermediate strengths of interfacial cohesion.[24-26]

Previous studies demonstrated that, PRISM captures the observed changes in the microstructure of nanocomposites melts as polymer chemistry is altered. For example, PTHF 1000 segments were shown to bind with a lower interfacial strength ($\varepsilon_{pc,m}$ = 0.35kT) than PEG 1000 ($\varepsilon_{pc,m}$ = 0.55kT).[24] In the following, all values of ε_{pc} are given in units of kT for a convenience. In the case of a mixture of polymer and solvent, PRISM treats the solvent as implicit. As a result, the interfacial attraction strength ε_{pc} represents the overall enthalpic gain of transferring a monomer from the continuous suspending phase to the particle surface.[24] Thus,

one can observe variations of ε_{pc} with R_p. In the current study we extract ε_{pc} from a best agreement of the predicted and experimental structure factors for each polymer type system.

4.3 Intrinsic Viscosity

Due to the Newtonian behavior of low molecular weight of polymer melts and solutions and large size ratios of *D/d* (~50) of the systems studied here, we approximate the suspensions as consisting of particles in a viscous continuum. Under this assumption, at low volume fractions the low shear relative viscosity, $\eta_{r,0}$ of the mixtures is characterized by Eq. (4.1) $\eta_{r,0}=\eta/\eta_0=1+[\eta]\phi_c+h\phi_c^2$. The low shear relative viscosity is measured in the zero shear limits where $\eta_{r,o}=\lim_{Pe\to 0}\eta/\eta_0$. The Peclét number is defined as $Pe=3\pi\eta_0\dot{\gamma}D^3$ where $\dot{\gamma}$ is the shear rate. $[\eta]$ is also defined here as $[2.5k]$, where 2.5 is Einstein's coefficient[31] and k is a parameter that defines how polymer adsorption influences the particle intrinsic viscosity.

In Fig. 4.1a $\eta_{r,0}$ is fitted to Eq. (4.1) with a least-squares nonlinear regression method for $\phi_c<0.10$ yielding k and h for each polymer types at $R_p=0.7$. Summaries of k and h and their uncertainties are found in in Table 4.2 along with values reported earlier by Anderson *et al.*[32] for silica particles of similar size prepared by the same methods suspended in polymer melts ($R_p=1$). At a fixed $R_p=0.7$, k varies with polymer type. For PEG 300, k =1.4 suggesting the adsorption of polymer segments increases the effective hydrodynamic volume fraction of the particles. On the other hand, k is close to the unity, the Einstein value, for PTHF 250 while k drops below unity for the case of PEGDME 250.

As a comparison, for silica particles of similar size suspended in melts ($R_p=1$) of PEG 1000, PEG 2000, PEG 8000 and PEG 20000, k =1.34, 1.48, 1.94 and 2.69.[32, 33] Anderson showed

that the zero shear rate viscosities of silica particle, PEG nanocomposite melts collapsed to a single curve when plotted as a function of the hydrodynamic volume fraction (ϕ_η) defined as: $\phi_\eta = k\phi$ demonstrating that at low volume fractions for a wide range of PEG molecular weights $\eta_{0,r} = 1 + 2.5\phi_\eta + 6\phi_\eta^2$ as expected for hard spheres with an effective diameter of $Dk^{1/3}$.[32, 33] Anderson went further to show that k can be written $k = (1 + 2.9R_g/D)^3$ suggesting PEG segments adsorb to the particle surface to form layers of thickness $1.45R_g$.[32, 33] These results also are in agreement with studies of polymer melts confined between two surfaces and suggest that attractions between polymer segments and the surface result in an increase in the particle's hydrodynamic size due to the formation of an adsorbed polymer layer.[34]

Based on the Anderson's relation, k for silica particles in PEG 300 melt (R_p=1) is expected to be 1.11 whereas we find that at R_p=0.7, k=1.4±0.2 suggesting that when the nanocomposite melt is diluted with solvent, from a hydrodynamic perspective, the particles look effectively larger while h/k^2=11.63 suggesting stronger interactions than expected for particles with an effective diameter of $Dk^{1/3}$.

On the other hand, Anderson reports that when suspended in a melt (R_p =1) of PTHF1000 and 2000, k=0.81 with h=42 and k=0.8 with h=383, respectively.[32] However, when PTHF 250 is diluted to R_p =0.7, we observe k=1 with h~6 suggesting hard sphere behavior.

For PEGDME 1000 and 2000 nanocomposite melts (R_p =1), k=1.26 with h=38 and k=1.25 and h=37, respectively[32] However, in dense solution of PEGDME 250, as R_p increases from 0.45 to 0.8, k rises from ~0.2 to ~0.5 showing values much below the Einstein limit shown in Fig. 4.1b.

These results demonstrate that the intrinsic viscosity of the silica particles is a function of polymer type and dilution ratio even when the polymer is below the entanglement molecular

weight. At first glance, we would expect the no-slip boundary condition to hold for all systems such that k=1 ([η]=2.5). This expectation is further emphasized by the index matching of the polymer solutions with the particles dramatically reducing van der Waals attractions and so that the particles experience only volume exclusion intrinsic interactions. Clearly, our results are not consistent with this interpretation raising questions about perturbation of polymer segment density profiles near the particle surface and relaxation of the no-slip boundary condition.

4.3.1 Continuum Model for Intrinsic Viscosity

Recently Wang and Hill developed an expression for the intrinsic viscosity of spheres suspended in a Newtonian fluid of viscosity (η_0) and density (ρ_0) where the fluid adsorbs to the particle surface creating a layer with a viscosity (η_i) and density (ρ_i).[27] Their model assumes continuity of stress and mass transfer at a distance $r' = D/2+\delta$ from the particle center and allows for slip at $r' = D/2$. Under conditions where the solvent in the surface layer has the same density as that in the bulk, this model contains parameters characterizing polymer layer thickness (δ), the degree slip along the particle surface (k_s) and layer viscosity ratio (χ) defined as $\chi=\eta_i/\eta_0$. k_s is referred to as a reciprocal slipping length ($2D/b$). The final result yields an expression for [η] with these parameters. The exact equation is found in Ref. (27).

For χ=1, this expression yields [η] =1 (k =0.4) for perfect slip (k_s =0) while no slip condition of k_s =∞ yields gives Einstein's value [η]=2.5 (k =1). For χ >1, increasing the layer thickness δ/D increases the intrinsic viscosity. Negative intrinsic viscosities are observed when χ <1.

For the experimental systems studied here, we expect the layer thickness to be on the order of the polymer radius of gyration or smaller such that $2\delta/D$ <<1. Thus within the framework of the Wang and Hill continuum model, $[\eta]$ >2.5 (k>1) occurs with viscous layers and no-slip while $[\eta]$ <2.5 (k<1) occurs with reduced layer viscosity and slip.

Thus, following the framework, the super–Einstein intrinsic viscosity (k>1) of the silica-PEG 300 solutions can be understood as resulting increased viscosity in adsorbed polymer layers and no-boundary slip conditions. On the other hand, the sub-Einstein intrinsic viscosity (k<1) observed in the silica-PEGDME 250 solution system would result from slip effects on the particle surface.

To understand what conditions might hold at the particle surface, in the following sections we use a combination of SAXS determined microstructures and PRISM to extract the strength of particle segment-particle surface interaction and predictions of polymer segment density fluctuations at the particle surface.

4.4 Polymer Segment-Particle Surface Interaction

In this section, we examine particle microstructure and stability through measurement of particle structure factors and compare these with PRISM predictions. From the comparison of theoretical and experimental structure factors, we extract the strength of attractions between polymer segments and the particle surface, $\varepsilon_{pc.}$

4.4.1 Experimental Structure Factors

Nanoparticle structure factors were measured under the conditions summarized in Table 4.1. In this section we present representative data, and discuss the key trends. Detailed discussion of methods to extract structure factors from scattering measurements are given in Ref. (25).

Examples of particle structure factors as a function of normalized wave vector, qD are found in Fig. 4.2. All experimental structure factors are liquid-like in the sense of showing a plateau value at low qD with a wide angle, amorphous, fluid-like peak that grows in magnitude and moves to larger qD as volume fraction is raised. For all systems reported here, the silica particles show no signs of aggregation as would be indicated by upturns in $S(q)$ as $qD \rightarrow 0$.

Following the methods described above, scattering intensities are converted to structure factors. Typical data for PTHF R_P=0.45 at 20˚C at various particle volume fractions are shown in Fig. 4.2. Three monotonic trends with particle volume fraction emerge that are typical of all our data; (i) the low wave vector amplitude ($S(0, \phi_c)$) strongly decreases with increasing ϕ_c corresponding to the nanoparticle subsystem becoming less compressible as particle volume fraction is raised. (ii) The intensity of the first peak, $S(q^*)$, initially increases very weakly, and then grows rapidly as ϕ_c increases. This behavior is expected for stable dispersions as $S(q^*)$ is a measure of the coherence of the nearest neighbor cage which increases as particles become more crowded. (iii) The wide angle peak at $q=q^*$ shifts from $q^*D \sim 4$ to $q^*D \sim 6$ corresponding to a shorter length scale of local cage order. This trend follows from $2\pi/q^*D$ being a measure of the mean distance between a central particle and its first nearest neighbor shell.

The behavior shown in Figure 4.2 is typical of all polymer types studied. Analysis of the effects of polymer types will focus on how these three features systematically evolve as a function of particle volume fraction.

4.4.2 Effects of Polymer Dilution

Before exploring how polymer chemistry affects the particle structures we discuss the effect of polymer to solvent ratios on the particle microstructure. Previous studies indicate that microstructural changes observed upon dilution of polymer melt with a solvent are sensitive to solvent type and reflect complex competitive solvent-surface, segment-surface and solvent-segment interactions.[24-26] For instance, for particle dispersions in PEG-ethanol mixtures, the particles experience stronger repulsive potentials of mean force and are less compressible as R_p increases. On the other hand when silica particles are dispersed in PEG-water mixtures, there are small microstructural changes as R_p varies from 1 to 0.5, indicating that dilution of the polymer has a negligible effect on particle interactions.

Since water is chosen as a solvent in these studies, we anticipate that, at least for the PEG solutions, structure factors $S(q,\phi_c)$ will have a weak dependence on R_p. To confirm this hypothesis and to investigate the effect of R_p on the other polymers studied, as shown in Table 4.1, structure factors were measured with increasing R_p from 0.45 to 0.7 for each polymer type. Inverse osmotic compressibilities ($1/S(0, \phi_c)$) are shown as a function of particle volume fraction for each polymer in Fig. 4.3. For PEG, as expected, $1/S(0, \phi_c)$ is insensitive to dilution for R_p =0.45 to 0.7. The same behavior is observed for PTHF where changing R_p results in minor changes to $1/S(0, \phi_c)$. These observations indicate that the potential of mean force experienced by the particles is indifferent to R_p for PEG and PTHF-water mixtures. Due to the low values of $1/S(0, \phi_c)$ in the PEGDME systems it was difficult to assess the dependency of $1/S(0, \phi_c)$ on R_p. A detailed discussion of the PEGDME case is given later. Nevertheless, the data shown in Fig 4.3 indicate that while $1/S(0)$ is sensitive to volume fraction, long wave length density fluctuations are insensitive to R_p for all three polymers.

4.4.3 Influence of Changing Polymer Chemistry

To explore the effects of polymer chemistry on the particle microstructure we fix R_p. For the systems studied, the degree of polymerization is approximately constant so that we are able to focus on changes in structure due to changes in polymer chemistry and not polymer chain length.

Fig. 4.4a shows the inverse osmotic compressibility as a function of ϕ_c for three different polymer systems at R_p =0.7. The nanoparticle subsystem is the least compressible in the PEG solutions. The PEGDME samples show a weak maximum as ϕ_c increases while PTHF solutions are intermediate between those for PEG and PEGDME.

The coherence of the nearest neighbor cage, $S(q^*)$ in Fig. 4.4b shows the same trends seen in $1/S(0)$. Particles are most structured in PEG solutions providing further evidence for substantial repulsive potentials of mean force. There is less coherent packing of the first nearest neighbor cage in PTHF and the suspensions show very weak structuring in PEGDME.

At a qualitative level, changes in $1/S(0)$ and $S(q^*)$ follow trends set by the variations in intrinsic viscosities with polymer type. Super-Einstein intrinsic viscosities with PEG are linked to dispersions having the smallest compressibility and the greatest degree of structuring while sub-Einstein intrinsic viscosities with PEGDME are associated with larger compressibility and weak liquid-like ordering. To quantify these correlations, we use PRISM to estimate the strength of particle segment/particle surface interactions, ε_{pc}. Methods used to extract ε_{pc} were discussed in details in 4.2 and Ref. (25).

As introduced in Section 4.2 the key parameter controlling microstructure of suspensions in PRISM is the strength of attraction between the polymer segment and the particle surface, ε_{pc}. Shown in Figs 4.4a and b, are PRISM predictions with different values of ε_{pc}. In these three

component systems, ε_{pc} should be interpreted as an overall gain of enthalpic energy when a segment moves from the bulk to the surface and thus will depend on polymer-polymer, polymer-solvent, solvent-surface and solvent-solvent interactions.[25, 26]

In Fig. 4.4a and b PRISM predicts the inverse osmotic compressibility (*1/S(0)*) decreases and the coherence of the nearest neighbors ($S(q^*)$) is decreased when ε_{pc} is decreased from 0.55 to 0.25. These changes follow from the loss of absorbed segments as the affinity of the segments for the surface is reduced. The absorbed segments generate a repulsive potential of mean force such that the signatures of smaller ε_{pc} are larger long wave length particle density fluctuations and weaker coherence in the first shell of nearest neighbors. From Fig. 4.4a we conclude ε_{pc} is quantified as 0.55, 0.45 and 0.25 for the PEG, PTHF and PEGDME systems, respectively.

In polymer melts (R_p =1) with molecular weights of ~1000-2000, both of intrinsic viscosities and ε_{pc} were ranked as PEG > PEGDME > PTHF.[24, 32] However, in the presence of solvent (R_p=0.7) and lower molecular weights, we clearly observe that both rank as PEG > PTHF >> PEGDME. The overturned rank of state of particle dispersions emphasizes the relative effect of end functional groups as the degree of polymerization decreases.

Both PEG and PEGDME have the same ethylene ($-CH_2CH_2O-$) backbone while PTHF have a butylene ($-CH_2CH_2CH_2CH_2O-$) backbone. The PEG and PTHF used here are hydroxyl terminated and PEGDME is methyl terminated. For high molecular weight polymers where end effects are relatively small, we expect the overall physical properties to be dominated by the backbone chemistry. As a result we expect the strength of interactions with the surface to be ordered as PEG 1000> PEGDME 1000> PTHF 1000.

On the other hand, as the polymer molecular weight is decreased to 250-300 where degree of polymerization is only 5~6, the end group effects will increase significantly. Thus we

anticipate that with strongly hydrogen bonding end groups, PEG and PTHF will show the largest values of ε_{pc}, while the inability of the PEGDME chain ends to hydrogen bond will reduce the interfacial affinity of PEGDME to below that of PTHF. As a result, we suggest the ordering of the strength of interactions results from a growing importance of end group effects as polymer molecular weight decreases.

When suspended in PEGDME solutions, the particles show very weak structuring as volume fraction is raised. In the low volume fraction limit, the osmotic pressure of the particles can be written:

$$\lim_{q\to 0}\frac{1}{S(q,\phi_c)}=\frac{V_c}{kT}\frac{\partial\Pi}{\partial\phi_c}=1+2B_2\phi_c+O(\phi_c^{\,2}) \qquad (4.2)$$

where Π is the particle contribution to the suspension osmotic pressure, V_c is the volume of the particle and B_2 is second virial coefficient. The results in Fig. 4.4a suggest B_2 decreases from PEG to PTHF to PEGDME. If $d\Pi/d\phi_c$ drops to zero, the suspension is thermodynamically unstable and will phase separate.[4, 5] In developing phase diagrams for polymer-particle mixtures showing regions of particle aggregation and regions of homogeneous phases, Hall and Schweizer approximate the location of spinodal for this phase separation as occurring at $1+B_2\phi_c=0$. As a result, PRISM associates the extremely low $1/S(0)$ of PEGDME with the approach to a spinodal and that the onset of phase separation driven by weak affinity of segments for the particle surface. Within this approximation, PRISM predicts that the critical point occurs at ε_{pc} ~0.15. Although there are no sign of aggregation (i.e., we do not see large upturns of $S(q,\phi_c)$ as wave vector goes to zero or have visual evidence of macroscopic phase separation), the weak increases of $1/S(0)$ and $S(q^*)$ with ϕ_c for the PEGDME systems suggest marginal stability when ε_{pc}=0.25. In Fig. 4.5 we show the predicted phase diagrams over a range of volume fractions and ε_{pc}. These phase

boundaries were calculated for D/d=10, α=0.5 and R_p =0.7. Variations in these parameters do not greatly change the qualitative nature of the predicted phase boundaries.

4.4.4 Microstructure of Particles Suspended in PEGDME at R_p = 0.45

Particle dispersions show R_p independent structures in PEG-water or PTHF-water mixtures while we find different trends in PEGDME-water mixtures. For example, at a fixed ϕ_c, when R_p decreases from 0.7 to 0.45, repulsive potentials of mean force drop dramatically as indicated by a rise in $S(0)$ and a decrease in $S(q^*)$. (inset of Fig. 4.6a) Figure 4.6a shows the structure factor of R_p=0.45 PEGDME system with varying particle volume fraction. From 0.07 < ϕ_c < 0.17, $S(0)$ decreases following the general trend of liquid-like systems. However, an upturn at low qD appears at higher ϕ_c indicating the onset of attractions. PRISM predictions drawn in Fig. 4.6b reflects the experimental trend of $1/S(0)$ with ε_{pc} =0.15. One notes that the structural data is best captured with ε_{pc} of PEGDME lowered from 0.25 to 0.15 when is R_p decreased from 0.7 to 0.45. PRISM predicts that at ε_{pc} ~0.15 one enters a region of instability where phase separation is expected. Phase separation is driven by attractive potentials of mean force arising from depletion of polymer segments from the particle surface. The lack of observed macroscopic phase separation suggests the approximate methods used by Hall and Schweizer to locate the bimodal require fine tuning to generate greater predictive capability.[4] Nevertheless the qualitative and near quantitative ability to predict microstructure demonstrate clear trends. As nanocomposite melts of silica in PEGDME 250 are diluted with water at fixed ϕ_c, the systems approach a phase boundary and within the frame of PRISM, this is interpreted as resulting from a reduction in ε_{pc}.

In summarizing the findings of this section, we have shown that particle microstructure is sensitive to polymer chemistry and that these changes are captured by PRISM predictions with chemical system specific but volume fraction independent values of ε_{pc}. These results are emphasized by the ability of PRISM to capture microstructures as depletion attraction driven phase separation is approached. Values of ε_{pc} for each polymer type and dilution ratio are given in Table 4.2.

4.5 Linking Intrinsic Viscosities to Polymer Chemistry

By adding previously gathered data for silica particles of the same size suspended in PEG 1000 and PTHF 1000 melts where k and ε_{pc} were reported, we show the direct link between k and ε_{pc} in Fig. 4.7. Noting k and ε_{pc} are independently obtained, the correlation has a remarkably simple linear form as shown in Fig. 4.7. This correlation is expected to hold only for polymers of approximately the same molecular weight as Anderson has shown that k increases with polymer molecular weight for ε_{pc} =0.55.[33] Nevertheless, for the range of polymer molecular weights studied here, we conclude that as polymer segments bind less strongly to the particle surface, the intrinsic viscosity decreases such that for ε_{pc} <0.1, the intrinsic viscosity will be negative.

In our study, i) D/R_g ratios are always large, ii) polymers are always below the entanglement molecular weight and iii) particles are non-deformable. These are the common conditions yielding Einstein values of the intrinsic viscosity and are far from conditions where negative intrinsic viscosities have been reported. However, our results show systematic variation of intrinsic viscosities from super to more interestingly, sub-Einstein values by varying polymer properties.

The continuum model of Wang and Hill[27] introduced in 4.3 suggests the connection between these separate data sets can be interpreted as being associated with variable properties of a layer of polymer segments at particle surfaces. Super- Einstein intrinsic viscosities are associated with the layer having a higher viscosity than the bulk polymer while sub-Einstein viscosities are associated with the layer having a lower viscosity than the bulk or having the layer slip over the particle surface. Figure 4.8 shows pair correlation functions predicted by PRISM for particle-polymer segment (g_{pc}) density fluctuations as a function of surface-to-surface separation for various ε_{pc}. At high ε_{pc} where super-Einstein values are observed there is a clear indication of polymer segment adsorption with $g_{pc}(0)$ ~1.5 to 2. Polymer segment densities oscillate with a period of approximately a segment diameter settling to g_{pc}=1, the random value and where we expect the polymer to reach its bulk density. This happens at particle surface to segment surface separations of approximately 5 segment diameters. The degree of enhancement of probability of polymer segments being at the particle surface decreases with reduction in ε_{pc}. For ϕ_c=0.10, when ε_{pc} <0.35, polymer segments are depleted near the particle surface where coincidently we found marginally stable particle dispersions for PEGDME and intrinsic viscosities suggesting the existence of slip at the particle surface. Based on the continuum model of Wang and Hill and studies on the slip of small molecule fluids over surfaces,[27] we would expect lower polymer segment densities to reduce the viscosity of the fluid next to the surface or enhance the tendency of polymer segments to slip over the particle surface in shear flow.

Negative intrinsic viscosities have been reported in polymer nanocomposite melts. While it would be tempting to argue that our results suggest that negative intrinsic viscosities occur when ε_{pc}<0.15, we caution against this extrapolation. Experimentally negative intrinsic viscosities are associated with i) particles being smaller that the tube radius for the polymer (i.e.,

the diameter of the tube through which a polymer diffuses in an entangled polymer melt (~4nm for PEG)), ii) the polymer being above the entanglement molecular weight, and iii) the particle spacing being on the order of the polymer radius of gyration. Furthermore, negative intrinsic viscosities are associated with the particles altering polymer dynamics by releasing slip-links such that polymer segments have greater mobility. However, in our case, $k<1$ occurs for polymers that are below the entanglement molecular weight and with $D/R_g>>1$.

The second reason we do not extend our results to the case where negative intrinsic viscosities are observed is that for ε_{pc} smaller than ~0.15, particles will experience strong depletion attractions and phase separate. However, for the cases where negative intrinsic viscosities are observed, the particles are well dispersed.[7-9]

The upshot of this comparison is that we believe the physics underlying sub-Einstein intrinsic viscosities measured here is distinct from that which gives rise to negative intrinsic viscosities.

4.6 Summary

In this study we measured the intrinsic viscosity of spherical particles with intrinsically hard sphere interactions suspended in concentrated polymer solutions. Intrinsic viscosities are found to vary with polymer type and for PEGDME, with polymer concentration. In addition we used small angle scattering to measure the particle structure factor showing that particles with larger intrinsic viscosities show greater structure suggesting a strong correlation between the single particle properties of intrinsic viscosity with the pair correlations as determined with $S(q)$. Using PRISM and measured values of $S(q)$, we extracted the strength of the polymer segment-

particle surface attraction, ε_{pc} and show that there is a linear dependence of the intrinsic viscosity on ε_{pc}.

PRISM predicts particle structure factors and pair correlation functions. Detailed measurements of experimental structure factors show that these predictions are well captured by a polymer chemistry dependent but volume fraction independent value of ε_{pc}. With this knowledge we look at the pair correlation function between particles and polymer segments. As ε_{pc} decreases through a range of values necessary to fit the measured particle structure factors, polymer segments become increasingly weakly associated with the particle surface and, right at the edge of particle miscibility with the polymer solution, the segments are depleted from the particle surface.

From these observations we conclude that even under conditions where polymer segments are enriched at the particle surface, we still observe sub-Einstein intrinsic viscosities. These results suggest that within the context of continuum models, decrease in intrinsic viscosity as shrinking ε_{pc} is associated with a combination of slip and reduction of adsorbed polymer layer effective viscosity. We do not expect to observe negative intrinsic viscosities in equilibrium dispersions of nanoparticles with $D/R_g>>1$ and the polymer below the entanglement molecular weight because, at the required small values ε_{pc}, the particles will phase separate from the polymer melt or solution. For these reasons we suggest the chemical dependence of the intrinsic viscosity behavior observed here has a different physical origin than the negative intrinsic viscosities observed with particles an order of magnitude smaller dispersed in entangled polymers.

4.7 Tables and Figures

Experiment	R_P	Polymer	Particle volume fractions (ϕ_c)					
Intrinsic viscosity	0.7	PEG	Various dilute ϕ_c (0.00~0.10)					
	0.45, 0.6, 0.7, 0.8	PEGDME	Various dilute ϕ_c (0.00~0.10)					
	0.7	PTHF	Various dilute ϕ_c (0.00~0.10)					
SAXS	0.45	PEG	0.087	0.120	0.181	0.238	0.294	0.349
		PEGDME	0.075	0.112	0.147	0.168	0.199	0.245
		PTHF	0.097	0.167	0.230	0.260	0.321	0.393
	0.7	PEG	0.090	0.128	0.171	0.205	0.353	0.398
		PEGDME	0.110	0.141	0.231	0.264	0.295	0.308
		PTHF	0.115	0.143	0.207	0.301[a]	0.411	0.446

a : noted as an example above

Table 4.1 Sample descriptions used for each experiment

Polymer	R_p	k	h	ε_{pc}
PEG 300	0.7	1.4±0.19	22.8±7	0.55
PTHF 250	0.7	1.0±0.2	7.2±7	0.45
PEGDME 250	0.45	0.23±0.08	17±3	0.15
PEGDME 250	0.6	0.44±0.07	18±2	
PEGDME 250	0.7	0.53±0.06	18±2	0.25
PEGDME 250	0.8	0.49±0.05	23±2	
PEG 1000	1	1.34±0.05[b]	10.1±1.3	0.55[c]
PEGDME 1000	1	1.26±0.07[b]	37±1	
PTHF 1000	1	0.81±0.03[b]	383±42	0.35[c]

b, c: data was obtained from Ref. (30) and (24), respectively.

Table 4.2 Calculated intrinsic viscosities and ε_{pc}

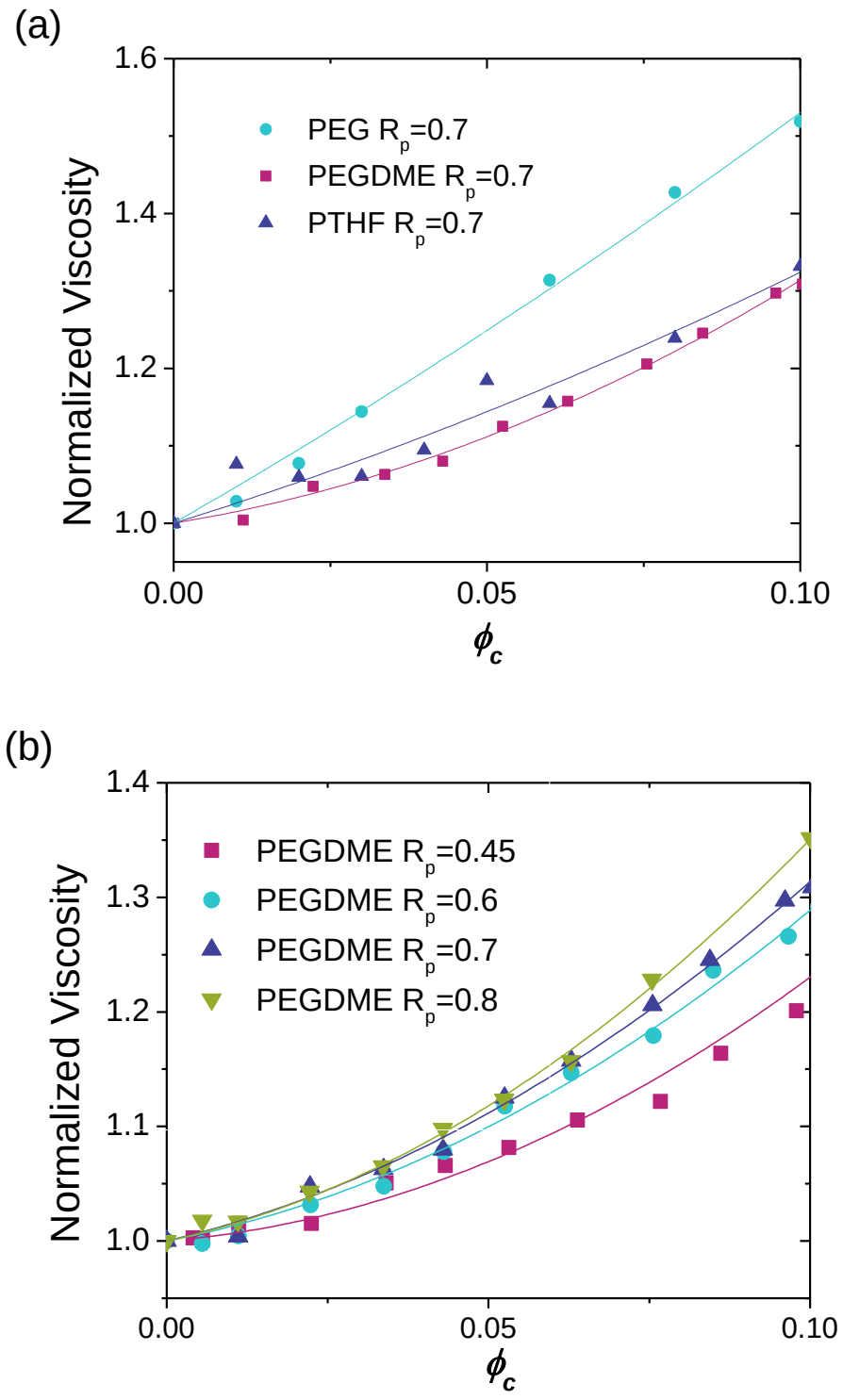

Figure 4.1 (a) Normalized viscosity as a function of ϕ_c at R_p=0.7 with PEG, PTHF and PEGDME (b) with PEGDME only but varying R_p from 0.45 to 0.8 as indicated in the legend. Fitted lines from of Eq. (4.1) are drawn.

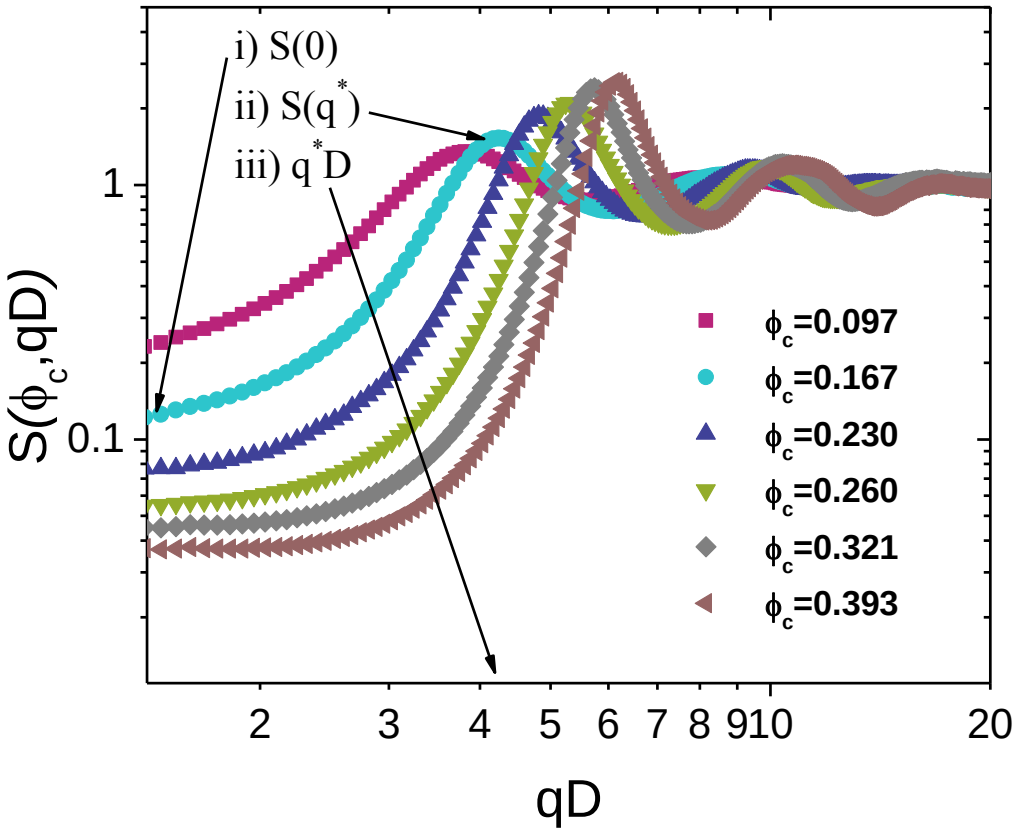

Figure 4.2 Experimental structure factor at R_p=0.45 with PTHF in water with increasing ϕ_c as indicated in the legend.

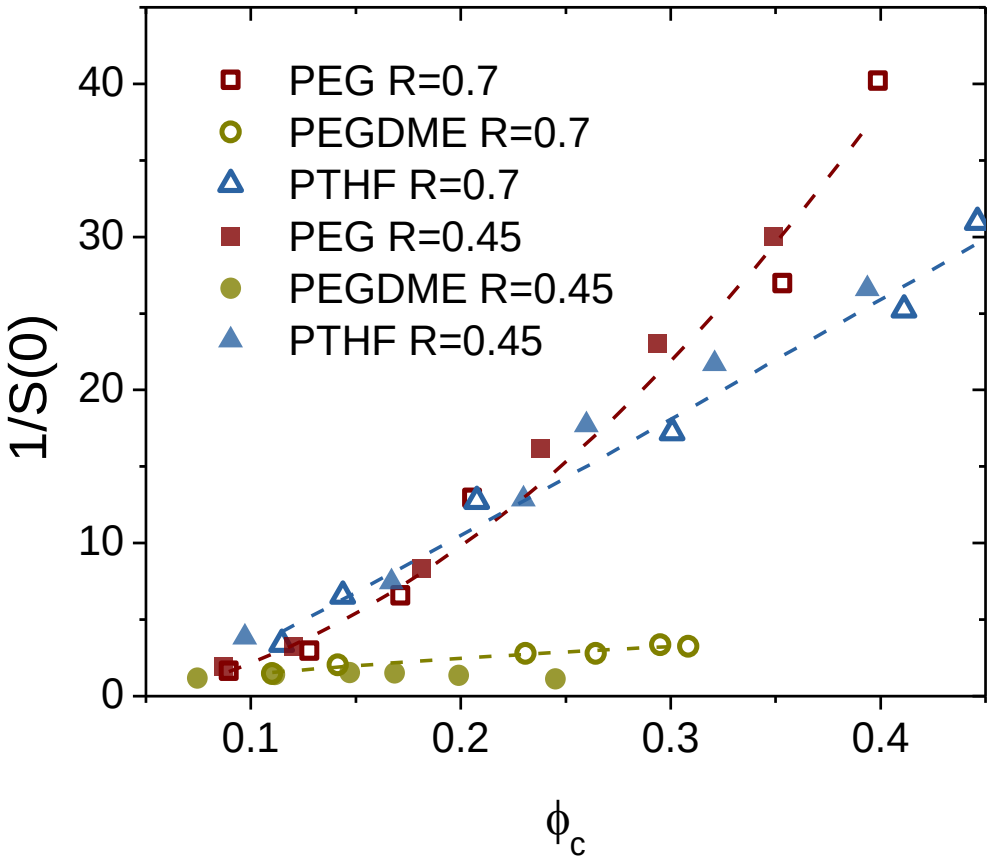

Figure 4.3 Experimental inverse osmotic compressibility *(1/S(0, ϕ_c))* as a function of ϕ_c with different polymers at R_p =0.7 and 0.45 as shown in the legend. *1/S(0)* is plotted by taking the value of *S(qD)* as *qD* goes to zero at each ϕ_c such as that from Fig. 4.2. Dash curves are drawn to guide eyes.

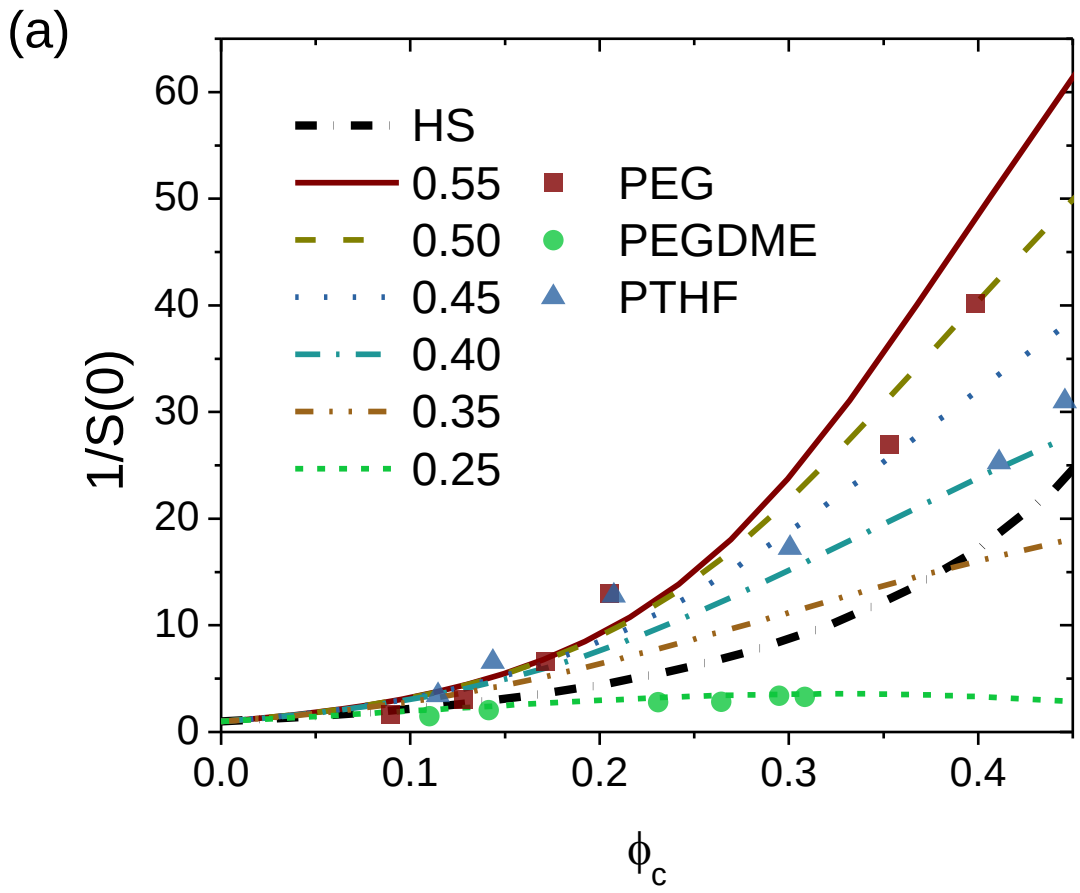

Figure 4.4 (cont. on next page)

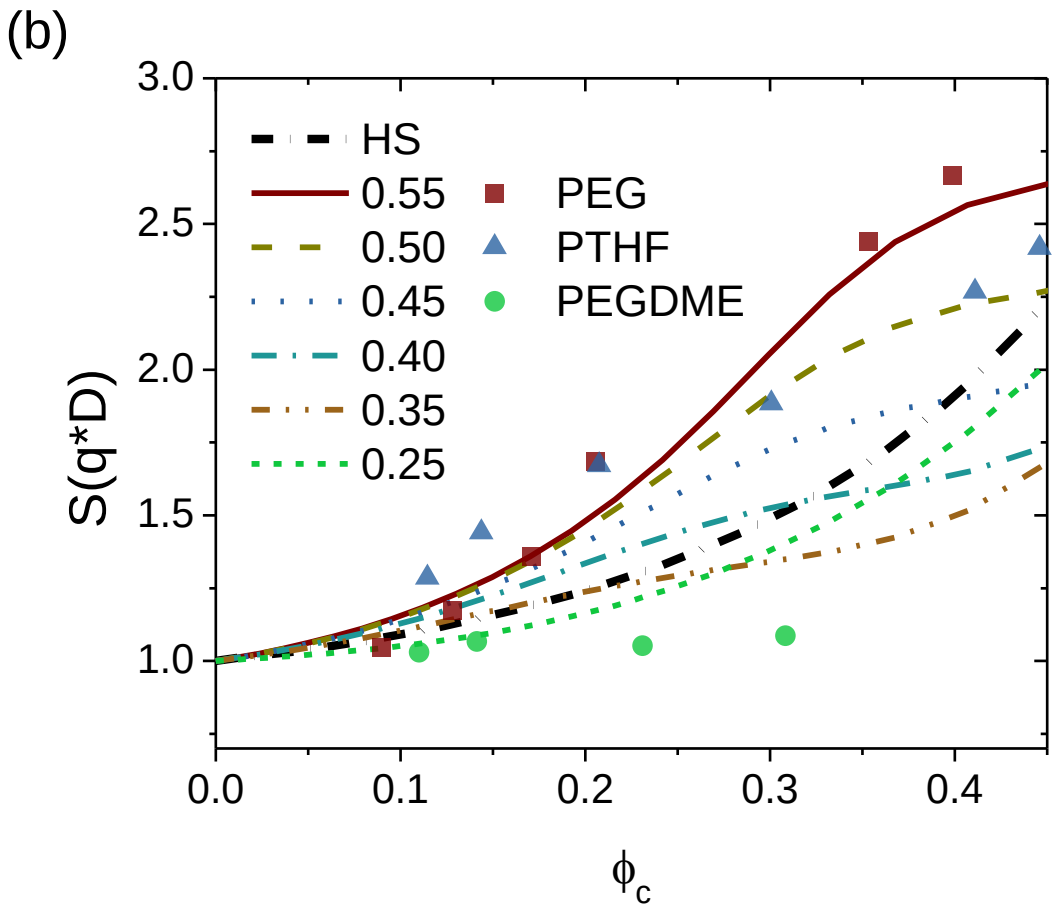

Figure 4.4 (a) Experimental inverse osmotic compressibilities ($1/S(0,\phi_c)$) as a function of particle volume fraction (ϕ_c) at a fixed R_P =0.7 (b) Height of the cage peak of the particle structure factor ($S(q^*,\phi_c)$) as a function of ϕ_c at a fixed R_P =0.7 The corresponding PRISM predictions with varying ε_{pc} at a given R_P=0.7 are plotted with curves in (a) and (b)

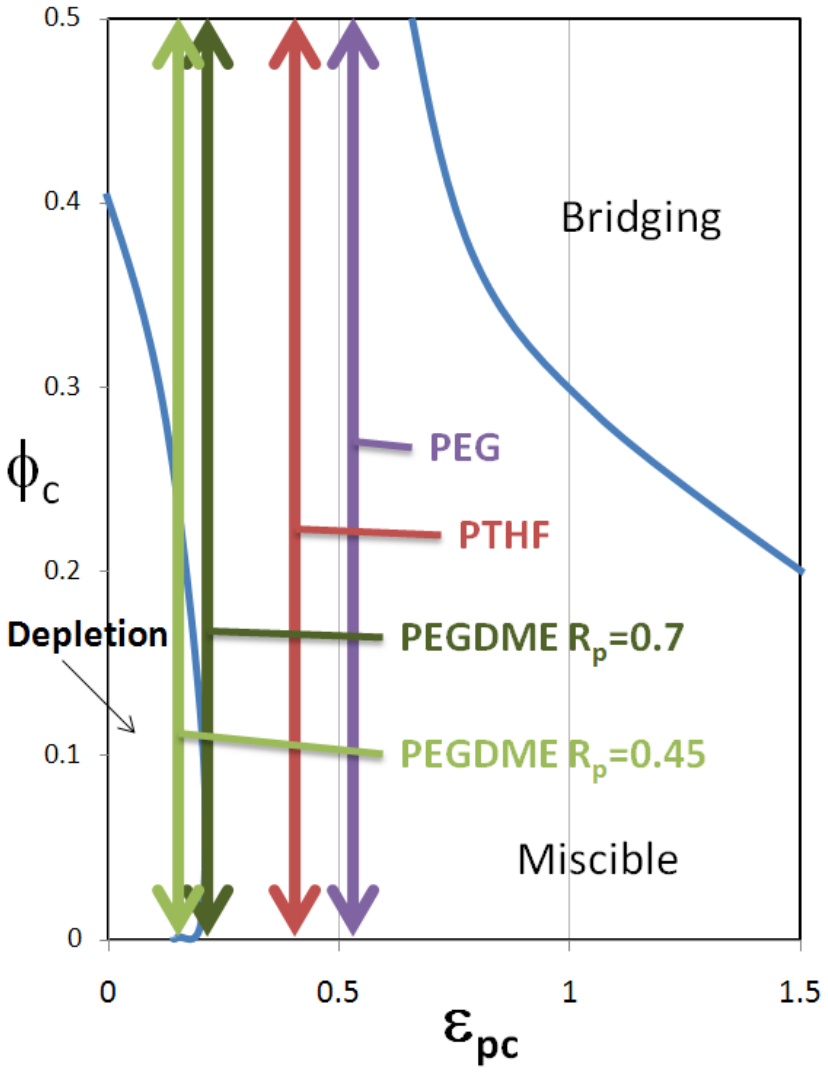

Figure 4.5 Predicted phase diagram at R_p=0.7 for PEG, PTHF and PEGDME

(a)

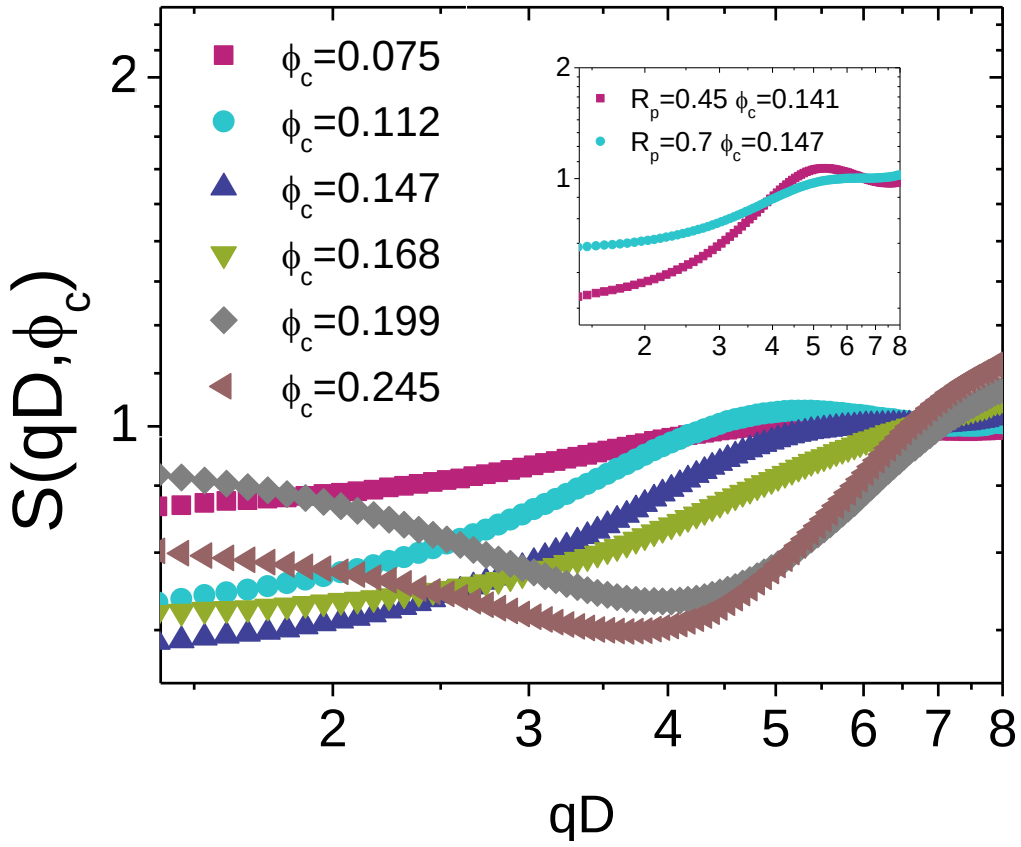

Figure 4.6 (cont. on next page)

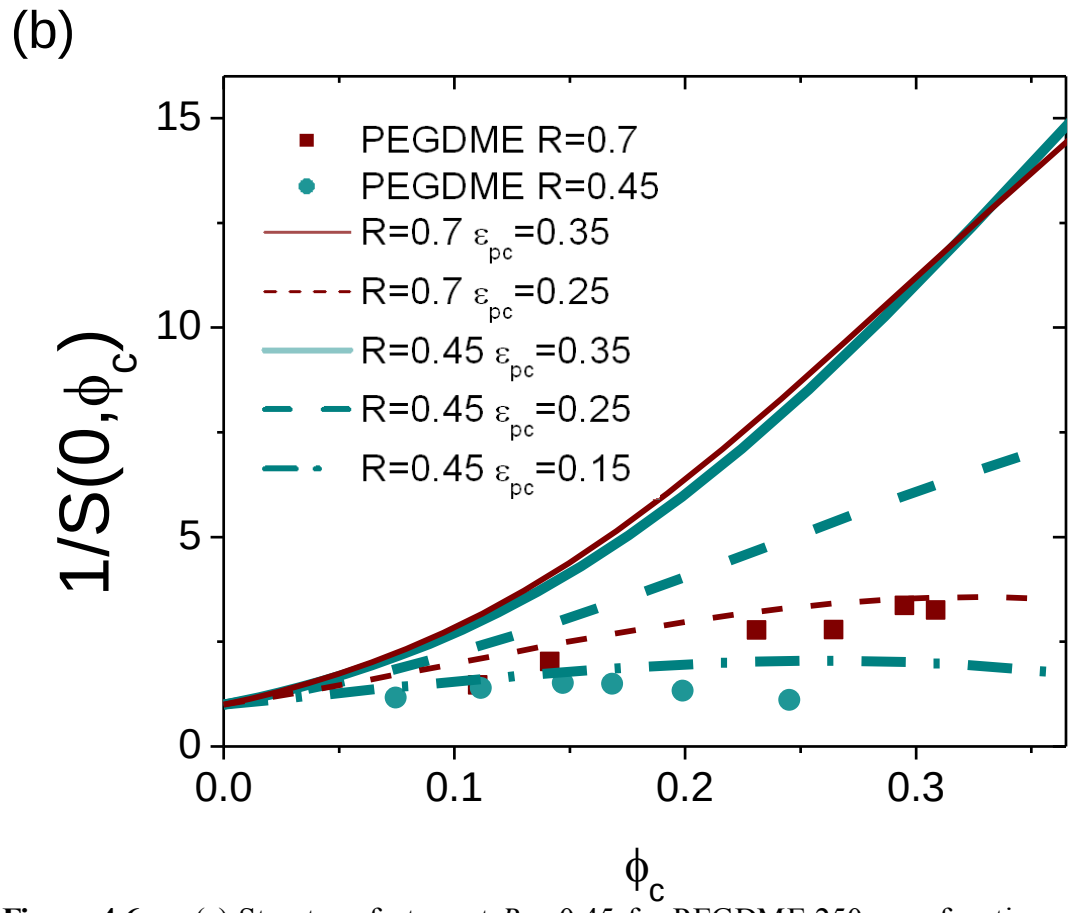

Figure 4.6 (a) Structure factors at R_p =0.45 for PEGDME 250 as a function of wave vector with increasing ϕ_c as shown in the legend. (inset) Comparable structure factors as a function of wave vector with ϕ_c=0.141 at R_p=0.7 and ϕ_c=0.147 at R_p =0.45 for PEGDME 250 (b) Inverse osmotic compressibility as a function of ϕ_c at R_p =0.7 and 0.45. The corresponding PRISM predictions with varying ε_{pc} at a given R_P=0.7 and 0. 45 are plotted with curves as indicated in the legend.

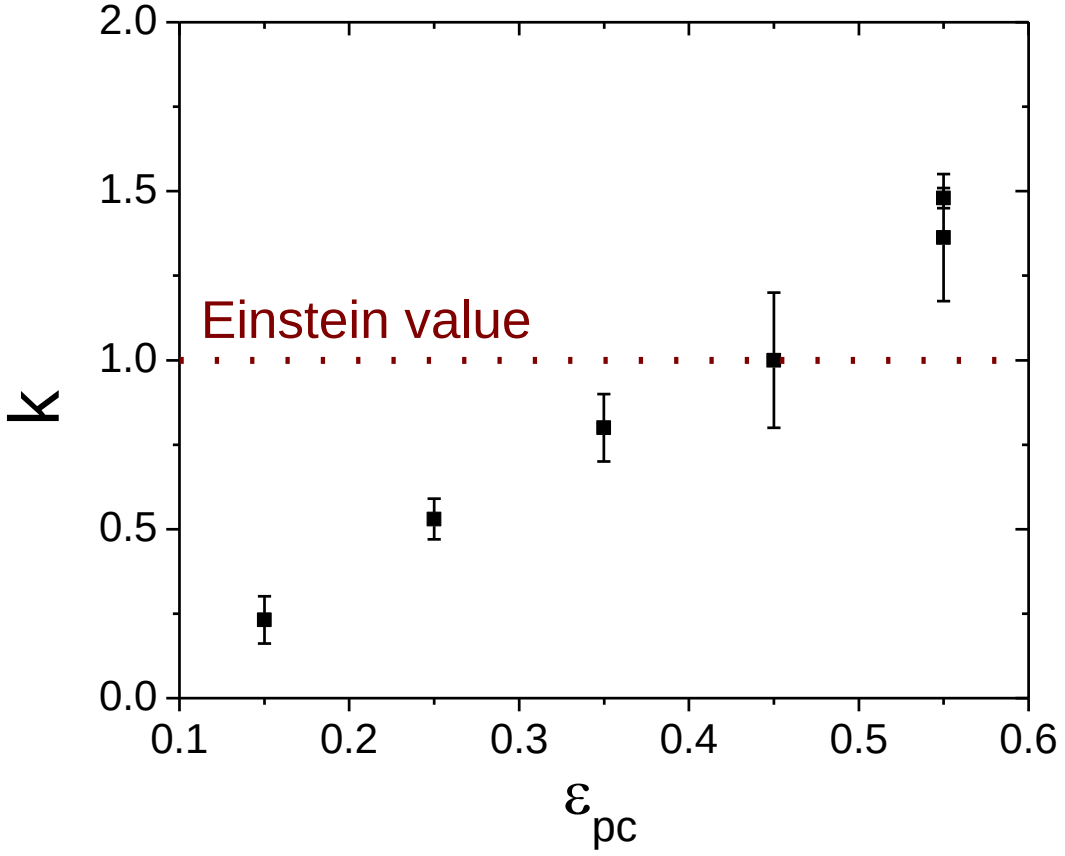

Figure 4.7 Intrinsic viscosity factor, k versus ε_{pc} based on Table 2.

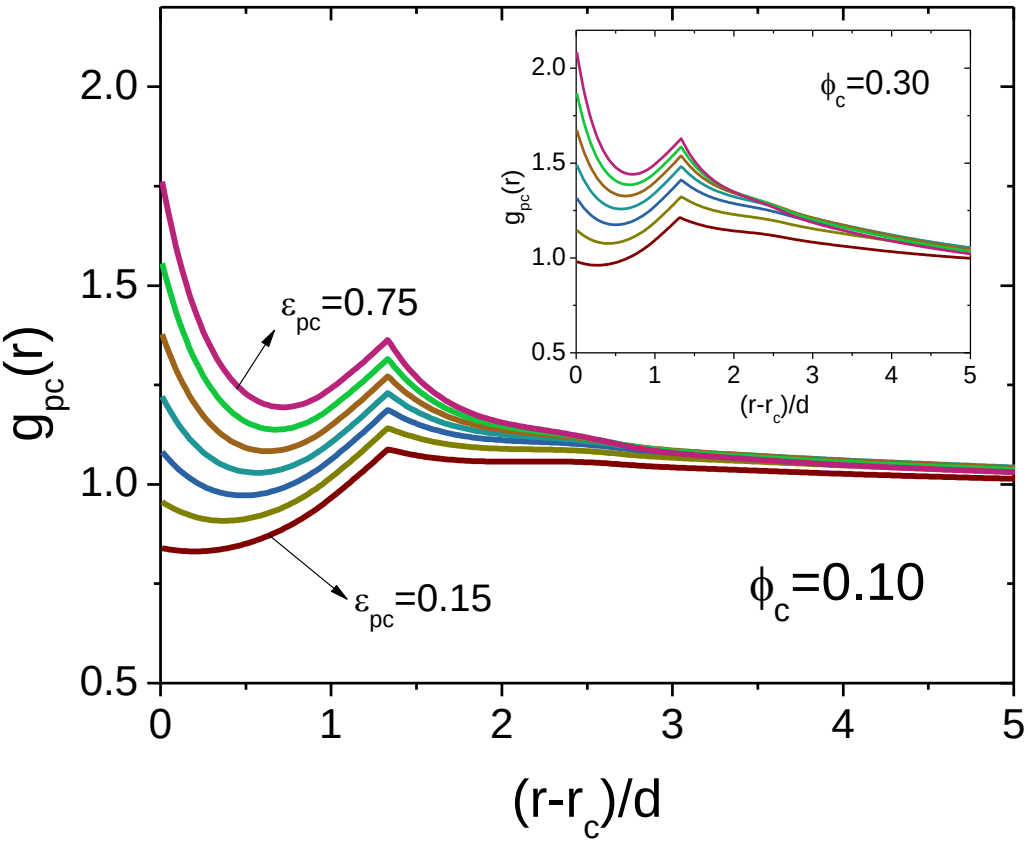

Figure 4.8 Particle-polymer monomer pair correlation function for various ε_{pc} at ϕ_c=0.1. (inset) at ϕ_c =0.3. ε_{pc} decreases from top (0.75 kT) to bottom (0.15 kT) by 0.1 kT. $r-r_c$ is the particle surface-to-polymer segment surface distance where r_c is defined as ½(D+d).

4.8 References

1. Ajayan, P. M.; Schadler, L. S.; Braun, P. V. *Nanocomposite Science and Technology*; Wiley-VCH: Weinheim, 2003.
2. Balazs, A. C.; Emrick, T.; Russell, T. P. *Science* **2006**, *314*, 1107.
3. Wang, M. J. *Rubber Chem. Technol.* **1998**, *71*, 520.
4. Hall, L. M.; Schweizer, K. S. *J. Chem. Phys.* **2008**, *128*, 234901.
5. Hooper, J. B.; Schweizer, K. S. *Macromolecules* **2005**, *38*, 8858.
6. Hooper, J. B.; Schweizer, K. S. *Macromolecules* **2006**, *39*, 5133.
7. Schmidt, R. G.; Gordon, G. V.; Dreiss, C. A.; Cosgrove, T.; Krukonis, V. J.; Williams, K.; Wetmore, P. M. *Macromolecules* **2010**, *43*, 10143.
8. Gordon, G. V.; Schmidt, R. G.; Quintero, M.; Benton, N. J.; Cosgrove, T.; Krukonis, V. J.; Williams, K.; Wetmore, P. M. *Macromolecules* **2010**, *43*, 10132.
9. Mackay, M. E.; Dao, T. T.; Tuteja, A.; Ho, D. L.; Van Horn, B.; Kim, H. C.; Hawker, C. J. *Nat. Mater.* **2003**, *2*, 762.
10. Ganesan, V.; Pryamitsyn, V.; Surve, M.; Narayanan, B. *J. Chem. Phys.* **2006**, *124*, 221102.
11. Tuteja, A.; Mackay, M. E.; Hawker, C. J.; Van Horn, B. *Macromolecules* **2005**, *38*, 8000.
12. Tuteja, A.; Mackay, M. E.; Narayanan, S.; Asokan, S.; Wong, M. S. *Nano Lett.* **2007**, *7*, 1276.
13. Barrat, J. L.; Bocquet, L. *Phys. Rev. Lett.* **1999**, *82*, 4671.
14. Joly, L.; Ybert, C.; Bocquet, L. *Phys. Rev. Lett.* **2006**, *96*, 046101.
15. Pahlavan, A. A.; Freund, J. B. *Phys. Rev. E. Stat. Nonlin. Soft Matter Phys.* **2011**, *83*, 021602.
16. Priezjev, N. V. *Phys. Rev. E* **2010**, *82*, 051603.
17. Schmatko, T.; Hervet, H.; Leger, L. *Phys. Rev. Lett.* **2005**, *94*, 244501.
18. Priezjev, N. V.; Troian, S. M. *Phys. Rev. Lett.* **2004**, *92*, 018302.
19. Zhu, L.; Attard, P.; Neto, C. *Langmuir* **2011**, *27*, 6701.
20. Baeumchen, O.; Jacobs, K. *Soft Matter* **2010**, *6*, 6028.
21. Hervet, H.; Leger, L. *C. R. Phys.* **2003**, *4*, 241.
22. Honig, C. D. F.; Ducker, W. A. *J. Phys. Chem. C* **2007**, *111*, 16300.
23. Niavarani, A.; Priezjev, N. V. *Phys. Rev. E. Stat. Nonlin. Soft Matter Phys.* **2008**, *77*, 041606.
24. Hall, L. M.; Anderson, B. J.; Zukoski, C. F.; Shweizer, K. S. *Macromolecules* **2009**, *42*, 8435.
25. Kim, S. Y.; Hall, L. M.; Schweizer, K. S.; Zukoski, C. F. *Macromolecules* **2010**, *43*, 10123.
26. Kim, S. Y.; Zukoski, C. F. *Langmuir* **2011**, *27*, 10455.
27. Wang, M.; Hill, R. J. *Soft Matter* **2009**, *5*, 3940.
28. Stober, W.; Fink, A.; Bohn, E. *J. Colloid Interf. Sci.* **1968**, *26*, 62.

29. Kim, S. Y.; Zukoski, C. F. *Langmuir* **2011**, *27*, 5211.
30. Anderson, B. J.; Zukoski, C. F. *Langmuir* **2010**, *26*, 8709.
31. Einstein, A. *Ann. Phys.* **1906**, *19*, 289.
32. Anderson, B. J.; Zukoski, C. F. *Macromolecules* **2008**, *41*, 9326.
33. Anderson, B. J.; Zukoski, C. F. *Macromolecules* **2009**, *42*, 8370.
34. Granick, S.; Hu, H. W. *Langmuir* **1994**, *10*, 3857.

CHAPTER 5 A UNIFIED APPROACH TO UNDERSTANDING MULTISCALE STRUCTURE, INTERFACIAL COHESION, ADSORBED LAYERS AND THERMODYNAMICS IN DENSE POLYMER-NANOPARTICLE MIXTURES[4]

5.1 Introduction

The aggregation of particles in concentrated polymer solutions, melts and crosslinked elastomers fundamentally alters the mechanical, optical and electrical properties of nanocomposites.[1-8] For example, in recent years, great strides have been made is reducing rolling resistance in truck tires by fully dispersing carbon black in the rubber matrix, resulting in substantial improvement in fuel consumption and energy efficiency tied directly to better particle dispersion.[9] Despite such advances in practical know-how, understanding the factors controlling the degree of nanoparticle dispersion in concentrated polymer liquids, and its connection to property optimization, has proven difficult.[10] Conceptual frameworks in both colloid and polymer science often rely on the existence of physically bound (adsorbed) polymer layers,[11,12] of equilibrium or non-equilibrium origin, to induce repulsive interparticle potentials-of-mean-force in order to achieve good dispersion.[13-15] Challenges to confirming these concepts in concentrated solutions and polymer nanocomposites lie in: (i) differentiating between polymer segments in the bulk and those adsorbed on the particle surface, (ii) in situ characterization of the material-specific strength of the polymer-particle interfacial attraction, and (iii) measuring the packing structure over a wide range of length scales of *both* the polymers and nanoparticles in the strongly interacting dense mixture.

[4] This work in part is reproduced from *Physical Review Letters* DOI 10.1103/PhysRevLett.107.225504. Copyright © 2011 American Physical Society.

To address these issues in a unified manner, we have employed carefully designed, thermodynamically stable (miscible) concentrated ternary solutions of polymers, nanoparticles, and solvent in conjunction with contrast matching small angle neutron scattering and the microscopic "Polymer Reference Interaction Site Model" (PRISM) statistical mechanical theory (Fig. 5.1). Use of a high polymer concentration (45%) ensures physical behavior representative of melts since the monomer collective density fluctuation correlation length is of order the segment size, a nanometer. In contrast to typical x-ray or neutron scattering experiments[7,16,17] which probe only the nanoparticle microstructure or its polymer analog, we are able to extract, for the first time, all three partial structure factors that quantify polymer-polymer, particle-particle, and interfacial polymer-particle concentration fluctuations.

Experimental knowledge of the full statistical microstructure affords us the unprecedented opportunity to make progress on the three key challenges described above. In this article, we address from a unified perspective four specific and inter-related issues: (1) Quantitatively test the ability of PRISM theory [18-20] to predict polymer nanocomposite structure, and demonstrate its remarkable accuracy for all spatial correlations. As a consequence, we firmly establish that by combining theory and experiment the effective monomer-particle attraction strength parameter can be uniquely and accurately determined. This has large implications since the interfacial attraction strength must be tightly controlled in order to avoid entropy (depletion) or enthalpy (bridging) driven clustering and macrophase separation.[18,21] (2) Definitively test the widely employed incompressible random phase approximation (IRPA)[22] that successfully relates the 3 partial structure factors in polymer blends and block copolymer materials and allows extraction of mixture thermodynamic information,[23,24] but is of unknown validity for strongly structurally asymmetric polymer-nanoparticle mixtures. (3) Deduce the in situ physical nature of

adsorbed polymer layers in dense nanocomposites. (4) Establish the theory as a design tool for manipulation of thermodynamic properties, specifically the nanocomposite bulk modulus, via rational variation of the polymer-nanoparticle interfacial attraction.

5.2 Experiments

5.2.1 Sample Preparation

Silica nanoparticles were synthesized based on the method of Stöber *et al.*[25], using the base-catalyzed hydrolysis and condensation of tetraethylorthosilicate (TEOS) yielding particles with diameters of 40±5nm as determined from both SEM micrographs and fitting the particle form factor determined by the angle dependence of neutron scattering from a dilute suspension. PEG 400 was purchased from Sigma-Aldrich, and pure ethanol was supplied from Decon Lab. Inc. After particle synthesis, the alcosol was concentrated approximately 10 times by heating in a ventilation hood. During this process, the excess ammonium hydroxide was removed. For the preparation of polymer suspensions, the exact mass of each component (silica, PEG 400, water) was determined in order to create the desired particle and polymer concentrations.

Particle volume fractions were calculated using the masses of each component and their densities. The silica particle density is 1.6 g/cm^3. In making the nanocomposite melts, a defined mass of alcosol is mixed with a defined mass of PEG 400. Samples were heated in a vacuum oven to drive off ethanol. The vacuum oven was purged several times with nitrogen followed by evacuation of the chamber to remove oxygen. Once the ethanol was evaporated, the necessary amount of D_2O and H_2O were added to the sample to produce the desired concentrations of particles and PEG. Index of refraction matching of silica in concentrated polymer solutions

minimizes van der Waals attractions producing hard sphere direct interactions between the particles.[26]

5.3 Small Angle Neutron Scattering

SANS experiments were performed on the NG7 30 m SANS instrument in NIST Center for Neutron Research, National Institute of Standards and Technology (NIST). Samples were loaded into 1mm path length demountable titanium cells. The cell temperature was maintained to 20±0.1 ˚C using the 10CB sample holder with a NESLAB circulating bath. A large range in scattering wave vector, q ($0.004A^{-1} \rightarrow 0.1A^{-1}$), was obtained by combining the sector-averaged scattering intensity from two different instrument configurations at 4 and 13.5 m detector distances. SANS data reduction of the scattering intensity, $I(q)$, was performed using the SANS data reduction program with IGOR Pro available from NIST.[27]

The intensity, $I(q)$, of scattered neutrons at wave vector q, has three contributions:

$$I(q) = n_c \Delta\rho_c^{\,2} P_c(q) S_{cc}(q,\phi_c) + 2\Delta\rho_c \Delta\rho_p \sqrt{n_c n_p P_c(q)} S_{cp}(q) + n_p \Delta\rho_p^{\,2} S_{pp}(q) \qquad (5.1)$$

where $n_j = \rho^*_j V_j^2$, and ρ^*_j and V_j are number density and unit volume of the jth component, respectively. $\Delta\rho_j$ is the difference of scattering length density of component j and the medium, $P_c(q)$ is the particle form factor, and $S_{ij}(q)$ are the structure factors associated with two components (pp, pc, cc) where the subscript p (c) indicates polymer segments (colloids). To extract partial collective structure factors, at each ϕ_c, $I(q)$ was measured at 4 ratios of deuterated water (D_2O) ratio to water (H_2O) corresponding to $\Delta\rho_p \sim 0$, $\Delta\rho_c \sim 0$ and two intermediate values close to $\Delta\rho_c = 0$.

5.3.1 Scattering Length Density Calculations

To achieve the contrast matching criteria, the scattering length density (SLD) of nanoparticles, polymer segments and solvent in highly concentrated polymer/particle solutions must be determined. While the cross sections of silica nanoparticles and PEG are fixed, the contrast relative to the background can be tuned by varying the D_2O:H_2O ratio in the solvent phase as shown in Fig. 5.2.

In concentrated polymer solutions, the solvent cross section reflects its composition and is written: $\rho_s = x_H\rho_H + x_D\rho_D + x_P\rho_p$, where ρ_H and ρ_D are the cross sections of H_2O and D_2O, respectively, while ρ_p is the polymer scattering cross section. Here, x_H, x_D and x_P represent the mass fractions of H_2O, D_2O and polymer in the continuous phase, respectively, such that $x_H+x_D+x_P=1$. We fixed $x_P=0.45$ ($R_{PEG}=0.45$) and varied $x_D/(x_H+x_D)$. Our initial studies established $\rho_c=3.85\times10^{-6}A^{-2}$, $\rho_p=6.60\times10^{-7}A^{-2}$, $\rho_H=-5.60\times10^{-7}A^{-2}$, $\rho_D=6.33\times10^{-6}A^{-2}$ such that the contrast match condition for silica is achieved at $x_D/(x_H+x_D)=1$ (labeled as condition 'D') and for PEG at $x_D/(x_H+x_D)=0.175$ (labeled as 'A'). Under condition D, the measured scattering will be dominated by scattering from the polymer where contributions from $S_{pp}(q)$ and $S_{pc}(q)$ will be present since $\Delta\rho_c \sim 0$ in Eq. (5.1).

5.3.2 Particle Form Factor

The particle form factor, P_c, was measured with silica particles at low $\phi_c=0.02$. When scattering is dominated by silica particles, Eq. (5.1) is simplified as $I(q) \sim P_c(q)S_{cc}(q,\phi_c)$. Since no interparticle interactions exist at low $\phi_c=0.02$, $S_{cc}(q)=1$. Therefore, one can measure the particle form factor from the scattering intensity and fit to the spherical particle (diameter, D) form factor equation:

$$P_c(q) = (3\frac{\sin(qD/2) - (qD/2)\cos(qD/2)}{(qD/2)^3})^2 \qquad (2.2)$$

. Moderate nanoparticle polydispersity was taken into account using a Gaussian diameter distribution to calculate an average form factor [26]. Fitting the experimental form factor to this equation yields a bare particle diameter of D=39.4 ±4 nm with a standard deviation in size of 0.12D, as shown in Fig. 5.8.

5.3.3 Determination of Partial Structure Factors: Methods and Example

Scattering measurements at a fixed ϕ_c were made at four D_2O/H_2O ratios corresponding to $\Delta\rho_p \sim 0$, $\Delta\rho_c \sim 0$ and two intermediate values close to $\Delta\rho_c$=0, from A, B, C to D in Figure 5.2. Incoherent background scattering is subtracted from the blank composed of PEG and D_2O/H_2O at each ratio. After the subtraction, we obtained Eq. (5.1).

Changes in the scattering profile with variations in x_H/x_D are shown in Fig. 5.3 for a silica volume fraction sample of ϕ_c=0.2 in a solution containing R_{PEG}=0.45 PEO 400 where only the D_2O/H_2O ratio is varied. At low D_2O concentrations (labeled as 'A'), the scattering is dominated by the particles, which is proportional to $P_c(q)S_{cc}(q)$. One sees the existence of a well-defined zero angle limit indicating a stable particle suspension, a first peak in $S_{cc}(q)$ associated with liquid-like particle packing, and decaying intensity as wave vector increases in $P_c(q)$ associated with the spherical particle diameter. As the D_2O concentration increases, substantial qualitative changes are observed in the scattering profile. At $x_D/(x_H+x_D)$ =0.90 (labeled as 'B'), the first peak in S_{cc} decreases as expected for decreasing $\Delta\rho_c$, while losing information about P_c at high q. At $x_D/(x_H+x_D)$=0.95 (labeled as 'C'), the first peak in S_{cc} is no longer observable, while the S_{pc} and S_{pp} contributions begin to dominant the measured scattering intensity as the condition $\Delta\rho_p >> \Delta\rho_c$

is approached. At $x_D/(x_H+x_D)$=1 (labeled as 'D'), scattering from the polymer dominates the signal. These results demonstrate that the contrast matching method in concentrated polymer solution is possible.

To extract each $S_{ij}(q)$ from Eq. (5.1), we first determine $\Delta\rho_c$ and $\Delta\rho_p$ from the known ρ_c and ρ_s at each D_2O/H_2O ratio using the information in Fig. 5.2. The quantities n_c and n_p are determined from the mass and size of the silica particles and polymers for each sample, respectively. At point 'A' in Fig. 5.3 where $\Delta\rho_p$=0, Eq. (5.1) is simplified as $I(q)=n_c\Delta\rho_c^2P_c(q)S_{cc}(q,\phi_c)$. $P_c(q)$ is experimentally determined as explained above. $S_{cc}(q)$ is obtained by dividing the scattering intensity from the concentrated particle suspension by its dilute limit analog at the same R_{PEG}: $S_{cc}(q,\phi_c)=\frac{I(q,\phi_c)}{I_{ds}(q,\phi_c)}\frac{\phi_{c,low}}{\phi_c}$. After the second step using the measurement 'A', only $S_{pp}(q)$ and $S_{pc}(q)$ remain unknown. At each scattering vector, one then has three experimental data points at points 'B', 'C' and 'D' and two unknowns allowing us to minimize uncertainty in the two unknowns at each q.

At point 'D' where $\Delta\rho_c$~0 there is still a small contribution from silica since it is difficult to perfectly match the scattering from a large porous particle. Thus, we account for the first term in Eq. (5.1) based on knowledge of n_c, P_c, S_{cc} and the changed $\Delta\rho_c$ determined at 'D'. Once all the known parameters are employed, Eq. (5.1) is simplified to $I_k(q)=a_k+b_kS_{pc}(q)+c_kS_{pp}(q)$ where a and b are q-dependent constants and c is a q-independent constant. Subscript k denotes the D_2O ratio such as B, C and D. These constants change with D_2O content in a known manner. With two unknowns and three equations, we solve $S_{pp}(q)$ and $S_{pc}(q)$ using multiple linear regression fitting method. For example, from initial intensity data in Fig. 5.3 at ϕ_c=0.2, Figs. 5.4 and 5.5

demonstrate that $S_{pp}(q)$ and $S_{pc}(q)$ can be extracted with *R*-square statistics of 0.993~0.999 over the range of *qD*.

5.3.4 Sphere and Core-shell Model Form Factors

The form factor for a polymer shell, $P_s^*(q)$, is obtained from the ratio S_{pp}/S_{cc} fitted to a core-shell model form factor using NCNR scattering fitting program[22,27]:

$$P_s^*(q) = \frac{C'}{V_{shell}}\left[\frac{3V_c(\rho_c - \rho_{shell})\, j_1(qr_c)}{qr_c} + \frac{3V_{shell}(\rho_{shell} - \rho_s)\, j_1(qr_{shell})}{qr_{shell}}\right]^2 \qquad (5.2)$$

where C' is a constant, $j_1(x) = (\sin x - x\cos x)/x^2$, $r_{shell} = r_c + t$, t is the layer thickness, r_c is the radius of particle, $V_i = (4\pi/3)r_i^3$, and ρ_{shell} is average value of exponential decay of scattering length density from particle surface to the end of adsorbed polymer layer. Particle polydispersity is taken into account, while the ratio r_c/r_{shell} is held constant also using the NCNR curve fitting program [27].

With the known r_c =19.7 (D = 39.4) nm from the particle form factor measurement, ρ_c, ρ_s and the calculated ρ_{shell}, an average layer thickness, t, is calculated from P_s fittings to the model at each ϕ_c. The average ρ_{shell} is determined considering adsorbed polymer layer profiles decaying exponentially. When ρ_c=3.85×10^{-6}A^{-2}, ρ_s=3.90×10^{-6}A^{-2} and ρ_{shell}=3.51×10^{-6}A^{-2} at the match point 'D' in Fig. 5.2, the fitting results indicate the thickness t decreases as 0.91, 0.87, 0.84 and 0.84 nm for ϕ_c =0.05, 0.1, 0.2 and 0.3, respectively. We note the value of ρ_{shell} can vary depending on the concentration of adsorbed polymer segments in direct contact with the surface. For example, if ρ_{shell} decreases to 3.34×10^{-6}A^{-2}, t decreases 0.71, 0.69, 0.66 and 0.60 nm at each ϕ_c. Despite some ambiguities concerning the determination of ρ_{shell}, the thickness of polymer layers remains in the range of 0.6 to 1.2 nm.

5.4 PRISM Theory

The theory used here is the same as in prior studies where all details are thoroughly documented.[18,20,28,29] The homopolymer is a freely jointed chain composed of N spherical sites (diameter d) with a bond (persistence) length of l/d=4/3, nanoparticles are spheres of diameter D, and all species interact via pair decomposable hard core repulsions. PRISM theory consists of three coupled nonlinear integral equations for the site-site intermolecular pair correlation functions, $g_{ij}(r)$, where i and j refer to the polymer monomer (p) or nanoparticle (c), from which dimensionless partial structure factors, $S_{ij}(q)$, can be computed. To link the elementary intermolecular site-site potentials and pair correlations functions, the site-site Percus-Yevick closure for p-p and p-c correlations and the hypernetted chain closure for c-c correlations are employed, in conjunction with the 3 coupled nonlinear PRISM integral equations which are then solved numerically. The use of the hypernetted closure is necessary for the large size asymmetry situation (D/d>>1) and is accurate based on comparisons with simulations. The number densities for polymer segments and particles are $\rho^*_p=\phi_p/(d^3\pi/6)$ and $\rho^*_c=\phi_c/(D^3\pi/6)$ where ϕ_p and ϕ_c are the polymer and particle volume fractions, respectively.

The chemical nature of the mixture enters solely via the two parameters of an attractive monomer-particle interfacial attraction: the strength at contact ε_{pc} and spatial range α (in units of the monomer diameter). Beyond the hard core distance of closest approach, the exponential interfacial potential is given.

$$U_{pc}(r) = -\varepsilon_{pc} \exp\left(\frac{-(r-(D+d)/2)}{\alpha d} \right) \qquad (2.9)$$

For the present comparisons N=100, D/d=10, and α=0.5d, which are typical values as motivated from previous studies. [28,29] In the presence of particles, total volume fraction (ϕ_t),

(colloid plus polymer segments) is adjusted[28,29] to account for the ability of polymer segments to pack in the interstices between particle segments.

Briefly, to link intermolecular potentials and direct pair correlations functions we employ the site-site Percus-Yevick closure for *p-p* and *p-c* correlations and the hypernetted chain closure for *c-c* correlations, in conjunction with the 3 coupled nonlinear PRISM integral equations which are then solved numerically. For the present comparisons N=100, D/d=10, and α=0.5, which are typical values as motivated from previous studies. In the presence of particles, total particle volume fraction (ϕ_t), (colloid plus polymer segments) is adjusted to account for the ability of polymer segments to pack in the interstices between particle segments.

5.5 Results and Discussion

As described in Section 5.2.1, the experimental system consists of silica nanoparticles of diameter D=40nm synthesized using the Stőber method[25] suspended in mixtures of poly(ethylene glycol) (PEG) 400, D_2O and H_2O. This system is chosen to allow an intermediate interfacial cohesion strength (and hence miscibility over a wide range of volume fractions) to be realized, and structure to be probed from the local "cage" scale that quantifies short range nanoparticle order to wavelengths larger than both polymers and nanoparticles. Polymer concentration is described by the ratio of polymer volume to polymer plus solvent volume, R_{PEG}, which is held constant at 0.45. Silica volume fraction (ϕ_c) is varied widely from 0.05 to 0.30. For this system there is no evidence of aggregation or phase separation.

Recall that the intensity, $I(q)$, of scattered neutrons at wave vector q, has three contributions:

$$I(q) = n_c \Delta\rho_c^2 P_c(q) S_{cc}(q,\phi_c) + 2\Delta\rho_c \Delta\rho_p \sqrt{n_c n_p P_c(q)} S_{cp}(q) + n_p \Delta\rho_p^2 S_{pp}(q) \quad (5.1)$$

where n_j is the number density of the jth component, $\Delta\rho_j$ is the difference of scattering length density of component j and the medium, $P_c(q)$ is the particle form factor, and $S_{ij}(q)$ are the structure factors associated with two components (pp, pc, cc) where the subscript p (c) indicates polymer segments (colloids).

Experimental partial structure factors at ϕ_c=0.2 are shown in Fig.5.4. $S_{cc}(q)$ describes correlated particle density fluctuations on a length scale $2\pi/q$. Its qualitative form is characteristic of a fluid with the most prominent feature a peak at $qD \sim 5$ which is a signature of short range spatial order on the nanoparticle diameter length scale. The collective polymer concentration fluctuation structure factor, S_{pp}, displays a peak on a similar length scale due to spatial correlations between adsorbed polymers with non-bulk-like properties and the nanosilica. The first peak is significantly larger than unity implying a large degree of coherence in the correlation of polymer segment concentration fluctuations at a wavelength that greatly exceeds the polymer radius-of-gyration.

The experimental results are compared with PRISM theory predictions for concentrated polymer-nanoparticle solutions where the solvent enters implicitly.[29] Details of the model and theory can be found in the literature[18,20,28,29], and the methods section below. Briefly, the homopolymer is a freely jointed chain of N spherical interaction sites (diameter d) with a bond (persistence) length of l/d=4/3. All species interact via pair decomposable hard core repulsions. The chemical nature of the mixture enters via an exponential interfacial attraction, $U_{pc}(r) = -\varepsilon_{pc} \exp\left(-(r-(D+d)/2)/\alpha d\right)$, where ε_{pc} quantifies the energy to transfer a monomer from a concentrated polymer solution environment to the nanoparticle surface, and αd is the

spatial range. All real and Fourier ($S_{ij}(q)$) space site-site pair correlations are predicted from three coupled nonlinear integral equations for the intermolecular pair correlation functions, $g_{ij}(r)$.

Figures 5.4 plot the theoretical predictions of $S_{cc}(q)$ and $S_{pp}(q)$ over a wide range of interface attraction strengths, $0.25\ kT < \varepsilon_{pc} < 1.05\ kT$. For both structure factors, note the high sensitivity of the scattering patterns to the value of ε_{pc}. Strikingly, the predicted values of $S_{cc}(0)$ and the position of the first peak, q^*D, in $S_{cc}(q)$ pass through a minimum at $\varepsilon_{pc} \sim 0.45kT$, while the height of the first peak grows monotonically. The minimum in $S_{cc}(0)$ and q^*D are associated with a qualitative crossover in structural organization from a situation where polymer-mediated interparticle repulsions first intensify with stronger polymer adsorption, to when polymers begin to bridge nanoparticles and thereby separate them at well-defined distances. Good agreement between the theoretical and experimental $S_{cc}(qD)$ is found for $\varepsilon_{pc} = 0.45kT$.

The inset of Fig. 5.4 shows the analogous comparison for collective polymer concentration fluctuations. With increasing ε_{pc}, theory predicts a suppression of the dimensionless osmotic compressibility, $S_{pp}(0)$, and the emergence of a "microphase" peak at nonzero wave vector. This peak moves to larger qD with increasing strength of cohesion between polymer segments and the particle surface, and is the physical consequence of strong coupling of (adsorbed) polymer and nanoparticle concentration fluctuations. As ε_{pc} decreases, the particles experience weaker steric repulsions and become less well correlated with the nanoparticles resulting in shifts in the first peak to lower qD values and enhanced long wavelength polymer concentration fluctuations. The theory-experiment agreement is again excellent for the same value of $\varepsilon_{pc}=0.45\,kT$, demonstrating for the first time the accuracy of PRISM theory for polymer microstructure. Theory and experiment comparisons for the cross correlation structure factor, $S_{pc}(q)$, are given in Fig. 5.5.

The measured and predicted values of $S_{cc}(q)$, $S_{pp}(q)$, and $S_{pc}(q)$ are shown at all volume fractions studied in Fig. 5.6 for the same single value of $\varepsilon_{pc} = 0.45kT$. Increasing ϕ_c suppresses long wavelength nanoparticle concentrations fluctuations, but enhances polymer fluctuations, as accurately captured by the theory. With increasing ϕ_c, the particles are on average closer, and the increased height of the cage peak in S_{cc} indicates enhanced packing coherency of the first shell of nearest particle neighbors. As the nanoparticles are concentrated and pack better, a well-defined correlation distance grows in between adsorbed polymer segments. The experimental trends are predicted nearly quantitatively by PRISM theory based on single interface attraction strength parameter.

The right panel of Fig. 5.6 shows the cross partial structure factor which quantifies the spatially resolved correlation between polymer and nanoparticle concentration fluctuations. This quantity can change sign as a function of probing length scale, indicating positive or negative correlation. One sees that $S_{pc}(q=0)$ is negative, and with increasing qD, $S_{pc}(q)$ decreases and goes through a well-defined minimum near qD~4-6. The negative values of S_{pc} and peak indicate anti-correlation of particle and polymer segment concentration fluctuations. As ϕ_c increases, the minimum in S_{pc} grows in magnitude and occurs at larger qD, tracking the increased correlation between particles in first nearest neighbor shells. The theory again captures the experimental trends very well.

Taken together, there is remarkable agreement between all three experimental structure factors and PRISM theory predictions based on a single value of the interfacial attraction energy, ε_{pc}. This provides significant support for the intrinsic origin of the latter material parameter, and the dominance of interfacial cohesion in determining the full mixture microstructure. Given the high sensitivity of all partial structure factors to the magnitude of ε_{pc}, the demonstrated

agreement also provides powerful evidence for the accuracy of PRISM theory, and the ability to combine it with scattering measurements to determine the interfacial cohesion strength. Deviations between experiment and theory observed at high qD~10-12 are attributed to experimental difficulties arising from low intensity of the raw data.

Often the microstructure of multi-component polymeric materials (blends, block copolymers) on length scales well beyond the atomic scale is accurately described (in theories and small angle scattering experiments) by the idealized incompressible random phase approximation (IRPA)[22] corresponding to direct inter-relations between the three partial collective structure factors: $S_{RPA}(q) = \rho_c K_{cc} S_{cc}(q) = \rho_p K_{pp} S_{pp}(q) = (\rho_c \rho_p)^{0.5} K_{pc} S_{pc}(q)$, where $K_{ij}=v_i v_j/(\phi_t (v_p v_c)^{1/2})$, v_i is the site volume of species i and ρ_i is the number density of component, i.[23] The total density fluctuation structure factor, $S_{tot}(q)= \rho_c K_{cc} S_{cc}(q) + \rho_p K_{pp} S_{pp}(q) - 2(\rho_c \rho_p)^{0.5} K_{pc} S_{pc}(q)$, is zero by assumption. Traditionally, the IRPA is applied to polymeric systems where effective interactions are weak and structural differences between species are small. This is not the case for a polymer nanocomposite where interactions can be strong, there is a massive asymmetry of length scales and intermolecular structure, and the physics of packing polymers at hard curved internal interfaces is relevant. Hence, the validity of the IRPA is unknown. It is important to resolve this question since if the IRPA fails, then measurement and computation of all three structure factors is necessary to fully understand mixture microstructure and predict thermodynamic properties. In our comparisons below, a pseudo-two component, implicit solvent model is adopted; explicit accounting for solvent would only serve to suppress deviations from incompressibility.

The IRPA idea predicts the peaks in S_{pp}, S_{cc} and S_{pc} should all occur at the same value of qD. As shown in the inset to Fig. 5.7, at a constant nanoparticle volume fraction there are

systematic, ϕ_c-dependent differences in the partial structure factor peak locations, indicating a breakdown of the incompressibility assumption. The main frame of Fig. 5.7 shows $S_{tot}(q)$ at each ϕ_c. For the IRPA to apply, S_{tot} must be a small constant (ideally zero) independent of qD. In the regime where fluctuations have a wavelength corresponding to $qD<4$, the total density fluctuations do reach a q-independent constant, but are not necessarily small and vary with nanoparticle volume fraction. Moreover, for shorter wavelength density fluctuations ($qD > 4$), but still long compared to the monomer and polymer chain sizes, the total density fluctuations become larger, depend on length scale, and grow significantly with ϕ_c. Thus, the strong packing asymmetry of polymers and particles results in total density fluctuations of significant magnitude and spatial variation. As expected from Fig. 5.6, there is a striking agreement between theory and experiment in peak positions for S_{pp}, S_{cc} and S_{pc} and the wave vector dependence of S_{tot}.

In order to both shed more light on the failure of the IRPA, and to in situ characterize the properties of adsorbed polymer layers, we consider scattering in a system where $\Delta\rho_c=0$. Imagine the scattered intensity is due to adsorbed spherical polymer shells with segment density fluctuations that differ from those in the bulk due to the polymer-nanoparticle surface attraction. Under these conditions the scattered intensity can be written as $\sim P_s(q)S_{pp}^*(q)$, where $P_s(q)$ is the polymer shell form factor that would be measured at low volume fraction, and $S_{pp}^*(q)$ is the structure factor associated with correlations between the shell centers-of-mass (CM). Following well-established procedures,[30,31] $P_s(q)$ can be estimated at low ϕ_c where $S_{pp}^*(q)$ is close to unity. To characterize the density fluctuations associated with the CM of polymer shells, the measured $I(q)$ is divided by $P_s(q)$ to determine $S_{pp}^*(q)$ at nonzero volume fractions. For the system studied here, the above procedure incurs some ambiguity since both the shell form factor and shell CM structure factor can vary with shell volume fraction.[32] To resolve this issue, we note that the

adsorbed polymer shell CM will, to a good approximation, have the same correlations as experienced by the CM of the nanoparticles. As a result, we argue that the scattered intensity at $\Delta\rho_c=0$ can be written as $I(q)\sim S_{pp}(q)\sim CS_{cc}(q)P_s^*(q)$, where C is a normalization constant varying with volume fraction.

In Fig. 5.8 we present the experimentally-deduced $P_s^*(q)$, and compare it with the form factors predicted by PRISM theory determined in the same manner. The resulting $P_s^*(q)$ overlap well, with the first minimum shifting slightly to lower q as ϕ_c is increased. Using the scattering length density parameters at a match condition and a core-shell model form factor,[31] the thickness of polymer shells is extracted to be ~0.7-1 nm, which is modestly larger than the PEG statistical segment length. We note that previous studies have shown that at all volume fractions up to ϕ_c~0.45 in the melt state (R_{PEG}=1), particles behave rheologically as hard spheres with apparent diameters of ~1.06D nm for PEG 400, which suggests a rheological polymer layer thickness of ~1.1 nm.[33] It is notable that PRISM theory is able to capture well the signatures of a shell of adsorbed polymer with different density fluctuations than observed in the bulk as shown by the solid curve in Fig. 5.8.

Physically, our results demonstrate that the failure of the IRPA arises largely from the adsorption of polymer on nanoparticles surfaces and the resulting alteration of local polymer segmental density fluctuations at wavelengths on the order of the particle diameter and smaller. As a result, $S_{pp}(q)$ and $S_{pc}(q)$ contain information about shell-like intramolecular polymer segment density fluctuations in the adsorbed layer, thereby providing an experimental (and theoretical) route to deducing the adsorbed layer thickness under dense conditions. We also note that as ϕ_c increases, the data suggests the polymer layer thickness decreases slightly from ~1.1 to

~0.9 nm, which can be understood as resulting from the suppressed density fluctuations as adsorbed polymer experiences greater confinement due to the nanoparticles.

Finally, we consider thermodynamic properties based on the quantitatively validated theory. Previous experimental and PRISM theory studies[34,35] for a model system different from what we have studied suggested that polymer-particle attractions result in a decrease in the nanocomposite bulk modulus with increasing particle volume fraction. Shown in Fig. 5.9 are theoretical predictions of the bulk modulus K_B normalized to its pure polymer melt analog, K_{B0}. At higher ε_{pc} where adsorbed layers are well-developed and polymers mediate repulsive interparticle interactions, K_B does indeed decrease with increasing ϕ_c. However, for smaller ε_{pc} where polymers adsorb less, and repulsive and attractive (entropic depletion) effects coexist in the nanoparticle potential-of-mean force,[11,18,36] the bulk modulus increases with particle loading over that of the polymer melt. Hence, we predict a direct connection between changes of polymer organization around nanoparticles and mixture microstructure with nanocomposite stiffness. We emphasize that in our implementation of PRISM theory, the polymer density in the interstitial regions between nanoparticles retains its value in the absence of particles, and hence the total volume fraction (particles plus polymer) varies with ϕ_c in a manner consistent with experiment.[28] Enforcing this condition is crucial to the striking prediction that lowering ε_{pc} towards the depletion miscibility boundary stiffens the nanocomposite, while increasing the attraction strength away from the depletion miscibility boundary results in softening. Thus, the magnitude of the bulk modulus, and its response to nanoparticle loading, can be controlled via rational manipulation of polymer-particle interfacial cohesion.

5.6 Summary

In summary, using contrast matching neutron scattering we have successfully measured, for the first time, all partial structure factors in concentrated polymer-particle mixtures. Both polymer and particle concentration fluctuations, and their cross-correlation, are predicted very well by microscopic PRISM theory based on a single key parameter, the strength of polymer segment–particle interfacial attraction, ε_{pc}. Moreover, by combing experiment and theory, ε_{pc} can be accurately determined. We also demonstrate the results are consistent with particle miscibility being associated with thin adsorbed (thermodynamically stable) polymer layers that provide steric stability for a window of segment/surface attraction strengths. The broader implication of this work lies in our demonstration that, by altering the magnitude of ε_{pc} through changes in particle surface chemistry and/or polymer chemistry, the microstructure and bulk material properties of nanocomposites and concentrated polymer solutions can be tuned to achieve desired goals.

5.7 Figures

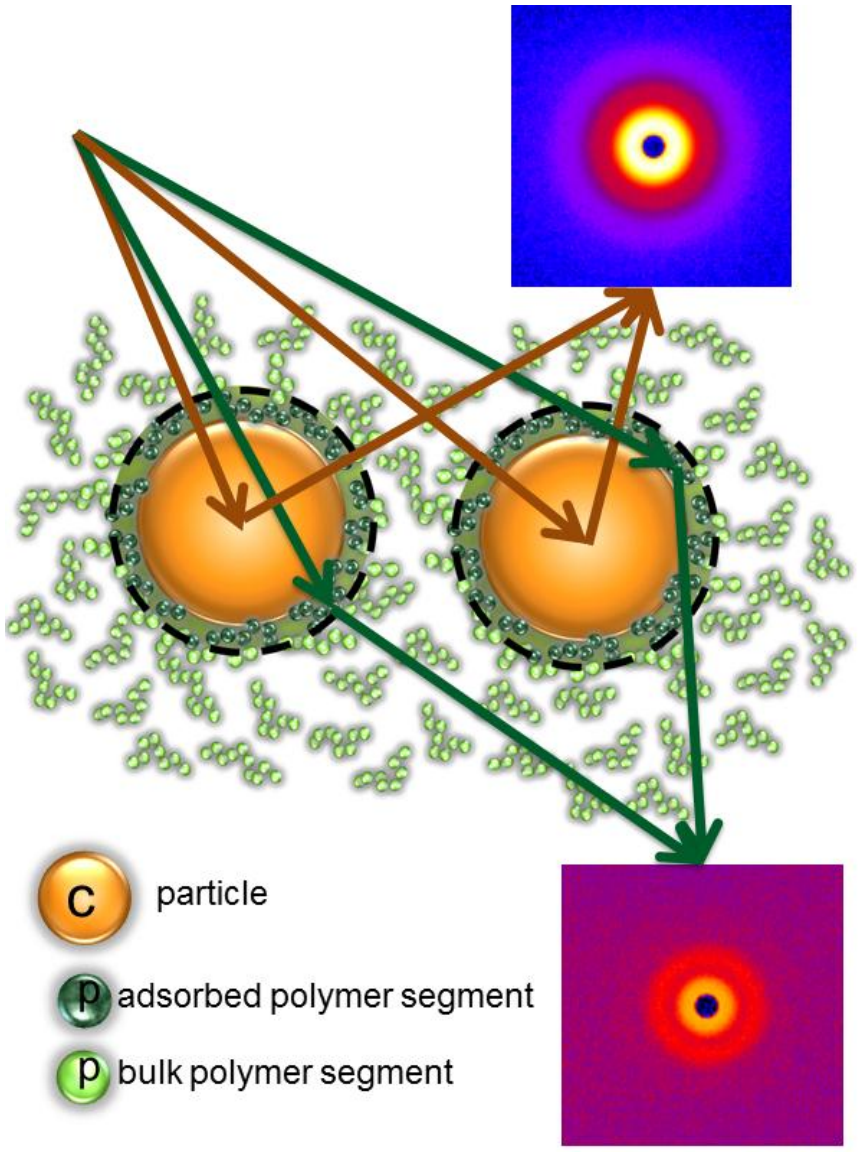

Figure 5.1 Schematic diagram of the experimental system. When $\Delta\rho_p \sim 0$ in Eq. (5.1), scattering is dominated by the particles and an example of raw intensity data from the 2D SANS detector is shown in the top rectangle. When $\Delta\rho_c \sim 0$, scattering is dominated by polymer segments and an example of raw intensity is shown in the bottom rectangle.

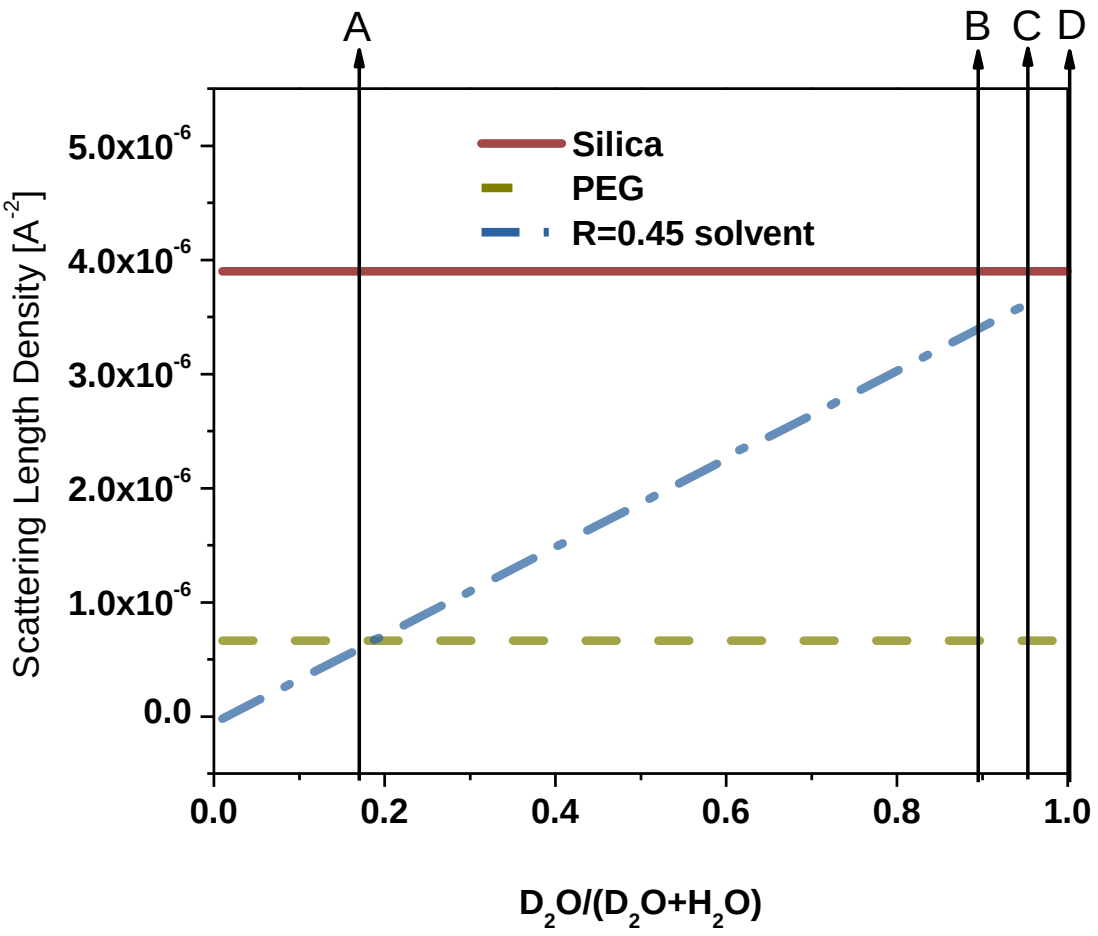

Figure 5.2 Scattering length density as a function of $D_2O/(D_2O+H_2O)$ ratio. Solid, dash and dash-dot lines are used for the silica nanoparticle, PEG polymer and R_{PEG}=0.45 solvent, respectively. A, B, C and D indicate four different solvent compositions where experiments were measured at R_{PEG}=0.45.

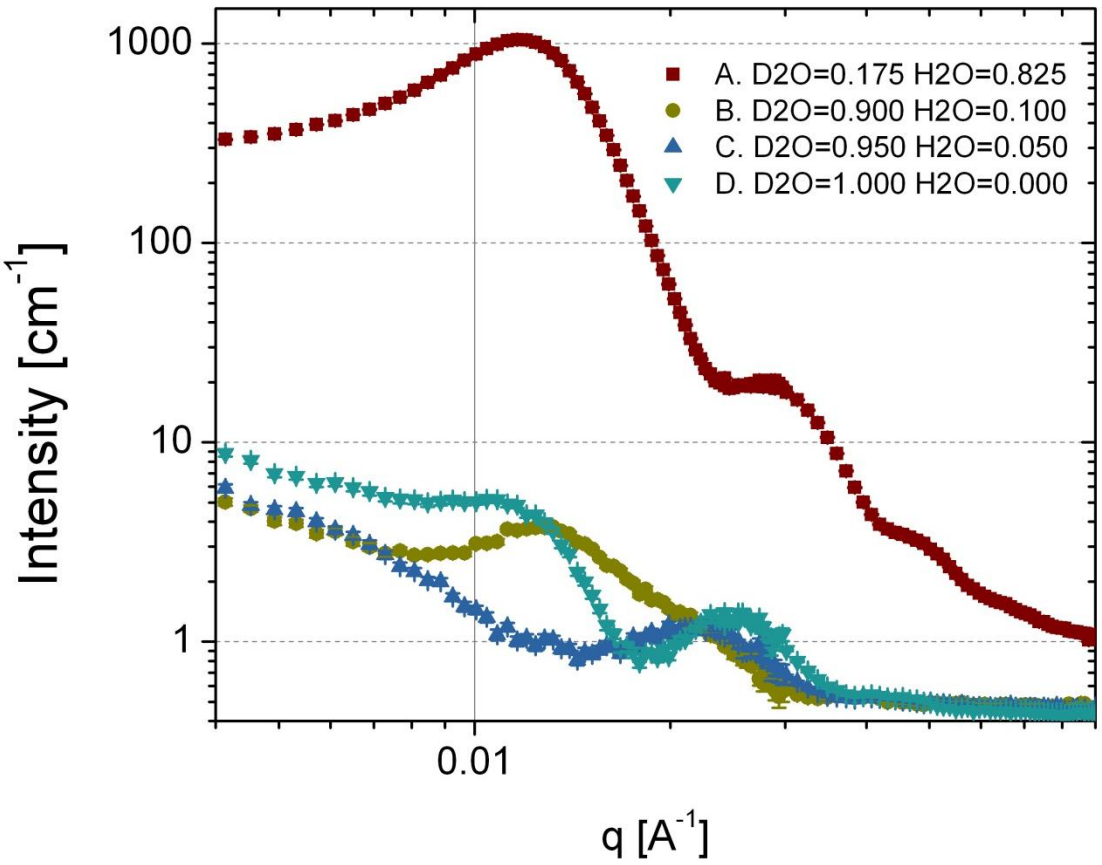

Figure 5.3 Scattering data for R_{PEG}=0.45 ϕ_c=0.20 at varying D_2O ratios Scattering intensity (*I(q)*) data as a function of wave vector. While particle volume fraction is fixed at 0.2 and R_{PEG}=0.45, $D_2O/(D_2O+H_2O)$ ratios are varied as pointed out in Figure S1.

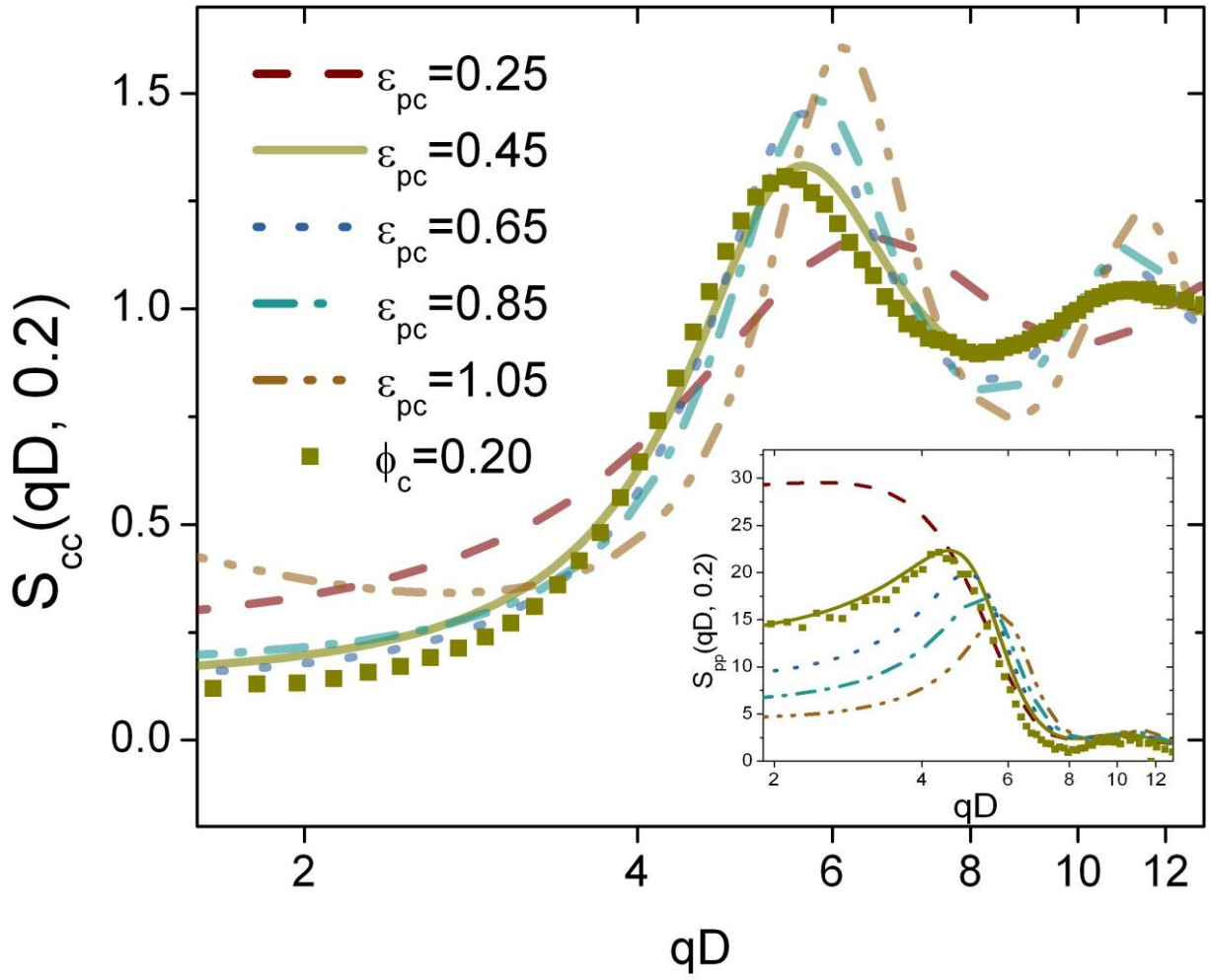

Figure 5.4 Nanoparticle collective structure factor as a function of reduced wave vector at ϕ_c=0.2. Experimental data are shown as squares, and PRISM theory predictions as curves which illustrate the effect of changing the segment-nanoparticle attraction strength, ε_{pc}. (inset) Corresponding collective polymer structure factors and theoretical calculations.

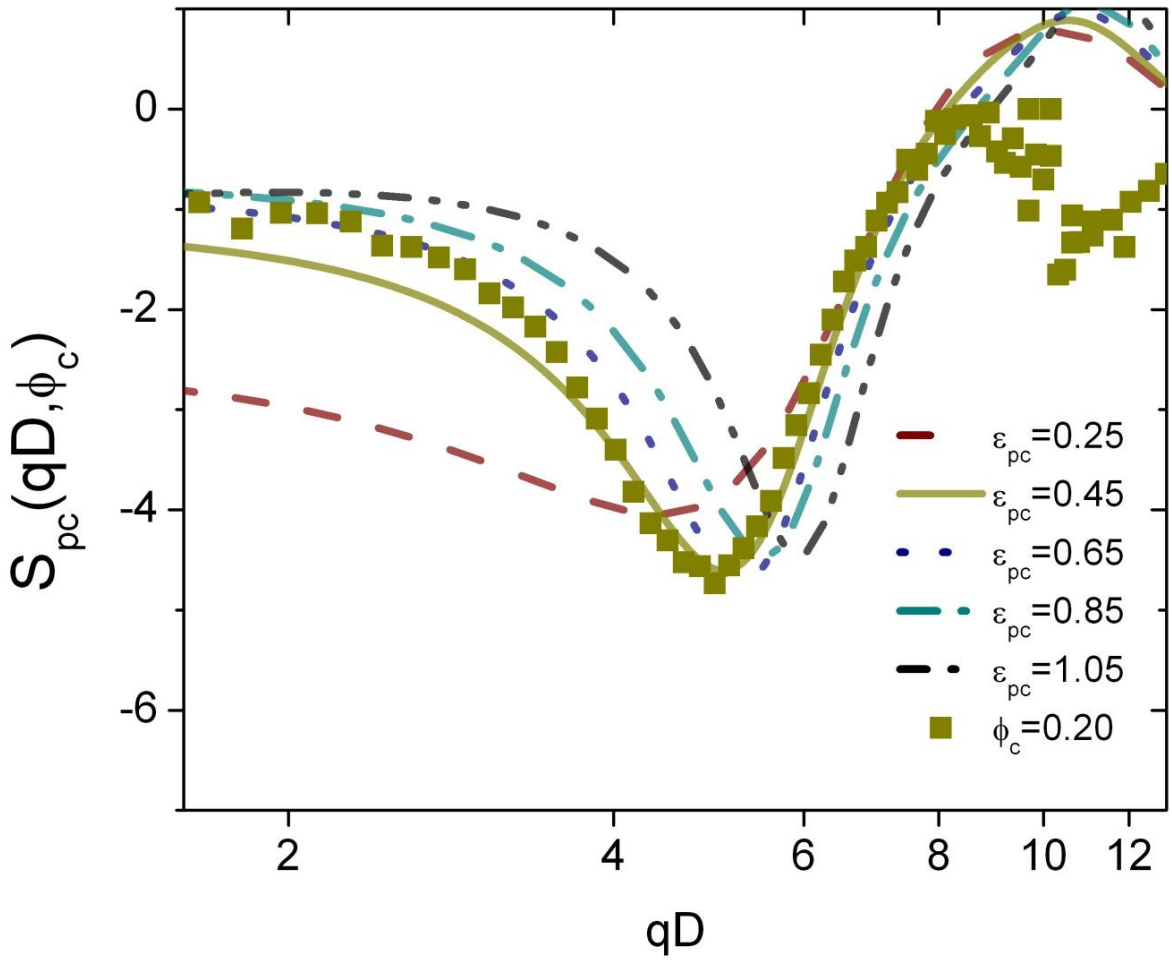

Figure 5.5 Cross correlation structure factor, S_{pc} as a function of reduced wave vector at ϕ_c=0.2. Experimental data are shown as dots, and PRISM theory predictions as curves which illustrate the effect of changing the segment-nanoparticle attraction strength, ε_{pc}. The deviation at high qD~10-12 is arisen from the low intensity data at high q shown in Fig. 5.3, thus, makes the extraction difficult.

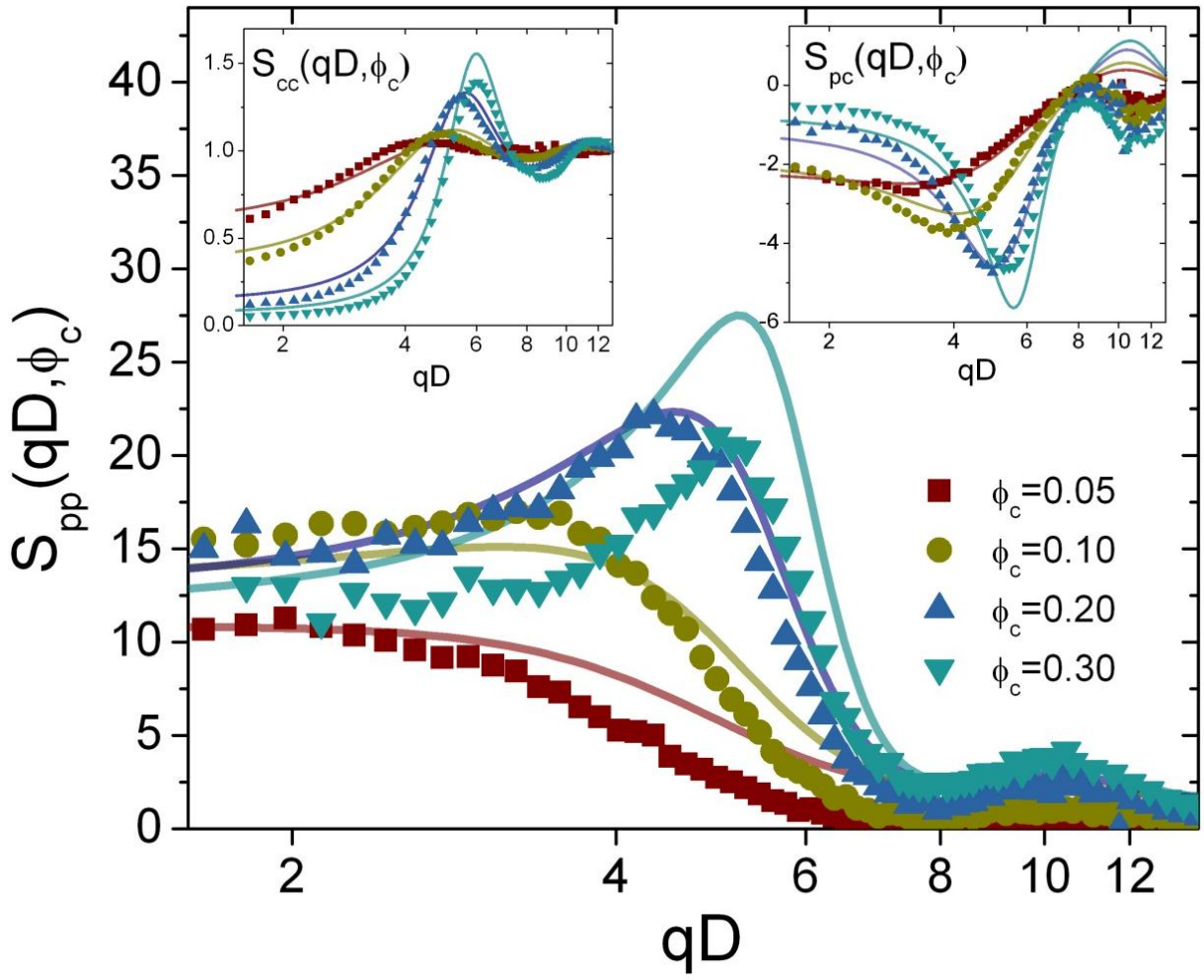

Figure 5.6 Polymer collective structure factor as a function of reduced wave vector at different nanoparticle volume fractions, ϕ_c, as indicated in legend. Corresponding smooth curves are the PRISM theory results for ε_{pc}=0.45kT. (Upper left inset) Nanoparticle collective structure factor, S_{cc}, under the same conditions. (Upper right inset) Cross fluctuation structure factor, S_{pc}, under the same conditions. Deviations at qD-10-12 are attributed to the low intensity of the raw data which renders accurate of extraction of S_{pc} difficult.

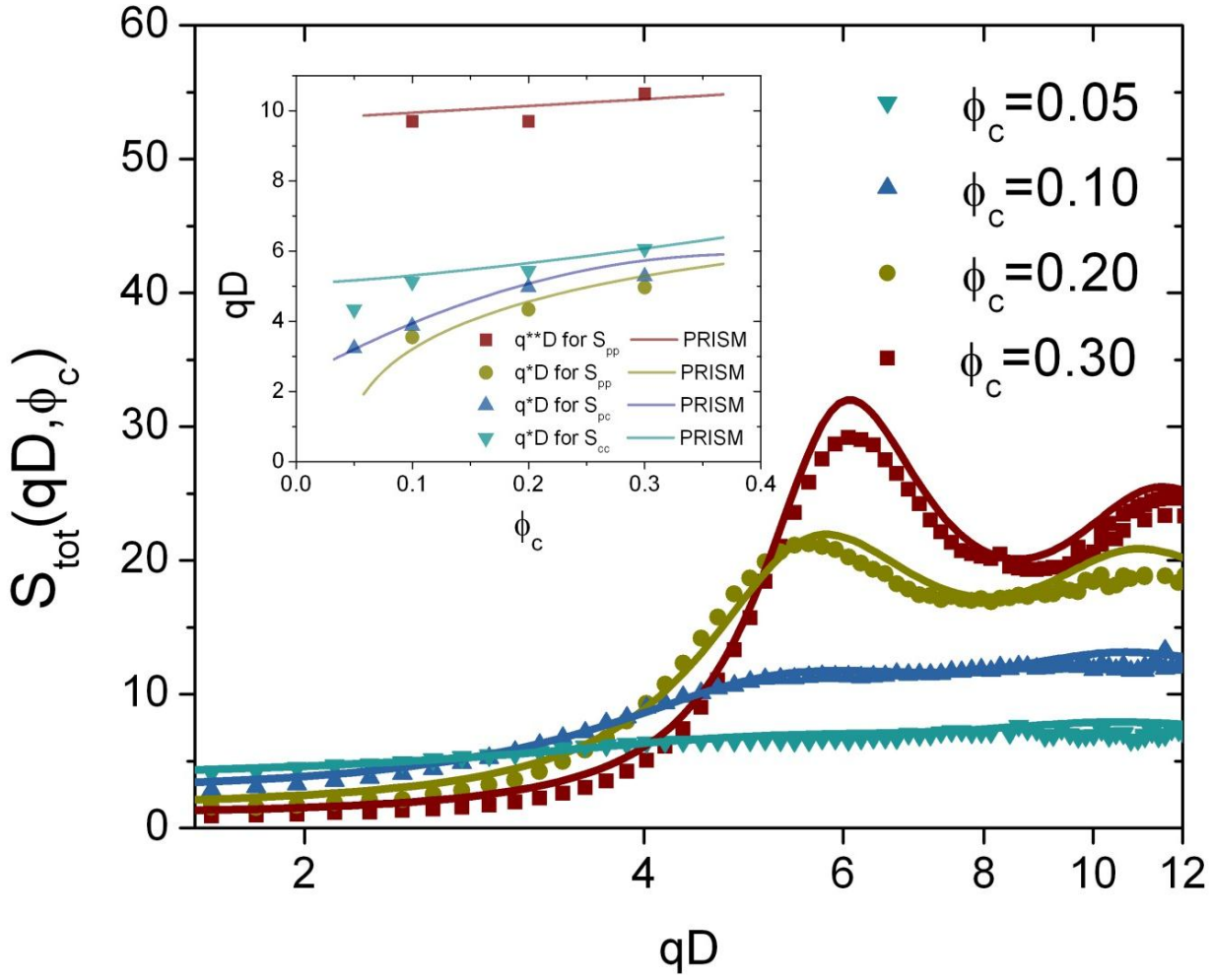

Figure 5.7 Dimensionless total density fluctuation structure factor as a function of reduced wave vector at the different nanoparticle volume fractions, ϕ_c, indicated in legend. Corresponding smooth curves are the PRISM theory predictions for ε_{pc}=0.45kT. (inset) Positions of first (q^*D) and second peaks ($q^{**}D$) as a function of ϕ_c. Dots are experimental data and curves are the PRISM theory predictions with ε_{pc}=0.45kT.

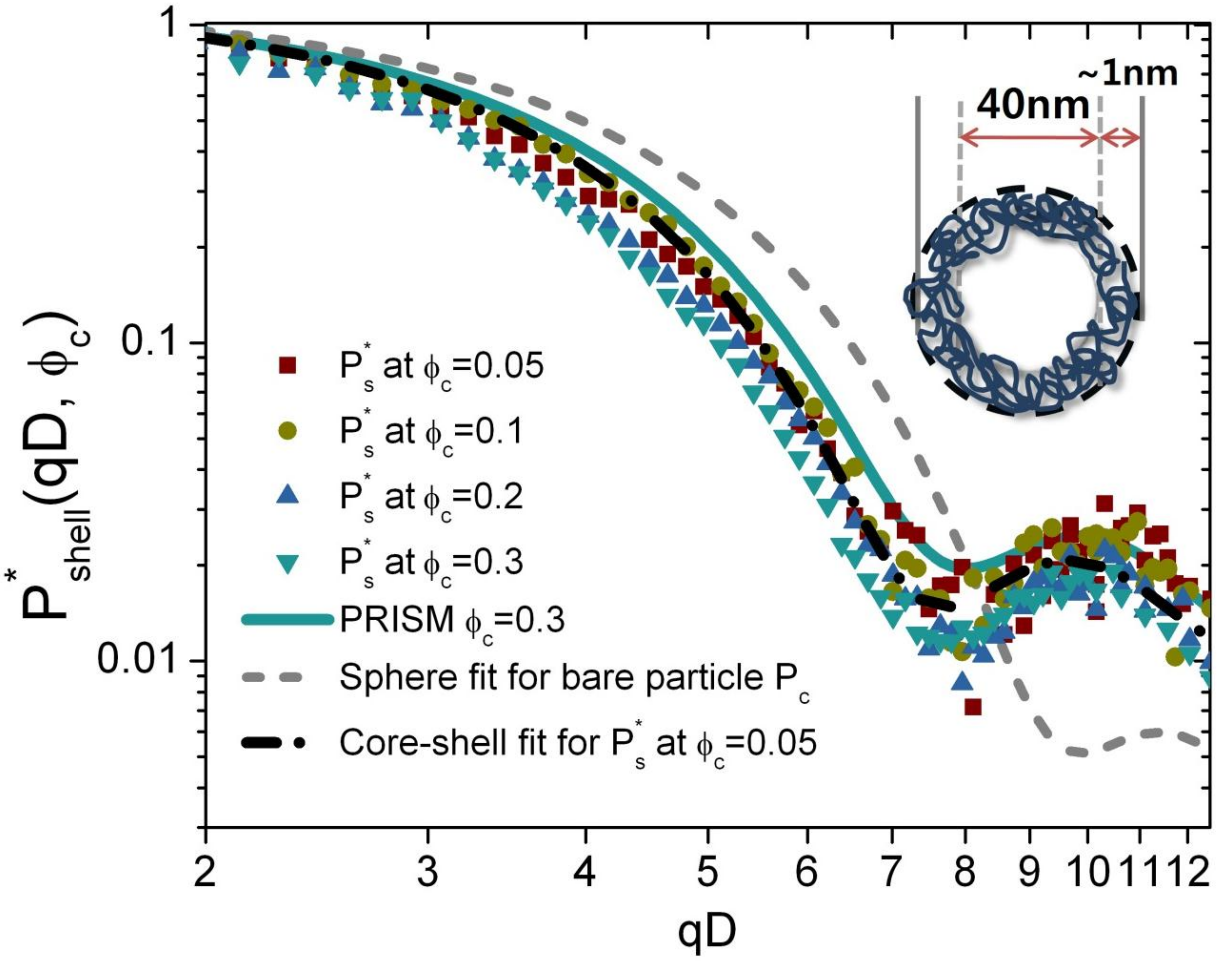

Figure 5.8 Polymer layer shell form factor as a function of reduced wave vector. $P_s^*(q)$ is determined from PRISM theory (solid curve) and experiment (dots) at four volume fractions. The dash-dot line is a fit to the polymer shell form factor using a core-shell model. The bare spherical-particle form factor, $P_c(q)$ based on Eq. (2.2) is shown as the short dashed curve for comparison to $P_s^*(q)$, experimentally obtained from dilute particle suspensions and fitted to the standard homogeneous sphere model. Fitting equations are found in Eq. (5.2).

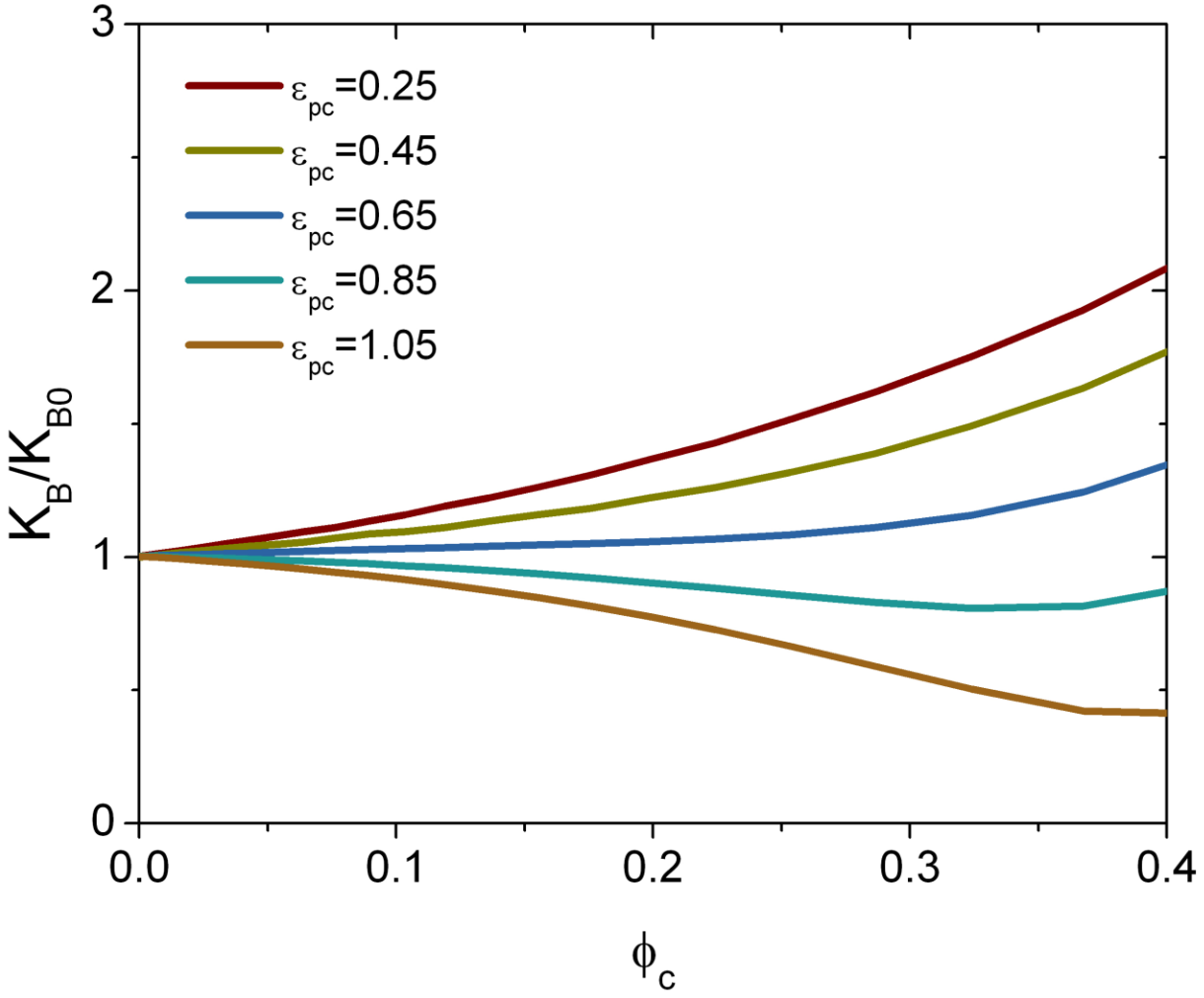

Figure 5.9 PRISM theory calculations of the nanocomposite bulk modulus (normalized by its pure polymer melt value) for several values of interfacial attraction strength, ε_{pc}, which increases from 0.25 kT (top) to 1.05 kT (bottom).

5.8 References

1. Bansal, A.; Yang, H.; Li, C.; Cho, K.; Benicewicz, B. C.; Kumar, S. K.; Schadler, L. S. *Nat. Mater.* **2005**, *4*, 693.
2. Mackay, M. E.; Dao, T. T.; Tuteja, A.; Ho, D. L.; Van Horn, B.; Kim, H. C.; Hawker, C. J. *Nat. Mater.* **2003**, *2*, 762.
3. Ajayan, P. M.; Schadler, L. S.; Braun, P. V. *Nanocomposite Science and Technology* Wiley-VCH: Weinheim, 2003.
4. Wang, M. J. *Rubber Chem. Technol.* **1998**, *71*, 520.
5. Oh, H.; Green, P. F. *Nat. Mater.* **2009**, *8*, 139.
6. Oberdisse, J.; Hine, P.; Pyckhout-Hintzen, W. *Soft Matter* **2007**, *3*, 476.
7. Oberdisse, J. *Soft Matter* **2006**, *2*, 29.
8. Rittigstein, P.; Priestley, R. D.; Broadbelt, L. J.; Torkelson, J. M. *Nat. Mater.* **2007**, *6*, 278.
9. Wang, M. J.; Zhang, P.; Mahmud, K. *Rubber Chem. Technol.* **2001**, *74*, 124.
10. Khounlavong, L.; Pryamitsyn, V.; Ganesan, V. *J. Chem. Phys.* **2010**, *133*.
11. Ganesan, V.; Ellison, C. J.; Pryamitsyn, V. *Soft Matter* **2011**, *6*, 4010.
12. Akcora, P.; Liu, H.; Kumar, S. K.; Moll, J.; Li, Y.; Benicewicz, B. C.; Schadler, L. S.; Acehan, D.; Panagiotopoulos, A. Z.; Pryamitsyn, V.; Ganesan, V.; Ilavsky, J.; Thiyagarajan, P.; Colby, R. H.; Douglas, J. F. *Nat. Mater.* **2009**, *8*, 354.
13. Mackay, M. E.; Tuteja, A.; Duxbury, P. M.; Hawker, C. J.; Van Horn, B.; Guan, Z. B.; Chen, G. H.; Krishnan, R. S. *Science* **2006**, *311*, 1740.
14. Olsson, R. T.; Hedenqvist, M. S.; Strom, V.; Deng, J.; Savage, S. J.; Gedde, U. W. *Polym. Eng. Sci.*, *51*, 862.
15. Pomposo, J. A.; de Luzuriaga, A. R.; Garcia, I.; Etxeberria, A.; Colmenero, J. *Macromol. Rapid Comm.* **2011**, *32*, 573.
16. Schaefer, D. W.; Rieker, T.; Agamalian, M.; Lin, J. S.; Fischer, D.; Sukumaran, S.; Chen, C.; Beaucage, G.; Herd, C.; Ivie, J. *J. Appl. Crystallogr.* **2000**, *33*, 587.
17. Koga, T.; Hashimoto, T.; Takenaka, M.; Aizawa, K.; Amino, N.; Nakamura, M.; Yamaguchi, D.; Koizumi, S. *Macromolecules* **2008**, *41*, 453.
18. Hall, L. M.; Schweizer, K. S. *J. Chem. Phys.* **2008**, *128*.
19. Hooper, J. B.; Schweizer, K. S. *Macromolecules* **2005**, *38*, 8858.
20. Schweizer, K. S.; Curro, J. G. *Adv. Chem. Phys.* **1997**, *98*, 1.
21. Gupta, S.; Zhang, Q.; Emrick, T.; Balazs, A. C.; Russell, T. P. *Nat. Materials* **2006**, *5*, 229.
22. De Gennes, P. G. *Scaling Concepts in Polymer Physics*; 2nd ed.; Cornell University Press: Ithaca, 1979.
23. Curro, J. G.; Schweizer, K. S. *Macromolecules* **1991**, *24*, 6736.
24. Leibler, L. *Macromolecules* **1980**, *13*, 1602.
25. Stober, W.; Fink, A.; Bohn, E. *J. Colloid Interface Sci.* **1968**, *26*, 62.

26. Anderson, B. J.; Zukoski, C. F. *Macromolecules* **2007**, *40*, 5133.
27. Kline, S. R. *J. Appl. Cryst*. **2006**, *39*, 895.
28. Hall, L. M.; Anderson, B. J.; Zukoski, C. F.; Schweizer, K. S. *Macromolecules* **2009**, *42*, 8435.
29. Kim, S. Y.; Hall, L. M.; Schweizer, K. S.; Zukoski, C. F. *Macromolecules* **2010**, *43*, 10123.
30. Higgins, J. S.; Benoit, H. C. *Polymers and Neutron Scattering* Oxford University: Oxford, 1996.
31. Guinier, A.; Fournet, G. *Small-Angle Scattering of X-Rays*; John Wiley and Sons: New York, 1955.
32. Qiu, D.; Flood, C.; Cosgrove, T. *Langmuir* **2008**, *24*, 2983.
33. Anderson, B. J.; Zukoski, C. F. *Macromolecules* **2008**, *41*, 9326.
34. Hooper, J. B.; Schweizer, K. S. *Macromolecules* **2007**, *40*, 6998.
35. Frischknecht, A. L.; McGarrity, E. S.; Mackay, M. E. *J. Chem. Phys.* **2010**, *132*.
36. Hall, L. M.; Jayaraman, A.; Schweizer, K. S. *Curr. Opin. Solid St. M.* **2010**, *14*, 38.

CHAPTER 6 POLYMER DYNAMICS IN POLYMER NANOCOMPOSITES: EFFECTS OF POLYMER MOLECULAR WEIGHT, TEMPERATURE AND SOLVENT DILUTION

6.1 Introduction

Polymer nanocomposites have been spot-lightened due to their potential to enhance mechanical, optical and/or rheological properties in a variety of products containing polymer and colloids. One advantage of employing polymer nanocomposites is that the existence of strong interactions between nanoparticle surface and polymer can enhance the mechanical properties over those of the polymer melt. These effects are associated with changes in polymer dynamics created by polymer adsorption to particle surfaces.

Changes in polymer dynamics due to the presence of closely spaced solid surfaces is inferred from changes in composite glass transition temperatures.[1-3] These changes have been linked to polymer dynamics in the work of Cohen-Addad *et al.*[4-7] who used free induction decay analysis obtained with multi-quantum NMR techniques to demonstrate that multiple hydrogen bonds between surface-OH groups of fumed silica and PDMS main chains yield a layer of glassy polymer segments 1-2 nm thick irrespective of PDMS end-groups or whether the chains are grafted or adsorbed to the particle surfaces.[8-10] Extensive studies of silica-poly(ethyl acrylate) also demonstrate that polymer segments are held in a highly confined, glass-like state near the particle surfaces even when the bulk polymer is highly cross linked.[11] In addition, Krutyeva *et al.* reported observation of an immobilized contribution to the inelastic neutron scattering resulting from glassy/adsorbed layers of PEG with alumina and concluded "confinement effects" are important in to introducing network-like dynamics in polymer relaxations in nanocomposites.[12,13] These results suggest that strong association of segments with the surface result in the formation

of regions with relaxation rates faster than would be expected in the bulk. One consequence of this behavior is that as the polymer exceeds the entanglement molecular weight (M_w) and the particle surfaces are brought into close proximity by increasing particle volume fraction (ϕ_c), the nanoparticles will enhance polymer network formation.

While there is a broadly accepted consensus that composite glass transition temperatures increase for strongly adsorbing polymers, there remains debate on the influence of weakly adsorbing polymers on T_g. Evidence for decreases in T_g for with weak interactions suggests that non-wetting surfaces enhance polymer relaxation rates.[14-18] One key limitation in understanding these phenomena lies in developing independent measures of the strength of cohesion of polymer segments to particle surfaces.

In this paper we use proton spin relaxation methods to investigate the impact of dispersing 40 nm silica particles in concentrated PEG solutions and melts. Our goal is to examine the impact of particle volume fraction and solvent dilution on the existence of entanglements and glassy layers. We undertake these studies for polymers with molecular weights spanning nearly two orders of magnitude (300-20,000). This experimental system is chosen because: i) particles are miscible with concentrated polymer solutions and melts, ii) we can explore the influence of particles on entanglements in the absence of bulk chemical cross-links, and iii) these systems have been extensively studied using small angle scattering techniques and the Polymer Reference Interaction Model (PRISM) to extract the adhesive strength of polymer segment- particle surfaces interactions.[19-21] Of particular interest are the effects of increasing volume fraction on the formation of polymer networks and the influence of these networks on composite flow properties. As an example, in Fig. 6.1 we compare two samples composed of PEG 8000 containing 44 nm silica and both at a particle volume fraction of ~0.30. In Fig. 6.1a the particles

are suspended in a nanocomposite melt. In the second sample (Fig. 6.1b) the particles are suspended in a polymer solution that contains 50% by volume polymer and 50% water. The melt fails in a brittle manner while the diluted sample is a liquid. Below we explore the origin of these differences by investigating polymer mobility from the particle surface to the bulk and the formation of networks with changes in volume fraction, polymer molecular weight, and dilution. Our results show that polymers adsorb more weakly and have fewer fast relaxing interactions for the diluted polymer. From this we conclude that the brittle behavior observed in the melt results from entanglement of strongly tethered polymer chains. When polymer chains have weaker tethering with the surface, chains relax more slowly and entanglements of tethered chains play a minor role in controlling composite rheology.

Below we detail how polymer dynamics can be quantified with proton NMR techniques and how polymer segment relaxation processes are altered in the presence of particles as functions of filler concentration, temperature, polymer molecular weight and dilution with solvent. Exploiting magic-sandwich echo (MSE) experiments, which refocus the initial part of the free-induction decay (FID) and thus avoid the dead time issue we were able to capture polymer relaxations at short time scales (less than 0.2ms).[22,23] On the other hand, multiple-quantum (MQ) experiments were carried out to link to the presence of topological constraints such as cross-links and/or entanglements where the relaxation time scale is much slower (0.1-3 ms).[24-26] The MQ experiments provide a sensitive measure of spin relaxation since they measure the residual dipolar coupling and thus the local dynamic order parameter on an absolute scale. Polymer mobility and network chain lengths are analyzed through the fittings to both MSE and MQ data.

We link obtained information on the polymer dynamics to the thermodynamic state of particle dispersions providing an example with small angle neutron scatterings. Through these experiments, one can gain an understanding of the influence of particle surfaces on polymer segment dynamics.

6.2 Experiments

6.2.1 Sample Preparation

Silica nanoparticles were synthesized based on the method of Stöber *et al.*[27], using the base-catalyzed hydrolysis and condensation of tetraethylorthosilicate (TEOS) yielding particles with diameters of 40±5nm as determined from both SEM micrographs and fitting the particle form factor determined by the angle dependence of neutron scattering from a dilute suspension. All various M_w of PEG were purchased from Sigma-Aldrich, and pure ethanol was supplied from Decon Lab. Inc. After particle synthesis, the alcosol was concentrated approximately 10 times by heating in a ventilation hood. During this process, the excess ammonium hydroxide was removed.

Particle volume fractions were calculated using the masses of each component and their densities. The silica particle density is 1.6 g/cm^3. In making the nanocomposite melts, a defined mass of alcosol is mixed with a defined mass of PEG. Samples were heated in a vacuum oven to drive off ethanol. The vacuum oven was purged several times with nitrogen followed by evacuation of the chamber to remove oxygen, yielding polymer nanocomposites. For the preparation of polymer suspensions for dilution experiment, the exact mass of each component (silica, PEG, D_2O) was determined in order to create the desired particle and polymer concentrations. Once the ethanol was evaporated, the necessary amount of D_2O was added to the sample to produce the desired concentrations of particles and PEG. Index of refraction matching

of silica in concentrated polymer solutions minimizes van der Waals attractions producing hard sphere direct interactions between the particles.

6.2.2 Low-Field NMR

The NMR measurements were performed on a Bruker Minispec mq20 at 20 MHz proton resonance frequency. The sample temperature was controlled with a BVT3000 heater working with air gas at each temperature of 70±0.1, 100±0.1°C and reached quickly its equilibrium state in 10 minutes but waited enough for 1 hour. Samples were loaded in a conventional NMR tubes and flame-sealed to avoid evaporation. The minispec has typical $\pi/2$ pulse lengths of down to 2 μs showing a reliable phase cycling in $\pi/2$ steps. Number of scans was varied from 128 to 512 depending on the sample conditions to obtain good quality of signals and the delay time was also varied from 1 to 4 s.

6.2.3 Magic-Sandwich Echo Experiments

The shape of the H-NMR time domain signal is mainly influenced by strong dipolar ^{1}H-^{1}H-couplings and thus provides information about the polymer's molecular structure and dynamics. The higher mobility in the mobile phase results in a stronger motional averaging of the dipolar couplings and a longer transverse relaxation time (T_{2m}) while stronger dipolar couplings in the rigid phase induce a fast transverse relaxation of the signal (T_{2r}) and a shorter relaxation time. As a consequence changes in relaxation time scales depend on the ^{1}H environment. Measurement of the free induction decay (FID) NMR time domain signal thus allows quantification of the proton relaxation rates and fractions of protons in mobile and rigid

environments. Although ^{1}H-FID analysis has become popular since it is readily available with low-field NMR spectrometers, the inherent noise in the initial part of the FID often caused by rf-pulse breakthrough leads a time delay in the start of the acquisition time and obscures the initial rapid decay associated with protons in glassy environments. To avoid this "dead-time" issue, we use dipolar time-reversed mixed magic sandwich echo (MSE). The MSE refocuses the dipolar couplings and gives a time-reverse of the signal decay. This method results in much greater sensitivity to short time relaxation processes thus nearing that we obtain the complete FID signal.

Figure 6.2a shows an example of typical FID with a sample at ϕ_c=0.4 PEG 20000 at 70 'C. The loss of initial decay signal in FID is restored with the use of MSE. However, there is a loss of intensity due to the additional pulse sequences. FID or MSE-FID is a consequence of different spin-spin proton relaxations, which allows quantifying the polymer mobility with different relaxation times. A detailed discussion of the technique used in this study can be found in the literature. [22,23]

In this process we use elective filters to emphasize different time domains. For example, a dipolar "magic-angle-polarization" (MP) is used for the mobile phase in order to remove unwanted contributions from the fast relaxation processes. Briefly, by increasing the overall cycle time of the central spin-lock portion of the MSE sequence with increasing interpulse spacing time (τ_ϕ), the echo becomes inefficient for strong dipolar-coupled spins and their signal is suppressed while the magnetization of mobile segments remains due to weak dipolar coupling and a resulting smaller dephasing of the spins. When τ_ϕ increases to 1.2272 ms in the MP filter at the given example of Fig. 6.2a, the fast decay from rigid part of polymer no longer contributes and the FID signal only contains contributions from the slowly decaying or mobile polymer segments as shown in the same Fig 6.2a. In this process we note that there is additional loss of

intensity due to increasing filter length which becomes important when we combined short and long time relaxations to count the total number of relaxing spins. For all samples studied here we found that setting $\tau_\phi = 1.2272$ ms removed all fast relaxing contributions.

On the other hand, selective magnetization of the rigid phase is realized with ^{1}H-double quantum (DQ) filter. The detailed information is also provided in the literatures.[11,22,23] The selective polarization of the rigid phase by a DQ-filter is based on the excitation of double quantum coherences in the rigid region. The excitation and reconversion of DQ-coherences depends on the DQ-excitation time (τ_{DQ}) determined in advance to be that time where the excitation intensity is the largest. The lowest curve in the Fig. 6.2a shows the intensity decay when the DQ filter is used.

6.2.4 Multiple-Quantum (MQ) NMR

The extended and complete descriptions of MQ-NMR are well-established and documented previously.[24-26] ^{1}H MQ-NMR measures segmental dynamics in terms of an orientation autocorrelation function of the second Legendre polynomial $C(t)=<P_2(\cos\theta(t))P_2(\cos\theta(0))>$, where θ is the segmental orientation relative to the external magnetic field. The time dependent correlation function measures the probability for a segment in a certain orientation at t=0 to be same orientation at later time, t. At short times, fast local fluctuations of polymer segments result in loss of configurational memory and thus $C(t)$ decays rapidly. At long times, however, long range or slower motion of polymer segments are hindered by the presence of topological constraints such as entanglements and cross-links and therefore, $C(t)$ decays very slowly, often seen as a plateau. The hindering factors such as the degree of the cross-link density and characteristic length of the network structure delay the decay of $C(t)$ and

thus, the height of a plateau accordingly correspond to the square of a dynamic order parameter of the polymer backbone (S_b).[24] The major benefit of using MQ-NMR differentiated from conventional experiments such as FID or Hahn echo is that this technique can separate and remove the dynamic effects on relaxations so that only structural information remains in the signal.

For a freely moving polymer chains without any topological constraints, the chain angles fluctuate due to the motion of chains and fluctuations average coupling tensors, thus no residuals remain. However, when the motion of the chains in networks is partially restricted by the existence of crosslinks, a partial alignment of two spins in a molecule yields an incomplete average dipolar coupling. Therefore, one can observe the residual dipolar couplings (D_{res}) in the presence of crosslinks, entanglements and networks and it can be calculated from MQ-NMR experiments. Since D_{res} is a measure of anisotropic residual of coupling tensors in entanglements or networks, D_{res} is directly proportional to the crosslink density and inversely proportional to the network chain molecular weights. Here we measure D_{res} in each sample so we can analyze the heterogeneity and quantify the network formations.[24,28]

MQ-NMR experiments yield two signal functions as a function of the MQ pulse sequence time τ_{DQ}, (i) the decaying sum MQ intensity (ΣMQ) and (ii) the double-quantum (DQ) build-up intensity. ΣMQ decay is dominated by the timescale of segmental orientation fluctuations, while the DQ build-up is governed by residual dipolar couplings (D_{res}), related to entanglements as well as cross-link effects rendering the motion anisotropic on the ms timescale. The decay of the DQ signal at longer times depends on faster segmental modes as well as slower chain modes. However, dividing DQ by ΣMQ yields a normalized DQ (nDQ) build-up function that in a sample containing a network depends exclusively on structural information in D_{res}. In

this experiment, τ_{DQ} was varied between 0.01 and 100 ms. Procedures for MQ experiments will be discussed in Section 6.4.

6.2.5 Small-Angle Neutron Scattering (SANS)

SANS experiment was performed on the NG7 30 m SANS instrument in NIST Center for Neutron Research, National Institute of Standards and Technology (NIST). Samples were loaded into 1mm path length demountable titanium cells. The cell temperature was maintained to 70±0.1 ˚C using the 10CB sample holder with a NESLAB circulating bath. A large range in scattering wave vector, q (0.001 ~ $0.1A^{-1}$), was obtained by combining the sector averaged scattering intensity from two different instrument configurations at 4, and 13.5 m detector distances. SANS data reduction and analysis of the scattering intensity, I, versus Q was performed using the SANS reduction and analysis program with IGOR Pro available from NIST. Detailed discussion of data reduction techniques is given in refs. (29)

6.3 FID Measurement

Polymer mobility can be easily approached with FID measurements. Figure 6.2 shows an example of typical FID result with a sample at ϕ_c=0.4 with PEG 20000 at 70˚C. Silica nanoparticles are stably dispersed in the PEG matrix in a miscible window where neither depletion forces nor bridging drive particle aggregation. Rheological experiments confirm that in melts[30,31] and when the polymer is diluted with water shown in Chapters 4 and 5, PEG adsorb onto silica particles. Thus, changes to the FID curve are associated with the presence of particles and the restrictions to polymer segment motion due to physical adsorption of polymer segments

to the particle surface. The rapid relaxations at short times indicate the presence of proton spins that are highly constrained and relax quickly. This phenomenon is correlated with fast diffusing spin-spin relaxations or glassy environments. As described above, by using with the MP and DQ filters we are able to accurately capture relaxation of all the spins in the system. The MP filter provides a measure of the relaxation time of mobile polymers in the bulk and the DQ filter yields the relaxation time and quantity of spins in the glassy state. In this process we recognize contributions from spins that have intermediate relaxation times which arise due to gradients in environment as segments move away from the particle surface.[11]

We find that an excellent representation of the data is found through a combination of stretched exponential functions of the form: $\exp(-(t/\tau)^b)$ where τ is a relaxation time and b is a constant. At short times we assume a Gaussian decay for the segments that are in glassy environments with b=2 while for that of mobile polymer segments the decays require b<2. We find that three decay processes represents the data well and write the fitting function for the free induction decay as:

$$I(t) = I_0(f_g \exp(-t(\tau_g)^{b_g} + f_i \exp(-t(\tau_i)^{b_i} + f_m \exp(-t(\tau_m)^{b_m}) \qquad (6.1)$$

where I_0 is an amplification factor, f_j is the fraction of the component j, τ_j is the jth relaxation time with subscript, g, i and m denoting glassy, intermediate and mobile segment contributions. Fitting the short time relaxations determined with the DQ pulse sequences in Fig. 6.2 yields b_g=2 and τ_g=0.034ms while to the long time decay process determined by MP yields b_m=0.8 and τ_m=19.28 ms. Fixing τ_g, b_g, τ_m and b_m at the values determined from the DQ and MP experiments, then, total FID curve is fit. In this process, f_g, f_m, τ_i and b_i remain unknown parameters noting $f_g+f_i+f_m=1$.

In our fitting process, we first set f_i = 0 as shown in Fig. 6.2b. This process fails to capture the data implying the existence of a spectrum of intermediate polymer relaxation times. When we assume there is a third relaxation process, we obtain good fits as shown in the same Fig. 6.2b. Three stretched exponential decays determine f_g and f_m. One notices that there are large uncertainties in the absolute values of τ_i and b_i as there no discrete information available for these intermediate relaxation processes. Thus, there many combinations exist to fit FID when τ_i, and b_i are allowed to vary freely. With the obvious conditions that $\tau_g < \tau_i < \tau_m$ and $0.7 < b_i < 1.7$ for reasonable decay of intermediate relaxation processes, minima in residuals are found for (τ_i, b_i) to be (0.418, 1.63) or (2.40, 0.884). The choice of (τ_i, b_i) alters the fraction of spins that relax with intermediate times, f_i. However, the glassy fraction is insensitive to the choice of (τ_i, b_i). For example, (τ_i, b_i) = (0.418, 1.63) yields f_g=0.095 and f_i=0.081, while (τ_i, b_i) = (2.40, 0.884) yields f_g=0.097 and f_i=0.51 when other values are fixed to be same for two cases. Consistently, we find that the fraction of intermediate relaxing polymers is associated with the choice of matching point between intermediate relaxations and longtime relaxations such that different choices of (τ_i, b_i) result in variations in f_i and f_m but not f_g. As a result, we focus on changes to f_g with varying conditions and analyze the mobility of glassy parts and non-glassy proton relaxation rates.

6.3.1 Particle Concentration and Molecular Weight Effects

The overall disturbance to the polymer relaxation rates grows with particle volume fraction. In Figure 6.3 we show how both f_g and f_g+f_i change with volume fraction for different molecular weights. Here f_g+f_i is referred as the immobile fraction (i.e., the fraction of spins that have relaxation processes different from those in the bulk). We note again that there are large

uncertainties in f_i. As a result, the immobile fraction is only used for a reference and holding τ_i, and b_i are constant at different volume fractions. For consistency, we have chosen τ_i =0.418 ms and b_i=1.63 for all comparisons made.

For each PEG molecular weight, f_g increases with particle volume fraction. For PEG 300, f_g~0.02 at ϕ_c=0.1 and it increases to f_g=0.079 at ϕ_c=0.4. Similar trends are found in PEG 3000, 12000 and 20000 as shown in Fig. 6.3. In the absence of particles where f_g=0, glassy-like and intermediate relaxations are absent. The linearity of data for each molecular weight in figure 6.3 clearly indicates that fast relaxations are correlated with the presence of particles. Surprisingly at a fixed ϕ_c, f_g is independent of molecular weight. If we assume the glass fraction results from polymer segments bound to the particle surfaces, $f_g = A_s\delta$ where $A_s = 6\phi_c/D$ is the specific surface area of silica in the composite and δ is the layer thickness. The linear fits to the data in Fig. 6.3 yield nearly constant layer thicknesses of 1.4, 1.7, 1.6 and 1.7 nm for PEG 300, 3000, 12000 and 20000 respectively.

The statistical segment length of PEG is ~0.6nm.[32] The polymer radius of gyration varies from ~0.6nm to 10nm as the polymer molecular weight moves from 300 to 20000.[32] These results clearly indicate that polymer segments are held in a glassy in a zone 2-3 polymer segments in width independent of polymer molecular weight.

The fraction of immobile polymer segments at each ϕ_c shows variations depending on molecular weight. While the absolute value of f_g+f_i is dependent on choice of (τ_i, b_i), if we hold the τ_i fixed as volume fraction and molecular weight are varied, we consistently find that f_g+f_i grows with ϕ_c at fixed polymer molecular weight and, at fixed ϕ_c, with polymer molecular weight. Generally higher molecular weight polymers have a larger fraction of spins relaxing at rates different from the bulk. These results are expected as the loops and tails of the adsorbed polymer

chains have mobility intermediate between glass and bulk behavior. Adsorbing a polymer of greater molecular weight will restrict the mobility of a larger number of polymer segments. Interpretation of the move from a near surface glass state to a bulk relaxation in terms of a layer thickness is complicated by expected gradients in mobility moving from the surface to bulk.[11] As a result we do not attempt to calculate a thickness of a zone of polymer where polymer dynamics is altered from that in the bulk. Nevertheless, we note that f_g+f_i increases with volume fraction with an apparent rapid increase in moving from ϕ_c=0.3 to ϕ_c=0.4 for the largest molecular weights.

The average particle surface to surface spacing (h) normalized to the polymer radius of gyration (R_g) can be written $h/R_g = (D/R_g)((\phi_m/\phi_c)^{1/3}-1)$ where ϕ_m is a maximum particle volume fraction taken here to be 0.64. At ϕ_c=0.4, h/R_g= 17, 5.6, 2.8, and 2.1 for molecular weights of 300, 3000, 12,000 and 20,000 respectively. The results in Figure 6.3 are suggestive of enhanced regions of restricted segment mobility as spacings of particle surface approach the size of polymer chains in the bulk.

We conclude that introducing silica nanoparticles into PEG polymer melts produces glassy layers ~1.4-1.7 nm thick and that this layer is independent of volume fraction and polymer molecular weight. Furthermore, the volume of polymer with restricted motion increases with polymer molecular weight in a manner suggesting enhanced restrictions as particle surfaces reach separations characterizing the size of unperturbed polymer chains.

6.3.2 Effect of Temperature

In investigating the stability of particles in the presence of adsorbed polymer, temperature becomes an important variable for polymers suspended in a thermal solvent near phase

separation boundaries[33-36] and in cases where variations in temperature alter the strength of polymer segment- particle surface attraction. Under these conditions we expect polymer adsorption and polymer chain dynamics to be sensitive functions of temperature. On the other hand, in case of polymer melts as we studied here, we are well away from phase boundaries and we expect the polymer matrix behaves like a theta solvent such that we would expect to see no change to the strength of adhesion with variations in temperature.[19]

In the absence of solvent, we examined the polymer mobility at various molecular weights as we increased temperature 70°C to 100°C. FID was measured for all samples with ϕ_c=0.4 at various polymers molecular weights and fitted with three stretched exponential decays as demonstrated above. Fig. 6.4 shows glassy or immobile polymer fractions at 70 and 100°C. For all polymer molecular weights, the glassy and immobile fractions are independent of temperature indicating elevated temperature has no effect polymer segment mobility. In other words, the fraction of polymer segments in the glassy state is unaltered by a temperature increase of 30°C suggesting that for the strongly adsorbed surface layers have T_g higher than 100C.

It is noticeable that in the presence of solvent, the fraction of proton spins associated with glassy relaxation times decreases significantly as temperature increases which will be introduced in Chapter 8, but in the polymer melt, polymer mobility is insensitive to temperature assuring silica particles in an athemal state in PEG melt.

6.3.3 Effect of Dilution

Fixing particle volume fraction at 0.3, we investigated the effect of reducing the polymer concentration by diluting the polymer with D_2O. In all samples the polymer concentration is

defined as R_p which is the ratio of polymer volume over the volume of polymer plus solvent. In the absence of solvent, R_p is 1, while R_p =0.5 when polymer solution contains 50% solvent and 50% polymer. As shown in Figure 6.5, at 70°C, f_g drops dramatically upon dilution of the polymer melt with water. This result suggests the mobility of the polymer segments is greatly enhanced by the addition of solvent and many fewer segments are adsorbed to the particle surface.

Our previous studies reported in Chapter 3 that at low temperature particle microstructure is weakly dependent on R_p for the same system studied here. This lack of sensitivity of microstructure to R_p was determined at 25°C for PEG molecular weights of 400 and the results we found to be compatible with the strength of polymer segment-particle surface attraction being independent of R_p implying polymer adsorption is insensitive to R_p. At room temperature, water is a good solvent and far below the lower critical solution temperature (LCST).[37] As a result at room temperature the structural data is consistent with minimal change in enthalpic gain of transferring monomer from the bulk in the presence or absence of water.

However, the results shown here seem to be contrary to the observations made at room temperature above at first glance, demonstrating substantial changes to the fraction of protons with glassy relaxation times when composite is the diluted at raised temperature 70°C. We attribute this to the system approaching the LCST where water is no longer a good solvent for the PEG. For example, water-PEG 20000 mixtures show a lower critical solution temperature near 100°C.[37] The approach of marginal solvent conditions as a temperature is raised has two consequences for the nanocomposite. First polymer-polymer attractions drive increased polymer segment density fluctuations such that there is enhanced tendency for polymer segments to associate with themselves than with the solvent. Second, the segments have a weaker tendency to

adsorb to the particle surface. This acts to destabilize the particles by reducing the magnitude of the potential of mean force stabilizing the particles from aggregation.

6.3.4 Hydroxyl Groups from Silica Surface

A challenge in interpreting the ^{1}H signals comes from hydroxyl group of silica particles. Noting that hydroxyl groups of silica particle can be present as many different types (i.e., silanol)[38-40] contributing to the overall ^{1}H signals as if they are glassy polymers, to determine its contribution to the ^{1}H signals is critical because glassy polymer fractions can be overestimated. The content of –OH groups in silica has been estimated by various methods.[39-41] For example, Kim *et al.* reported[41] that the –OH mass fraction in silica is 0.03 wt% corresponds to hydroxyls that can contribute to the rigid part signals or less in other literatures.[39,40]

In the present study, for instance, PEG 300 at ϕ_c=0.3 has approximately 4% of glassy polymers shown in Fig. 6.3 which compromise to 3 wt % (=(1-0.3)×0.04) of polymer segments in a total sample mass while OH mass fraction in silica is 0.01 wt% (=0.3×0.03) of the sample corresponds to hydroxyls that can contribute to the rigid part signals. Thus we estimate that less than 1% of the rigid signal may correspond to proton spins associated with the particle irrespective of the presence of monomer.

The other indication of negligible contribution of silica hydroxyl group is found in dilution experiments. Fig. 6.5 showed at R_p=0.5 glassy fraction of polymers are almost absent or very small. Even if dilution of nanocomposites desorbs all polymer segments from the silica surface, when silica hydroxyl groups greatly contribute to ^{1}H signals, calculated f_g will be much larger than the current results.

With thus evidences we conclude the contribution of silica hydroxyl groups to the ^{1}H signals to the glassy fraction is negligible.

6.4 MQ Experiments

The goal of the MQ experiments is to study polymer structures that contribute to elastically active networks such as crosslinks or entanglements. Recalling that the measurements are associated with a time autocorrelation function of the orientational angles of paired spins, the MQ experiment generates two signals, ΣMQ and DQ. While DQ is a measurement of the residual dipolar couplings, ΣMQ is a measurement of relaxation of the molecular motions and both due to the presence of the crosslinks or entanglements.

However, it is often difficult to solely look at the effect of active networks as additional components such as short dangling chains or tails are present in MQ signals. These effects are particularly important when the polymer is close to entanglement weight and only small fraction of crosslinks exists. Under these conditions, characterization of the active network requires careful attention. To be specific, the two measured signals of ΣMQ and DQ have contributions from segments that have fast melt-like mobilities which give rise to long relaxation times for the ΣMQ and DQ signals. Thus, before processing the data for nDQ, ΣMQ and DQ should be corrected. The analytical decay function of ΣMQ is written as

$$f_{net}\Sigma MQ_{,corr}(\tau_{DQ}) = \Sigma MQ(\tau_{DQ}) - f_{dang}\exp^{-2\tau_{DQ}/T^{*}_{2B}} - f_{tail}\exp^{-2\tau_{DQ}/T^{*}_{2C}} \qquad (6.2)$$

where f_{net}, f_{dang} and f_{tail} are network, dangling and tail fractions, respectively and T^{*}_{2B} and T^{*}_{2C} are relaxation times for dangling and tail polymers, respectively. Detailed discussion of this process is given in references ([24-26,28]). Fig. 6.6a shows the effects of subtracting the tails and the

dangling. The tail and dangling exponential fits were performed on ΣMQ data from semi-logarithmic plot of ΣMQ vs. τ_{DQ} where dangling and tails components decays linearly with much longer relaxation times. PEG-silica nanocomposites are expected to have a small fraction of networks segments with short relaxation times due to the absence of cross-links and relatively low polymer molecular weight. This expectation is supported in Table 6.1 where the contribution to the decay of the ΣMQ and DQ signals show large fractions of f_{dang} and f_{tail} and small fraction of network relaxation modes. After subtraction, ΣMQ only contains oriental fluctuations of network-like polymer segments and point-by-point division of the DQ signal by the ΣMQ was carried out to obtain the nDQ intensity. nDQ intensity is analyzed and fitted with

$$I_{nDQ}(\tau_{DQ}) = \int_0^\infty \frac{1}{2}(1-\exp\left\{-\frac{2}{5}D_{res}^2\tau_{DQ}^2\right\})P(D_{res})\exp\left\{-\frac{\tau_{DQ}}{T_2^*}\right\}dD_{res} \qquad (6.3)$$

where a gamma distribution function of couplings is $P(D_{res}) = \frac{2}{\sqrt{\pi}}\sqrt{\frac{27|D_{res}|}{8\bar{D}_{res}^3}}\exp^{-3|D_{res}|/2(\bar{D}_{res})}$ and T_2^* is an apparent T_2 relaxation time. The result of the fitting allows us to extract D_{res} and is shown in the Fig. 6.6b with a solid curve.

6.4.1 Particle Concentration and Molecular Weight Effect

Figure 6.7a, b and c show the nDQ build up curves and their fits to Eq. (6.3). Since the residual dipolar couplings are the origin of the appearance of nDQ build-up, their strength is directly proportional to the cross-link density. In the short τ_{DQ} limit, nDQ is proportional to $D^2_{res}\tau^2_{DQ}$ in Eq. (6.3).[24,28,42] Thus, qualitative and quantitative estimations for molecular weight of network chains and cross-link density are available throughout the build-up curves. [24,28,42]

For PEG molecular weights studied, nDQ increases and reaches its plateau value more rapidly as particle volume fraction increases as shown in Figs 6.7a-c indicating a systematic increase in D_{res} with volume fraction. For PEG 3000 at ϕ_c=0.1, no detectable DQ data could be obtained (i.e., the ΣMQ signal was dominated by tails and end group relaxations.) This effect is expected because the entanglement molecular weight of PEG lies near 3000. Thus the lack of a signal indicates a lack of entanglements even in the bulk. However as volume fraction is increased to 0.3-0.4 where the surface to surface separation is less than $6R_g$, the residual dipolar coupling, D_{res}, increases substantially.

D_{res} is dominated by a partial alignment of two spins in a molecule and an incomplete averaging of anisotropic magnetic interactions. As a result D_{res} is a measure of the presence of factors hindering the alignments such as entanglements and chemical cross links. As shown in Table 6.1, D_{res} increases from 0 to 62.1 to 103 Hz as ϕ_c moves from 0.0 to 0.3 and 0.4 implying the existence of entangled polymers. Thus, in PEG 3000 there is no residual dipolar coupling in the absence of particles, however, as particles reach a surface to surface spacing of $6R_g$, particles induce substantial residual orientational correlations.

When polymer is above entanglement molecular weight such that in PEG 12000 and 20000, nDQ build-up rises even in the absence of particles due to the attributes of entangled polymers, but increase slowly. Added particles in the melts of PEG 12000 and 20000 accelerate the formation of these networks indicated by fast rising nDQ and increased D_{res}. Below, we analyze the molecular weight dependent effect in details with rheologically defined specific particle volume fractions.

One notes increasing the molecular weight affects not only the network fractions but also the magnitude of the residual dipole coupling. For all M_w, f_{net} and D_{res} grow together indicating

as network fractions increases crosslink densities and molecular weight of network chains also increased shown in D_{res}.

We show above that in the melts, polymer is adsorbed to the particle surface forming a glassy layer with thickness weakly dependent on molecular weight. The result will be a corona of loops and dangling polymers associated with this adsorbed layer the thickness of which is expected to increase with molecular weight. Supporting this hypothesis, Anderson *et al.* showed that at low volume fraction the viscosity of suspensions of silica particles in PEG melts followed behavior expected for suspension of hard spheres as if silica particles had a diameter of $D(1+2.8R_g/D)$.[30,31] In their studies, R_g was varied by an order of magnitude.[31,32] As the volume fraction was increased, Anderson defined a series of critical volume fractions at each molecular weight where interactions between polymers in the bulk and polymers adsorbed to the particle surface significantly altered the nanocomposite melt rheology;[31] (i) $\phi_{c,e}$: As particle volume fraction is increased, strong hydrodynamic interactions first occur at a point where *secondary* entanglement can occur ($\phi_{c,e}$). This rheological transition is observed at surface-to-surface separation of ~$6R_g$ due to the entanglement of free polymer between adsorbed polymer on neighboring particles. (ii) ϕ^*: At higher volume fraction, a stronger rheological transition occurs when adsorbed polymer is confined between two neighboring particles. This volume fraction defines overlap of adsorbed polymer layers at a surface separation of $3.6R_g$. (iii) ϕ_g: Finally a rheological transition occurs when the effective volume fraction defined as ($\phi_c(1+2.8R_g/D)^3$) = 0.58 where the suspension of effective hard spheres will form a glass (ϕ_g).

For PEG20000, $\phi_{c,e}$ =0.012, ϕ^*=0.192 and ϕ_g =0.22. We estimate that for PEG12000, $\phi_{c,e}$ =0.04, ϕ^* ~0.25 and ϕ_g =0.23 and for PEG3000, $\phi_{c,e}$ =0.17, ϕ^*~0.38 and ϕ_g ~0.38. Molecular

weights of PEG 1000 and PEG 2000 are below the entanglement M_w, such that only glass transitions at ϕ_g were observed.

These critical volume fractions can be used to understand molecular weight dependent residual dipolar couplings shown in Fig. 6.8a. For PEG 3000, ϕ_c=0.1 is below $\phi_{c,e}$=0.17 such that we could not observe particle enhanced entanglements while for PEG 12000 and 20000, ϕ_c=0.1 is above $\phi_{c,e}$ (=0.04 and 0.012, respectively). Residual dipolar coupling results suggest that secondary entanglements are important in controlling suspension rheology in Fig. 6.7a. At ϕ_c=0.3, where secondary entanglements are expected for the PEG 3000 case, there is a rapid build-up of the nDQ curve indicating the presence of residual dipolar coupling associated with these secondary entanglements. Therefore, we conclude that in the PEG-silica composites where PEG is above the entanglement molecular weight, particles induce network formation when particle are spaced at a distance where secondary entanglements can occur.

At ϕ_c=0.4 where all ϕ_c is above ϕ^* and ϕ_g for all PEG molecular weights, all three composites show the presence of the residual dipolar couplings as indicated in Fig. 6.8b. Physically formed the entanglements hinder the slow motions of the segments yielding non-zero average dipolar couplings. Due to the reduced surface-to-surface separations with increasing PEG M_w and thus, R_g, molecular weight of formed network chains and crosslink density also increases such that nDQ rises up more quickly at higher M_w.

Conclusively, networks and entanglements in silica polymer nanocomposites are induced by adding particles and more importantly degree of the formed networks and chain length depend upon the PEG molecular weight. At ϕ_c=0.4 PEG 300 show glassy and confined polymer

properties while PEG 12000 is gel and brittle and PEG 20000 is also gel and ductile with strong primary entanglements.[31]

Most of nDQ data fits well with Eq. (6.3) applying $T_2^* \rightarrow \infty$. However, since the data is quite noisy for cases with low network fractions, some of samples in Table 6.1 could not be fitted. Furthermore, those cases with low ϕ_c or at R_p=0.5 are difficult to calculate network and/or dangling fractions when the intensity was too low to fit with Eq. (6.2) and network and dangling signals are indistinguishable, thus, they failed to reach 0.5 plateau for nDQ build-up curves.

6.4.2 Dilution Effect

Diluting polymer nanocomposites with solvent clearly reduced glassy polymer fractions changing the adsorption/desorption equilibrium. At a fixed ϕ_c=0.3, nanocomposites (R_p=1) with PEG 3000 and 12000 are substituted with R_p=0.5 polymer solution and MQ-NMR experiments were carried out and shown in Fig. 6.9. Both nDQ build-up curves for PEG 3000 and 12000 become much noisier and suppressed when R_p decreases from 1 to 0.5. Moreover, nDQ build-up curves at R_p=0.5 could not be fitted with Eq. (6.3) due to the insufficient signal. The dramatic decrease of nDQ intensity indicate networks were not formed at dilute conditions even at high ϕ_c=0.3 and M_w=12000. On the other hand, solvent addition and heating to 70°C speeds up the reptation process, which make the time scale of reptation reduced and therefore, almost no DQ intensity is observed under these conditions.

6.5 Connections to the Particle Dispersions and Physical Properties

From FID and MQ-NMR experiments, one understands that there are substantial changes in polymer mobility and network formations as R_p lowers from 1 to 0.5 and furthermore expect subsequent changes in the particle microstructure. Origin of varying polymer mobility and length of network chain is due that circumambient polymer environment is changed with heating and adding solvent. As a consequence, the state of particle dispersions related to changing polymer-induced interactions can be altered upon the solvent dilution.

Recently, particle stability was simply described with the strength of attraction between polymer segments and particle surface, ε_{pc}.[19,21,43] For very small ε_{pc} compared to the average thermal energy of the system, kT (a "dewetting" interface), depletion attractions make nanoparticles aggregate into compact clusters at nearly all particle volume fractions. For large ε_{pc}, polymers form tight bridges between the nanoparticles, resulting in phase separation or perhaps formation of non-equilibrium polymer-particle networks. Only at intermediate ε_{pc}, adsorbed polymer segments form discrete, nonoverlapping, and *thermodynamically stable* layers, resulting in a net repulsive interparticle potential of mean force (PMF) between the nanoparticles. Qualitative and Quantitative analysis for particle microstructures are performed via structure factors ($S(q)$) from small angle scattering experiment.[19-21]

In Fig. 6.10 we show the inverse of osmotic compressibilities ($1/S(0)$) as a function of particle volume fraction for PEG 8000 R_p=1and R_p=0.5. The initial observation is that particles were nicely stable without any aggregation implying an intermediate ε_{pc} governs the system from the structure factor ($S(q, \phi_c)$). The insert of Fig. 6.10 shows the height of the first peak in $S(q)$ as a function of volume fraction. This peak height is a measure of the coherence of the first nearest neighbor shell. Greater coherence is associated with more strongly interacting particles. These

measurements were made at 75°C and 70°C, respectively for R_p=1and R_p=0.5 and the dramatic changes seen between R_p=1 and R_p=0.5 indicate that the solvent is playing a substantial in altering suspension microstructure.

Increases in *1/S(0)* indicate the particle sub-system becomes less compressible and while increases $S(q^*)$ suggest particles are more structured. Two distinctive features are found in Fig. 6.10. First, when particles are suspended in the PEG 8000 melt, *1/S(0)* is not a monotonic function of particle volume fraction. Without any signs of aggregation, at low ϕ_c, the system becomes less compressible and more repulsive with increasing ϕ_c, due to the increasing number of particle volume fraction. However, near ϕ_c =0.25 *1/S(0)* passes through a maximum. We note near ϕ_c =0.25 the system reaches its primary entanglement point (ϕ^*=0.282) and glass transition point (ϕ_g=0.305). Therefore, the formed networks between the adsorbed polymer layer could bring additional attractions resulting in the maximum in *1/S(0)*. The same trends are observed in $S(q^*)$ from the inset of Fig. 6.10.

Second, as R_p decreases from 1 to 0.5, both *1/S(0)* and $S(q^*)$ are greatly reduced. These features indicate particles experience weaker repulsive potentials of mean force upon dilution. These observations are consistent with weaker adsorption of polymer segments to the particle surfaces, the decreased amount of glassy relaxations observed in the FID experiments and the reduced degree of network formation that in melts is associated with primary and secondary entanglements.

Overall, through the comparisons to scattering structure factor, one can clearly see that polymer entanglements directly affects the state of particle dispersion thus connecting network formation to the thermodynamics associated with particle stability and phase separation.

The result particle enhanced polymer entanglements is clearly evident in Figure 6.1. At ϕ_c =0.314 $>\phi^*$ polymer nanocomposite melts of PEG 8000 behave like brittle gels (Fig. 6.1a). However, at R_p=0.5 at the same volume fraction the composite retains liquid-like properties (Fig. 6.1b). While the polymer is diluted, it remains in the concentrated region such that chains will remain entangled. However, the weak coupling of the polymer segments with the particle surfaces allows for enhanced polymer relaxations and thus the composite remains in a liquid-like state.

6.6 Summary

The goal of the current study is to observe the change of polymer dynamics in nanocomposites composed of silica and PEG with varying conditions of particle volume fraction, polymer molecular weight, temperature and the dilution with a low molecular weight solvent. Our result show that for all molecular weights studied, physical adsorption of PEG segments to the silica surface produces a glassy polymer layer. The fraction of glassy polymer segments is invariant with polymer molecular weight implying the layer thickness of glassy layers is independent of polymer molecular weight. Furthermore, the fraction of segments in the glassy layers does not change as the temperature is increased from 70 to 100°C suggesting the adsorption is sufficiently strong that the glass transition temperature for this layer is greater than 100°C. If the nanocomposites are diluted with solvent at high temperature, we observe significant changes polymer dynamics indicating substantially fewer segments are in a glass state on the particle surface.

MQ-NMR experiments enabled us to examine the development of networks upon the increasing molecular weight and filler concentration and decline of them upon solvent dilution.

Above the entanglement molecular weight, the silica-PEG nanocomposite melt shows that entanglements grow as particle spacings drop below those that enable a polymer in the bulk to entangle with chains adsorbed to two different particles. The amount of particle induced network formation grows with polymer molecular weight and filler concentration. These observations are consistent with measures of the suspension microstructure showing weaker polymer adsorption with increasing dilution at 70°C. Conclusively, this study shows that FID and MQ NMR techniques can be used to quantify the state of polymer segment mobility and the onset of network formation in nanocomposite systems where the physically adsorb to particle surfaces.

6.7 Table and Figures

Mw, ϕ_c, R_p	$T_{2,tail}$ (ms)	$T_{2,dang}$ (ms)	f_{tail}	f_{dang}	f_{net}	$D_{res}/2\pi$ (Hz)
20k ϕ_c=0.4 R_p=1	48.0	13.0	0.652	0.261	0.087	196
12k ϕ_c=0.4 R_p=1	42.0	13.0	0.824	0.118	0.059	180
3k ϕ_c=0.4 R_p=1	130.0	20.0	0.838	0.100	0.062	103
12k ϕ_c=0.3 R_p=1	58.0	27.0	0.674	0.302	0.023	82.0
3k ϕ_c=0.3 R_p=1	150.0	14.0	0.884	0.070	0.047	62.1
20k ϕ_c=0.1 R_p=1	73.3	12.9	0.857	0.116	0.027	84.4
12k ϕ_c=0.1 R_p=1	64.0	25.2	0.951	0.042	0.007	69.7
3k ϕ_c=0.1 R_p=1	213.0		0.956			
20k ϕ_c=0 R_p=1	46.7		0.992	0.000	0.008	37.8
12k ϕ_c=0 R_p=1	65.2		0.982	0.000	0.018	32.7
3k ϕ_c=0.3 R_p=0.5	159.0		0.900			
12k ϕ_c=0.3 R_p=0.5	181.0		0.906			

Table 6.1 nDQ fitting results to Eq. (6.3)

(a)

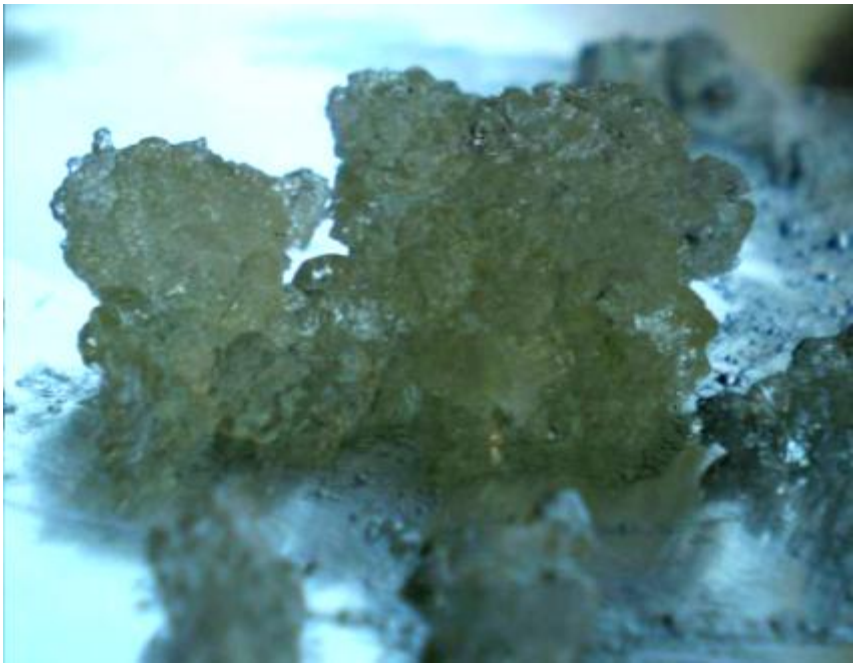

(b)



Figure 6.1 (a) silica nanoparticles in PEG 8000 at ϕ_c =0.315 at R_p=1 (b) same particles in PEG 8000 at ϕ_c =0.300 at R_p =0.5

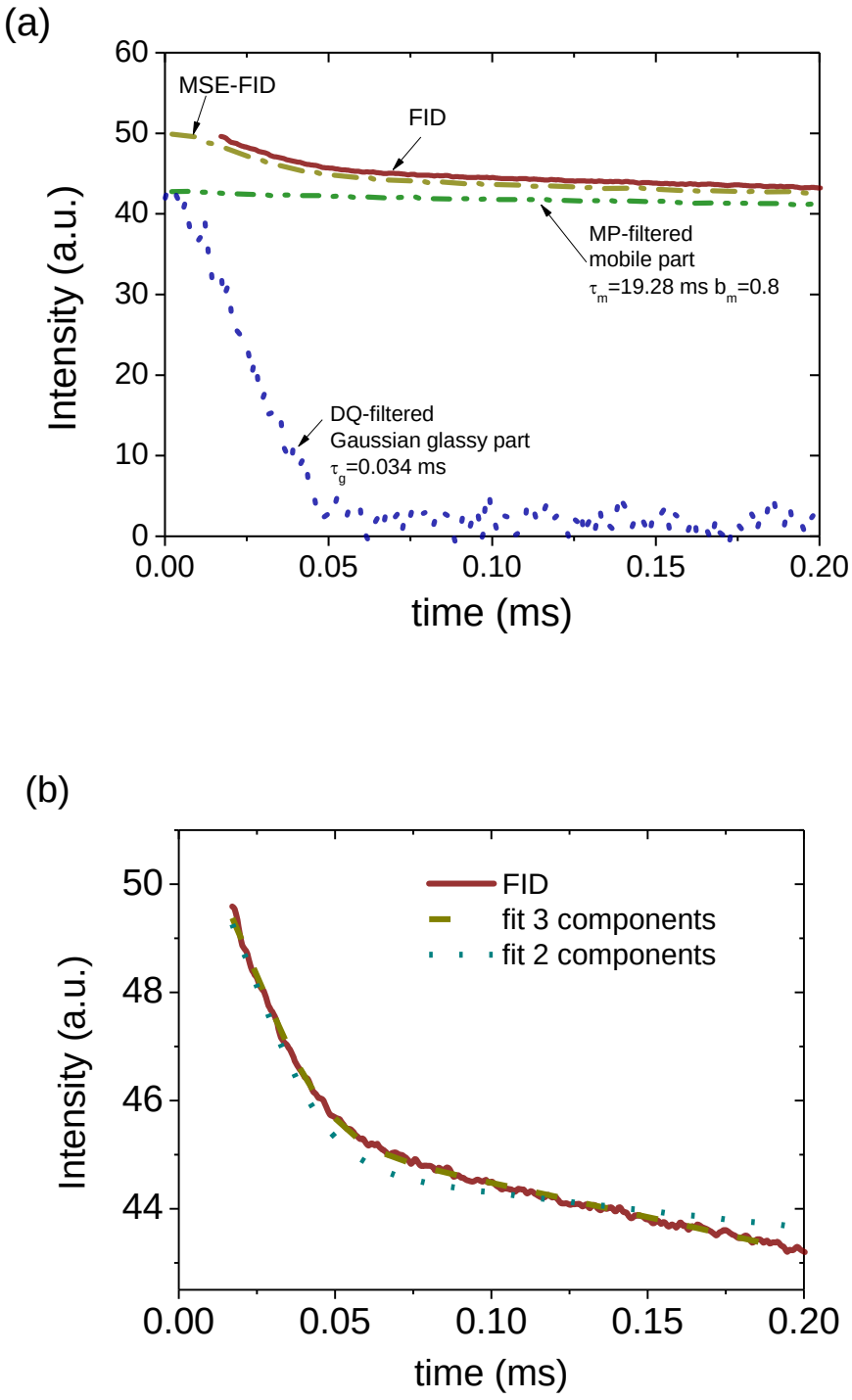

Figure 6.2 (a) FID, MSE-FID, MP and DQ signal as a function of the acquisition time for ϕ_c=0.4 PEG 20000 at 70°C. DQ signals are amplified to show with MP signals (b) FID fittings to Eq. (6.2) with the sum of 2 or 3 modified exponentials

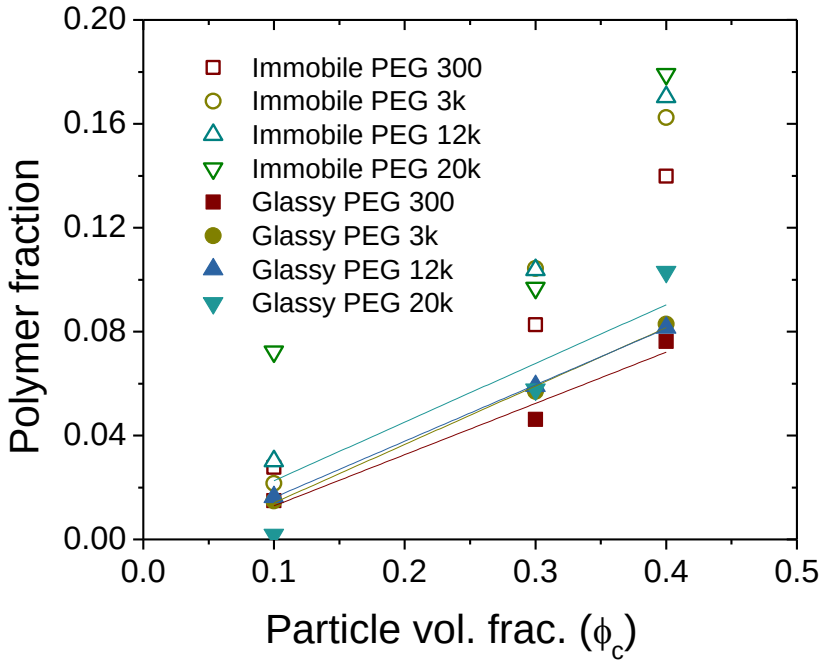

Figure 6.3 Glassy and immobile polymer fractions as a function of particle volume fraction with varying PEG molecular weight at 70°C

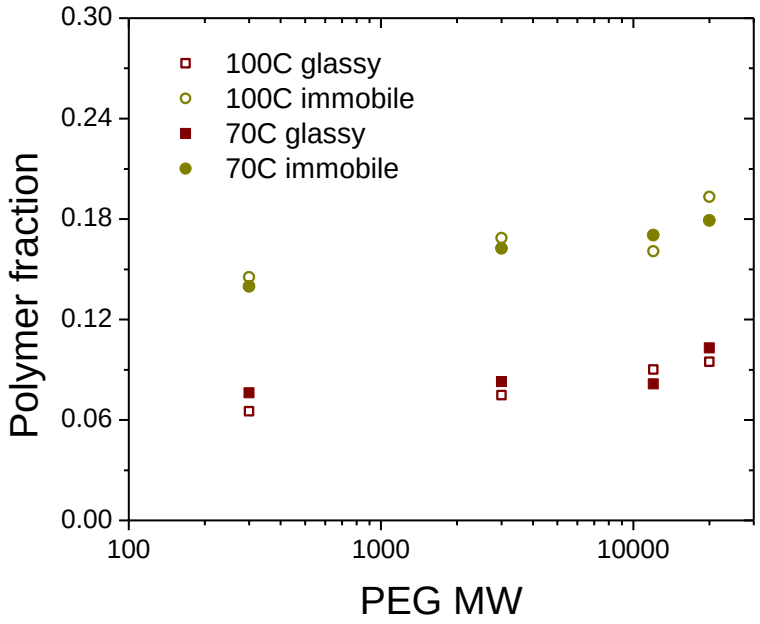

Figure 6.4 Polymer glassy and immobile fractions with varying molecular weight at two different temperature, 70°C and 100°C.

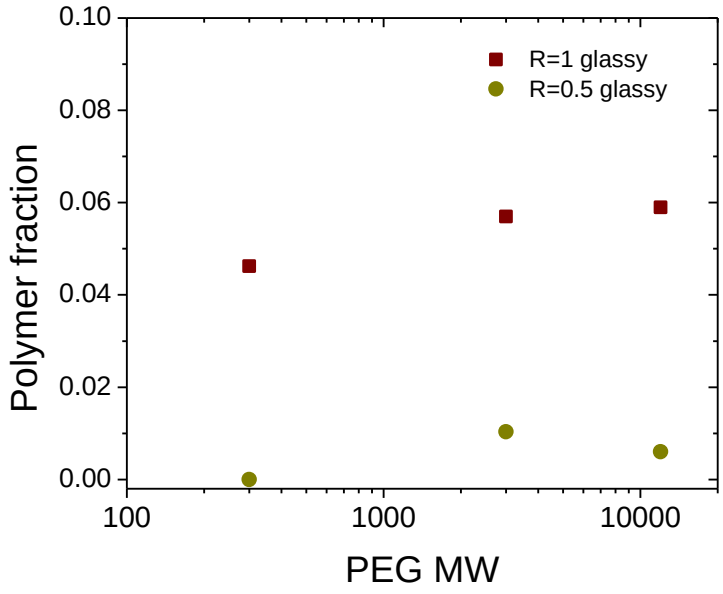

Figure 6.5 Polymer glassy fractions at polymer melt (R_p=1) and polymer solutions (R_p=0.5) with varying molecular weight

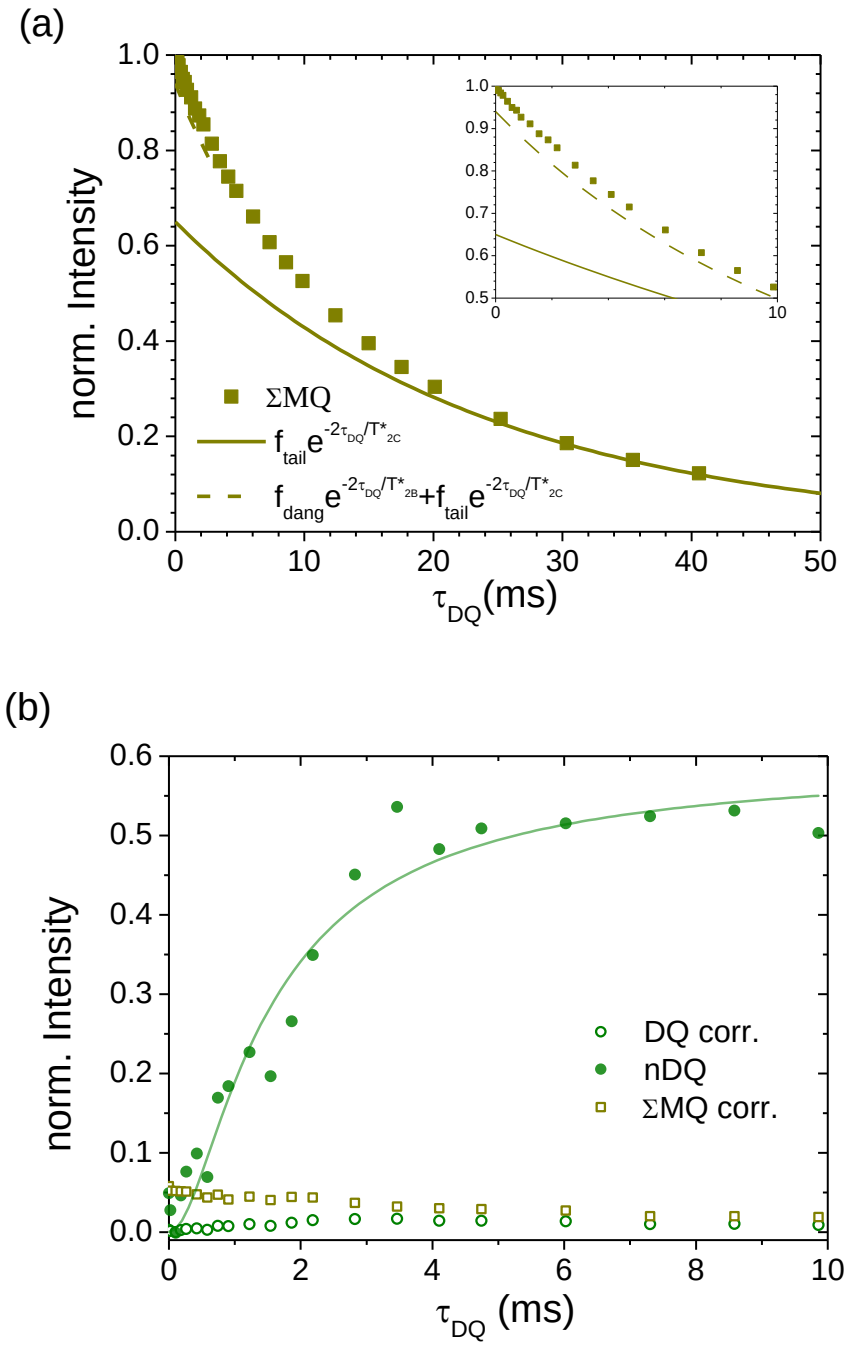

Figure 6.6 MQ NMR data decomposition for PEG 20000 ϕ_c=0.4 at 70C (a) The full $I_{\Sigma MQ}$ decay function and its fits to Eq. (6.2) for the determination of melt-like fractions (inset) expanded view at short time scale (b) After subtraction of the melt-like parts, data for ΣMQ and DQ is corrected. Empty squares and circles are corrected data to the overall signal functions, ΣMQ and DQ, respectively. Filled circles are normalized DQ build-up curves (nDQ) characterizing the network-like component, D_{res}. Solid curve is its fit to Eq. (6.3).

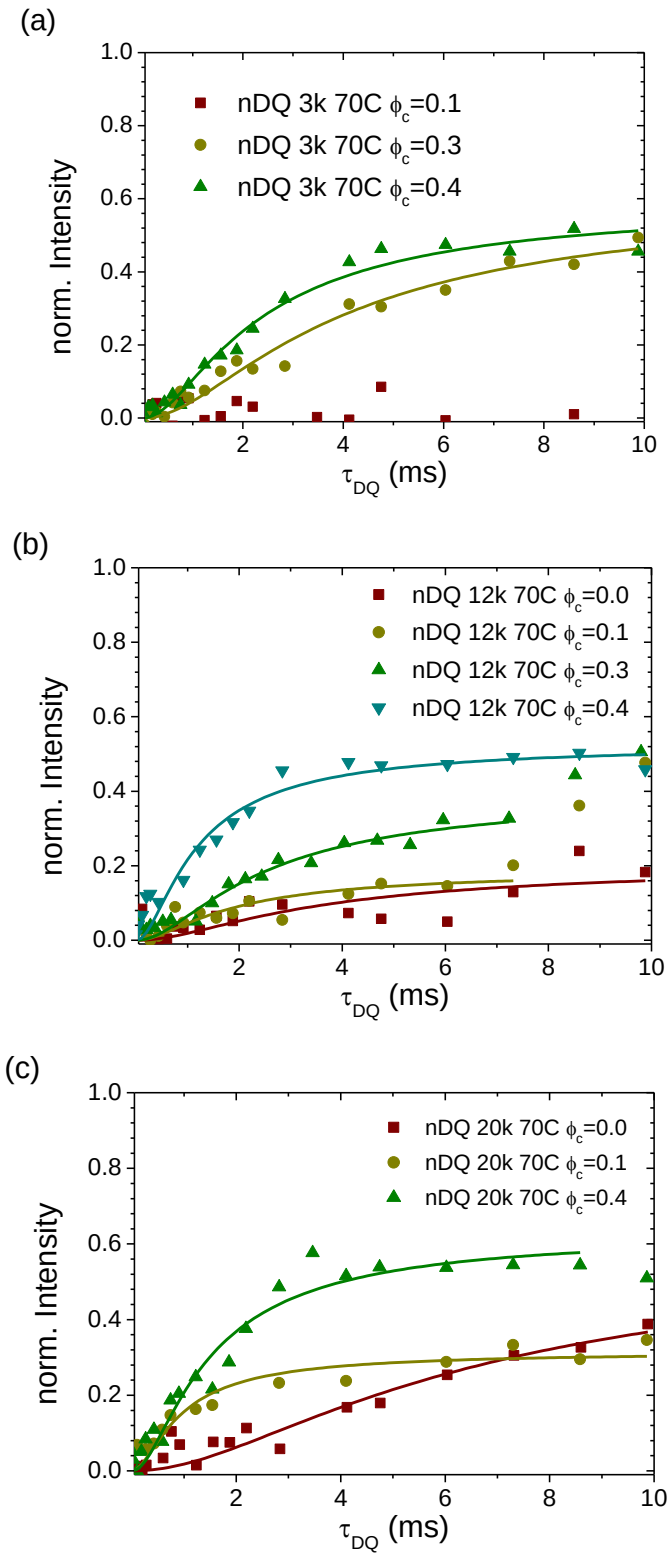

Figure 6.7 nDQ build-up curves of Silica-PEG composites with varying particle volume fractions (a) PEG 3000 (b) PEG 12000 and (c) PEG 20000

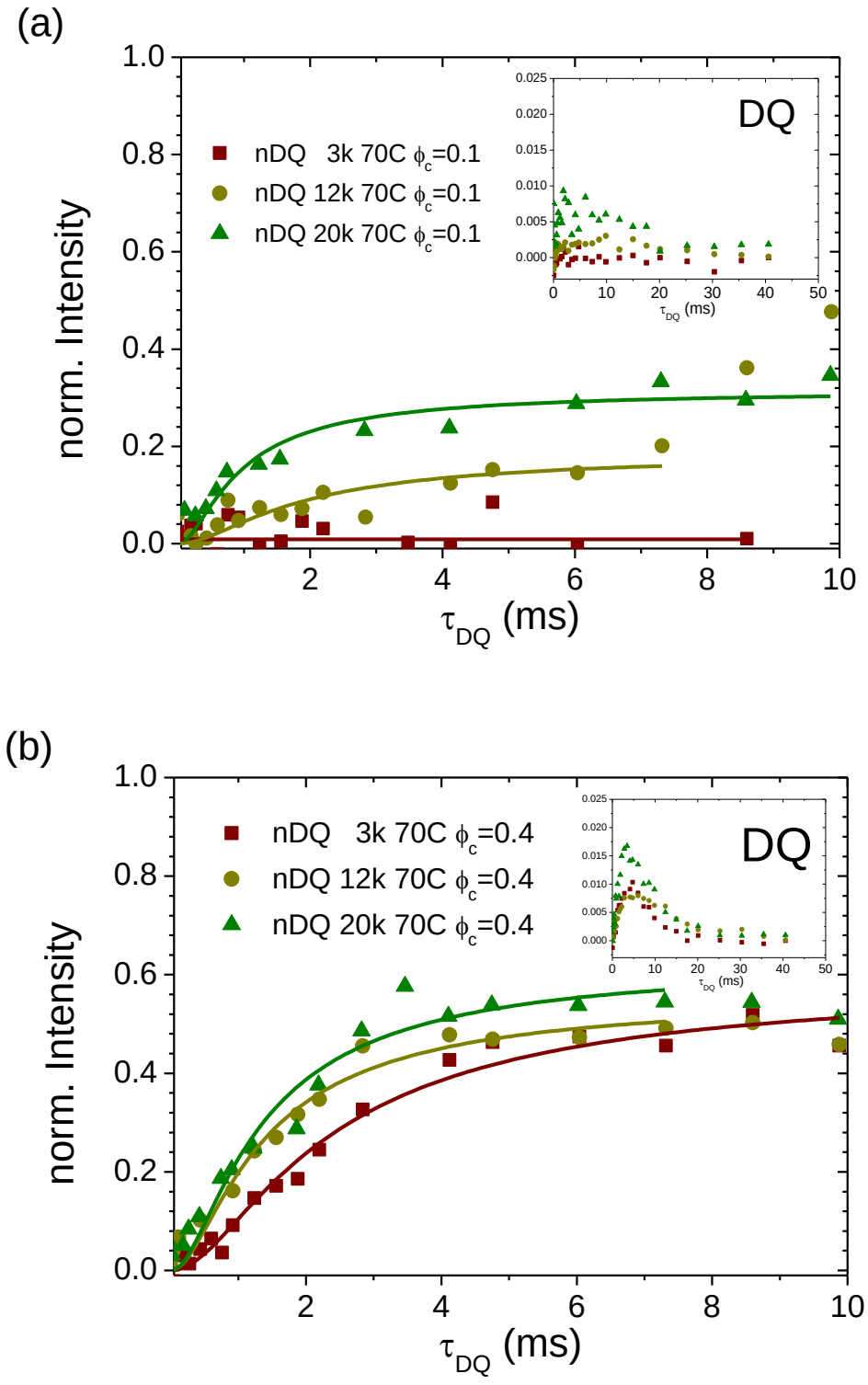

Figure 6.8 nDQ build-up curves and DQ intensity of Silica-PEG composites with varying polymer molecular weight (a) ϕ_c=0.1 (b) ϕ_c=0.4

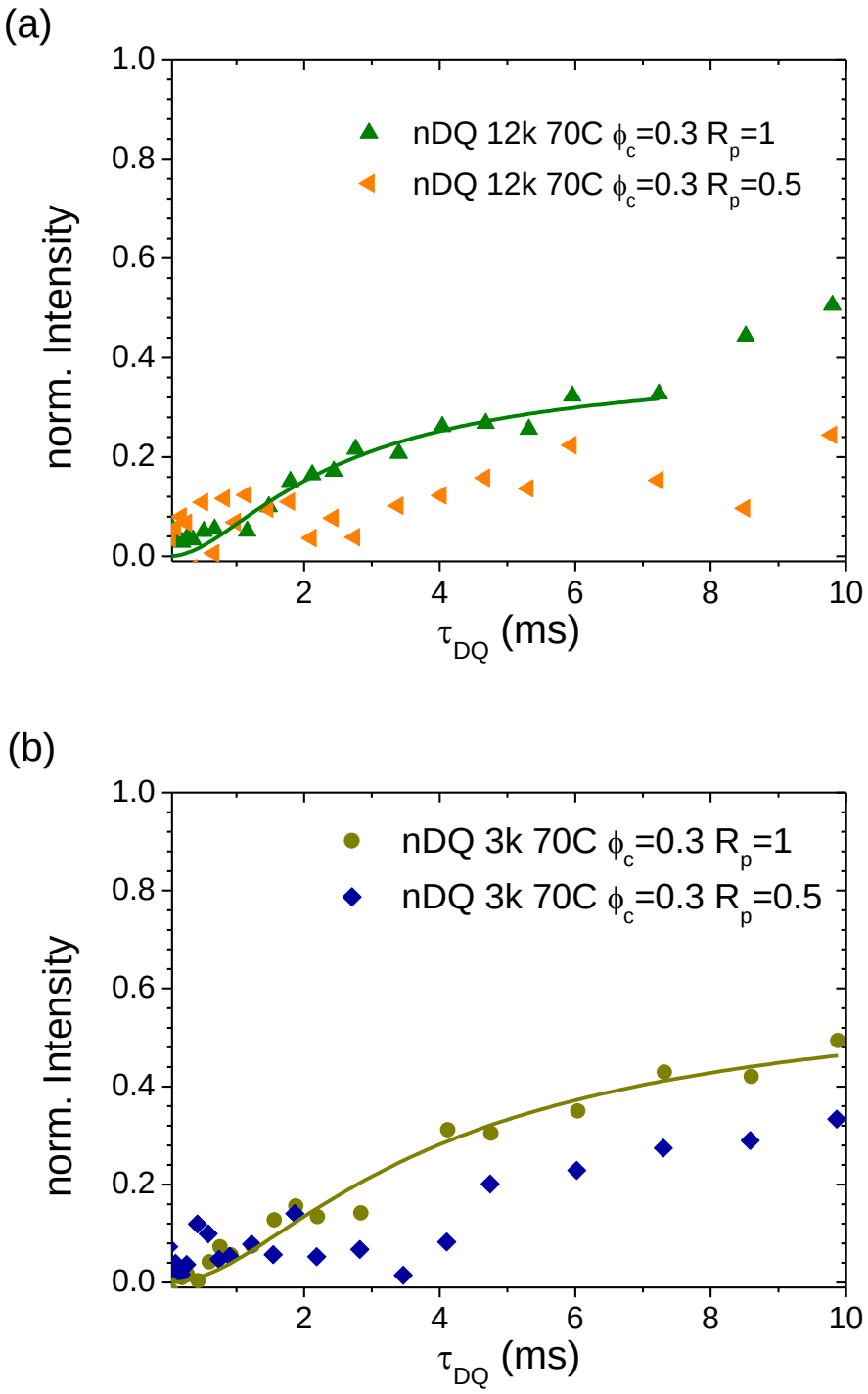

Figure 6.9 nDQ build-up curves of Silica-PEG composites and silica in polymer solutions at a fixed ϕ_c=0.3 at 70'C (a) PEG 12000 (b) PEG 3000

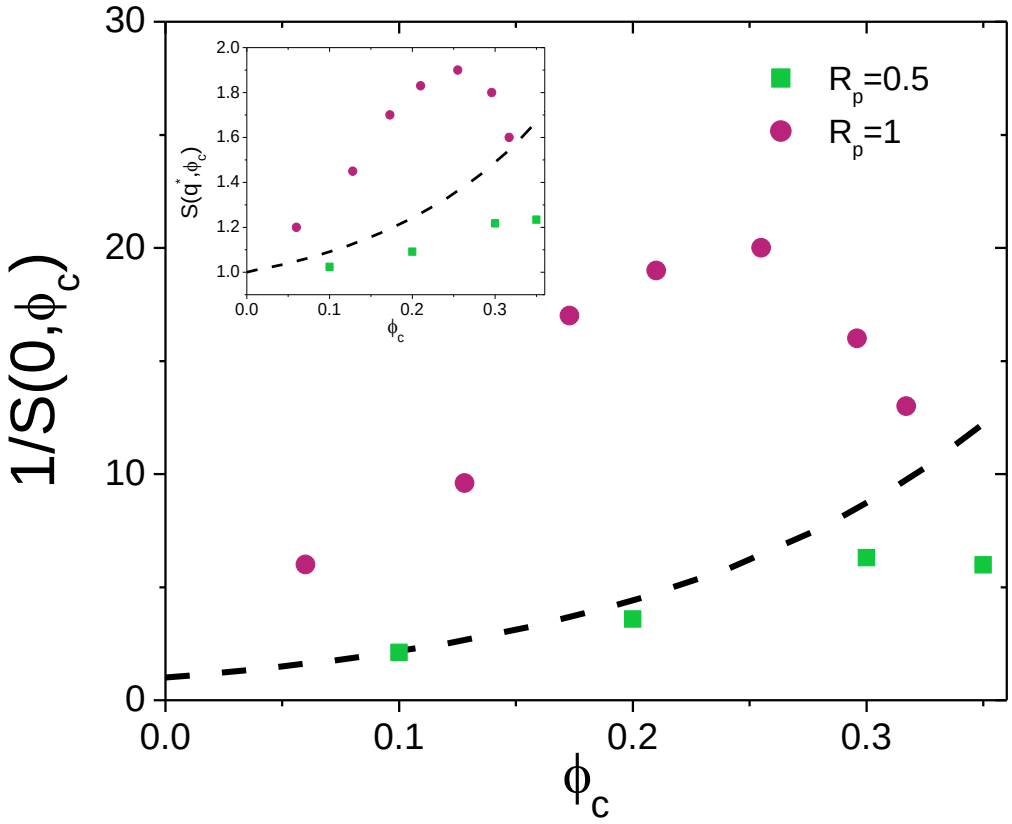

Figure 6.10 **(a)** Experimental inverse osmotic compressibilities (*1/S(0, ϕ_c)*) as a function of particle volume fraction (ϕ_c) for different R_p=0.5 and 1 for PEG 8000. (inset) Height of the cage peak of the particle structure factor (*S(q^*, ϕ_c)*) as a function of ϕ_c at the same condition.

6.8 References

1. Berriot, J.; Montes, H.; Lequeux, F.; Long, D.; Sotta, P. *Macromolecules* **2002**, *35*, 9756.
2. Long, D.; Lequeux, F. *Eur. Phys. J. E* **2001**, *4*, 371.
3. Fryer, D. S.; Peters, R. D.; Kim, E. J.; Tomaszewski, J. E.; De Pablo, J. J.; Nealey, P. F.; White, C. C.; Wu, W. L. *Macromolecules* **2001**, *34*, 5627.
4. Cohenaddad, J. P. *Polym. Commun.***1987**, *28*, 121.
5. Cohenaddad, J. P. *Polymer* **1992**, *33*, 2762.
6. Cohenaddad, J. P.; Roby, C.; Sauviat, M. *Polymer* **1985**, *26*, 1231.
7. Cohenaddad, J. P.; Viallat, A. *Polymer* **1986**, *27*, 1855.
8. Kirst, K. U.; Kremer, F.; Litvinov, V. M. *Macromolecules* **1993**, *26*, 975.
9. Litvinov, V. M.; Barthel, H.; Weis, J. *Macromolecules* **2002**, *35*, 4356.
10. Litvinov, V. M.; Zhdanov, A. A. *Vysokomol. Soedin. A+* **1987**, *29*, 1021.
11. Papon, A.; Saalwächter, K.; Schäler, K.; Guy, L.; Lequeux, F.; Montes, H. *Macromolecules* **2011**, *44*, 913.
12. Krutyeva, M.; Martin, J.; Arbe, A.; Colmenero, J.; Mijangos, C.; Schneider, G. J.; Unruh, T.; Su, Y.; Richter, D. *J. Chem. Phys.* **2009**, *131*.
13. Martín, J.; Krutyeva, M.; Monkenbusch, M.; Arbe, A.; Allgaier, J.; Radulescu, A.; Falus, P.; Maiz, J.; Mijangos, C.; Colmenero, J.; Richter, D. *Phys. Rev. Lett.* **2010**, *104*.
14. Serghei, A.; Mikhailova, Y.; Eichhorn, K. J.; Voit, B.; Kremer, F. *J. Polym. Sci. Pol. Phys.* **2006**, *44*, 3006.
15. Sangoro, J. R.; Iacob, C.; Serghei, A.; Friedrich, C.; Kremer, F. *Phys. Chem. Chem. Phys.* **2009**, *11*, 913.
16. Huth, H.; Minakov, A. A.; Serghei, A.; Kremer, F.; Schick, C. *Eur.Phys. J-Spec. Top.* **2007**, *141*, 153.
17. Napolitano, S.; Wübbenhorst, M. *Polymer* **2010**, *51*, 5309.
18. Napolitano, S.; Wübbenhorst, M. *Nature Comm.* **2011**, *2*.
19. Hall, L. M.; Anderson, B. J.; Zukoski, C. F.; Shweizer, K. S. *Macromolecules* **2009**, *42*, 8435.
20. Kim, S. Y.; Zukoski, C. F. *Langmuir* **2011**, *27*, 10455.
21. Kim, S. Y.; Hall, L. M.; Schweizer, K. S.; Zukoski, C. F. *Macromolecules* **2010**, *43*, 10123.
22. Mauri, M.; Thomann, Y.; Schneider, H.; Saalwächter, K. *Solid State Nucl. Mag.* **2008**, *34*,125.
23. Maus, A.; Hertlein, C.; Saalwächter, K. *Macromol. Chem. Physic* **2006**, *207*, 1150.
24. Saalwächter, K. *Prog. Nucl. Mag. Res. Sp.* **2007**, *51*, 1.
25. Saalwächter, K.; Herrero, B.; López-Manchado, M. A. *Macromolecules* **2005**, *38*, 9650.
26. Saalwächter, K. *J. Am. Chem. Soc.* **2003**, *125*, 14684.
27. Stober, W.; Fink, A.; Bohn, E. *J. Colloid Interf. Sci.* **1968**, *26*, 62.
28. Saalwächter, K.; Heuer, A. *Macromolecules* **2006**, *39*, 3291.

29. Kline, S. R. *J. Appl. Cryst.* **2006**, *39*, 895.
30. Anderson, B. J.; Zukoski, C. F. *Macromolecules* **2008**, *41*, 9326.
31. Anderson, B. J.; Zukoski, C. F. *Macromolecules* **2009**, *42*, 8370.
32. Rubinstein M.; R.H., C. *Polymer Physics*; oxford University Press: New York, 2003.
33. Cox, H. L.; Cretcher, L. H. *J. Am. Chem. Soc.* **1926**, *48*, 451.
34. Malcolm, G. N.; Rowlinson, J. S. *T. Faraday Soc.* **1957**, *53*.
35. Polik, W. F.; Burchard, W. *Macromolecules* **1983**, *16*, 978.
36. Saeki, S.; Kuwahara, N.; Nakata, M.; Kaneko, M. *Polymer* **1976**, *17*, 685.
37. Kjellander, R.; Florin, E. *J. Chem. Soc. Farad. T. 1* **1981**, *77*, 2053.
38. Papirer, E. *Adsorption on silica surfaces* New York, 2000; Vol. 90.
39. Holík, M.; Matějková, B. *J. Chromatogr. A* **1981**, *213*, 33.
40. Ek, S.; Root, A.; Peussa, M.; Niinistö, L. *Thermochim. Acta* **2001**, *379*, 201.
41. Kim, J. M.; Chang, S. M.; Kong, S. M.; Kim, K. S.; Kim, J.; Kim, W. S. *Ceram. Int.* **2009**, *35*, 1015.
42. Şerbescu, A.; Saalwächter, K. *Polymer* **2009**, *50*, 5434.
43. Hall, L. M.; Schweizer, K. S. *J. Chem. Phys.* **2008**, *128*.

CHAPTER 7 MOLECULAR WEIGHT EFFECTS ON PARTICLE AND POLYMER MICROSTRUCTURE IN CONCENTRATED POLYMER SOLUTIONS

7.1 Introduction

When the size of particles blended with polymers shrinks, properties emerge that cannot be predicted by standard mixing rules.[1,2] Understanding these properties has focused attention on the role of the particle interface in altering polymer configurations, degrees of entanglement and segment mobility. One of the most successful is the polymer reference site interaction model (PRISM)[3-6] of Schweizer and coworkers who have developed integral equation based models capable of predicting particle correlation functions for particles, polymers and their interface. This theory predicts that the state of particle dispersion is very sensitive to the strength of polymer segment- particle surface cohesion.[3,4] In the absence of sufficiently strong attractions the particles aggregate due to depletion forces. If the strength of cohesion between polymer segments and the particle surface is too strong, the polymer segments bridge particles, resulting in aggregation. Only at intermediate strengths of attraction between segments and the particle surface results in thermodynamic stability of particles in concentrated polymer solutions and melts. This theory has been tested in detail for low molecular weight polymers showing the capacity to predict particle and polymer density fluctuations over a wide range of length scales.[7-9] Key experimental results show that the strength of cohesion is independent of particle volume fraction but is sensitive to polymer type and can be varied by diluting the polymer with different solvents and altering temperature. Here we explore the effects of polymer molecular weight on suspension microstructure.

In our current study, 40 nm of diameter silica nanoparticles are suspended in dense polyethylene glycol (PEG) solutions. While PEG molecular weight varies from 300 to 20,000, PEG can adsorb on the silica particles, which affects the state of polymer and particle dispersions and thus, polymer mobility changes from bulk to near particle surface. In this regard, systematic variations on the microstructure of nanoparticles and polymers in dense polymer solutions and their stability are examined focusing on the molecular weight effect linking to the polymer dynamics.

We show substantial variations in microstructure of silica particles suspended in polymer solutions. Polymer concentration is described by the ratio of PEG to PEG plus solvent volumes (R_p) which is fixed at a high value of 0.45 which ensures physical behavior representative of melts since the monomer collective density fluctuation correlation length is of order the segment size, a nanometer. First, small angle x-ray scattering technique is used to show methodical variations of osmotic compressibility and particle orderings upon molecular weight changes. Secondly, these results are compared with PRISM theory. With all other parameters held constant, PRISM predicts a weak sensitivity to the polymer's degree of polymerization. To understand the differences between model predictions and experimental observations we explore the changes in polymer environment using free induction decay NMR relaxation techniques demonstrating that the presence of particle surfaces produces glassy polymer relaxation states where the fraction of spins in glassy environments is independent of polymer molecular weight. We further explore the properties of the polymer near the particle surface using contrast matching small angle neutron scattering experiments yielding polymer and particle partial structure factors from which the form factor of the adsorbed polymer layer can be extracted. This provides evidence for changes in polymer layer thickness with varying particle volume fraction and polymer molecular

weight. These results combine to suggest that polymer adsorbs to the particle surfaces in a largely molecular weight independent manner. Thus it is not clear if the observed structural changes can be attributed to variations in the strength of segment- surface cohesion. Within the context of PRISM, extensive calculations suggest the changes in polymer structure can only be captured by varying the size ratio of particle diameter to polymer radius of gyration.

7.2 Experiment and Theory

7.2.1 Sample Preparation

Particle synthesis and sample preparation were already introduced in Section 2.2.1. Table 7.1 provides all sample descriptions used in this study. Polymer concentration is expressed in terms of the parameter, R_p, defined in Sections 2.2.1 and 4.2.2. In all experiments R_p is fixed to be 0.45 or 0.5 depending on the experiments shown in Table 7.1 to only observe the effect of the molecular weights. Deionized water (H_2O) was used for solvent for SAXS experiments and D_2O was used for NMR experiments. To use contrast matching method for SANS, ratio of H_2O to D_2O varied as described in Section 5.3.1 and will be discussed in Section 7.2.5.

7.2.2 Small Angle X-ray Scattering

Small angle x-ray scattering is performed at Sector 5 of the Advanced Photon Source (Argonne National laboratory). Details were given in Section 4.2.4 and scattering principles were given in 2.2.3.

7.2.3 PRISM theory

As already introduced in previous chapters, PRISM theory[3-5,10] has been extensively applied to polymer nanocomposites melts and concentrated polymer solutions. The mixture model and PRISM theory employed here are identical to prior studies. (See Sections 2.3 and 3.3) The homopolymer is a freely jointed chain composed of N spherical sites (diameter d) with a bond length of l/d=4/3, nanoparticles are spheres of diameter D, and all species interact via pair decomposable hard core repulsions. The chemical nature of the polymer-particle mixtures enters via a two-parameter Yukawa interfacial attraction with contact attractive energy of ε_{pc} and decay length of the segment-colloid interaction of αd.

In the Sections 2.3 and 3.3, we vary several parameters to capture the effect of increasing molecular weight; i) degree of polymerization (N), ii) the interaction potential of polymer segments and particles via the range of interfacial attraction (α) and iii) via the strength of attraction (ε_{pc}), and iv) the size ratio of particle to polymer, (D/d) is varied.

7.2.4 MSE-FID

Fundamental details for MSE-FID are found in Section 6.2.3.

7.2.5 Small Angle Neutron Scattering (SANS)

The intensity, $I(q)$, of scattered neutrons at wave vector q, has three contributions:

$$I(q) = n_c \Delta\rho_c^{\,2} P_c(q) S_{cc}(q,\phi_c) + 2\Delta\rho_c \Delta\rho_p \sqrt{n_c n_p P_c(q)} S_{cp}(q) + n_p \Delta\rho_p^{\,2} S_{pp}(q) \qquad (5.1)$$

where $n_j = \rho^*_j V_j^2$, and ρ^*_j and V_j are number density and unit volume of the jth component, respectively. $\Delta\rho_j$ is the difference of scattering length density of component j and the medium,

$P_c(q)$ is the particle form factor, and $S_{ij}(q)$ are the structure factors associated with two components (*pp, pc, cc*) where the subscript *p (c)* indicates polymer segments (colloids).

As introduced in Chapter 5, to employ the contrast matching method, the scattering length density (SLD) of nanoparticles, polymer segments and solvent are determined. Since increasing molecular weights does not affect the scattering length density of polymer, the matching criteria remain the same with increasing PEG molecular weight. As a result, we confirmed again that the SLD of silica satisfies $\Delta\rho_p \sim 0$ at $x_D/(x_H+x_D)=0.175$ in Eq. (5.1) and thus, scattering is dominated by particles. At $x_D/(x_H+x_D)=1$, scattering from the polymer dominates the signal where $\Delta\rho_c \sim 0$ is satisfied. [11]

As shown in Fig. 5.2, scattering measurements at a fixed ϕ_c were made at two D_2O/H_2O ratios corresponding to $\Delta\rho_p \sim 0$ at $x_D/(x_H+x_D) = 0.175$ (labeled as 'A'), $\Delta\rho_c \sim 0$ at $x_D/(x_H+x_D)$ =0.100 (labeled as 'D') and four intermediate values close to $\Delta\rho_c=0$ at $x_D/(x_H+x_D)$=0.90, 0.925, 0.95 and 0.975 (labeled as 'B', 'B*', 'C' and 'C*').

Changes in the scattering profile with variations in x_H/x_D are shown in Fig. 7.1 for a silica volume fraction sample of ϕ_c=0.2 suspended in a solution containing R_p=0.45 PEG1000 where only the D_2O/H_2O ratio is varied. At low D_2O concentrations (labeled as 'A'), the scattering is dominated by the particles, such that the intensity is proportional to $P_c(q)S_{cc}(q)$. One sees the existence of a well-defined zero angle limit to the scattered intensity indicating a stable particle suspension, a first peak in $S_{cc}(q)$ associated with liquid-like particle packing, and decaying intensity as wave vector increases following $P_c(q)$. The height of the first peak is greatly reduced from that of PEG 400 in Fig. 5.3. As the D_2O concentration increases, substantial qualitative changes are observed in the scattering profile. At $x_D/(x_H+x_D)$ =0.90 (labeled as 'B'), the first peak in S_{cc} moves and decreases as expected for decreasing $\Delta\rho_c$ and second peak moves to the higher

q-vector while losing information about P_c at high q. At $x_D/(x_H+x_D)$=0.925, and 0.95 (labeled as 'B*' and 'C'), these trends are accelerated. At $x_D/(x_H+x_D)$=0.975 (labeled as 'C*'), the first peak in S_{cc} is no longer observable and a new peak emerges near at q~0.02 A^{-1}, while the S_{pc} and S_{pp} contributions begin to dominate the measured scattering intensity as the condition $\Delta\rho_p >> \Delta\rho_c$ is approached. At $x_D/(x_H+x_D)$=1 (labeled as 'D'), scattering from the polymer dominates the signal.

To extract each $S_{ij}(q)$ from Eq. 5.1, we first determine $\Delta\rho_c$ and $\Delta\rho_p$ from the known ρ_c and ρ_s at each D_2O/H_2O ratio using the information in Fig. 5.2. The quantities n_c and n_p are determined from the mass and size of the silica particles and polymers for each sample, respectively. At $x_D/(x_H+x_D)$ = 0.175 where $\Delta\rho_p$=0, Eq. 5.1 is simplified as $I(q) = n_c \Delta\rho_c^2 P_c(q) S_{cc}(q,\phi_c)$. $P_c(q)$ is experimentally determined as explained above. $S_{cc}(q)$ is obtained by dividing the scattering intensity from the concentrated particle suspension by its dilute limit analog at the same R_p : $S_{cc}(q,\phi_c) = \frac{I(q,\phi_c)}{I_{ds}(q,\phi_c)} \frac{\phi_{c,low}}{\phi_c}$. After the second step using the measurement 'A', only $S_{pp}(q)$ and $S_{pc}(q)$ remain unknown. At each scattering vector, one then has three experimental data points at points 'B', 'B*', 'C', 'C*' and 'D' and two unknowns allowing us to minimize uncertainty in the two unknowns at each q.

At point 'D' where $\Delta\rho_c$~0 there is still a small contribution from silica since it is difficult to perfectly match the scattering from a large porous particle. Thus, we account for the first term in Eq. 5.1 based on knowledge of n_c, P_c, S_{cc} and the changed $\Delta\rho_c$ determined at 'D'. Once all the known parameters are employed, Eq. 5.1 is simplified to $I_k(q)=a_k+b_kS_{pc}(q)+c_kS_{pp}(q)$ where a_k and b_k are q-dependent constants and c_k is a q-independent constant. The subscript k denotes the D_2O ratio such as B, B*, C, C* and D. These constants change with D_2O content in a known

manner. With two unknowns and four equations, we solve $S_{pp}(q)$ and $S_{pc}(q)$ using multiple linear regression fitting method at each q.

7.3 Results

7.3.1 Small Angle X-ray Scattering

State of particle dispersions and osmotic compressibility are analyzed with small angle x-ray scatterings. Scattering density for x-ray is determined from the electron density. In Eq. (5.1), $\Delta\rho_p \sim 0$ is satisfied in that silica is much electron denser than that of PEG. Thus, Eq. (5.1) is simplified to $I(q) = n_c \Delta\rho_c^2 P_c(q) S_{cc}(q,\phi_c)$. When the light source of scattering is x-ray, it becomes

$$I(q,\phi_c) = \phi_c V_c \Delta\rho_e^2 P_c(q) S_{cc}(q,\phi_c) + B \quad (2.1)$$

With Eq. (2.4), collective particle structure factors are calculated so that we can observe the change in particle structures with varying molecular weight. We first look at the change of structure factors with increasing particle volume fraction. Figure 7.2 shows the structure factors at a given PEG 300 R_p=0.45 with varying ϕ_c. As described in Section 2.2.3, the anticipated trends with increasing particle volume fractions are shown in Fig. 7.2: (i) long wavelength density fluctuations are suppressed ($S_{cc}(0)$ decreases), (ii) coherency of the cage scale order increases ($S(q^*)$ increases), and (iii) the position of the cage peak moves to the higher value of qD.

Figure 7.3 shows the structure factors at a fixed ϕ_c =0.17, but with increasing polymer molecular weights. From PEG 300 to PEG 400, no quantitative difference is found. However, when molecular weight increases from 300 to 3000, 8000 and 12000, features are distinctively changed. First, the zero angle limit structure factor ($S_{cc}(0)$) continuously increases as molecular

weight increase. This suggests long wavelength density increase and particle subsystem becomes more compressible with higher molecular weight. Second, the height of the first peak decreases significantly. Particle structures are less ordered as molecular weight increases. When PEG molecular weight is 12000, there is only weak structure with *S(q)* approaching unity at all length scales. Lastly, position of the first peak moves to the higher wave vector suggesting the distance between particle centers of mass are closer at higher molecular weights in a qualitative similar manner as seen when particle volume fractions are increased (Fig. 7.2). With increasing molecular weights, the observed trends consistently indicate the silica particle subsystem becomes less stable suggesting a change from repulsive to attractive pair potentials of mean force.

To clarify the variations in the structures more quantitatively, we plot the osmotic compressibility from the inverse of zero-limit structure factors ($S_{cc}(0)$) as a function of particle volume fractions.

Fig. 7.4 shows the inverse osmotic compressibility as a function of particle volume fractions with different polymer molecular weights; 300, 400, 3000 and 8000. As indicated in Fig. 7.3 the system is least compressible when particles are suspended in PEG 300- water mixtures and become more compressible at higher molecular weights for a wide range of particle volume fractions. Below we present PRISM predictions at different conditions to capture the variations of particle microstructures upon molecular weight change.

7.3.2 PRISM

Previous studies shown in Chapters 2, 3 and 4 demonstrate the sensitivity of particle microstructure to changes in polymer-to-solvent ratio, solvent quality, polymer types, and temperatures. Further, the observed changes in local order, long wave length density fluctuations

and collective structure factors are well captured by PRISM predictions when the strength of attraction between polymer segments and particles, ε_{pc} is methodically varied.

Indeed, ε_{pc} which represents the overall enthalpic gain of transferring a segment from the suspending phase to the particle surface is a critical parameter to determine the system stability and is thus sensitive to the chemical nature of the particles, polymer and solvent. However, one notes the chemical nature of the mixtures enters with not only the strength of an interfacial attraction at contact, ε_{pc} but spatial range α (in units of the monomer diameter). The polymer segment- particle surface pair potential is written as:

$$U_{pc}(r) = -\varepsilon_{pc} \exp\left(\frac{-(r-(D+d)/2)}{\alpha d} \right) \tag{2.9}$$

Furthermore, models contain the degree of polymerization, *N* and size ratio, *D/d*. The effects of variations of all these parameters have been undertaken revealing the dependency of particle miscibility and structures on *N*, ε_{pc}, α and *D/d*. For the present comparisons in Chapters 2, 3, 4 and 5, *N*=100, *D/d*=10, and α=0.5*d*, which are typical values as motivated from previous studies and ε_{pc} is effectively controlled. These parameters are chosen because of an observed weak dependency of predictions on *N*, asymptotic predictions as *D/d* gets large (experimentally we are have a system where *D/d*= 44/0.6), and physically realistic extend of interaction between polymer segments and particle surfaces under the action of van der Waals forces. Nevertheless, the comparisons with between experiments and theory have all be undertaken for molecular weights of 2000 g/mol and smaller.

When polymer molecular weight is increased, the first assumption one can make in PRISM theory is *N* should need to be increased as well. Fig. 7.4a shows the PRISM predictions when is increased from 100 to 400, 2000, and 10000. The lack of change in microstructure with

variations in N was reported by Hall *et al.* who associate the weak dependence on a high total volume fraction.[3,7] Furthermore, a weak dependency is to be expected in equilibrium when the polymer melt density correlation length is of the order of a monomer diameter. Indeed, varying N will fine-tune the potential of mean force (PMF) by enhancing or suppressing local minimum features. All other parameters held constant, PRISM does not predict variations in $S_{cc}(0)$ with changes in N.

The amplitude and range in PMF are controlled by the segment diameter and are identified with the incomplete screening of the polymer correlation hole.[4,5] There is theoretical precedence for a long-range part of $g_{cc}(r)$ in polymer-colloid suspensions. However, this contribution to the PMF is so weak under nearly incompressible melt conditions that it likely has negligible consequences.[7,12]

Within the theory, a primary effect of increasing N is to decrease bulk modulus; the N=10000 system appears less dense than N=100 system in the sense that interchain packing is worse due to the interchain overlaps.[12,13] However, this effect is minimized at high total volume fractions. In experimentally accessible constant pressure systems, the bulk modulus should be approximately N-independent, so increasing or decreasing N would not likely be critical in determining phase stability or particle microstructure.[7] Experimentally, however, we see substantial changes as we vary molecular weight. (Fig. 7.4a) In keeping with previous studies, the next logical parameter within PRISM to vary is the interfacial attraction, ε_{pc} in the manner done in Chapters 2, 3, 4 and 5. PRISM predictions are drawn in Fig. 7.4b showing the effect of varying ε_{pc} on the compressibility. When ε_{pc} increases from 0.15 to 0.45 kT, increased adsorption of polymer segments to the particle provide additional steric stability yielding reduced osmotic compressibility. However, when ε_{pc} further increases up to 0.95 and 1.05 kT, bridging between

particle segments is predicted to occur- driving particle aggregation. Thus, if the strength of attraction is too large, strong interfacial attractions increase system compressibility. Variable ε_{pc} partially captures the molecular weight effects based on the idea that increasing polymer molecular weight decreases the interfacial attraction ε_{pc}.

Another idea is to vary the spatial range of attraction, α. We show the effect of changing α on the osmotic compressibility in Figure 7.4c. As shown in Eq. (2.9), increasing α brings about a similar effect as increasing ε_{pc}. But, a minimum is $1/S_{cc}(0)$ with increasing α is not observed in Fig 7.4c.

Lastly, we focus on the size ratio of particle to monomers, *D/d*. The polymer radius of gyration is approximated as $R_g \sim \sqrt{N}d$. One obvious observation from the increasing molecular weight is that the polymer radius of gyration is also increased. Thus, as *d* is a segment size and not a physical monomer size, one can imagine that increasing molecular weight will increase *N* or *d*. Due to the dense polymer system envisioned, PRISM shows a weak dependency on *N*, which is clearly out of step with experimental observations. Here we explore an alternative way of characterizing changes in polymer degree of polymerization by imagining that changes in *N* can be captured by PRISM through alterations in *d*.

Changing *D/d* will have an initial impact by altering the absolute decay length of Yukawa potentials in Eq. (2.9) for the interfacial attraction of polymer segments and particles. In addition, however, the total volume fraction will be a function of *d/D*. As introduced in Eq. (2.11)

$$\phi_t = \phi_c + \phi_{p0}\left(1-\phi_c\left(1+\left(d/D\right)\right)^3\right) \qquad (2.11)$$

Where ϕ_t is the total volume fraction in the system, ϕ_c is the colloid volume fraction and ϕ_{p0} is the polymer concentration in the absence of particles. When increasing molecular weight is

understood as increasing polymer segment size, *D/d* values will be reduced. Therefore, at fixed ϕ_c, the total volume fraction of the system is decreased. A unique feature of decreasing total volume fraction is that as *D/d* is reduced, the bulk modulus of the composite decreases (or the composite becomes more compressible.) This equation neglects the consequences of overlap of the excluded volume shells of particles. A more accurate expression for the free volume is given in Ref. [14,15]. However, for the large *D/d* values and particle volume fractions below than 0.5, the differences are negligible.

In this regard, we plot PRISM predictions on the osmotic compressibility with various *D/d* values in Fig. 7.4d. Generally, reducing *D/d* yields enhances density fluctuations. One notes this is contrary to the conventional depletion attraction theories where a decrease in *D/d* with all other parameters held constant will reduce the strength of the depletion attraction. While PRISM is designed to maintain a constant segment density far from particle surfaces as ϕ_c is increased, by taking into account the volume around each particle where polymer segment centers cannot enter, as *D/d* is decreased, we reduce the number density of polymer segments per volume composite. Fig. 7.4 shows that in the concentrated polymer solution and melts, this reduction in overall polymer segment volume fraction dominates changes to the particle potential of mean force. More interestingly, of all the comparisons shown in Fig. 7.4, the best agreement between PRISM predictions and the experimental results occurs where molecular weight dependence is taken into account with variations in *D/d*. Experimentally increasing polymer molecular weights enhance intramolecular overlaps with increasing R_g, which translates to a smaller effective volume fractions and a higher compressibility.

To achieve a deeper understanding of how PRISM predictions change with variations in ε_{pc}, α and *D/d*, in Fig 7.5, we look at the polymer segment- particle pair correlation function.

Reducing the strength of attraction between polymer segments and particle reduces the concentration of polymer segments on particle surface. As briefly discussed in Section 4.5, the degree of enhancement of probability of polymer segments at the particle surface decreases with ε_{pc}. Thus, if the observed changes of structures result from the decreasing interfacial attraction upon increasing polymer molecular weights, one can expect to also observe systematically decreasing polymer adsorption. Below we explore this possibility with NMR experiments.

In the same context, variation of α yields a similar effect on $g_{pc}(r)$ in Fig. 7.5b. Although for the range of a values explored, the contract values for $g_{pc}(r)$ drop less than those shown for the ε_{pc} case, polymer segment concentration at the particle surface is reduced as the spatial range of the attraction is reduced.

Fig. 7.5c shows the $g_{pc}(r)$ with different D/d ratios. While reducing ε_{pc} or α suggest systematically and significantly reduced polymer adsorption, $g_{pc}(r)$ shows a weak dependency on the size ratio of D/d. The polymer segment to particle surface distance is re-scaled in the inset of Fig. 7.5c with particle diameter, D. Thus, if we interpret increasing molecular weight as a decrease in D/d while particle microstructures and composite compressibilities are changed greatly, the number of polymer segments next to the particle surface will remain relatively constant. Indeed Fig. 7.5c suggests that as D/d is reduced there is a small increase in the number of segments in the first adsorbed layer.

We are also able to calculate the potential of mean force between two particles in a dilute state. These are plotted in Fig. 7.6a, b and c. Fig. 7.6c is rescaled with the particle diameter in Fig. 7.6d. Consistent with Fig. 7.5, changes in ε_{pc} or α result in significant changes to the potential of mean force turning on or off the interfacial attractions while potential of mean force for two particles in dilute limit does not change with variations in D/d.

Below we examine the differentiation of polymer segment mobilities from MSE-FID measurements and link these to variations in polymer adsorption with molecular weight.

7.3.3 Polymer Mobility

The free induction decay of polarized proton spins is used here to probe the impact of silica nanoparticles on the dynamics of polymer segments. Specifically we focus on how changing the polymer molecular weight alters the polymer segment mobility. Using free induction decay techniques introduced in Section 6.3, we assume a multiple exponential spin-spin relaxation response (T_2) is associated with three different types of polymer segmental mobility; (i) mobile and melt-like polymer segments as would be observed in the bulk far from the particle surfaces or in the absence of particles, (ii) intermediately perturbed polymer segments such as loops and tails near the particle surface, but not directly in contact with the particle surface and (iii) rigid and glassy polymer segments in direct contact with the particle surface. In the bulk there is weak coupling and the spin polarization decays slowly. In the glassy state the spins are strongly coupled and polarization decays rapidly. To avoid dead time issues that occur due to the rapid decay of glassy spins,[16,17] we employed MSE pulse sequences which restore the relaxation decays at short times so fully recovered FID signals obtained.[16-18] Thus by measuring a complete free induction decay (FID) polarization spin relaxation time spectrum, we are able to estimate the fraction of spins in these different states. The differentiation of polymer dynamics using MSE-FID has been well-established and employed in many studies.[16-18] The FID time spectrum is written:

$$I(t) = I_0(f_g \exp(-t(\tau_g)^{b_g} + f_i \exp(-t(\tau_i)^{b_i} + f_m \exp(-t(\tau_m)^{b_m}) \qquad (6.1)$$

I_0 is the intensity at t=0, f_k is the fraction of the component k, τ_α are relaxation times for the α process with α=g, i and m corresponding to glassy, intermediate and mobile parts, respectively.

Figure 7.7a shows MSE-FID for PEG 300 at R_p=0.5 with ϕ_c is fixed at 0.0 and 0.3. With no particles in the polymer solution, the intensity decays exponentially with a single relaxation time. As particles are added, the relaxation time spectra changes dramatically suggesting at least two different polymer relaxation processes exist. While it is clear that many of the spins retain their bulk relaxation times, the growth of fast relaxation processes suggests that there is strong coupling of spins associated with physically adsorbed polymer segments. For the molecular weights studied, the MSE-FID spectra are fit with Eq. (6.1) to quantify the polymer dynamics more precisely.

Figure 7.7b shows FID relaxations at a fixed particle volume fraction of ϕ_c=0.3 with various polymer molecular weights. Interestingly, all four signals decay in a similar manner despite the large changes seen in structure factors. (Fig. 7.4)

Detailed methods for the determination of each polymer fractions, f_k and relaxation time constants (τ_k, b_k) are well-established and introduced in Section 6.3. As a result, we discuss the methods of extracting the fitting parameters only briefly. First, glassy polymer segment constants (τ_g,b_g) are determined by using ^{1}H-double-quantum filters, where selective magnetization of only rigid phase is realized and a Gaussian decay of the intensity is assumed.[16-18] τ_g was 0.028-0.031 s for various PEG molecular weights indicating mobility of glassy polymer segments at the surface is insensitive to polymer molecular weights. Then, the relaxation parameters of the mobile polymer segments constants (τ_m, b_m) are determined by using ^{1}H-"magic angle polarization" filters for a selective polarization of the mobile phase in order to remove unwanted rigid and

intermediate contributions. After the two steps, only f_g, f_i, τ_i and b_i remain unknown in Eq. (6.1) and thus determined by fitting to Eq. (6.1).

A challenge in interpreting the ^{1}H signals comes from hydroxyl group of silica particles. Note that less than 3 % of total polymer segments are rigid or glassy in our system and therefore, to determine the contribution of hydroxyl groups of silica to the ^{1}H signals is critical because glassy polymer fractions can be overestimated. The content of hydroxyl groups in silica has been estimated by various methods.[19-21] Assuming approximately 3 wt% of polymer segments are in a rigid state corresponds to 1% of the total mass of polymer for ϕ_c=0.3 and R_p=0.5 whereas Kim *et al.*[21] reported that the hydroxyl mass fraction in silica is 0.3 wt% of the sample corresponds to hydroxyls that can contribute to the rigid part signals. Thus we estimate that up to 10 % of the rigid signal may correspond to proton spins associated with the particle irrespective of the presence of monomer.

The fraction of spins in the glassy polymer fraction at a fixed ϕ_c=0.3 with various polymer molecular weights are almost independent of polymer molecular weight (Fig. 7.8). This suggests that there is little variation in the number of polymer segments in contact with the surface as we increase molecular weight. As we discussed in Chapter 6, we observed that the fraction of proton spins in a glassy state increases in a linear manner with particle volume fractions for PEG 300, 3000, 12000 and 20000. Fig. 7.9 confirms this trend in both PEG molecular weights studied here suggesting 1-2 polymer segments are in direct contact with the particle surface. The glassy fraction does not take into account the polymer segments which are not in contact but are anchored near surface as a part of polymer chain. Thus, to consider the exact amount of polymer adsorption one needs to consider the fraction of glassy plus intermediate polymers. The detailed discussion is found in Section 6.3. The consistency of the

glassy fractions may suggest that the probability of finding a polymer segment at the particle surface does not vary with polymer molecular weight. This conclusion is consistent with the predictions in Fig 7.5c and 7.5d where we see the effect of *D/d* variations. However this cannot be explained with predictions of Fig. 7.5a and 7.5b where ε_{pc} and α are varied since amount of glassy layers need to be decreased with polymer molecular weights to be consistent.

7.3.4 Polymer-Polymer Density Fluctuations

In Section 5.6 we examined the all partial structure factors at R_p=0.45 for PEG 400 with different particle volume fractions. Before discussing molecular weight effect, we observe some trends of collective particle and polymer structure factors in Fig.7.9. Motivated from the previous sections, PRISM predictions are made at *D/d*=5 as an analogue of Fig. 5.6. The good agreements found between the experiments and theory with ε_{pc}=0.45, α=0.5*d* and *D/d=5* for all particle volume fractions.

However, there are qualitative differences in Fig. 7.10 for PEG 1000 from the data on Fig. 5.6 for PEG 4000. Generally, for PEG 1000, the particle subsystem is more compressible from the zero limit structure factor, $S_{cc}(0)$ and there is less coherence and structures implied from the height of the first peak. These effects are emphasized for a wider range of polymer molecular weights in Fig. 7.3.

Furthermore, the well-defined peak of $S_{pp}(q)$ is significantly reduced from PEG 400 in Fig. 5.6 to PEG 1000 in Fig. 7.10b. Figure 7.11 shows the trends more clearly with adding more data at higher polymer molecular weights. As polymer molecular weight increases there is a suppression of the dimensionless osmotic compressibility, $S_{pp}(0)$, and the a "microphase" peak at nonzero wave vector continuously decreases. Generally as molecular weight increases

correlations on the length scale of particle diameter quickly disappear and show longer range concentration fluctuations.

Finally, polymer shell form factors are calculated with the method described in Section 5.5. In Fig 7.12a we present the experimentally-deduced $P_s^*(q)$ and compare it with the bare particle form factors. At R_p=0.45 PEG 1000 the resulting $P_s^*(q)$ overlap well at all particle volume fractions indicating relatively constant layer thickness. Using the scattering length density parameters at a match condition in Section 5.3 and a core-shell model form factor in Eq. (5.2) the thickness of polymer shells is extracted to be ~2.0-2.4 nm, which is larger than the PEG statistical segment length. Thus, physical picture of polymer adsorptions with PEG 1000 is 3-4 polymer segments are attached on the silica particles.

Fig. 7.12b presents experimentally-deduced $P_s^*(q)$ along with bare particle form factors at all polymer molecular weights. Initially we reported $P_s^*(q)$ for PEG 400 decays faster than silica form factors and thus the peaks in $P_s^*(q)$ appear at lower qD than that of $P_c(q)$ suggesting physically stretched particle diameter with polymer adsorptions. When the particles are suspended in higher polymer molecular weights, $P_s^*(q)$ decays faster and the first minimum gradually moves to the lower qD.

Based on knowing that the scattering length density of the polymer is independent on molecular weights[22,23] we were able to use same SLD conditions used in Section 5.3. Using the scattering length density parameters at a match condition and a core-shell model form factor in Eq. (5.2)[11] the thickness of polymer shells is extracted to be ~0.8, 2.4, 4.4 and 6.4 nm for PEG 400, 1000, 3000 and 8000, respectively. The radii of gyration for these molecular weights are expected to be 0.7, 1.3, 2.0 and 3.8 nm, respectively. Two prominent features are found. First, we see increasing layer thickness with increasing polymer molecular weight revealing the possibility

of direct observations of polymer segments distinguished from that in the bulk. Second, based on the reasonable estimation of SLD, thicknesses of all polymer molecular weights are on the order of their radius of gyration.

Conclusively, PEG segments are adsorbed onto silica particle surface at all polymer molecular weights also supported by FID measurements. Moreover, particles behave effectively larger with polymer adsorptions and adsorption thickness increases with polymer molecular weights.

7.4 Summary

In this study, we showed the change of particle microstructures focused on the particle subsystem compressibility. As polymer molecular weight increases system becomes more compressible and particles are less stable. To capture the observations PRISM theories are tested with variation of number of monomer segments, the strength of interfacial attraction, the range of attraction and the size ratios of particle-to-polymers. Generally increasing chain length increases chain stiffness, reduces end-effects and increases intramolecular overlaps. Due to the weak dependency of particle microstructure on the degree of polymerizations in PRISM theory for dense melts, substantial changes of particle compressibility were not predicted. When holding all other parameters constant, only by varying the size ratio of particle diameter to polymer segment diameter can the experimental observations are captured with PRISM theory. As molecular weights increases, size ratios of particle diameter to polymer segments decreased. In adjusting total packing fractions, decreasing *D/d* ratios greatly reduces the polymer packing fractions, thus increasing system compressibility.

FID experiments showed anchored polymer segments which give rise to glassy properties are quite invariant with increasing molecular weights, excluding the possibilities of varying ε_{pc} or α to explain the enhanced compressibility. While PRISM predictions for pair correlation function, $g_{pc}(r)$ with varying *D/d* effects are consistent with FID experiments, we also note the size of polymer segments does not change with molecular weights and chain stiffness determining the segment length is an intrinsic nature of polymers based on backbone chemistry. Therefore, the good agreements between the experiments and theory predictions with *D/d* effects for the systematic changes on the particle microstructures perhaps could be coincident implying polymer molecular weights need to be considered from a mixing and packing fraction perspective. We note the trends observed in a ternary system of polymer, particles and polymer are also observed in polymer melts.[24,25] As a result, we do not attribute our observations to the ternary nature of the systems studied.

Polymer collective structure factors obtained with contrast matching neutron scatterings show that polymers have longer range correlations and increasing concentration fluctuations with increasing molecular weights. In addition the adsorbed polymer shell form factors indeed confirm that layer thicknesses increase when particles are suspended in concentrated solutions containing longer polymer chains.

7.5 Table and Figures

Techniques	R_p	PEG molecular weight	Particle volume fractions (ϕ_c)					
SAXS	0.45	300	0.087	0.120	0.181	0.238	0.294	0.349
		400	0.084	0.122	0.176	0.237		0.349
		3000	0.073	0.130	0.160	0.242	0.299	0.330
		8000		0.1	0.17	0.2	0.3	0.350
		12000			0.17			
		20000			0.17			
NMR(FID)	0.5	300	0.0				0.300	
		1000	0.0				0.300	
		3000	0.0	0.100	0.200		0.300	
		12000	0.0	0.100	0.200		0.300	
SANS	0.45	400	0.05a	0.100a	0.200a		0.300a	
		1000		0.100	0.200		0.300	
		3000				0.250		
		8000				0.250		

a : data is obtained from Chapter 5

Table 7.1 Sample descriptions used in this study

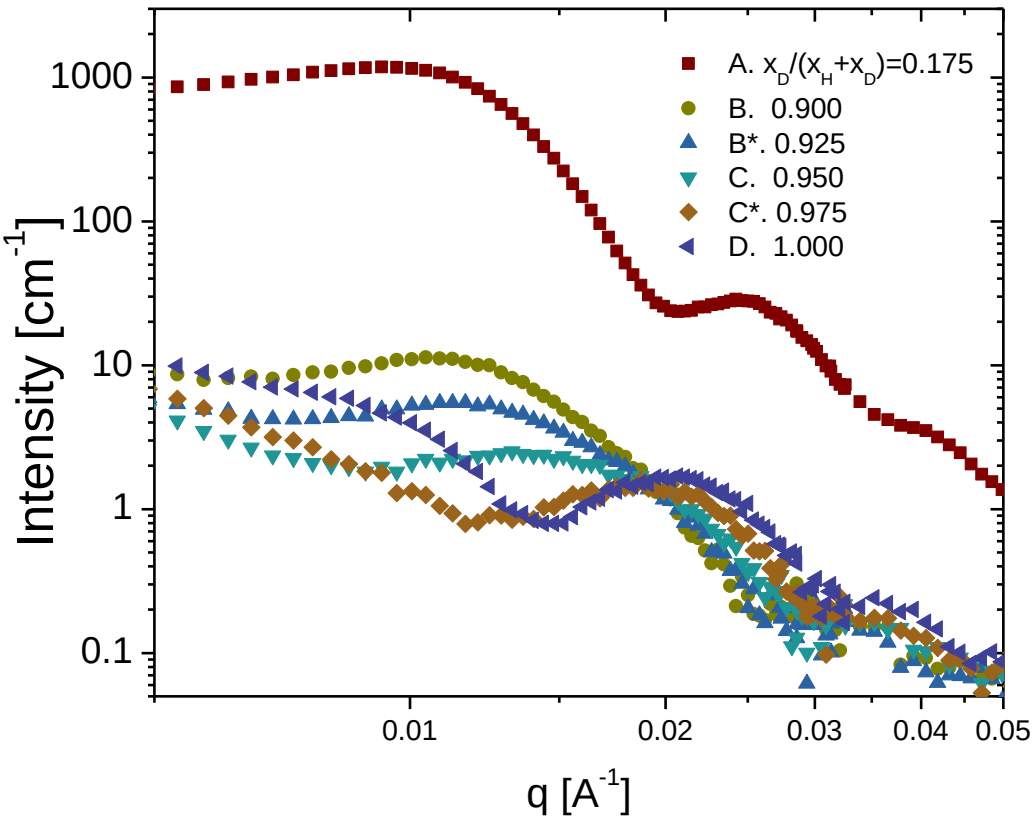

Figure 7.1 Scattering data (*I(q)*) as a function of wave vector for R_p=0.45 ϕ_c=0.20 at varying D_2O ratios. While particle volume fraction is fixed at 0.2 and R_p=0.45 for PEG 1000, $D_2O/(D_2O+H_2O)$ ratios are varied from 0.175, 0.900, 0.925, 0.950, 0.975 and 1.000 denoted as A, B, B*, C, C* and D.

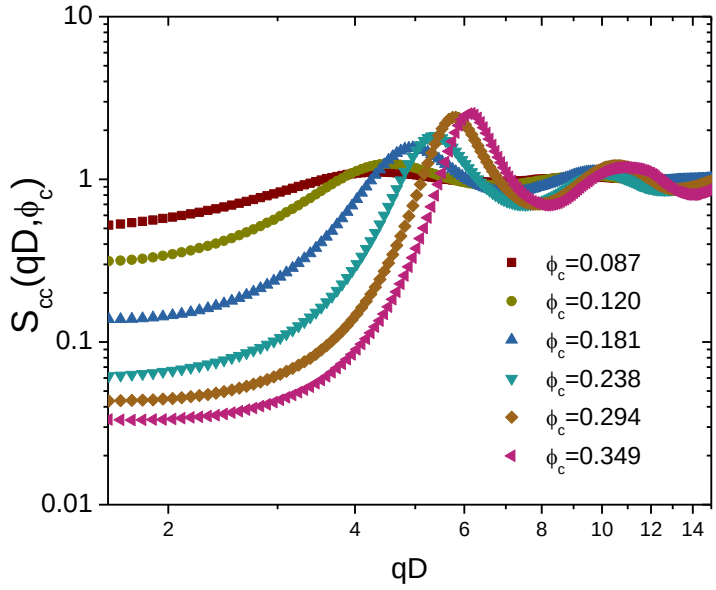

Figure 7.2 Particle structure factors for R_p=0.45 PEG 300 for varying ϕ_c ratios.

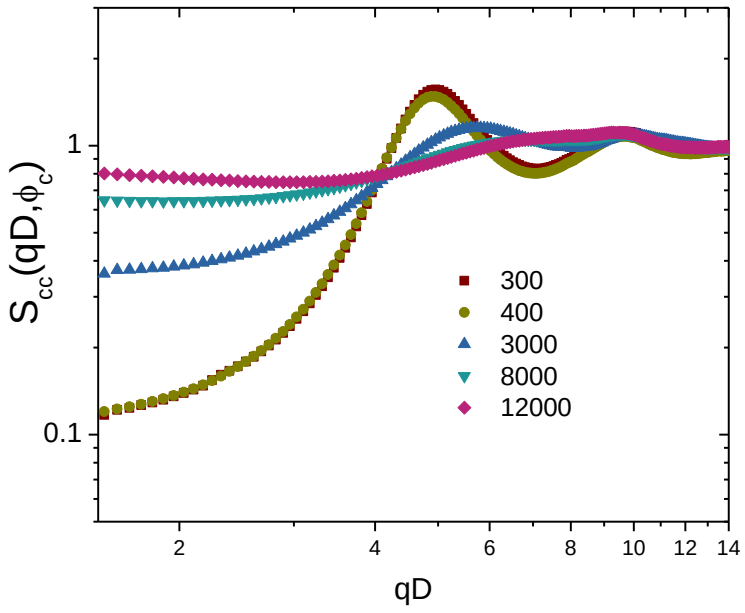

Figure 7.3 Particle structure factors at a fixed ϕ_c=0.17, R_p=0.45 with varying polymer molecular weights as shown in the legend.

(a)

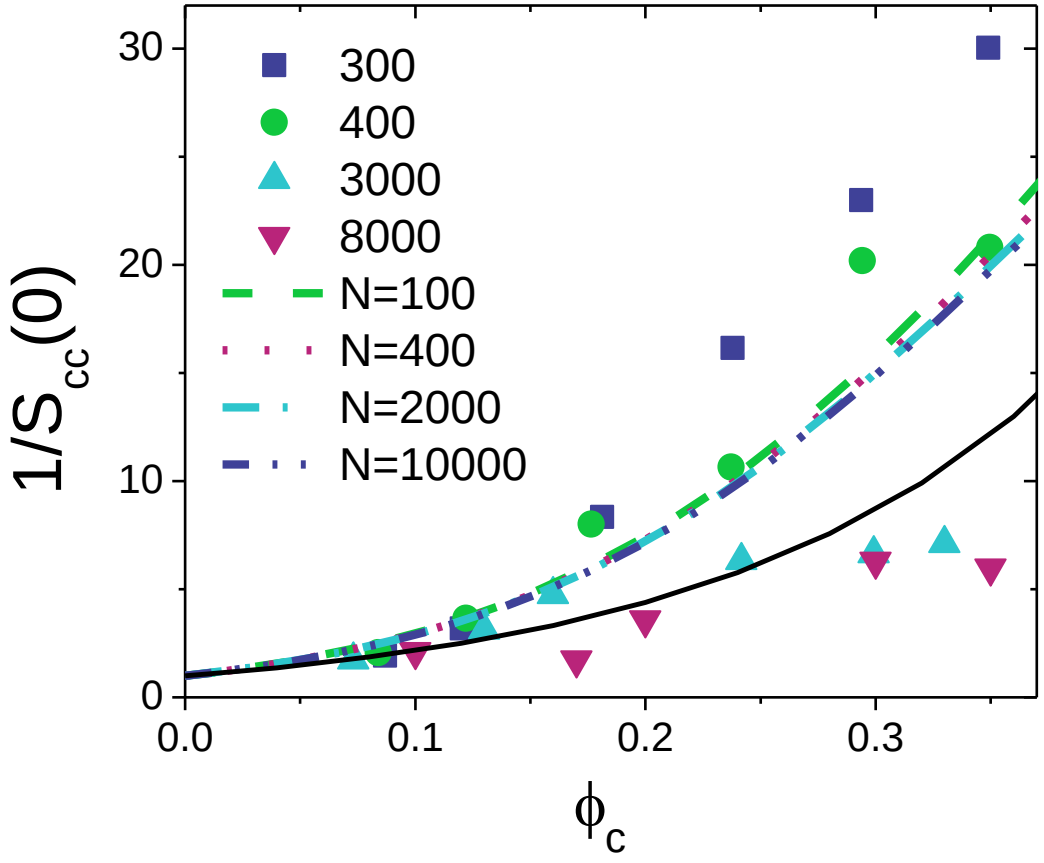

Figure 7.4 (cont. on next page)

(b)

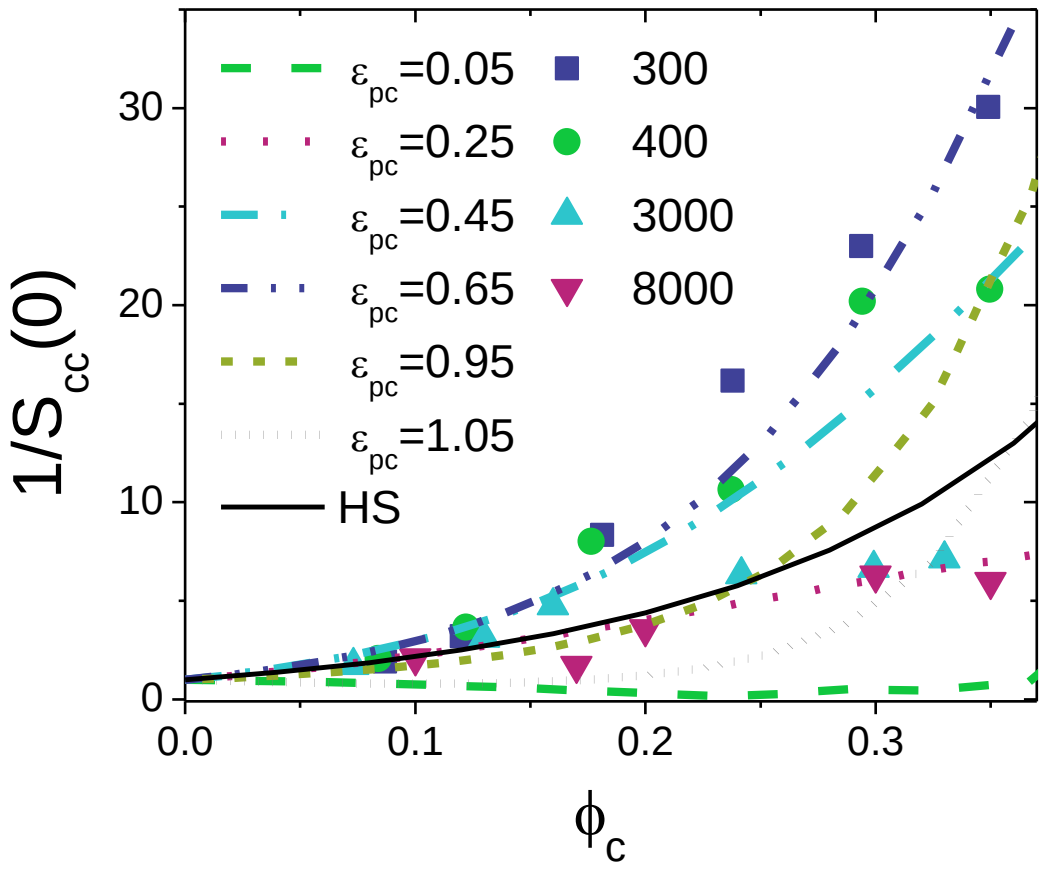

Figure 7.4 (cont. on next page)

(c)

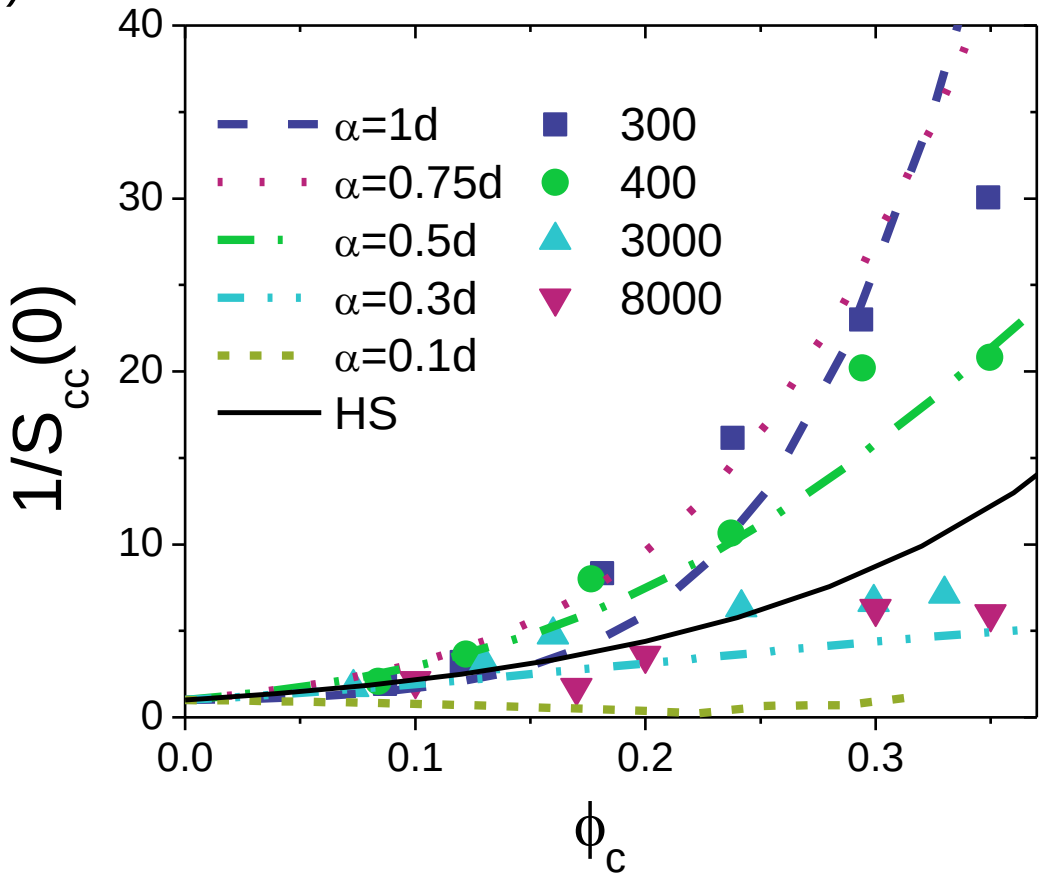

Figure 7.4 (cont. on next page)

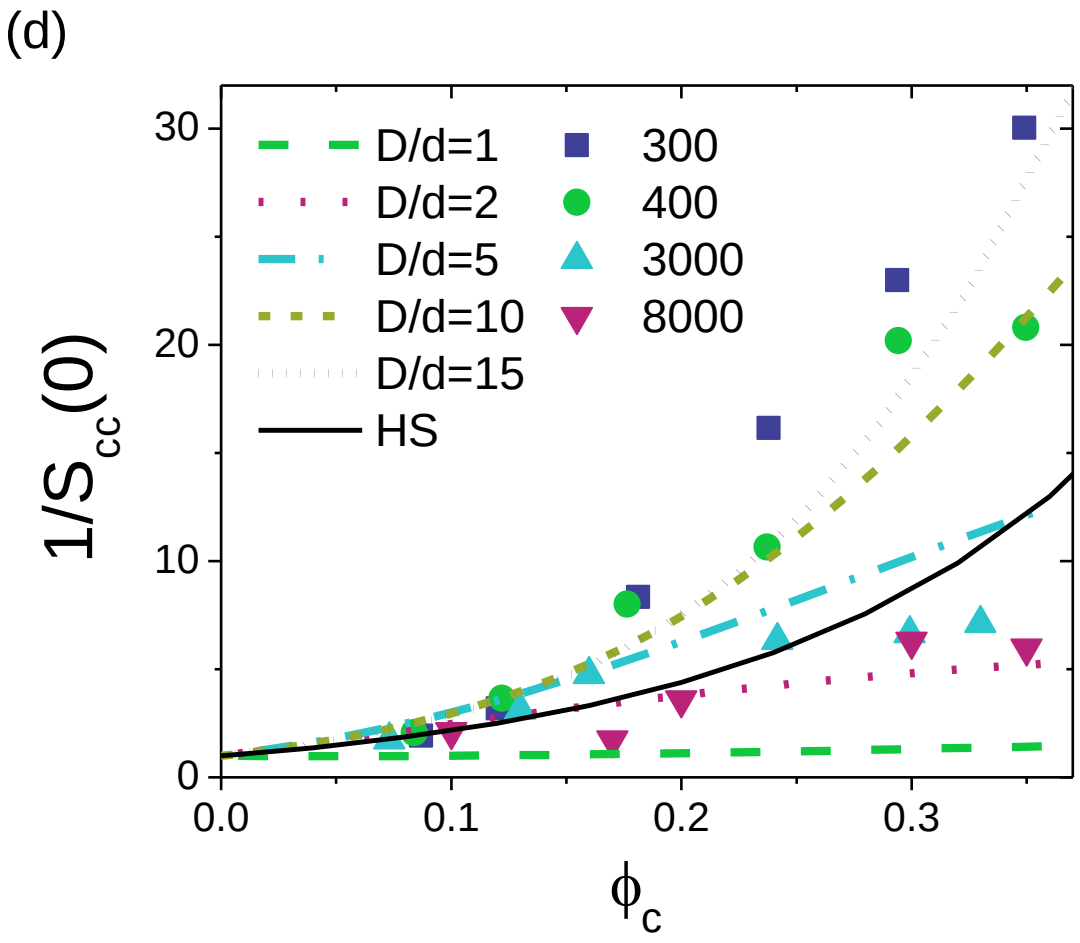

Figure 7.4 Experimental results and PRISM predictions for the inverse osmotic compressibility as a function of particle volume fraction (ϕ_c) with varying polymer molecular weight. Dots are experiments and predictions are shown with curves as shown in the legends. While same experimental data are used in (a), (b), (c), and (d), conditions of PRISM varied in each figures. (a) PRISM predictions at a fixed α=0.5d, ε_{pc}=0.45, D/d=10 with varying number of monomers, N. (b) PRISM predictions at a fixed α=0.5d, D/d=10, N=100 with varying strength of attraction between polymer segments and particle, ε_{pc} (c) PRISM predictions at a fixed D/d=10, ε_{pc}=0.45, N=100 with varying the range of attraction, α. (d) PRISM predictions at a fixed α=0.5d, ε_{pc}=0.45, N=100 with size ratio of particle to polymer, D/d.

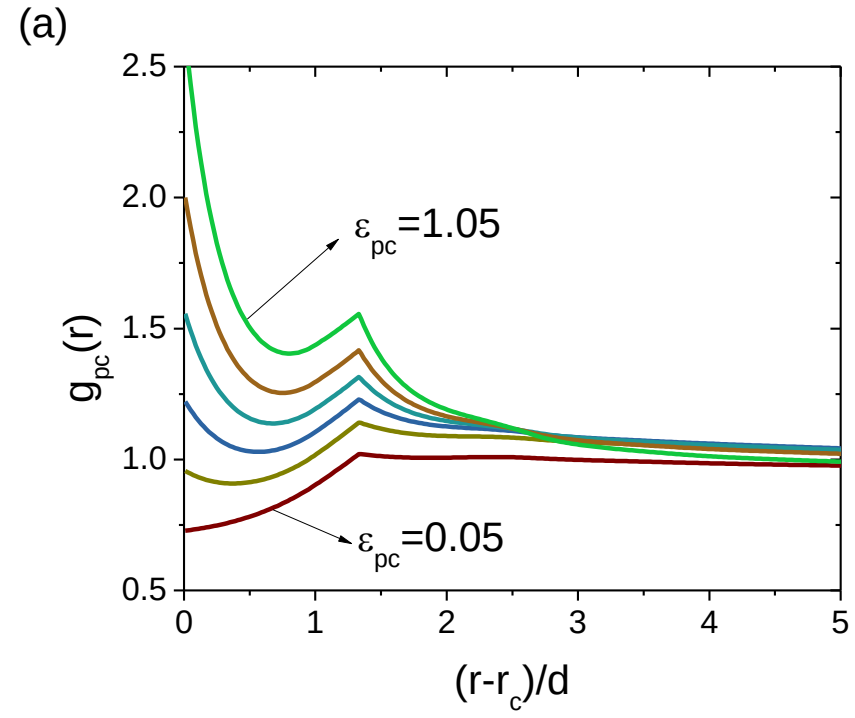

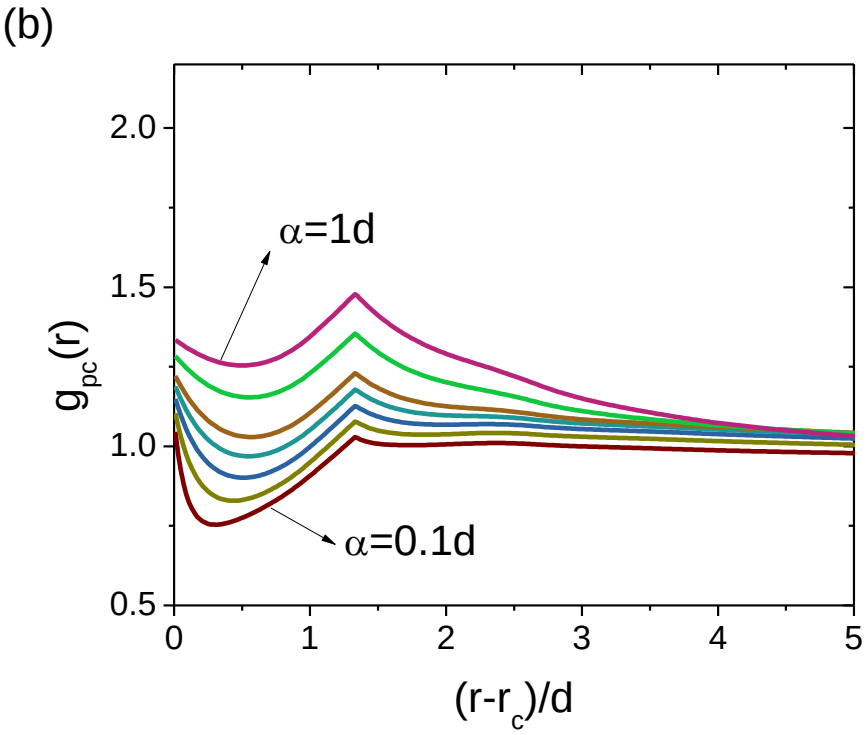

Figure 7.5 (cont. on next page)

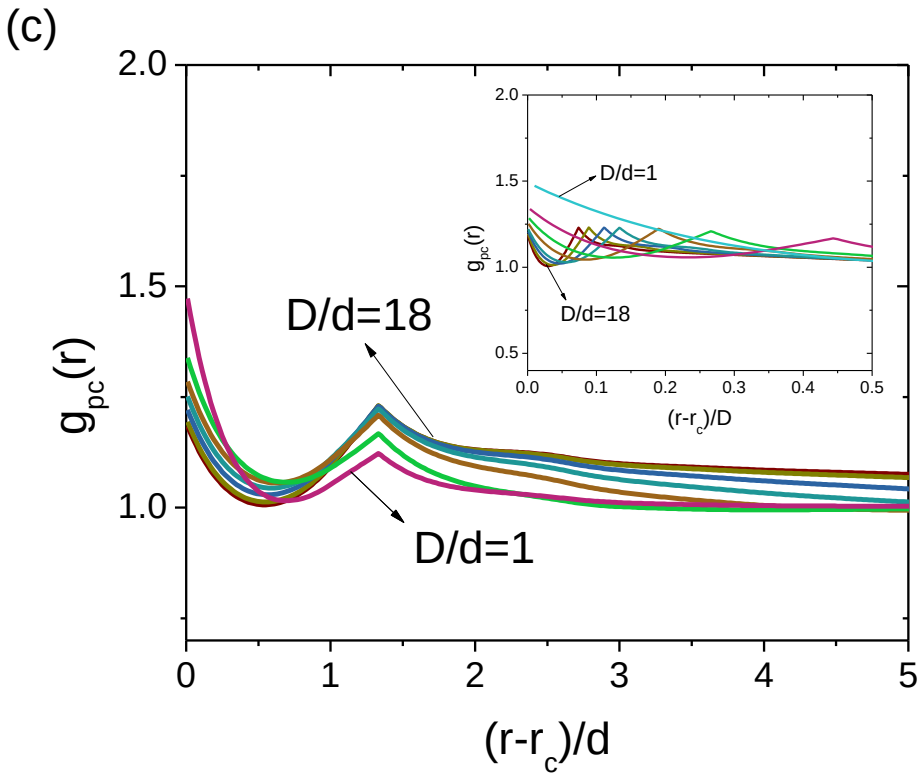

Figure 7.5 Particle-polymer monomer pair correlation function at ϕ_c=0.1. r-r_c is the particle surface-to-polymer segment surface distance where r_c is defined as ½(D+d). (a) D/d=10, α=0.5d, ε_{pc} decreases from top (1.05 kT) to bottom (0.05 kT) by 0.2 kT. (b) D/d=10, ε_{pc}=0.5d, α decreases from top to bottom, 1d, 0.75d, 0.5d, 0.4d, 0.3d, 0.2d and 0.1d, respectively. (c) α=0.5d, ε_{pc}=0.45 kT, D/d decreases from top to bottom, 18, 15, 10, 5 and 1, respectively. (inset) r-r_c is rescaled with the particle diameter.

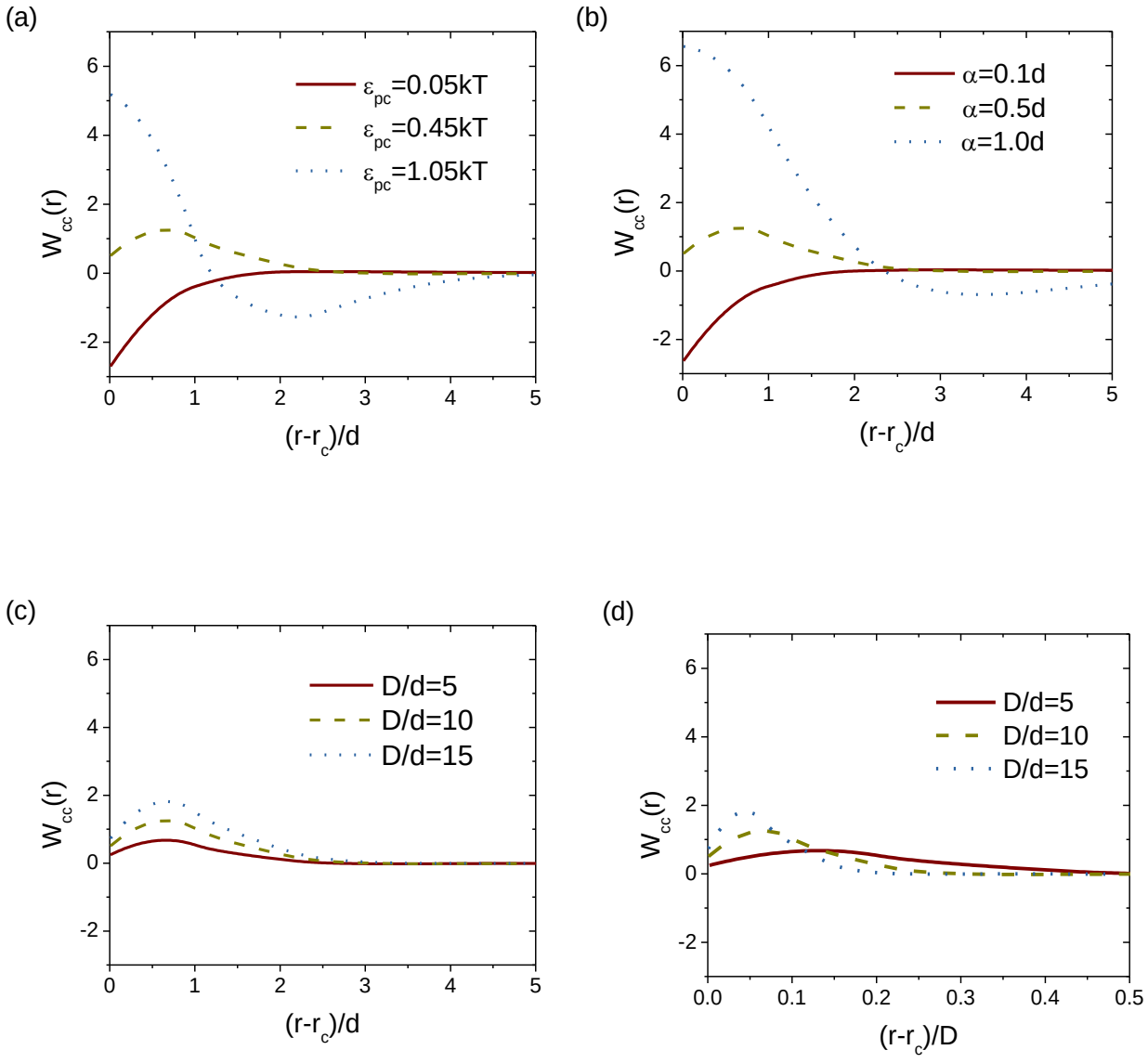

Figure 7.6 Particle potential of mean force in the dilute two particle limit for (a) D/d=10, α=0.5d, and varying ε_{pc} =0.05, 0.45, 1.05 kT (b) D/d=10, ε_{pc}=0.5d, and varying α=0.1d, 0.5d, 1.0d (c) α=0.5d, ε_{pc}=0.45 kT, and varying D/d=15, 10, 5. r-r_c is the particle surface-to-particle surface distance where r_c is defined as ½(D+D). (d) Re-plotted (c) where r-r_c is normalized with the particle diameter, D.

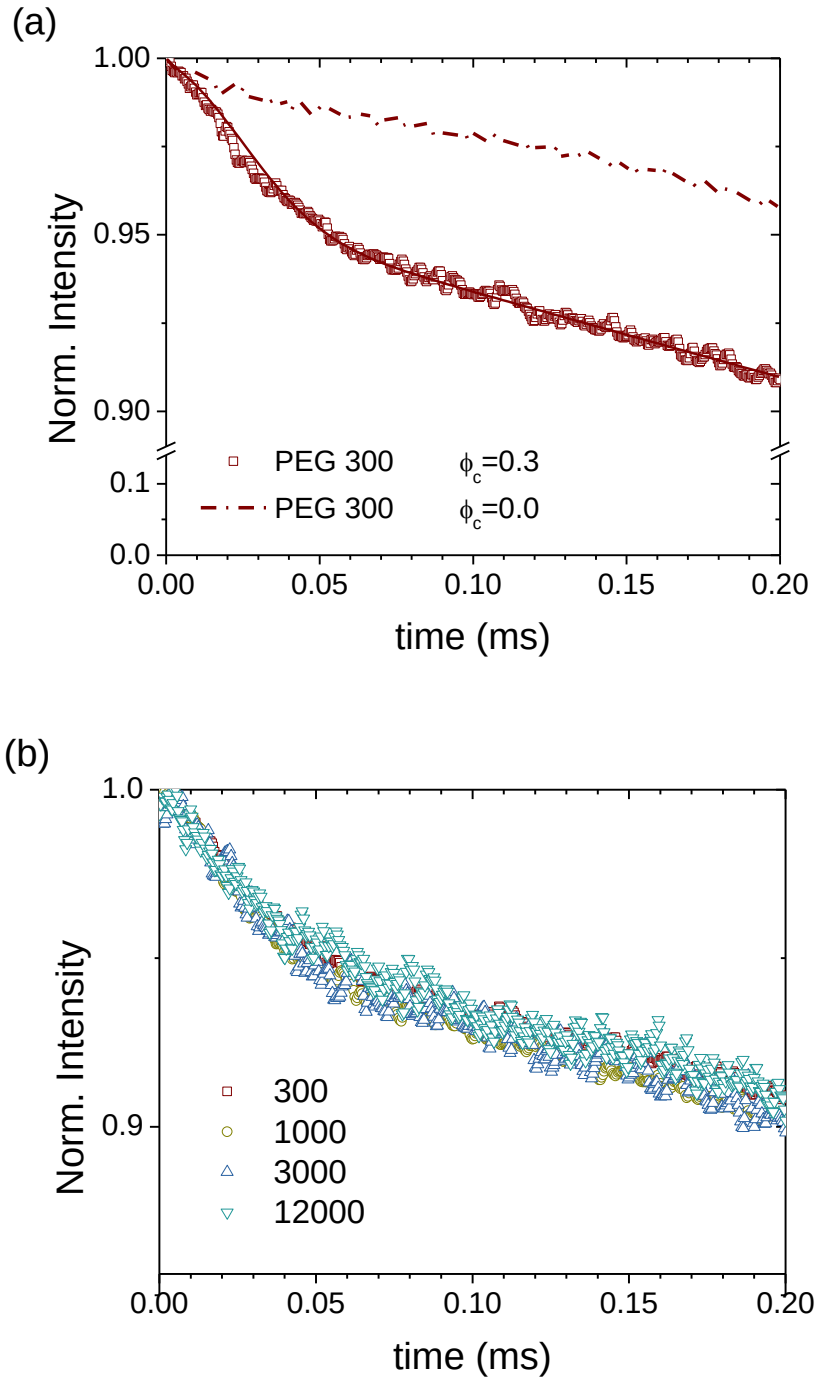

Figure 7.7 MSE-FID signals as a function of the acquisition time (a) for ϕ_c=0.0 and ϕ_c=0.3 for R_p=0.5 PEG 300 (b) at a fixed ϕ_c=0.3 for various PEG molecular weights at R_p=0.5 as shown in the legend.

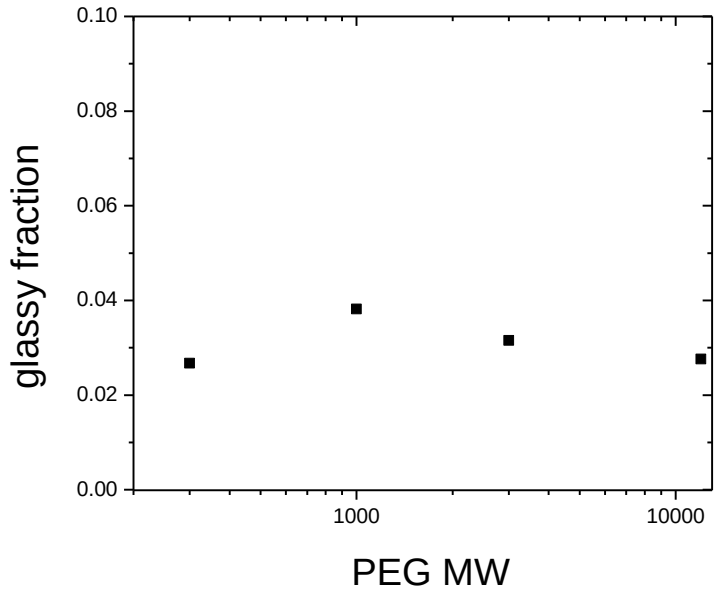

Figure 7.8 Polymer glassy fractions at a fixed ϕ_c=0.3 for various PEG molecular weights determined from Fig. 7.7 and fitted to Eq. (6.1).

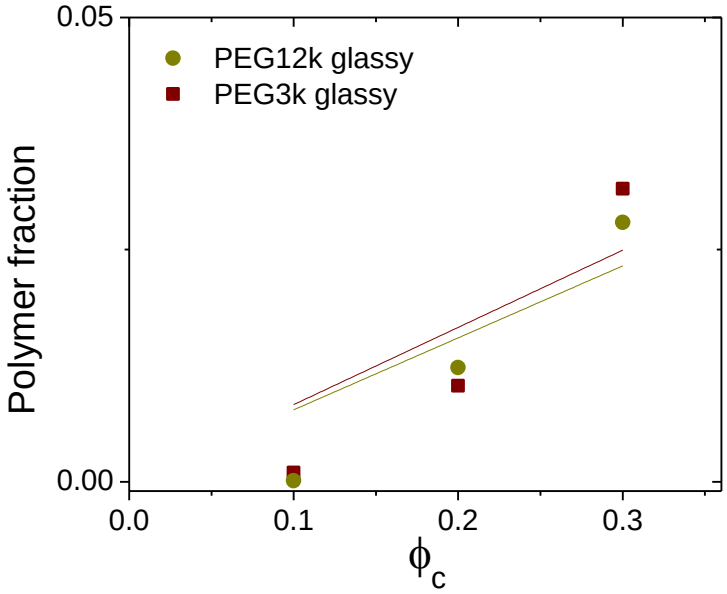

Figure 7.9 Polymer glassy fractions as a function of ϕ_c for two PEG molecular weights, 3000 and 12000.

(a)

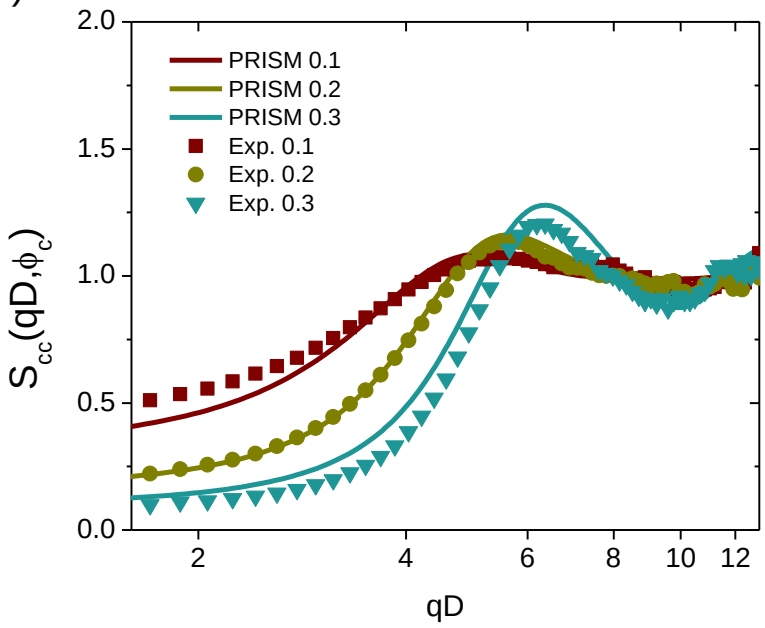

(b)

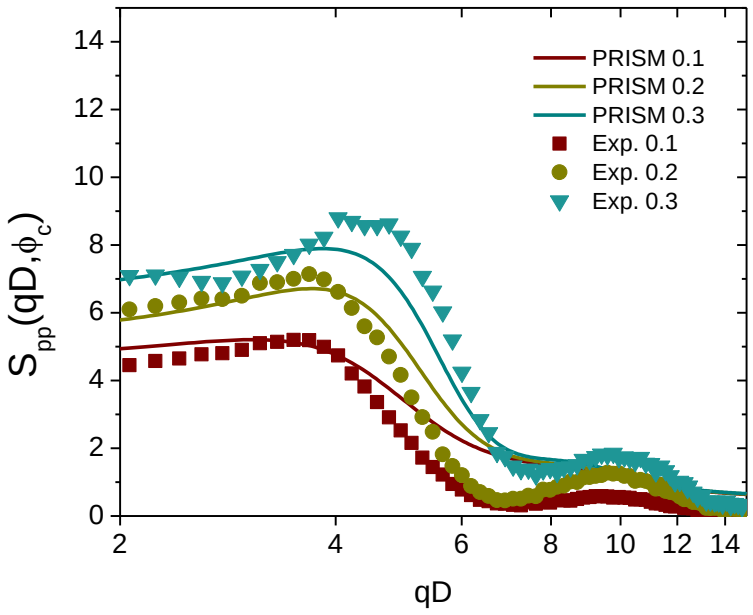

Figure 7.10 (cont. on next page)

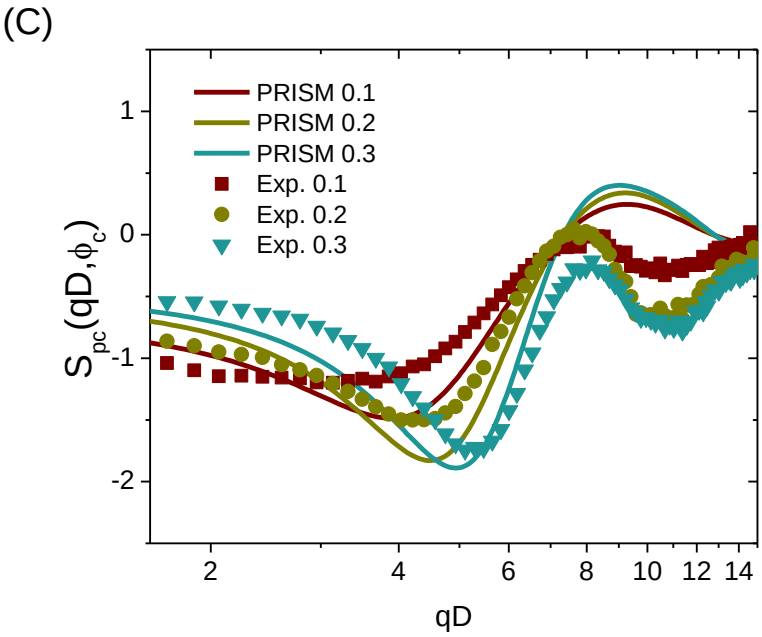

Figure 7.10 (a) Particle collective structure factor, S_{cc} as a function of reduced wave vector at different nanoparticle volume fractions, ϕ_c, as indicated in legend. Corresponding smooth curves are the PRISM theory results for ε_{pc}=0.45kT at D/d=5. (b) Polymer collective structure factor, S_{pp}, under the same conditions. (c) Interfacial collective structure factor, S_{pc}, under the same conditions.

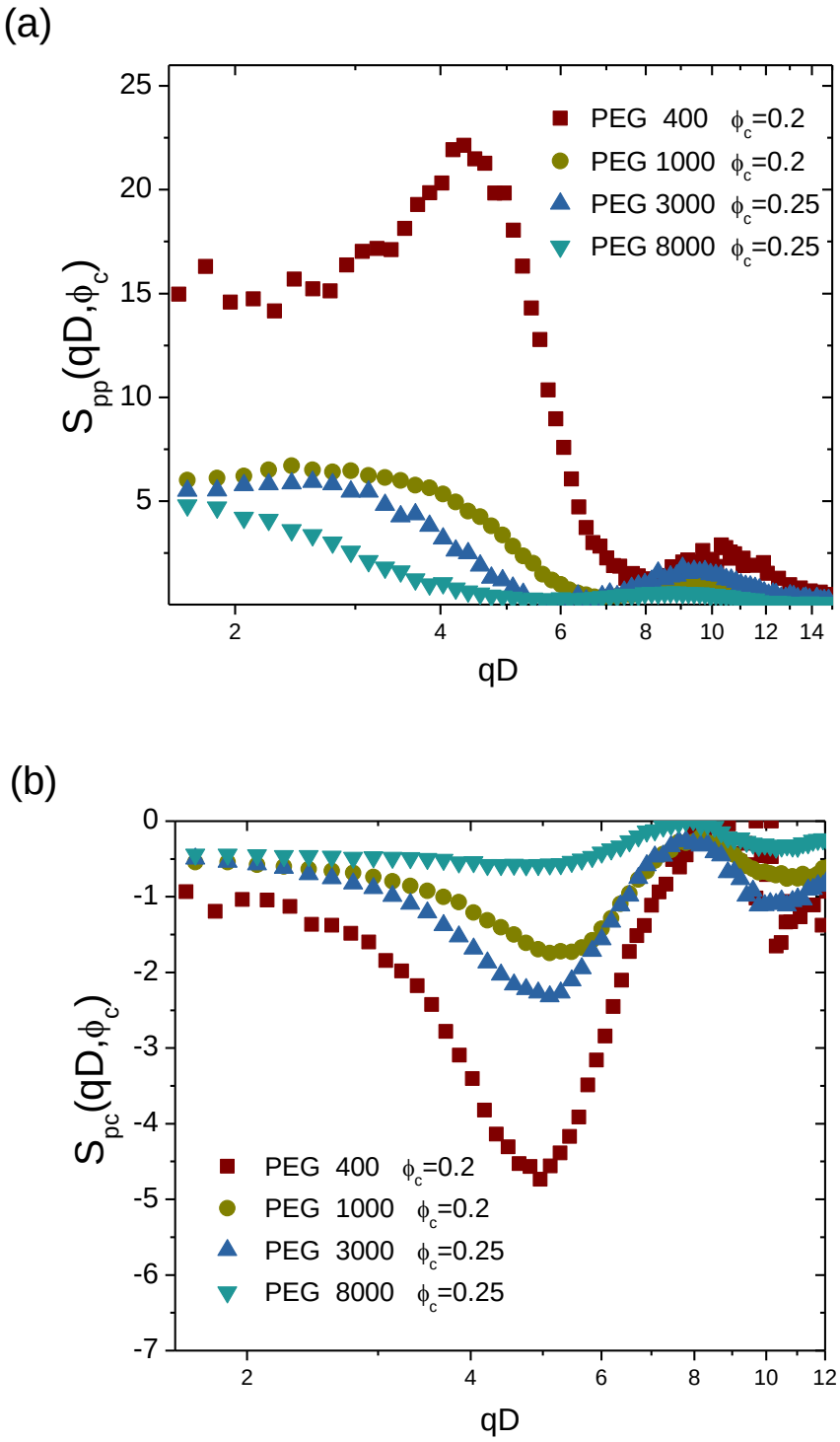

Figure 7.11 (a) Polymer collective structure factor, S_{pp} as a function of reduced wave vector at different polymer molecular weights as shown in the legends. (b) Interfacial collective structure factor, S_{pc}

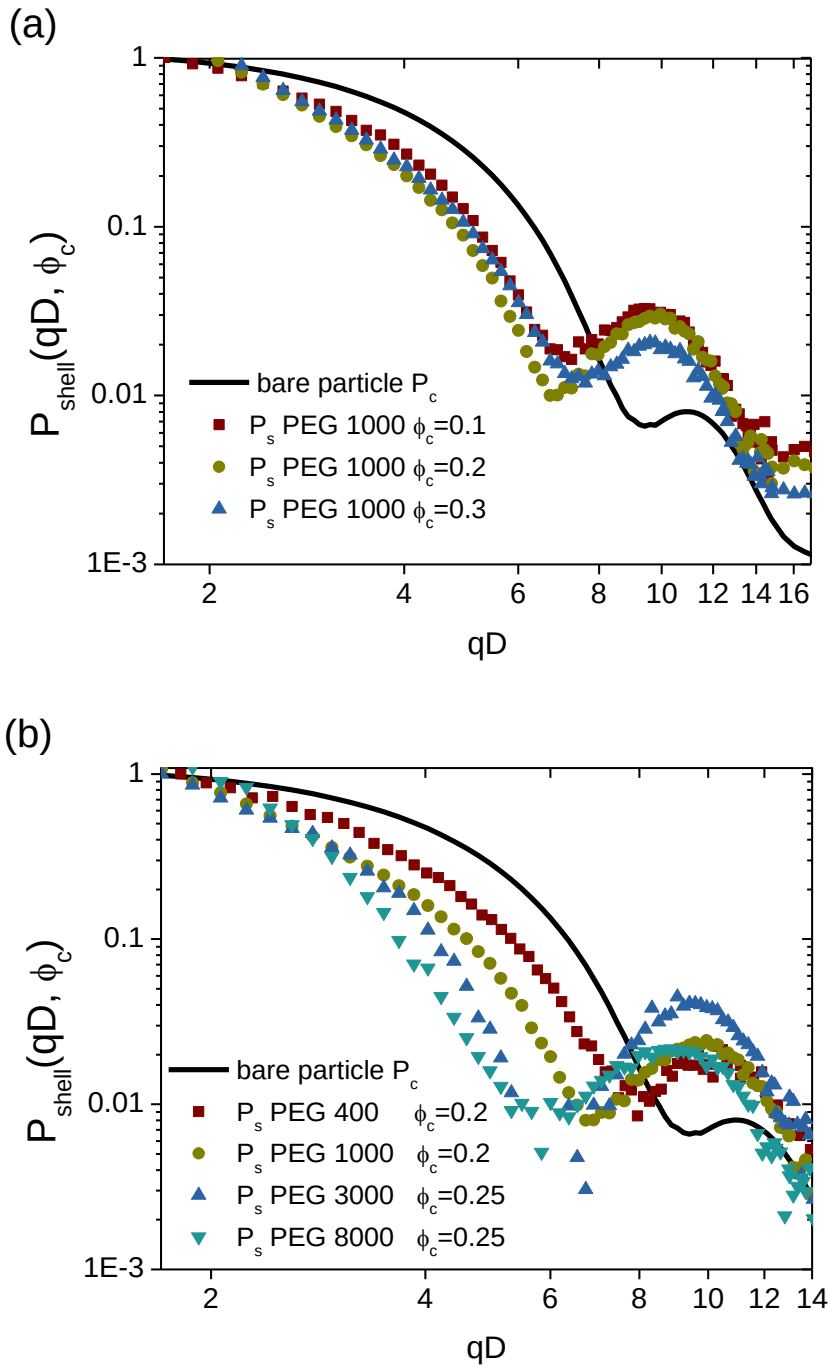

Figure 7.12 Polymer layer shell form factor as a function of reduced wave vector. The bare spherical-particle form factor, $P_c(q)$ based on Eq. (2.2) is shown as the solid curve for comparison to $P_s^*(q)$, experimentally obtained from dilute particle suspensions and fitted to the standard homogeneous sphere model. (a) PEG 1000 with varying ϕ_c (b) PEG 400, 1000, 3000 and 8000 at $\phi_c = 0.20$ or 0.25 as indicated in the legend.

7.6 References

1. Brouwers, H. J. H. *Phys. Rev. E. Stat. Nonlin. Soft Matter Phys* **2006**, *74*.
2. Greenwood, R.; Luckham, P. F.; Gregory, T. *J. Colloid Interface Sci.* **1997**, *191*, 11.
3. Hall, L. M.; Schweizer, K. S. *J. Chem. Phys.* **2008**, *128*.
4. Hooper, J. B.; Schweizer, K. S. *Macromolecules* **2005**, *38*, 8858.
5. Hooper, J. B.; Schweizer, K. S. *Macromolecules* **2007**, *40*, 6998.
6. Schweizer, K. S.; Yethiraj, A. *J. Chem. Phys.* **1993**, *98*, 9053.
7. Hall, L. M.; Anderson, B. J.; Zukoski, C. F.; Shweizer, K. S. *Macromolecules* **2009**, *42*, 8435.
8. Kim, S. Y.; Hall, L. M.; Schweizer, K. S.; Zukoski, C. F. *Macromolecules* **2010**, *43*, 10123.
9. Kim, S. Y.; Zukoski, C. F. *Langmuir* **2011**, *27*, 10455.
10. Hall, L. M.; Jayaraman, A.; Schweizer, K. S. *Curr. Opin. Solid St. M.* **2010**, *14*, 38.
11. Kim, S. Y.; Schweizer, K. S.; Zukoski, C. F. *Phys. Rev. Lett.* **2011**, *In press*.
12. Schweizer, K. S.; Curro, J. G. *Adv. Chem. Phys.* **1997**, *98*, 1.
13. Curro, J. G.; Schweizer, K. S.; Grest, G. S.; Kremer, K. *J. Chem. Phys.* **1989**, *91*, 1357.
14. Lekkerkerker, H. N. W.; Stroobants, A. *Physica A* **1993**, *195*, 387.
15. Biben, T.; Hansen, J. P. *Phys. Rev. Lett.* **1991**, *66*, 2215.
16. Mauri, M.; Thomann, Y.; Schneider, H.; Saalwächter, K. *Solid State Nucl. Mag.* **2008**, *34*, 125.
17. Maus, A.; Hertlein, C.; Saalwächter, K. *Macromol. Chem. and Physic.* **2006**, *207*, 1150.
18. Papon, A.; Saalwächter, K.; Schäler, K.; Guy, L.; Lequeux, F.; Montes, H. *Macromolecules* **2011**, *44*, 913.
19. Ek, S.; Root, A.; Peussa, M.; Niinistö, L. *Thermochim. Acta* **2001**, *379*, 201.
20. Holík, M.; Matějková, B. *J. Chromatogr. A* **1981**, *213*, 33.
21. Kim, J. M.; Chang, S. M.; Kong, S. M.; Kim, K. S.; Kim, J.; Kim, W. S. *Ceram. Int.* **2009**, *35*, 1015.
22. Sears, V. F. *Neutron News* **1992**, *3*, 26.
23. May, R. P.; Ibel, K.; Haas, J. *J. Appl. Cryst.* **1982**, *15*, 15.
24. Anderson, B. J.; Zukoski, C. F. *Macromolecules* **2008**, *41*, 9326.
25. Anderson, B. J.; Zukoski, C. F. *Macromolecules* **2009**, *42*, 8370.

CHAPTER 8 A DEFINITE APPROACH TO UNDERSTAND THE EFFECTS OF SOLVENT QUALITY ON THE PARTICLE AND POLYMER STABILITY

8.1 Introduction

In previous chapters, we showed that when silica particles suspended in PEG polymer melts behave as hard-spheres with an effective diameter larger than the core diameter. The increased effective diameter arises from polymer adsorption. Temperature-independent polymer dynamics in Chapter 6 support that in a melt, the particles are suspended in polymers in a theta state. On the other hand, when the particles are suspended in a concentrated polymer solution, the temperature dependency of particle microstructure reported in Chapter 3 shows that elevating temperature can change the solvent quality.

A common observation of the PEG-water phase diagram is that it displays a lower critical solution temperature (LCST) and a closed loop at high temperature.[1-5] Thus, the solvent quality of water for PEG becomes poorer as temperature increases, resulting in temperature-dependent polymer-polymer, polymer-solvent and solvent-solvent interactions. Pattanayek and Juvekar introduced a model for predicting adsorption of PEG from water to solid silica surfaces based on continuum form of the self-consistent mean field theory.[6] The concentration-dependent Flory-Huggins parameter is estimated from the water activity in PEG solutions, Kuhn length and polymer-surface affinity parameter through the specific enthalpy of displacement of water by PEG. The model predicted the adsorbed amount in trains, loops and tails and the hydrodynamic thickness of the adsorbed layer.[6] Mehrdad and Akbarzadeh measured intrinsic viscosity of PEG in water-ethanol solutions and showed the intrinsic viscosity decreases as temperature rises showing the mixtures of water and ethanol become an increasingly poor solvent for PEG with

increasing temperature and ethanol concentration.[7] Hammouda and Ho showed with small angle neutron scatterings PEG chains in water can be fully collapsed and coils are shrunk as temperature rises thus implying temperature dependent solvent quality can alter chain conformation.[8]

As a consequence when silica particles are added to PEG solutions one expects the state of the polymer to be temperature dependent. As particle stability is controlled by the extent to which polymer segments are attracted to the particle surface, particle stability will be altered by changing theta state.

Fig. 8.2 shows the optical picture of 44 nm diameter silica nanoparticles in PEG 400 - water solutions at R_p=0.2, ϕ_c=0.1.Here $R_p = V_p/(V_p+V_w)$ where V_p is the volume of polymer and V_w is the volume of water in the colloid of particle volume fraction ϕ_c. After first mixing, at both 25 °C and 60 °C, the suspensions are a transparent blue. As confirmed in previous studies,[9] at R_p=0.2 particles experience electrostatic steric repulsions and van der Waals attractions such that total interaction potentials yield stable particle dispersions at room temperature. On their own, electrostatic repulsions are insufficient to stabilize the particles such that stability requires steric repulsions. After 7 days at 60 °C, the suspensions become opaque and form a gel. This observation suggests the steric repulsions stabilizing the particles against aggregation are temperature sensitive and are reduced as the quality of the solvent decreases with increasing temperature.

Here we explore the degree of polymer adsorption using nuclear magnetic resonance (NMR) techniques exploiting magic-sandwich echo (MSE) experiments,[10,11] which refocus the initial part of the free-induction decay (FID) and thus avoid the dead time issue allowing us to capture polymer relaxations at short time scales (less than 0.2 ms). These studies allow us to

determine the temperature dependency of the fraction of proton spins that are trapped in the glassy state due to adsorption onto the particle surfaces. We find that less polymer is adsorbed at elevated temperature. The consequences of this result for polymer and particle density fluctuations are then studied using contrast matching small angle neutron scattering. These complimentary experiments confirm the existence of adsorbed polymer layers, the diminished strength of attraction between polymer segments and the particle surface with increasing temperature and the decrease in adsorbed layer thickness with increased temperature. Below in Section 8.2 we discuss experimental methods, while results are presented in 8.3 and a summary is presented in Section 8.4.

8.2 Experiments

8.2.1 Sample Preparation

Particle synthesis and sample preparation were already introduced in Section 2.2.1. Polymer concentration is expressed in terms of the parameter, R_p, defined in Sections 2.2.1 and 4.2.2.

For MSE-FID experiments, ϕ_c=0.3 of 40 nm silica nanoparticles are suspended in PEG-D2O mixtures with varying PEG molecular weight (300, 3000, 12000) at a fixed R_p=0.5. MSE-FID measured at 30 °C, 50 °C and 70 °C.

For small angle neutron scatterings, ϕ_c=0.3 of 40 nm silica particles are suspended in PEG 1000 -H_2O/D_2O mixtures. While R_p=0.45 is fixed, H_2O/D_2O ratios in solvent phase are methodically varied to change the scattering length density of the solvent phase. As introduced in Section 7.2.5 and based on Fig. 5.2, scattering measurements at ϕ_c=0.3 were made at two

D_2O/H_2O ratios corresponding to $\Delta\rho_p$ ~0 at $x_D/(x_H+x_D)$ = 0.175 (labeled as 'A'), $\Delta\rho_c$ ~ 0 at $x_D/(x_H+x_D)$ =0.100 (labeled as 'D') and four intermediate values close to $\Delta\rho_c$=0 at $x_D/(x_H+x_D)$=0.90, 0.925, 0.95 and 0.975 (labeled as 'B', 'B*', 'C' and 'C*') at 20 °C and 70 °C.

Once all 6 samples were measured at 20 °C, samples were kept in a 70 °C oven for 6 hours and held 30 minutes more in a sample holder at 70 °C before the measurement.

8.2.2 MSE-FID

The NMR measurements were performed on a Bruker Minispec mq20 at 20 MHz proton resonance frequency. The sample temperature was controlled with a BVT3000 heater working with air gas at each temperature of 30±0.1, 50±0.1 and 70±0.1 °C and waited for 1 hour to reach equilibrium. Samples were loaded in a conventional NMR tubes and flame-sealed to avoid evaporation. The minispec has typical π/2 pulse lengths of down to 2 μs showing a reliable phase cycling in π/2 steps. Number of scans was varied from 128 to 512 depending on the sample conditions to obtain good quality of signals and the delay time was also varied from 1 to 4 s. The detailed backgrounds and technical information are given in Section 6.2.3.

8.2.3 Small Angle Neutron Scattering

Small Angle Neutron Scattering (SANS) experiment was performed on the NG7 30 m SANS instrument in NIST Center for Neutron Research, National Institute of Standards and Technology (NIST). Samples were loaded into 1 mm path length demountable titanium cells. The cell temperature was maintained to 20±0.1 ˚C and 70±0.1 ˚C using the 10CB sample holder with a NESLAB circulating bath. A large range in scattering wave vector, q ($0.004A^{-1}$ ~ $0.1A^{-1}$) ,

was obtained by combining the sector averaged scattering intensity from two different instrument configurations at 4, and 13.5 m detector distances. SANS data reduction and analysis of the scattering intensity, I, versus Q was performed using the SANS reduction and analysis program with IGOR Pro available from NIST. [12] For the scattering measurement at the temperature of 70 °C, samples used at 20 °C were kept in a 70 °C oven for 6 hours and held 30 minutes more in a sample holder at 70 °C before the measurement.

8.3 Results and Discussion

8.3.1 Polymer Dynamics

Figure 8.2 shows MSE-FID signals as a function of the acquisition time for ϕ_c=0.3 at R_p=0.5 PEG 3000 at different temperatures of 30, 50 and 70 °C. The signals decay with time and curvature of each spectrum implies that the protons in the mixture have at least two different relaxations times. Polymer segments that are directly adsorbed to the particle surface will form the glassy layers where the nuclear coupling of the proton spins and those in the surface drive more rapid decay in the MSE FID signal that is observed in the bulk (and in the absence of particles). In addition to the glassy spins, there are polymer segments with intermediate relaxation times indicating that their mobility lies between that of the glassy and bulk states. In fitting the MSE-FIS spectra, $I(t)$, we assume three different relaxation times and signals,[10,11,13]

$$I(t) = I_0(f_g \exp(-t(\tau_g)^{b_g} + f_i \exp(-t(\tau_i)^{b_i} + f_m \exp(-t(\tau_m)^{b_m}) \qquad (6.1)$$

where I_0 is an amplification factor, f_j is the fraction of the component j, τ_j is the jth relaxation time with subscript, g, i and m denoting glassy, intermediate and mobile segment contributions.

Fitting results are drawn as solid curves in Fig. 8.2. With this interpretation in mind, as temperature increases from 30 to 70 °C, the short time decay signals occur faster indicating qualitatively that the fraction of polymer segments in the glassy state is reduced at higher temperatures.

Fitting the short time relaxations determined with the double quantum (DQ) filter in Fig. 8.2 yields b_g=2 and τ_g=0.0309, 0.02829 and 0.03304 ms while the long time decay process determined by a dipolar "magic-angle-polarization" (MP) filter yields (b_m, τ_m)=(0.61, 27.77), (0.61, 30) and (0.6, 38) at 30, 50 and 70 °C, respectively. Polymer segment mobility in the bulk increases with temperature, and thus with increasing MP relaxation times. While the fraction of glassy polymer is insensitive to the choice of (τ_i, b_i), in the following discussion we chose (τ_i, b_i) = (0.418, 1.63) for all temperatures for consistency. We extract the relaxation times and fraction of protons that relax with glassy and intermediate relaxation rates for all PEG molecular weights and temperatures. The results are summarized in Fig 8.3.

As temperature is raised, two clear features are observed. First, the fraction of proton spins trapped in a glassy state decreases in a linear fashion with temperature for all polymer molecular weights. Secondly, we see that, in agreement with previous studies, the fractions of spins trapped in a glassy state are independent of molecular weight at all temperatures. These results show that polymer segments are adsorbed to the same extent at all molecular weights but the amount of adsorbed polymer decreases with increasing temperature.

Below we describe the impact of the reduced polymer adsorption on polymer and particle density fluctuations and the resulting consequences for the state of the particle/polymer dispersion.

8.3.2 Local Structures and Compressibility of Particle and Polymer Interactions

The intensity, $I(q)$, of scattered neutrons at wave vector q, has three contributions:

$$I(q) = n_c \Delta\rho_c^2 P_c(q) S_{cc}(q,\phi_c) + 2\Delta\rho_c \Delta\rho_p \sqrt{n_c n_p P_c(q)} S_{cp}(q) + n_p \Delta\rho_p^2 S_{pp}(q) \qquad (5.1)$$

where $n_j = \rho^*_j V_j^2$, and ρ^*_j and V_j are number density and unit volume of the jth component, respectively. $\Delta\rho_j$ is the difference of scattering length density of component j and the medium, $P_c(q)$ is the particle form factor, and $S_{ij}(q)$ are the structure factors associated with two components (*pp, pc, cc*) where the subscript *p (c)* indicates polymer segments (colloids).

Choosing an D_2O/H_2O ratio where $\Delta\rho_p$=0, Eq. (5.1) is simplified to $I(q)=n_c\Delta\rho_c^2 P_c(q) S_{cc}(q,\phi_c)$. This allows determination of $P_c(q)$ at low ϕ_c =0.03 where interparticle correlations are absent ($S_{cc}(q,\phi_{c,low})$=1). $S_{cc}(q)$ is obtained by dividing the scattering intensity from the concentrated particle suspension by its dilute limit analog: $S_{cc}(q,\phi_c) = \dfrac{I(q,\phi_c)}{n_{c,low}\Delta\rho_c^2 P(q)} \dfrac{n_{c,low}}{n_c}$.

Following procedures described in Section 5.3, we extract the three partial structure factors for PEG 1000 R_p=0.45, and ϕ_c=0.3. Raw experimental scattering intensities are shown as a function of scattering vector in Fig. 8.4 for different D_2O/H_2O ratios.

Scattered intensity at 20 °C is shown in Fig. 8.4a at low D_2O concentrations (labeled as 'A') where the scattering is dominated by the particles and which is proportional to $\Delta\rho_c P_c(q)S_{cc}(q)$. One sees the existence of a well-defined plateau zero angle limit indicating a stable particle suspension, a first peak in $S_{cc}(q)$ associated with liquid-like particle packing, and decaying intensity as wave vector increases. The oscillations at large wave vector are associated with $P_c(q)$ as $S_{cc}(q)$ approaches unity. As the D_2O concentration increases, substantial qualitative changes are observed in the scattering profile. At $x_D/(x_H+x_D)$ =0.90 (labeled as 'B'), the first peak

in S_{cc} decreases as expected for decreasing $\Delta\rho_c$, while losing information about P_c at high q. Scattered intensity over the range of q-vector and the first peak in S_{cc} continuously decrease till $x_D/(x_H+x_D)$ reaches to 0.975. The second peak in $P_c(q)$ moves to high q-vectors implying new peaks associated S_{pc} and S_{pp} begin to emerge near the position of second peak of $P_c(q)$. At $x_D/(x_H+x_D)$=1.000 (labeled as 'D'), the first peak in S_{cc} is no longer observable, while the S_{pc} and S_{pp} contributions begin to dominate the measured scattering intensity as the condition $\Delta\rho_p >> \Delta\rho_c$ is approached.

At low temperature we assume $\Delta\rho_c$ to be 20 °C and determine the accurate n_c from

$$n_c = \frac{I_{20°C}(q)}{\Delta\rho_c^{\,2}{}_{20°C} P_c(q) S_{cc,20°C}(q,\phi_c)}.$$

At a particular D_2O/H_2O ratio, Eq.(5.1) is simplified to $I_k(q)=a_k+b_k S_{pc}(q)+c_k S_{pp}(q)$ where the only unknowns are $S_{pp}(q)$ and $S_{pc}(q)$, and a_k and b_k are known q-dependent constants and c_k is a known q-independent constant where the subscript k denotes the D_2O ratio. We solve these simultaneous equations via multiple linear regression fitting methods using $I(q)$ measured at 5 D_2O/H_2O ratios corresponding to $\Delta\rho_c$~0 and four intermediate values close to $\Delta\rho_c$=0, which thereby yields $S_{pp}(q)$ and $S_{pc}(q)$. We note calculated R-square statistics at 20 ^oC was close to the unity (0.9797) in Table 8.1 Fig. 8.4b shows the scattering intensity at 70 °C for the same set of samples. At low $x_D/(x_H+x_D)$=0.175, the peak associated with structure of the first nearest neighbors disappeared forming a plateau at low q-vectors. The loss of a peak indicates a reduction in correlations in the centers of mass of the silica particles and can be associated with a reduction in the magnitude of the potential of mean force. As the D_2O concentration increases, the scattering intensity decreases dramatically but one notes the scattering intensity at the same D_2O concentration at 70 °C is much higher than that of 20 °C. For example, at $x_D/(x_H+x_D)$ =0.90,

the intensity is in the order of 10^1 at 20 °C but in the order of 10^2 at 70 °C indicating scattering from the particles contributes to the total intensity more at 70 °C than at 20 °C. Even at $x_D/(x_H+x_D)$=1.000 the scattering patterns at long range of qD resemble the form factor with slight suppression of intensity at low qD. The peak associated with the form factor at qD~9-12 moves to the higher qD as D_2O concentration increases.

The extraction of all partial structure factors at high temperature become more challenging since i) scattering length density can vary with temperature,[14,15] ii) scattering from polymer-polymer density fluctuations is very weak due to reduced polymer adsorption, iii) the particle cross section may vary due to changes in porosity and adsorption of water and iv) due to the size of the particles, slight changes in $\Delta\rho_c$ can greatly amplify the scattering contribution of the particles. As a result in reducing the high temperature data we assume that at $x_D/(x_H+x_D)$ =0.175, particle scattering dominates the scattering intensity

In attempting to extract particle structure factors at 70 °C, we find that if we use $\Delta\rho_c$ =1.05×10^{-11} $Å^{-4}$ to solve the equation, which is calculated from 20 °C at R_p=0.45, R-square statistics drops to 0.2096 implying it is not at the match condition due to the experimental difficulties listed above. At 70 °C matching the cross section of silica particles at R_p=0.45 is challenged since scattering from silica is too strong due to its porous and relatively large volume. Thus, to take into account these effects, scattering length density for $\Delta\rho_c$ needs to be increased at 70 °C. There are two possible contributions to this change: i) the change in particle cross section or ii) the change in bulk scattering cross section. For our purposes we assume the changes arise solely due to changes in the particle cross section. Keeping cross sections of polymer, H_2O and D_2O constant noting $\rho_s= x_H\rho_H + x_D\rho_D + x_P\rho_P$, only ρ_c is allowed to vary with temperature. If one looks for the origin of increasing $\Delta\rho_c$ from ρ_s, one plausible idea is to increase x_P since the bulk

polymer concentration can be slightly increased in that desorbed polymer segments move to the bulk. However, even when x_P is allowed to increase within a reasonable range (0.45 to 0.55), we are unable to alter ρ_s sufficiently to predict the needed change for $\Delta\rho_c$. Temperature dependences of ρ_H, ρ_D and ρ_p could also alter $\Delta\rho_c$, but, remain unknown and these are not expected to vary sufficiently to yield the observed change. Essentially very small changes in ρ_c can result in particle scattering dominating the signal. To test this hypothesis, ρ_c is allowed to vary from 3.90×10^{-6} Å^{-2} at 20 °C to 4.40×10^{-6} Å^{-2} at 70 °C. *R*-square statistics are shown at different ρ_c in Table 8.1 giving more reliability as ρ_c is increased

In Fig. 8.5 the finalized collective structure factors are shown. $S_{cc}(q)$ which is insensitive to choice of ρ_c, shows the structure associated with a liquid-like nanoparticle packing. As expected from the study in Chapter 3, particles experience more attractive forces at higher temperature resulting in more compressible particle subsystem and reduced particle order. Also, the position of the first peak moves to higher values indicating the distance of particle center of masses is reduced. We attribute this to the reduced polymer adsorption with reduced solvent quality.

$S_{pp}(q)$ in Fig. 8.5b is obtained from the polymer segment-segment density fluctuations. At 20 °C the "microphase-like" peak in $S_{pp}(q)$ occurs at qD~5 on a particle length scale confirming that the physical origin is from spatial correlations between adsorbed polymer with non-bulk like properties mediated by nanoparticles. Thus, size scale deduced from the peak greatly exceeds the radius of gyration of PEG 1000 corresponding to $qD\sim 2\pi D/R_g$~193. As qD approaches to zero, the long wavelength concentration fluctuations slightly decrease and become nearly constant. At elevated temperature of 70 °C, the "microphase-like" peak disappears and is a shoulder implying fewer polymer segments are adsorbed. Still, a feature associated with perturbed adsorbed

polymer segments could exist on a particle length scale, however, it is buried under the concentration fluctuation on a larger wave vector scale related to long wave length density fluctuations. These observations at 70 °C is unique directly showing the change of polymer segment distributions upon a change in solvent quality with increased temperature and are consistent with FID experiments relating to the reduced fraction of glass-like polymers in the composites at elevated temperatures.

$S_{pc}(q)$ is also given in Fig. 8.5c supporting the observed trends.

To characterize adsorbed polymer layers, we consider the polymer shell form factors resulting from the non-bulk like polymer concentration fluctuations. As we already introduced in Chapter 6, the experimental shell form factor ($P_s(q)$) obtained from $S_{pp}(q)/S_{cc}(q)$ is given in Fig. 8.6. $P_s(q)$ also shows the effect of temperature change. At 20 °C $P_s(q)$ is distinguished from particle form factor and yield the adsorbed thickness ~1.5 nm when the cross section of particle, solvent phase and polymer layer was given as $\rho_c=3.90\times10^{-6}A^{-2}$, $\rho_s=3.85\times10^{-6}A^{-2}$ and $\rho_{shell}=3.51\times10^{-6}A^{-2}$ at the match point 'D'. With a given $\rho_c=4.50\times10^{-6}A^{-2}$ at 70 °C $P_s(q)$ yields a layer thickness of 0.25 nm also noting the first minimum of $P_s(q)$ moves to the high qD, and it becomes close to what is expected for a bare particle form factors again implying the reduced polymer adsorptions.

Taken together, this study shows the origin of changing particle stability with increasing temperature can be attributed to the decreased polymer adsorption. When solvent quality is decreased, it was not clear we would expect increased or decreased polymer adsorption as a composite strength of segment-surface interaction will depend on segment surface and solvent surface interactions as well as polymer-polymer, polymer solvent and solvent-solvent interactions encountered in standard definitions of solvent quality. The $S_{pp}(q)$ results indicate a

reduction in the amount of adsorbed polymer segments while FID results support there is increase of bulk-like polymers and a decrease of glass-like polymers upon temperature increase.

Hammouda showed the chain collapse of PEG in water at high temperatures with fitted scattered intensity to Porod model.[8] These scattering experiments were carried out in dilute conditions of 0.3 to 4 weight percent of PEG 41500 in D_2O at various temperatures from 10 to 80 °C. Scattering intensity was analyzed with Porod exponent showing that the polymer chain varied from swollen chains at low temperature to Gaussian coils even well below the LCST. We note our experimental system is well below the LCST (~180 °C for PEG 1000)[5] and polymer concentration is well above the critical concentration (R_p~0.3) where the minimum of LCST boundary starts. Based on the state points at which we worked, we might anticipate marginal changes to polymer structure. The observed significant changes in particle microstructure and polymer dynamics with the small changes expected in polymer structures are thus rather surprising.

PEG segments can adsorb on silica particles with hydrogen bonding, thus, interactions between SiO group on silica particle and OH of PEG are important. We expect collapsed chains can reduce the effective interaction with particle surface and therefore, the reduce polymer adsorption.

Russel *et al.* describe the interactions between polymer layers with terminally anchored chains onto particles. In this approach the Helmholtz free energy of a polymer solution is calculated and the solvent quality is taken into account with physical volume per polymer segments and excluded volume per segment.[16,17] The experiments were conducted with silica spheres (88 nm) with end-grafted polystyrene of M_w=26600 g mol^{-1}, suspended in cyclohexane and fitted to the free energy model. On moving from good to theta to poor solvents, the

stabilizing layers shrink and yield attractive pair potentials. Conclusively, the particle stability is reduced and particle subsystem becomes more compressible.

Interactions between the surface and polymer segments for physically adsorbed cases are more complicated. However, Russel *at al.* report trends similar to those observed here. The long range interaction is repulsive with adsorption and full coverage in theta or good solvent, but becomes attractive in poor solvent conditions.[17] Furthermore, strong attractions occur in poor solvents with the same mechanisms as for the anchored polymers.

8.4 Summary

In this study we employed new techniques to capture the variation of particle structures with polymer-induced interactions. Whereas solvent quality was known to change the relative interactions among polymer segments, particle surface and solvent, characterization of these effects has been challenging especially in concentrated systems. FID experiments show that PEG segments can desorb from silica particle surfaces with increasing temperature changing adsorption equilibrium. Small angle neutron scatterings enabled us to observe scatterings from polymer-polymer density fluctuations. Polymer segment collective structure factors show that increased temperature enhances the concentration fluctuations at a long range length scale and decreases the extent of polymer layers near particle surfaces. The results presented here strengthen the observations of collapsed or shrunken polymer chains in poor solvents that yield effective attractive potentials.

8.5 Table and Figures

Temp.	ρ_c(Å^{-2})	$\Delta\rho_p^2$ (Å^{-4}) at $x_D/(x_H+x_D)$=1	$\Delta\rho_c^2$(Å^{-4}) at $x_D/(x_H+x_D)$=1	Average R^2 at q-0.003~ 0.009Å^{-1}
20°C	3.90×10^{-6}	9.73E-12	1.47E-14	0.9797
70°C	3.90×10^{-6}	9.73E-12	1.47E-14	0.2096
	4.10×10^{-6}	9.73E-12	1.03E-13	0.8262
	4.30×10^{-6}	9.73E-12	2.71E-13	0.9244
	4.50×10^{-6}	9.73E-12	5.20E-12	0.9501

Table 8.1 Scattering length density calculation at $x_D/(x_H+x_D)$=1 for various ρ_c and R^2 statistics from the solution of simultaneous equations holding $\rho_p=6.60\times10^{-7}A^{-2}$.

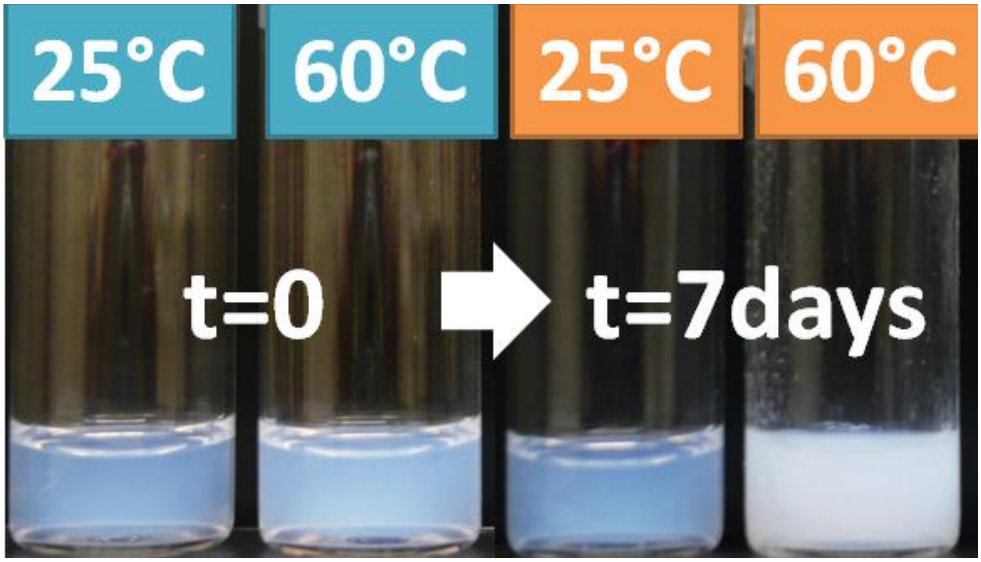

Figure 8.1 Observation of nanoparticle stability at PEG 400 R_p=0.2, ϕ_c=0.1

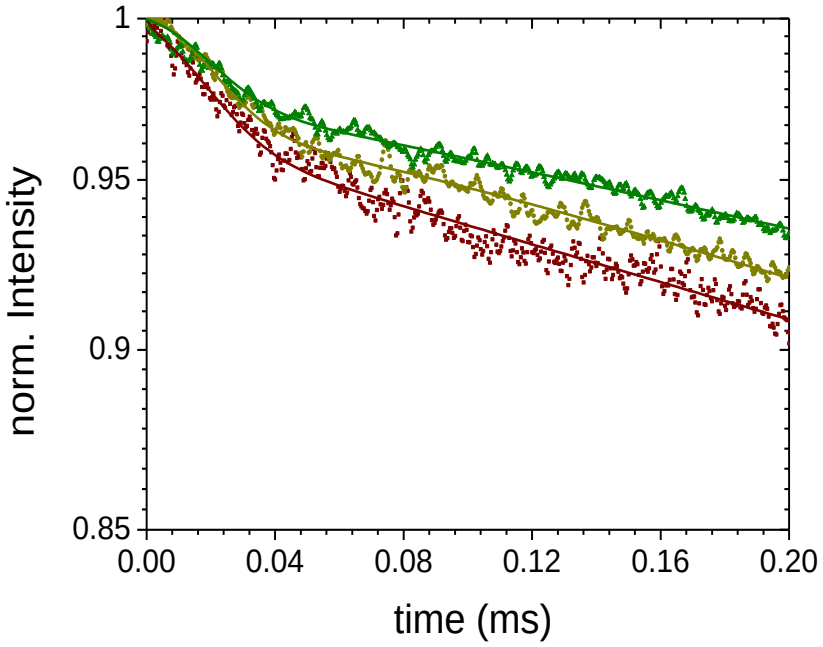

Figure 8.2 Normalized MSE-FID intensity as a function of time at R_p=0.5 PEG 3000 at ϕ_c=0.3 with varying temperature from 30 to 50 and 70 ℃.

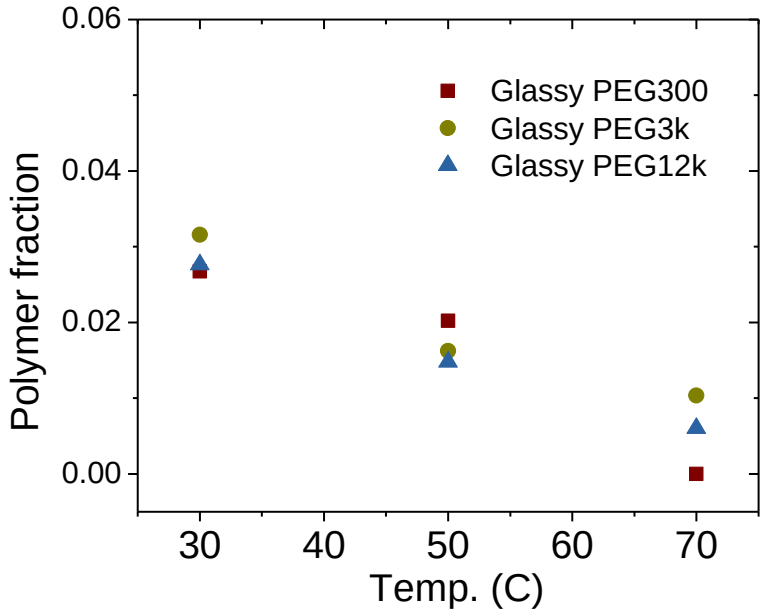

Figure 8.3 Glassy polymer fractions at each temperature with different PEG molecular weight.

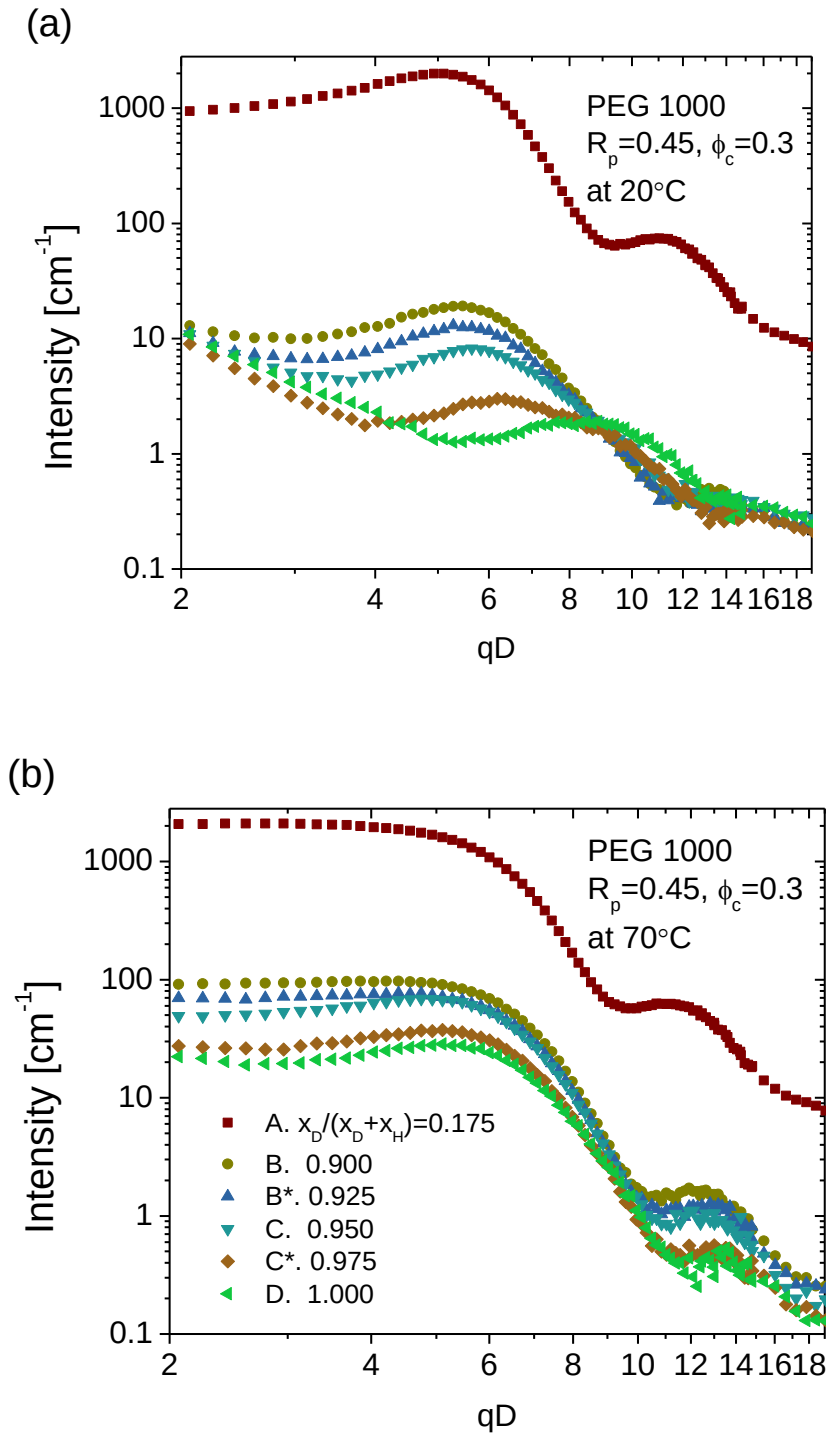

Figure 8.4 (a) Scattering intensity ($I(q)$) data at 20 °C as a function of normalized wave vector. While particle volume fraction is fixed at 0.3 and R_p=0.45. $x_D/(x_D+x_H)$ are varied as pointed out in the legend (b). (b) Scattering intensity ($I(q)$) data at 70 °C in the same way as (a).

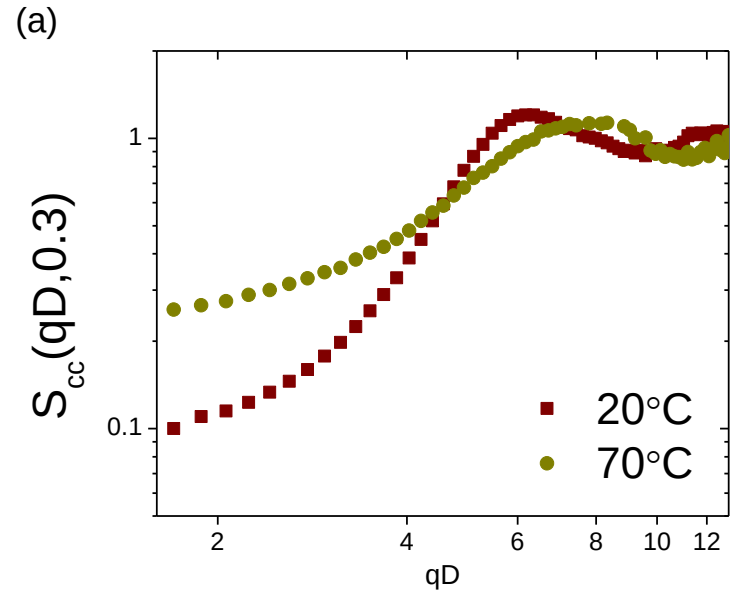

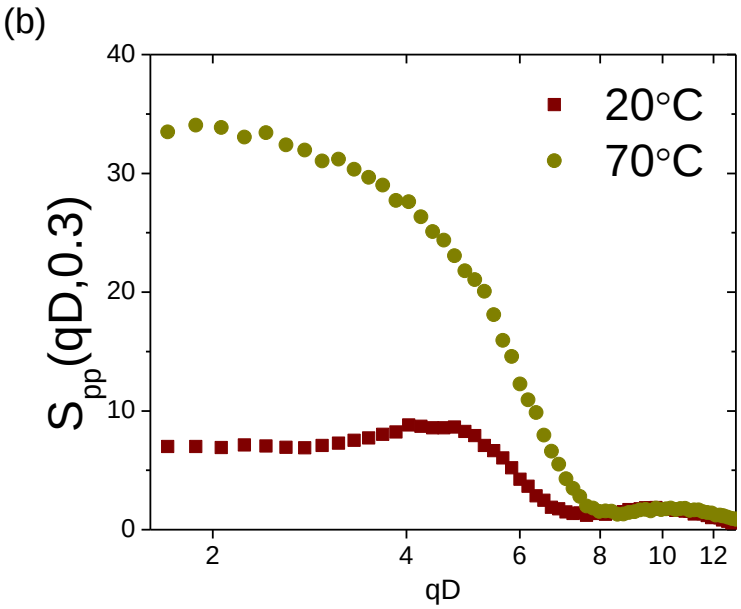

Figure 8.5 (cont. on next page)

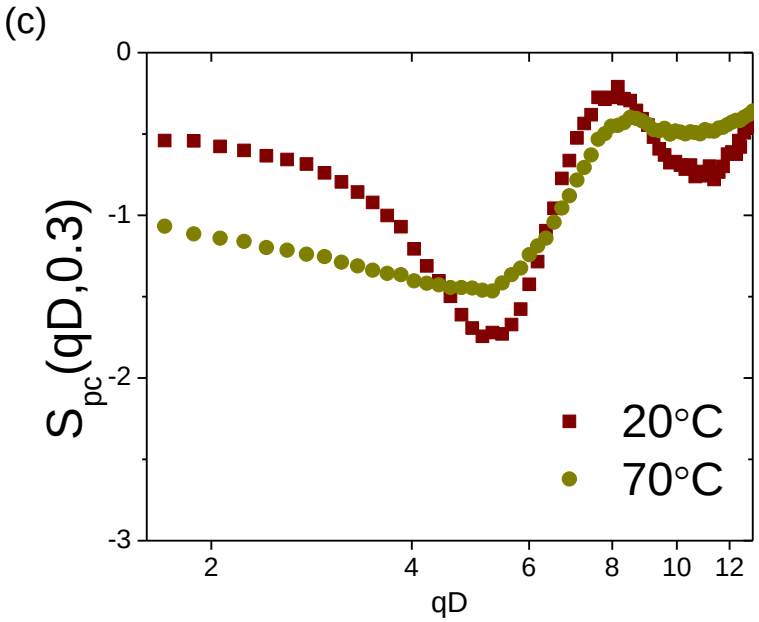

Figure 8.5 (a) Particle-particle correlation structure factor as a function of reduced wave vector at 20 °C and 70 °C at a fixed ϕ_c=0.3 (b) polymer segments-segments correlation structure factor under same condition (c) interfacial correlation structure factor under same condition.

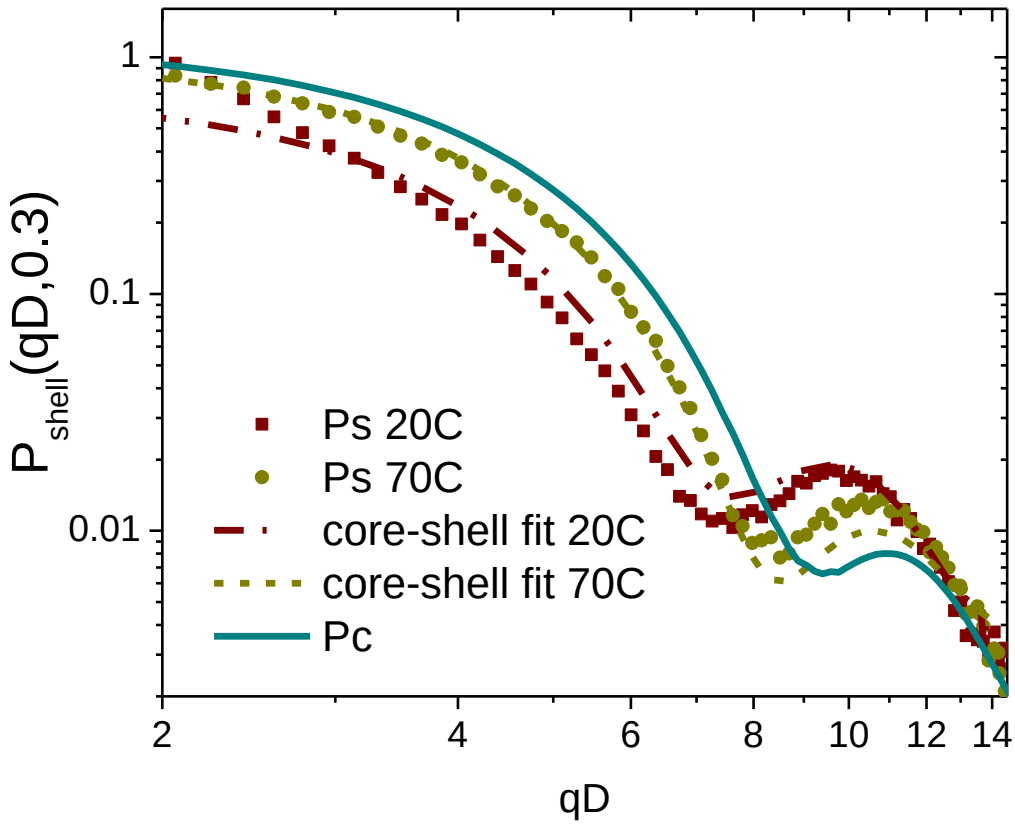

Figure 8.6 Polymer shell form factor as a function of reduced wave vector at 20 °C and 70 °C at a fixed ϕ_c=0.3.

8.6 References

1. Cox, H. L.; Cretcher, L. H. *J. Am. Chem. Soc.* **1926**, *48*, 451.
2. Kjellander, R.; Florin, E. *J. Chem. Soc. Farad. T.1: Physical Chemistry in Condensed Phases* **1981**, *77*, 2053.
3. Malcolm, G. N.; Rowlinson, J. S. *T. Faraday Soc.* **1957**, *53*.
4. Polik, W. F.; Burchard, W. *Macromolecules* **1983**, *16*, 978.
5. Saeki, S.; Kuwahara, N.; Nakata, M.; Kaneko, M. *Polymer* **1976**, *17*, 685.
6. Pattanayek, S. K.; Juvekar, V. A. *Macromolecules* **2002**, *35*, 9574.
7. Mehrdad, A.; Akbarzadeh, R. *J. Chem. Eng. Data*, *55*, 2537.
8. Hammouda, B.; Ho, D. L. *J. Polym. Sci. Pol. Phys.* **2007**, *45*, 2196.
9. Kim, S. Y.; Zukoski, C. F. *Langmuir* **2011**, *27*, 5211.
10. Mauri, M.; Thomann, Y.; Schneider, H.; Saalwächter, K. *Solid State Nucl. Mag.* **2008**, *34*, 125.
11. Maus, A.; Hertlein, C.; Saalwächter, K. *Macromol. Chem. Physic.* **2006**, *207*, 1150.
12. Kline, S. R. *J. Appl. Cryst.* **2006**, *39*, 895.
13. Papon, A.; Saalwächter, K.; Schäler, K.; Guy, L.; Lequeux, F.; Montes, H. *Macromolecules* **2011**, *44*, 913.
14. Sears, V. F. *Neutron News* **1992**, *3*, 26.
15. May, R. P.; Ibel, K.; Haas, J. *J. Appl. Cryst.* **1982**, *15*, 15.
16. Cosgrove, T. *Colloid Science principles, methods and applications*; Blackwell Publishing Ltd: Oxford, 2005.
17. Russel, W. B.; Saville, D. A.; Schowalter, W. R. *Colloidal Dispersions*; Cambridge University Press: Cambridge, UK, 1989.

CHAPTER 9 CONCLUSION

In this thesis the state of particle dispersions and polymer dynamics in concentrated polymer solutions and melts were examined with extensive small angle scattering and NMR experiments. The different particle microstructure resulted from suspending nanoparticles in low molecular weight polymer solutions, were explored for a wide range of condition.

Quantitative comparisons were made with the Polymer Reference Interaction Site Model (PRISM) predictions of structure factors. One key result is that the degree of particle stability is a nonmonotonic function of the strength of polymer segment-particle contact attraction strength, ε_{pc}. While a very small or large ε_{pc} compared to thermal energy results in depletion attractions and bridging aggregations, respectively, only at intermediate ε_{pc} adsorbed polymer layers form that remain discrete, nonoverlapping, and thermodynamically stable.

In dense polymer solutions, often polymer-to-solvent ratios in the suspending medium alter the particle stability. When 40 nm silica nanoparticles were suspended in poly(ethylene) glycol (PEG)-ethanol mixtures, increasing polymer concentrations increases the local order structures and decreases the compressibility resulting from the enhanced interfacial attraction between polymer segments and particles where ε_{pc} actually represents the overall enthalpic gain of transferring a monomer from the continuous suspending phase to the particle surface.

When water is substituted for ethanol for diluting the polymer the particle subsystem compressibility and local order become indifferent to changes in polymer-to-solvent ratios. In the presence of lower critical solution temperature (LCST) such as PEG-water solutions, particle stability is greatly reduced with increasing temperatures. While the observed changes were well-captured with PRISM predictions when ε_{pc} is varied, the effects of solvent quality were even

more pronounced at the temperatures well below LCST. In addition polymer collective structure factors showed the increased polymer concentration fluctuations, compressibility and decreased polymer adsorption as temperature rises. Free induction decay NMR experiments quantitatively support the reduced amount of adsorbed polymer segments on the particle surface probing different polymer dynamics.

The effect of polymer chemistry on the particle microstructures were examined when PEG was compared with poly(ethylene glycol) dimethyl ether (PEGDME) and polytetrahydrofuran (PTHF). From the analysis of the scattering structure factor ε_{pc} decreases reduced from PEG to PTHF and PEGDME demonstrating the decreased binding affinity to the particle surface and relative importance of backbone chemistry and end-group functionality. Flow properties such as intrinsic viscosity showed polymer segments can adsorb and increase effective particle diameter or can slip on the particle surface depending on the interfacial attractions ε_{pc}.

Using contrast matching neutron scattering all partial structure factors in concentrated polymer-particle mixtures were measured. Both polymer and particle concentration fluctuations, and their cross-correlation, are predicted very well by microscopic PRISM theory based on a single key parameter, the strength of polymer segment–particle interfacial attraction, ε_{pc}. The results were consistent with particle miscibility being associated with thin adsorbed (thermodynamically stable) polymer layers that provide steric stability for a window of segment/surface attraction strengths.

Exploiting magic-sandwich echo (MSE) NMR experiments, which refocus the initial part of the free-induction decay (FID) and thus avoids the dead time issue, we were able to capture polymer relaxations at short time scales. FID-NMR experiments quantified the polymer mobility

revealing the existence of glassy-like polymer in the presence of particles. Generally, the amount of glassy segments increases with particle volume fraction but, is independent of polymer molecular weight. Multiple-quantum (MQ) NMR experiments were carried out to link to the presence of topological constraints such as cross-links and/or entanglements. The MQ experiments provide a sensitive measure of spin relaxation since they measure the residual dipolar coupling and thus the local dynamic order parameter on an absolute scale. The amount of particle induced network formation grows with polymer molecular weight and particle concentration above the entanglement molecular weight. Increasing molecular weights help a polymer in the bulk to entangle with chains adsorbed to two different particles.

In silica-PEG solutions as the polymer molecular weight increases system becomes more compressible and particles are less stable. The observed trends were only captured when PRISM was allowed to vary the size ratio of particle diameter to polymer segment diameter such that molecular weights increases, such that the size ratios of particle diameter to polymer segments (*D/d)* decreased. In adjusting total packing fractions, decreasing *D/d* ratios greatly reduces the polymer packing fractions, thus, implying increasing polymer molecular weights needs to be considered from a mixing and packing fraction perspective. Polymers have longer range correlations and increasing concentration fluctuations with increasing molecular weights. In addition the adsorbed polymer shell form factors indeed confirm that layer thicknesses increase when particles are suspended in concentrated solutions containing longer polymer chains.

Overall, this thesis provided a detailed analysis on the state of particle dispersions when polymer induced interactions were differentiated from changes in experimental condition. With the ability of the theory to predict the local order, compressibility and collective structures small angle scattering experimental studies investigated how particles are dispersed

thermodynamically, while complementary NMR experiments revealed the variation of polymer dynamics. As a consequence the study showed the ability to control the particle dispersions in a desired manner while providing deeper understanding of a direct relation of dispersions to the physical properties remain a topic for further investigation. Practical studies on the precise control of particle dispersions via particle surface functionality and further studies on the structural changes at the instability regions resulting from depletions will be also worthwhile.